REPORT NO.
UCD/CGMDR-21/01

CENTER FOR GEOTECHNICAL MODELING

DATA REPORT FOR SKS02:

CENTRIFUGE TESTING OF LIQUEFACTION-INDUCED DOWNDRAG ON AXIALLY LOADED PILES

BY

S. K. SINHA

K. ZIOTOPOULOU

B. L. KUTTER

DEPARTMENT OF CIVIL & ENVIRONMENTAL ENGINEERING
COLLEGE OF ENGINEERING
UNIVERSITY OF CALIFORNIA AT DAVIS

January 2020
(Revised July 2020)

CENTRIFUGE TESTING OF LIQUEFACTION-INDUCED DOWNDRAG ON AXIALLY LOADED PILES
Centrifuge Data Report for SKS02

S.K. Sinha, K. Ziotopoulou, B.L. Kutter

Center for Geotechnical Modeling Data Report UCD/CGMDR – 21/01

Date:	January, 2020
Date of testing:	10-12th July, 2019
Project:	Validation of Design for Liquefaction-Induced Downdrag on Piles
Sponsor:	California Department of Transportation (CALTRANS)

ACKNOWLEDGEMENTS

This work was supported primarily by the California Department of Transportation (CALTRANS) under the project titled 'Validation of Design for Liquefaction-Induced Downdrag on Piles'. The contents of this report are solely the authors' and do not necessarily reflect the views or opinions of the sponsors. The authors would like to acknowledge the suggestions and assistance of Dan Wilson, Tom Kohnke, Chad Justice and Anatoily Ganchenko of the UC Davis CGM and the UC Davis undergraduate researchers Scott Proctor and Evan To. The author would also like to acknowledge the students of the Ziotopoulou research group (Brian Morales, Maya El Kortbawi, Renmin Pretell and Francisco Humire), researchers at CGM (Soham Banerjee, Srikanth Madabhushi and Professor Mohammad Khosravi) for their help during the various stages of model preparation. The author would also acknowledge the help towards the development of the large centrifuge at UC Davis, which was supported primarily by the National Science Foundation (NSF) via the Natural Hazards Engineering Research Infrastructure (NHERI) and Network of Earthquake Engineering Simulation (NEES).

CONDITIONS AND LIMITATIONS

CONTENTS

LIST OF FIGURES

LIST OF TABLES

1 ABSTRACT

Earthquake-induced liquefaction can cause soil settlement at pile interfaces, which can induce negative skin friction resulting in additional load (known as drag load) and drag the pile downwards (Figure 1). Despite significant research on the effects of liquefaction on structures and the seismic response of piles, there is still a knowledge gap in the evolution and assessment of liquefaction-induced downdrag on piles mainly related to the complex interplay and timing of the different mechanisms during/post liquefaction such as excess pore pressure generation/dissipation patterns, sequencing and timing of settlements, presence of interface gaps and ejecta, location of the initial neutral plane, and settlement around the tip. This has led to simplifying assumptions in current design procedures, which might result in over-conservatism in drag load estimation. Commonly used numerical tools lack the ability to model these mechanisms, while the absence of experimental data hinders the development and validation of new models. A series of centrifuge tests were planned to investigate the factors affecting the magnitude of liquefaction-induced drag load and pile settlement. This report describes the results for the first test series (SKS02). The soil profile included 1 m of coarse sand layer, underlain by 4 m of clay crust and 9 m of liquefiable soil over deeper dense soil. The test involved two medium diameter (D) piles, with their tip embedded to the depth of 0D and 5D in the dense sand. The model was shaken with multiple scaled Santa Cruz earthquake motions with peak horizontal accelerations ranging from 0.025 g to 0.4 g. With multiple shakings, drag loads were observed to increase on the piles. Higher drag loads were observed on deeply embedded (5D) piles as compared to the shallow embedded (0D) pile. While significant settlements occurred in soil during and post shaking, the piles recorded considerably smaller settlements. Most of the pile settlement occurred during shaking and very small settlements happened during the reconsolidation phase. It was observed, that with multiple shakings, the overall drag load on the piles saturated and could become as large as the one interpreted from considering the negative skin friction on the pile in the liquefiable soil taken equal to the positive interface drained shear strength.

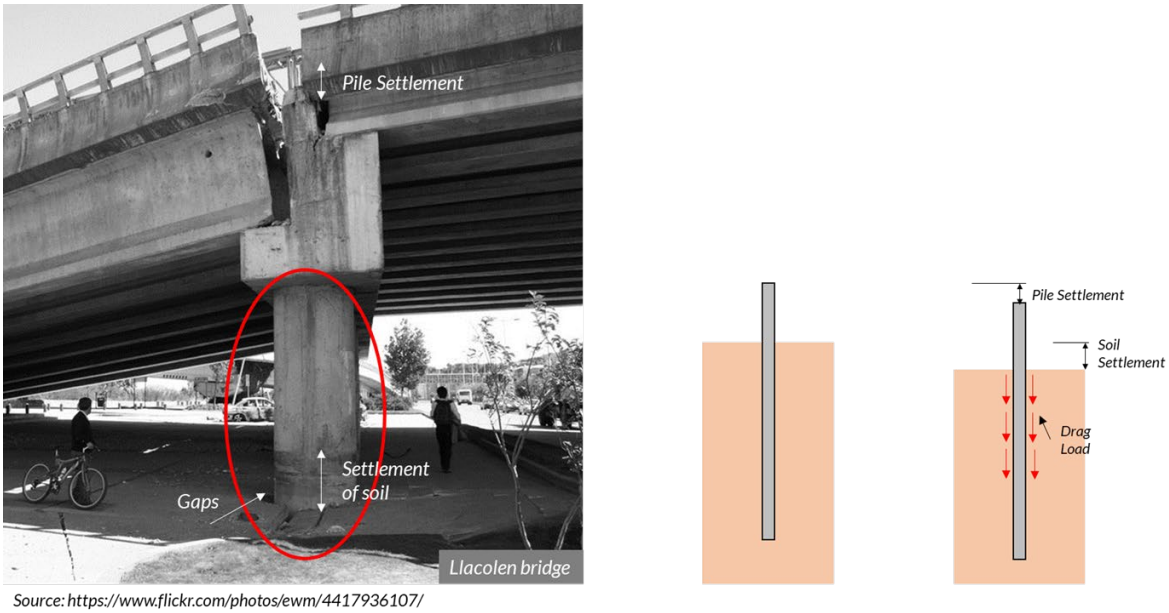

Figure 1. Liquefaction-induced settlement results in drag load and settlement in piles.

2 PROBLEM STATEMENT

During strong shaking events, excess pore pressure generated in saturated soils can cause liquefaction and an associated loss of strength, settlement, and depending upon the boundary conditions lateral spreading. This not only weakens the overall soil-pile stiffness but also imposes additional vertical and lateral loads on the pile, which can lead to several possible pile failure modes such as bearing failure, buckling, bending and excessive settlement. For axially loaded piles, the soil settlement shifts the neutral plane (i.e., location of zero relative soil-pile settlement) downwards and generates drag loads (see Figure 2). This not only increases the overall load on the pile but also reduces the overall resistance provided by skin friction (as only layers below the neutral plane are engaged), resulting in an overall increase of load and settlement at the tip. At the same time, the tip movement and the settlement of soil around it can also influence the axial load distribution in the pile i.e. the magnitude of drag load and location of neutral plane. (AASHTO 2014) uses the load-resistance method to design piles. It assumes that the neutral plane is located at the bottom of the deepest liquefiable layer, a "residual strength" acts on the pile in the liquefiable zone and non-liquefied skin friction acts on the pile in the non-liquefiable layers. In the absence of specific guidelines on how to determine the negative interface shear strength on the pile in the reconsolidated liquefied soil, it is often assumed to be equal to the positive interface drained shear strength. The assumptions of the negative interface shear strength and the use of a force-based approach may result in conservative (long piles) or unsafe design. At the same time in existing piles, the current procedure may lead to excessive demands resulting in pile settlement which may exceed the serviceability criteria.

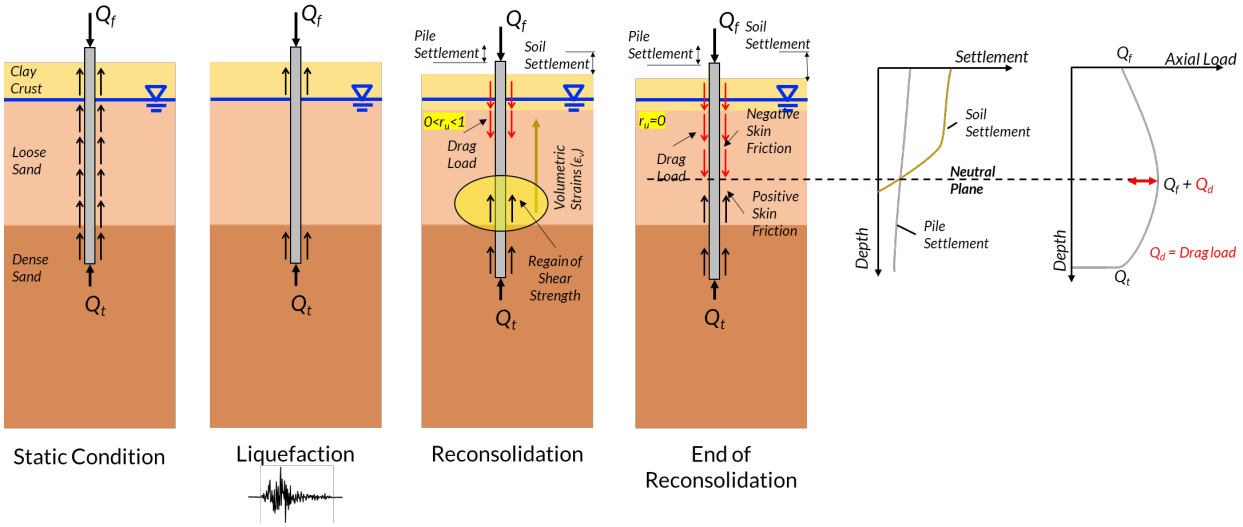

Figure 2. Conceptual schematic diagram of development of liquefaction-induced downdrag on piles.

2.1 Factors Affecting the Downdrag Phenomenon

The response of axially loaded piles in liquefiable soils is a continuous phenomenon from the beginning of earthquake to the end of the reconsolidation phase as shown in Figure 2. In the static state i.e., before the onset of earthquake, the neutral plane can be at the surface or it could be deeper due to consolidation-induced settlement in the soil arising from the application of surcharge load, changes in ground water condition and post installation effects. If the neutral plane is initially at the ground surface, the resistance to the pile head load (Q_f) is provided by the full skin resistance and the tip resistance. With the onset of strong seismic loading, the excess pore pressures start to develop in loose saturated soils, thus decreasing

the shear strength and lowering the skin friction. As a result, the tip settles to resist the extra load transferred. During full liquefaction, the skin friction of the liquefied soil can become essentially zero, resulting in further settlement of the tip. Once the reconsolidation phase starts, excess pore pressures in soil start to reduce, and the lost shear strength is regained. However, the reconsolidation results in soil settlement which develops negative skin friction at the pile's interface above the neutral plane. As a result, significant drag loads are developed which not only increase the load on the pile but also reduce the thickness of the soil layers that participate in resisting the load through skin friction. This extra load is again transferred to the tip. Upon full reconsolidation, the drag load fully develops, and the tip settles even more, which might lead to an exceedance of serviceability criteria.

While the above concepts are reasonable based on our current understanding, there is a complex sequence of many processes that could determine and influence the development of downdrag in axially loaded piles (Figure 3). The next section describes these factors affecting liquefaction-induced downdrag phenomenon.

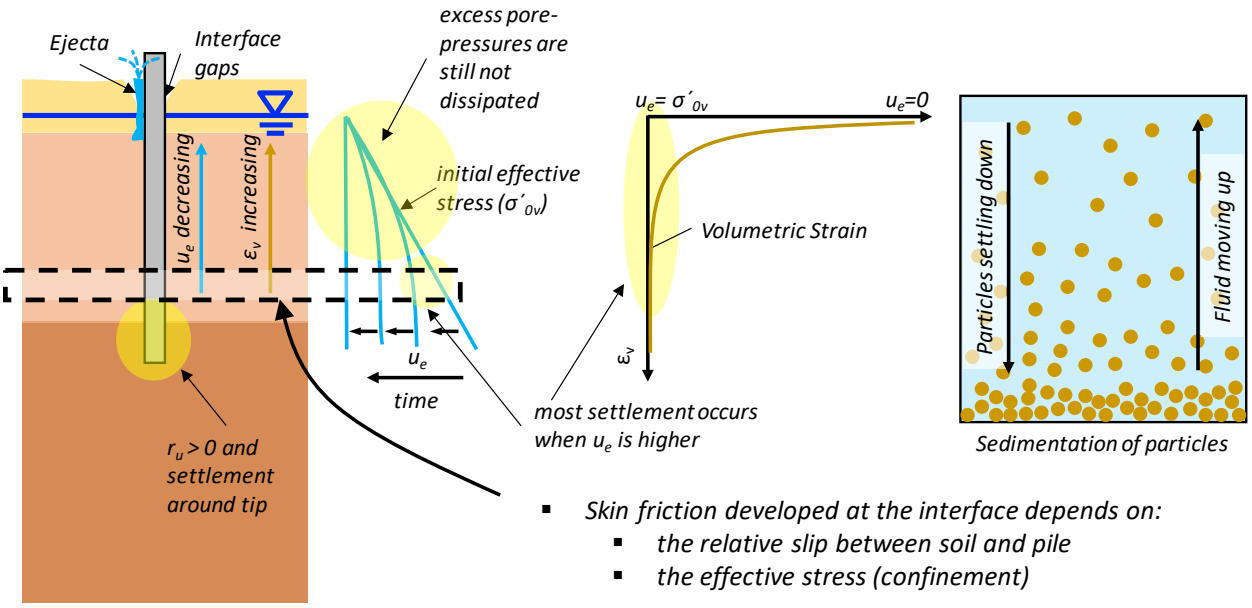

Figure 3. Illustration of the mechanisms affecting liquefaction-induced drag load.

2.1.1 Soil Profile and Pile Type

The soil profile itself can greatly influence the development of drag load. Presence of a liquefiable layer in interbedded deposits, below dense layer or clay layer has not been studied. A thicker liquefiable layer results in higher reconsolidation strains and thus higher drag loads. Another factor can be the pile diameter (L/D ratio) and tip condition. Since the neutral plane is the zone of zero relative movement between pile and the soil, a floating tip can result in less drag load and higher downdrag settlement as compared to the rigid tip**.** Consequently, a pile with larger diameter will result in smaller tip movements and higher drag loads. Sinha et al. (2019) discussed the effect of pile head load, pile tip condition, pile diameter, liquefiable layer thickness, reconsolidation strain and reconsolidation near tip on the generated drag load and downdrag.

2.1.2 Excess Pore Pressure Dissipation and Settlement Pattern

Coelho et al. (2004) performed dynamic centrifuge testing and showed that excess pore pressures and post-liquefaction reconsolidation does not only develop in loose but can also develop in dense saturated sands. Knappett and Madabhushi (2006) showed that as excess pore pressures at the pile tip increases, the load

carried by the pile tip reduces and settlement increases. This reduction in pile tip capacity and shaft friction could result in higher downdrag but a smaller induced drag load. Blast induced liquefaction studies by Rollins and Strand (2006), measured the skin friction in the reconsolidated soil to be around 50% of the positive skin friction before liquefaction. The skin friction in the non-liquefied soils was observed to decrease by 10-20%. However, these experiments have not been monitored for a long time after the event. It is possible that over time the skin friction in liquefied/non-liquefied soils might eventually re-develop to its full capacity.

The excess pore pressure generation/dissipation, its sequencing and duration not only affects the shear strength of soil but also its settlement. During liquefaction, pore pressures are generated from top to bottom and reconsolidation volumetric strains develop in bottom to top fashion. Ashford et al. (2004), Rollins and Hollenbaugh (2015), Rollins et al. (2005) and Rollins and Strand (2006) through blast induced liquefaction tests found out that, while it can take an hour or more to achieve full reconsolidation, 80% of the settlements happened within first 5-10 minutes of blasting. Since, majority of volumetric strain occurs at low effective stresses, the generated skin friction and thus the drag load is expected to be smaller. During reconsolidation, soil settlement at any depth drags the layers above it and induces large relative slip between the soil and pile. For the liquefied layer, the negative skin friction generated would still be smaller due to non-dissipated excess pore pressure. However, for a non-liquefiable layer (such as a clay layer), it may fully mobilize the negative skin friction (see Figure 3).

2.1.3 Interface Gaps and Ejecta

The presence of surface cracks in the crust and gaps at the interface near surface (developed due to shaking of the pile mass) (see Figure 3) can speed up the reconsolidation phase and influence the downdrag problem. The shaft resistance at the gap would essentially become zero and would provide a hydraulic exit for the fluid resulting in ejecta at the surface. This can lead to reduction of drag load as well as speed up the reconsolidation process.

These knowledge gaps have led to some simplifying assumptions in the current state of practice which might result in over conservatism in drag load estimation. The assumption of neutral plane being at the bottom of the liquefiable layer (AASHTO 2014) and the lack of guidelines for selecting the negative skin friction often result in design of piles which are long and expensive. Thus, understanding the above mechanisms is key in estimating and predicting the downdrag settlement and drag load and reducing some of the uncertainties associated in the design procedure. This would result in the cost-effective design of new piles and a more reliable evaluation of existing piles. This report describes the first large centrifuge test SKS02 performed on 10-12th July 2019 as an effort to understand the mechanisms of the downdrag problem.

3 CENTRIFUGE MODEL DESCRIPTION

Preliminary analyses that guided the design of the centrifuge model are described in (Sinha et al. 2019). A medium aluminum pipe pile of outer diameter D = 0.635 m and thickness of 36 mm with slenderness ratio L/D ≈ 20-25 was modeled in a submerged soil profile consisting of 4 m thick over-consolidated clay layer underlain by 9 m of loose sand layer and dense sand below it. A 1 m thick dense relatively permeable coarse grained Monterey sand layer was placed above the clay layer to prevent drying of clay surface from the spinning of the centrifuge and to further enhance the downdrag load. To study the effect of tip embedment, two heavily instrumented piles installed at 1 g were tested with their tip embedded 0D and 5D respectively into the dense sand layer. A mass was attached on the pile head to generate an equivalent axial load of 500 kN (56.4 tons). Dense instrumentation was implemented to track the pore pressure generation/dissipation, settlements in soil and pile, soil layer accelerations and axial loads generated in the piles. New modeling techniques like vacuum transportation to prevent any disturbance of the saturated model, new pore pressure sensors fabricated from an affordable potentiometer ($10/piece) and use of line lasers to track settlements were introduced and used for the first time, offering potential in the advancement of geotechnical centrifuge modeling. Figure 4 and Figure 5 illustrate model layout and instrumentation. The model was tested on the large 9 m radius centrifuge at the Center for Geotechnical Modeling at the University of California Davis.

3.1 Scaling Laws

All numerical quantities within this report unless explicitly specified have been converted into prototype units according to the scaling laws described by Kutter (1992). As an example, the model length is multiplied by the scale factor N to obtain the equivalent length in prototype scale, where N is the centrifugal acceleration applied to the model. For this test, the centrifugal acceleration was 40 g ($N = 40$) at the center of model (8.635 m from the axis of rotation). The angular speed of the centrifuge was 64.4 rpm.

Table 1. Scaling factors in centrifuge testing.

	Parameters		***Model/Prototype***
General	Length [m]	L	$1/N$
	Density [kg/m^3]	ρ	1
	Stress, Strain	σ,τ,ε	1
	Force [N]	F	$1/N^2$
	Mass [Kg]	M	$1/N^3$
	Time [s]	T	$1/N$
Dynamic	Time [s]	T	$1/N$
	Frequency [Hz]	f	N
	Velocity [m/s]	v	1
	Acceleration [g]	a	N
	Diffusion Time [s]	T_{dif}	$1/N^2$

3.2 Cross-section and Layout

Figure 4 shows the plan view of the model in model dimensions (in cm). To convert into prototype scale, all dimensions should be multiplied by the scale factor of N=40. The model consisted of two medium pipe pile: Pile 1 and Pile 2 installed in dense sand with tip embedded of 0D and 5D respectively in the dense

sand layer. The piles were installed in the middle section of the model container (Section E-E) and were separated by 40 cm (~25D) horizontally. The walls of the model container were about 40 cm (~25D) away from both the piles to minimize boundary effects in their responses. A vertical array of accelerometers (Section E-E) and pore pressure transducers (Section E-E and F-F) were placed at the center of the model in between the two piles. Soil settlement markers (SM_1, SM_2), pile linear potentiometers (P_1^{LP}, P_2^{LP}) and line lasers (Laser 1, Laser 2) were installed to track the settlement of the model surface and the piles. Additionally, centrifuge Cone Penetration Test ($CPT_{\#}$), centrifuge Pile Load Test ($PLT_{\#}$), Hand Vane Shear Test ($VS_{\#}$) were performed to monitor the strength of soil at different stages of the centrifuge test. The model consisted of 4 drainage holes (D_1-D_4) of diameter 3.8 cm installed to the depth of the liquefiable layer to allow the dissipation of excess pore pressures beneath the impermeable clay layer.

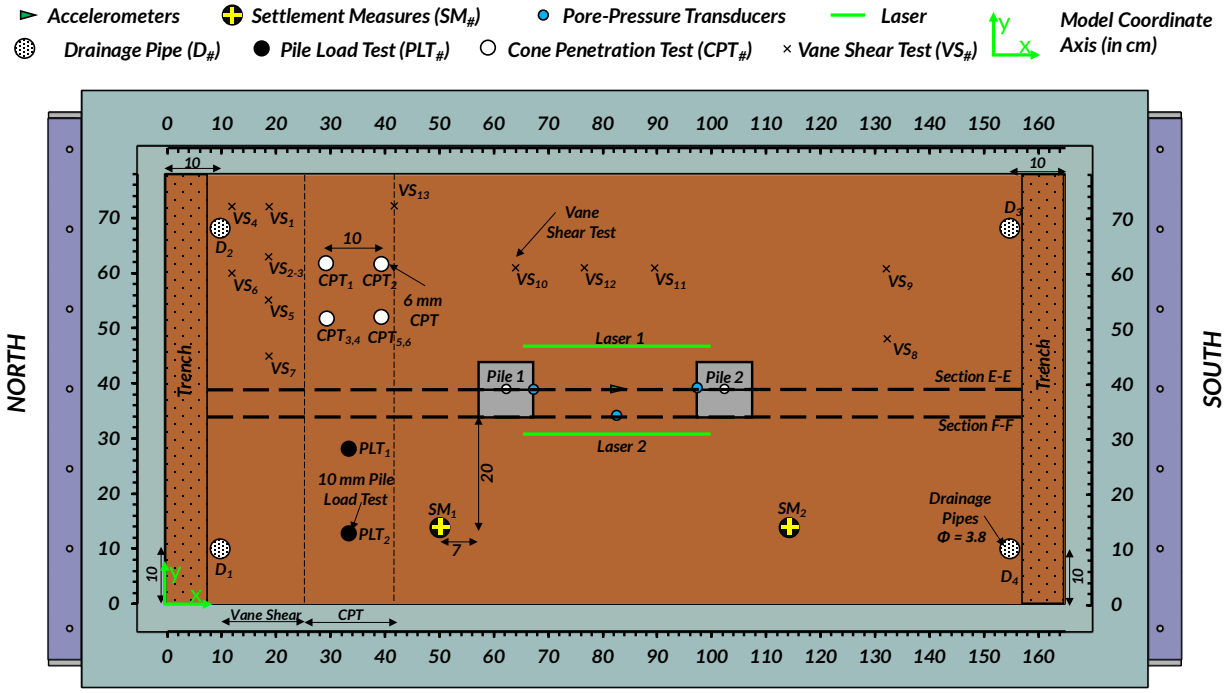

Figure 4. Plan view of the model (dimensions shown in model scale in cm).

Figure 5 shows the cross-section view of the model in model scale (in cm). Table 2 summarizes the soil layer thickness and saturated density. For convenience, on the right side of the model, the prototype depth (in m) measured from the soil surface are shown. The soil profile consisted of 1 m of Monterey sand, 4 m of over-consolidated clay (s_u≈20kPa), 9 m of loose sand (D_r=42 to 45%) and about 7 m of dense sand (D_r=86 to 88%) with the water table at the surface. The pile head mass of the installed piles (Pile 1 and Pile 2) was 1 m above the ground surface. Vertical and horizontal ICP accelerometers and MEMS accelerometer were installed on the pile head mass to monitor accelerations and rotation of pile masses during shaking events. The piles were instrumented with 9 full-bridge axial strain gages spaced 2 m (prototype scale) apart to fully capture their axial load distribution. Just below the clay layer, pore pressures transducers were placed to track the movement of the hydraulic head during and after the shaking event. Few accelerometers were also installed on the base of the model container to measure the input earthquake motion and any vertical accelerations generated. Additionally, horizontal accelerometers were installed on the 4th ring of the model container to measure the response of attached racks used for installing linear potentiometers for measuring the ground surface and pile settlement.

The new MS54XXX SMD PPTs (see Section 4.2.2) shown in yellow color in Figure 5, were used for the first time. The MS54XXX SMD pore pressure sensors were significantly cheaper than the more regularly used Keller PPTs (see Section 4.2.1). However, they had not been tested for dynamic centrifuge tests. The current centrifuge test was used to evaluate their capabilities in measuring dynamic pore pressures and help in the development of methodologies and procedures for their usage in centrifuge tests.

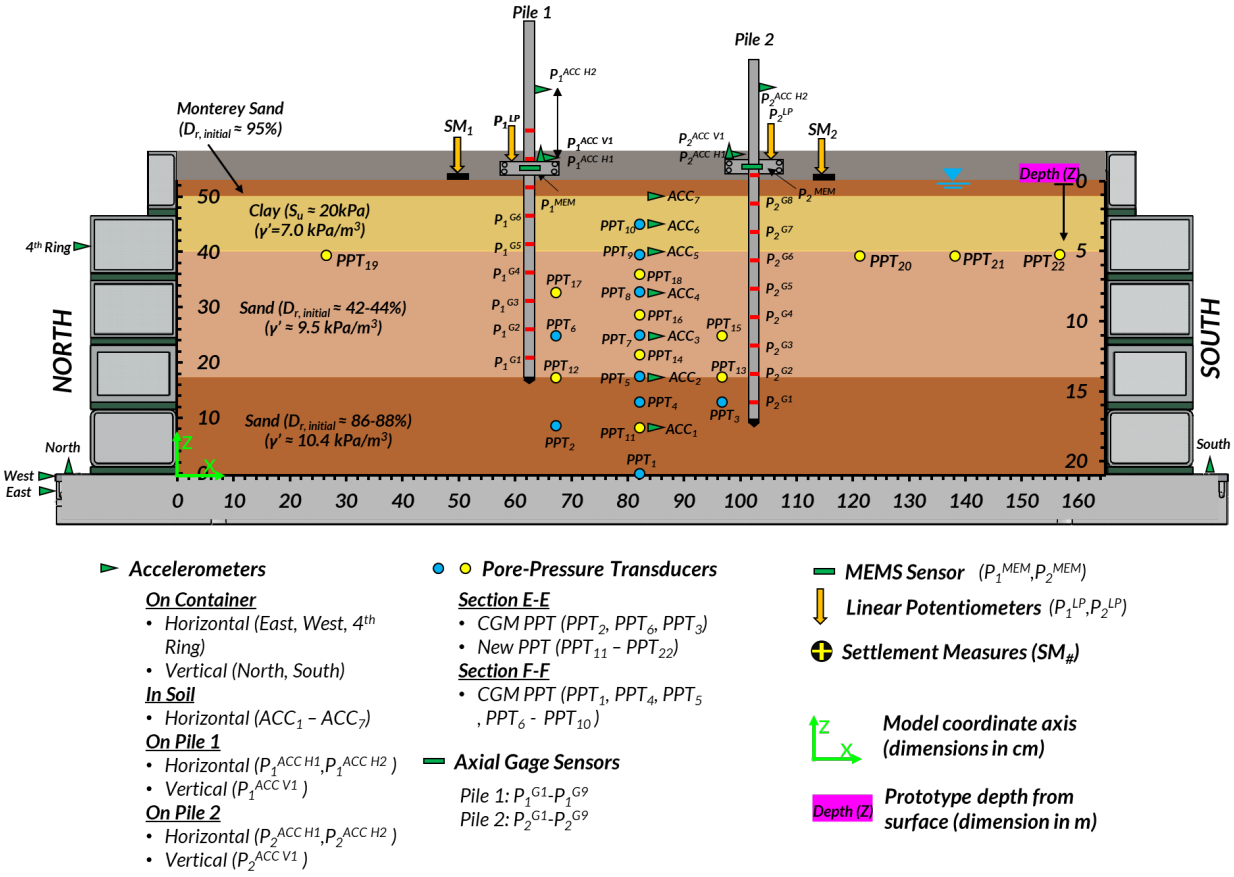

Figure 5. Cross-section view of the model (dimensions shown in model scale in cm).

Table 2. Soil layer thickness and saturated density.

Soil Layer	*Thickness [cm]*	*Saturated Density [Kg/m³]*
Monterey Sand	*2.5*	*2054*
Clay Layer	*10*	*1713*
Loose Sand	*22.5*	*1968*
Dense Sand	*18*	*2060*

3.3 Soil Properties

3.3.1 Sand

The loose and dense soil below the clay layer consisted of Ottawa F-65 sand purchased from US Silica Engineered Performance Materials. The top layer consisted of Monterey sand. A series of test were carried out to measure the maximum and minimum void ratio and grain size distribution curve for the Ottawa F-

65 batch used in the test. The Liquefaction Experiment and Analysis Projects' (LEAP) minimum and maximum density procedure (Carey et al. 2020) was used to perform these tests. The results are summarized in Table 3 below.

Table 3. Index properties of sand used in the test.

Soil Type	G_s	e_{min}	e_{max}	D_{50} ***[mm]***	***USCS***	***Description***
Ottawa F-65	2.65	0.52	0.83	0.2	SP	US Silica: F-65 whole grain Quartz sand
Monterey Sand	2.64	0.536	0.843	0.95	SP	Cemex: Clean graded kiln dried Monterey sands #0/30

To achieve the target relative density of (D_r = 40%), a pluviator with the hose with a wire mesh as shown in Figure 21 was used with a drop height of 50 cm. To achieve the target relative density of (D_r = 85%), a drum pluviator with speed level 4 and a drop height of 88 cm was used. A relative density of D_r = 42 to 44% in the loose layer and D_r=86 to 88% in dense layer was achieved (also shown in Figure 5).

3.3.2 Clay

For the clay layer, a coarse Kaolinite soil (Hydrite Flat DS) manufactured by the IMERYS Company was used. The index properties of the Kaolin soil used in the test are summarized below in Table 4.

Table 4. Index properties of clay used in the test (Stringer et al. 2013).

G_s	***Particle Size [μm]***	***LL [%]***	***PL [%]***	***PI [%]***	***USCS***	***Description***
2.58	4	46.8	28.3	18.5	ML	Hydrite Flat DS IMREYS Company

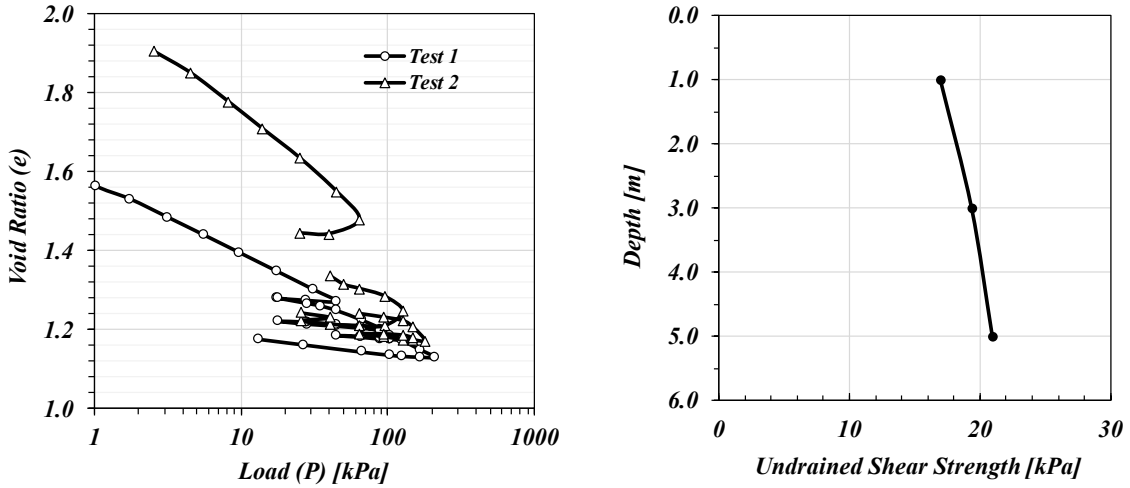

(a) Consolidation test on slurry ((Stringer et al. 2013)) (b) Target undrained shear strength profile

Figure 6. Consolidation tests performed on the clay slurry and target undrained shear strength.

Consolidation tests performed on the clay slurry by Stringer et al. (2013) was used to determine the required over consolidation stress to achieve the target undrained shear strength (s_u) of $s_u \approx 20$ kPa (see Figure 6). The distribution in Figure 6(b) was calculated assuming $s_u = (s_u/\sigma'_v)_{NC}\ \sigma'_v\ OCR^m$, with m = 0.8, and $(s_u/\sigma'_v)_{NC} = 0.3$. The clay slurry was placed at the water content of w = 80%. To achieve the target undrained shear strength, the clay was over consolidated under 110 kPa overburden stress at 1-g, producing a total volumetric strain(ε_v) of about 30%.

3.4 Pile Properties

Piles with prototype dimensions of diameter 0.635 m and thickness of 36 mm were considered for this test. The slenderness ratio (L/D) for the tip embedment of 0D and 5D were 24 and 29, respectively. To model the piles for the centrifuge test, an aluminum pipe pile of diameter of 15.9 mm and thickness of 0.9 mm were used. Table 5 summarizes the properties of the selected pile at prototype and model scale. The selected pile corresponded to an industrial medium steel pipe pile of diameter 0.635 m and thickness of 11 mm. To maximize drag load and study the effect of tip embedment, a smaller pile head load of Q_f=500kN were applied on both the piles.

Table 5. Properties of the instrumented pile.

Parameters	***Prototype***	***Model***
Material	Aluminum 6061	
Young's Modulus [GPa]	69	
Yield Stress [MPa]	290	
Outer Diameter [mm]	635	15.9
Thickness [mm]	36	0.90
Length [m]	27.6	0.69
Area [mm^2]	21563.9	41.9
Bending Stiffness (I) [mm^4]	3.02E+09	1179
Elastic Section Modulus S_y [mm^3]	9.50E+06	148.5
Plastic Section Modulus $S_{y,plastic}$[mm^3]	1.28E+07	199.9
Axial Load [kN]	19408	12.13
$M_{elastic}$ [kN-m]	2752	0.043
$M_{plastic}$ [kN-m]	3648	0.057
Pile head mass [Kg]	512000	0.8
Instrumentation Spacing [m]	2	0.05
Length with Embedment (0D) [m]	14.0	0.35
Length with Embedment (5D) [m]	17.2	0.43

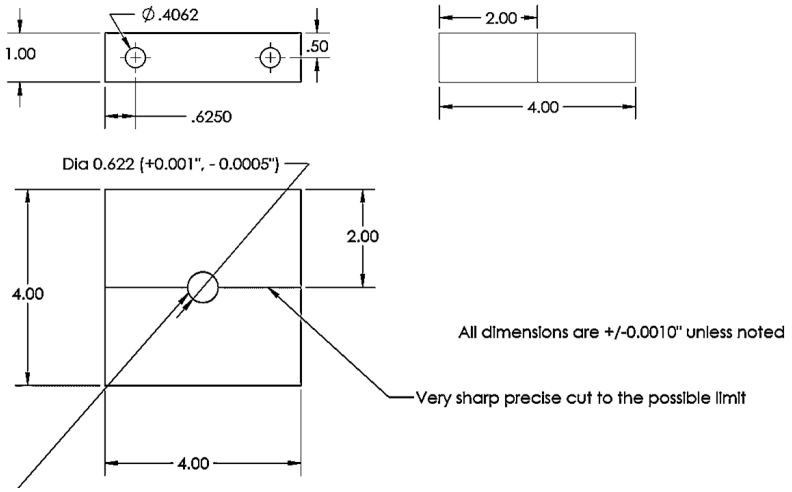

Figure 7. Pile head mass design (dimensions in inches)

3.5 Pile Assembly

A slidable adjustable split mass (4" x 4" x 1") blocks of 800 gm (see Figure 7) were designed to apply the axial load of 500 kN in accordance with the scaling factors presented in Table 5. The tip of the piles was designed with an O-ring seal mechanism (see Figure 8 (a)) to prevent infiltration of water inside the pile. To help guide the pile installation in dense sand, their tips were tapered at an angle of 120 degrees. It must be noted that that the design of the pile tip increased the length of the instrumented pile by 7.75 mm. To safely route the wires from the end of the instrumented pile and enable its attachment to an actuator, a pile cap (as shown in Figure 8 (b)) was also designed.

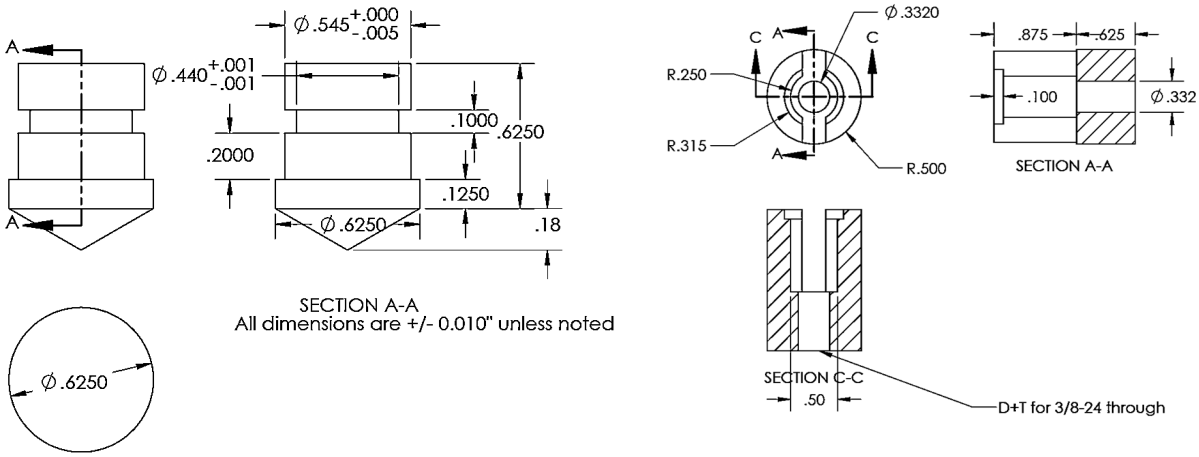

(a) Pile tip (b) Pile cap

Figure 8. Pile tip and pile cap design (dimensions in inches).

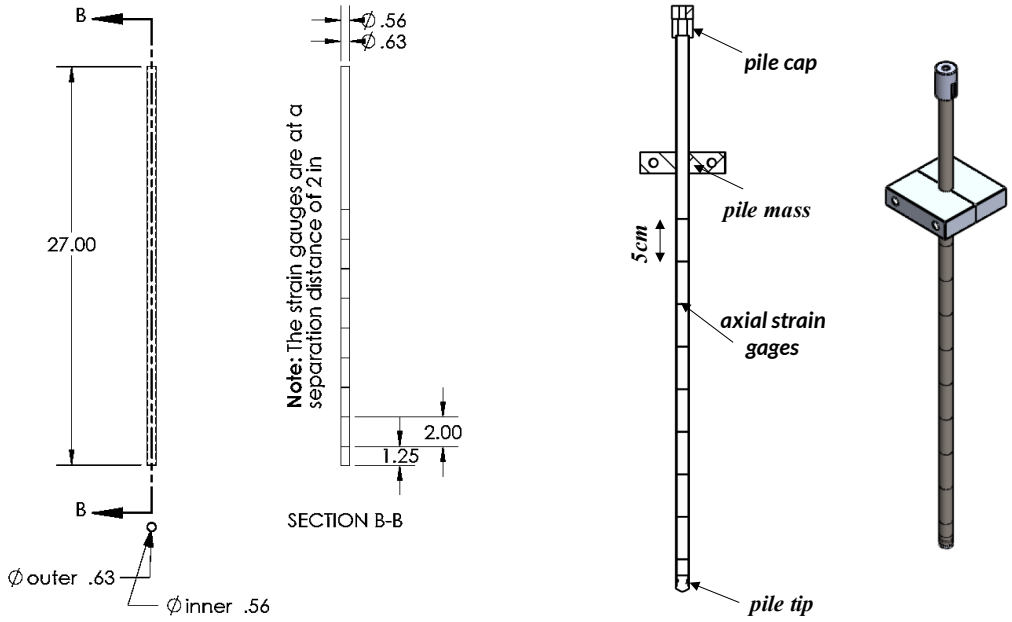

(a) Instrumentation in pile (dimensions in inches) (b) Full pile assembly

Figure 9. Instrumentation and full pile assembly.

Through multiple p-y string analyses, the horizontal first natural period of the fully assembled pile when placed in soil was estimated to be about 0.8-1.0 s. Furthermore, step wave tests (see Section 6.6) were carried out during the centrifuge test to determine the natural period of the piles.

3.5.1 Pile Instrumentation

The length of the piles was 68.6 cm (model scale) and were instrumented with 9 full bridge axial strain bridges installed in the interior diameter separated by 5 cm (i.e., 2 m in the prototype scale) as shown in Figure 9 (a). The bottom-most gage in the pile was 3.175 cm from the tip. Figure 9 (b) show the fully assembled pile from its parts. The strain gages were installed by HITEC Sensor Developments, Inc., Massachusetts, USA.

3.5.1.1 Bending Sensitivity of Axial Strain Gages

Although full bridge axial strain gages were installed in the piles, they had some sensitivity to bending moment. Two-point bending moment tests on different loading axis were conducted on the piles to determine the axis of least sensitivity (Figure 10). The piles were oriented accordingly in the centrifuge test to minimize the effects of bending moment in the direction of shaking.

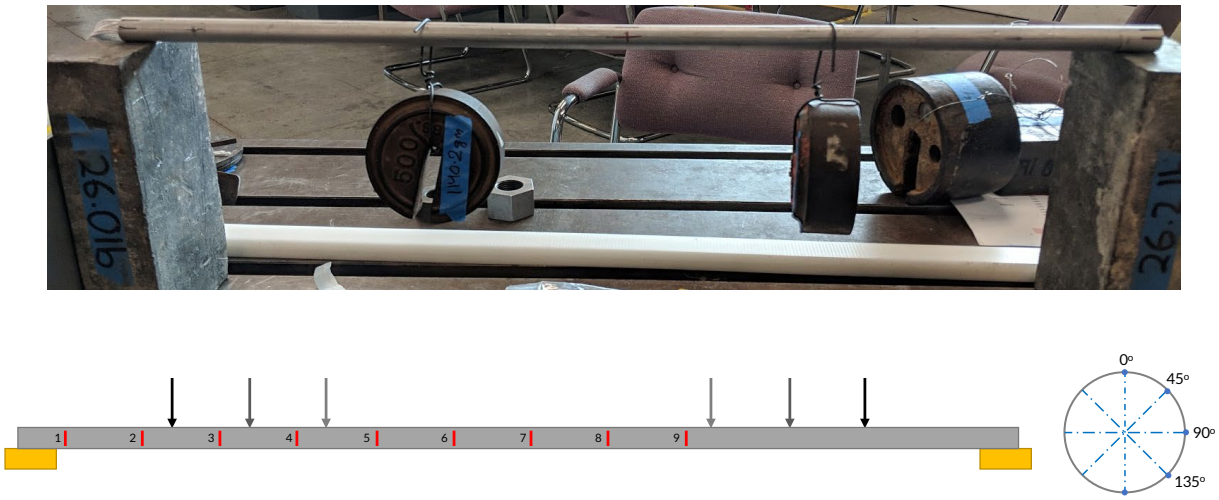

Figure 10. Two-point bending moment sensitivity test on instrumented piles.

Pile 1 and Pile 2 had bending moment sensitivity ranging from 0 to 80 N/N-m. The axis of least sensitivity determined from the above test was about 5-10 N/N-m. Analysis of expected bending moment determined from p-y curves with a conservative peak horizontal acceleration (PHA) of 0.5 g resulted in errors in axial load measurement to be within 15%. To limit the dynamic bending moments that could cause errors in the measurement of axial load, the pile head mass was placed closer to the ground surface. Furthermore, the ground motions (see Section 6.8) were accordingly selected to have their predominant period less than that of the piles.

3.5.2 Interface Roughness

The internal instrumentation facilitated the design of pile's interface surface roughness and its reusability for future tests. In order to maximize the drag load, the interface roughness was designed to fully mobilize the interface friction angle of δ=30° (Martinez and Frost 2017). Several trials made with sand/bead/garnet blasting and rubbing sandpapers with different grit sizes were unsuccessful in achieving sufficient average roughness $R_a = 0.02\ mm$. The option of gluing sand on the interface was not considered since this process did not fully produce a uniform thickness of glued surface and any wear in progressive testing could change their roughness. Other problem related to the sand gluing method are the increase in the diameter of the pile, non-uniform diameter profile, loss of sand at the interface during the test and shearing of the sand grains against the weak adhesive layer.

Use of a lathe to machine grooves on the interface offered promising results. Several trails were made to develop a procedure to safely and uniformly machine grooves on the surface. Care was taken to prevent bending of the pile (see Figure 11). The speed of the lathe and the penetration depth of the cutting tool was calibrated for 52 threads/inch (2 threads/mm) and 0.007 inch (i.e., 0.18 mm), respectively to achieve the target roughness.

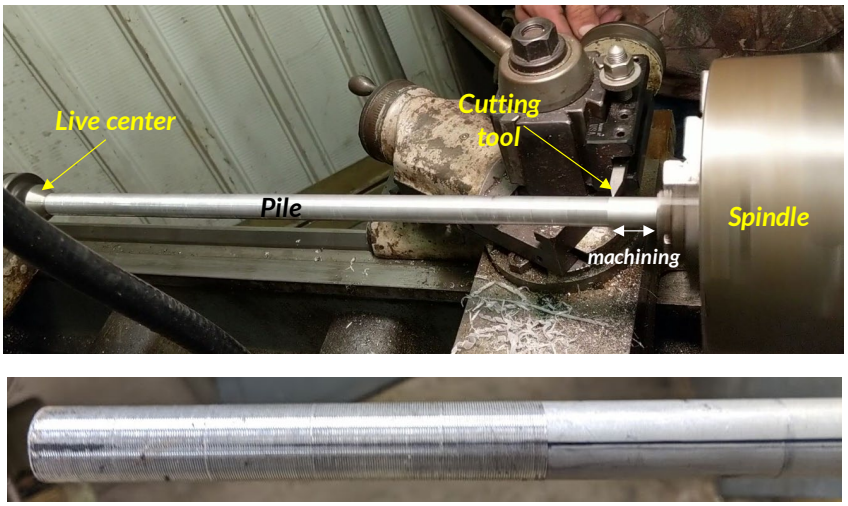

Figure 11. Use of lathe to machine interface roughness on the pile.

4 INSTRUMENTATION PLAN AND LAYOUT

Figure 4 and Figure 5 shows the instrumentations placed in the model. For defining sensor location (x,y,z), the origin was taken at the bottom north-west corner of the model. For convenience, the figure also has a scale on right to show the prototype depth (Z) measured form the surface of the model. In Figure 4, Section E-E represents the center of the model in transverse direction, whereas Section F-F is 5 cm (model scale) west of section E-E. The different types of sensors used in the model are shown in Figure 12. For an easier reference in the rest of the report, all the sensors were named as described in the sub-sections below.

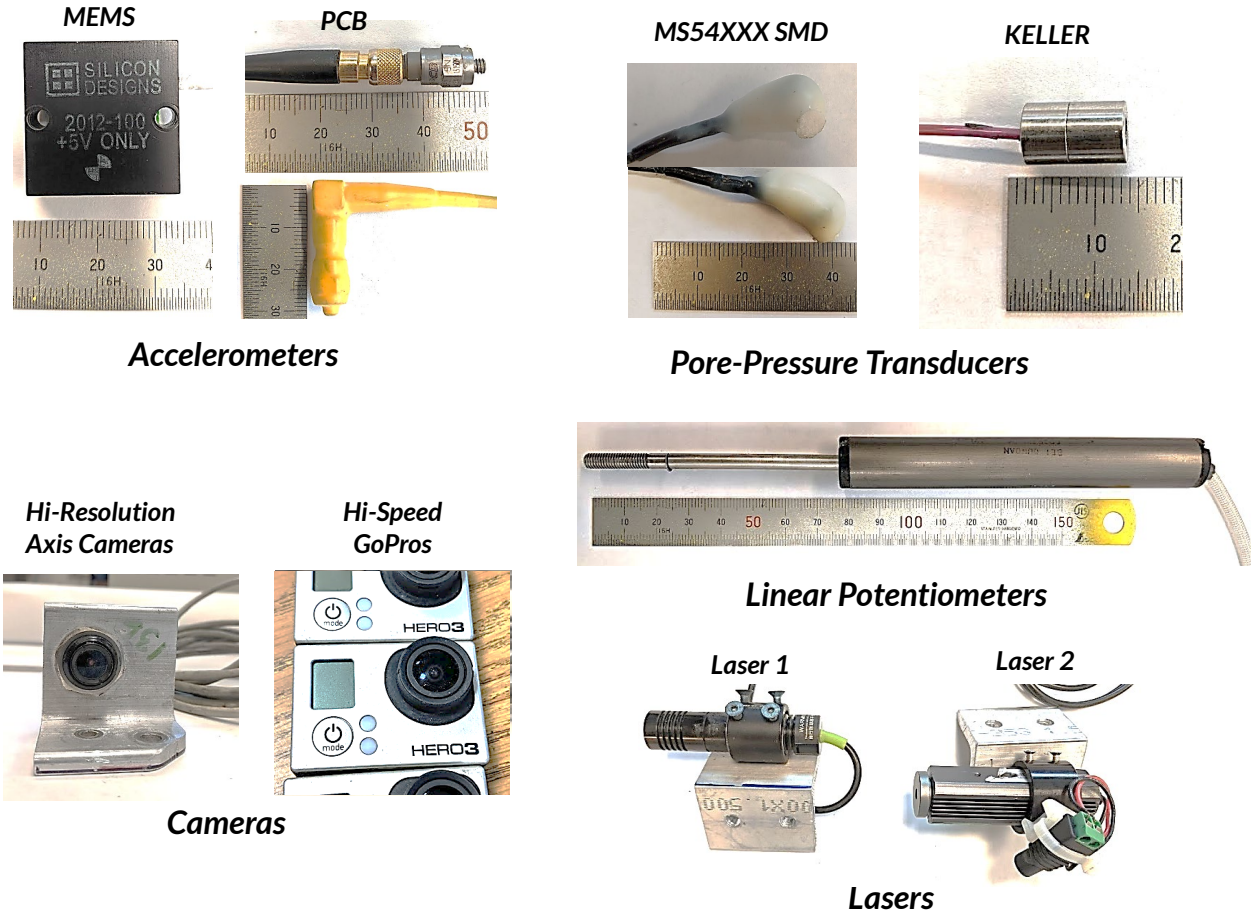

Figure 12. Sensors used in the centrifuge test.

4.1 Accelerometers

An array of horizontal piezoelectric accelerometers (PCBs) was placed in soil on Section E-E at the longitudinal center of the model as shown in Figure 5. The accelerometers in the soil were named as ACC_1 - ACC_7, beginning from the bottom of the soil layer to the top. Five accelerometers: EAST, WEST, NORTH, SOUTH and 4TH RING was installed on the model container. The descriptions of all the accelerometers in the model are shown below. Table 6 and Table 7 summarizes the location and RESDAQ configuration of the accelerometers. Accelerometers installed on piles are discussed in Section 4.3.

Accelerometers in Soil

- ACC_1 -ACC_7: measures acceleration in soil at different elevation in a central array

Accelerometers on Container

- EAST, WEST: placed on east and west of the base plate to measure applied input acceleration.
- NORTH, SOUTH: placed on north and south on the base plate to measure vertical acceleration.
- 4^{TH} RING: placed on the center of the 2^{nd} ring from the top, to measure horizontal acceleration.

Table 6. Accelerometers placed in the model and their location.

	Name	Serial Number	Location Description	x [mm]	y [mm]	z [mm]	
						Construction Phase	Post Excavation
Accelerometers on Container	EAST	East 6025	Model Base, East, facing south	-	-	-	-
	WEST	West 6021	Model Base, West, facing south	-	-	-	-
	NORTH	107644	Model Base North, facing down	-200	390	0	0
	SOUTH	21321	Model Base South, facing down	-200	390	0	0
	4^{TH} RING	36999	2^{nd} to top ring, facing south	-150	390	420	420
Accelerometers in Soil	ACC_1	21063	Section E-E, center, facing north	825	390	89.7	90.0
	ACC_2	21061	Section E-E, center, facing north	825	390	179.9	180.0
	ACC_3	108847	Section E-E, center, facing south	825	390	255.8	250
	ACC_4	99517	Section E-E, center, facing south	825	390	330.5	320
	ACC_5	99514	Section E-E, center, facing south	825	390	406.7	387
	ACC_6	127921	Section E-E, center, facing south	825	390	455.5	440
	ACC_7	107039	Section E-E, center, facing north	825	390	509.0	490

Table 7. RESDAQ configuration for all the accelerometers placed in the soil and on container.

	Name	Sensitivity		Sensitivity Units	Xdcr Range	Xdcr units	Bridge Type	Terminal Configuration	DAQ Range	DAQ Range Units	Excitation Source	Excitation Value	Excitation Units
		Construction Phase	Post Excavation										
Accelerometers on Container	EAST	52.4	52.4	mV/g	100	g	N/A	Pseudo	5	Volts	Internal	2	mA
	WEST	53.6	53.6	mV/g	100	g	N/A	Pseudo	5	Volts	Internal	2	mA
	NORTH	48.6	48.6	mV/g	100	g	N/A	Pseudo	5	Volts	Internal	2	mA
	SOUTH	50.9	50.9	mV/g	100	g	N/A	Pseudo	5	Volts	Internal	2	mA
	4TH RING	49.1	49.1	mV/g	100	g	N/A	Pseudo	5	Volts	Internal	2	mA
Accelerometers in Soil	ACC1	50.6	50.6	mV/g	100	g	N/A	Pseudo	5	Volts	Internal	2	mA
	ACC2	49.5	49.5	mV/g	100	g	N/A	Pseudo	5	Volts	Internal	2	mA
	ACC3	49.7	49.7	mV/g	100	g	N/A	Pseudo	5	Volts	Internal	2	mA
	ACC4	52	52	mV/g	100	g	N/A	Pseudo	5	Volts	Internal	2	mA
	ACC5	51.2	51.2	mV/g	100	g	N/A	Pseudo	5	Volts	Internal	2	mA
	ACC6	48.5	48.5	mV/g	100	g	N/A	Pseudo	5	Volts	Internal	2	mA
	ACC7	49.5	49.5	mV/g	100	g	N/A	Pseudo	5	Volts	Internal	2	mA

4.2 Pore pressure Transducers

Two different types of pore pressure transducers: Keller and MS54XXX SMD were placed in the model which are summarized in sub-sections below. The Keller transducers which are on expensive side are regularly used and tested sensors for centrifuge modeling applications at CGM, UC Davis. The MS54XXX SMD transducer have never been tested inside soil and that too for dynamic applications. As such, the Keller transducers were placed at all the critical locations whereas, the MS54XXX SMD transducers were installed at location where their failure would not affect any important measurements of the test.

It must be noted that the success of the experiment did not rely on working of MS54XXX sensors. While designing the experiment, it was kept in mind that the MS54XXX transducers might not provide any useful measurements. At the end of the test, less than 30% of the placed MS54XXX sensors property worked.

4.2.1 Keller Transducers

Pore pressure transducers from Keller company were more reliable and precise. They have been extensively used in the centrifuge tests at UC Davis in the past several decades. These transducers work well in capturing static and dynamic excess pore pressures. The only downside on using these sensors is their extremely high cost (roughly $1200/pc). The description of the location of Keller transducers are shown below. Table 7 and Table 8 shows the location and the RESDAQ configuration of these sensors.

Keller transducers

- PPT_1, PPT_4, PPT_5, PPT_6 – PPT_{10}: array placed at the center of the model on section F-F.
- PPT_2, PPT_6, PPT_3**:** placed close to the pile.

Table 8. Keller transducers placed in the model and their location.

	Name	***Serial Number***	***Description***	***x [mm]***	***y [mm]***	***z [mm]***	
						Construction Phase	***Post Excavation***
Keller PPTs	PPT_1	PPT_5881	Section F-F, center	825	340	1.50	1.50
	PPT_2	PPT_5754	Section E-E, center -15 cm	675	390	91.00	91.00
	PPT_3	PPT_6669	Section F-F, center	825	340	134.90	133.30
	PPT_4	PPT_6077	Section E-E, center + 15 cm	975	390	134.60	133.00
	PPT_5	PPT_6663	Section F-F, center	825	340	179.40	176.00
	PPT_6	PPT_6083	Section E-E, center - 15 cm	675	390	255.10	248.00
	PPT_7	PPT_5864	Section F-F, center	825	340	255.50	249.00
	PPT_8	PPT_5763	Section F-F, center	825	340	330.50	319.00
	PPT_9	PPT_6159	Section F-F, center - 4 cm	785	340	393.00	380.00
	PPT_{10}	PPT_6665	Section F-F, center	825	340	455.50	439.00

Table 9. RESDAQ configuration for all Keller transducers.

	Name	Sensitivity		Sensitivity Units	Xdcr Range	Xdcr units	Bridge Type	Terminal Configuration	DAQ Range	DAQ Range Units	Excitation Source	Excitation Value	Excitation Units
		Construction Phase	Post Excavation										
Keller PPTs	PPT_1	34.18	-	mV/Volt	689.5	kPa	Full	DIFF	25	mV	Internal	3.3	Volts
	PPT_2	33.05	33.05	mV/Volt	689.5	kPa	Full	DIFF	25	mV	Internal	3.3	Volts
	PPT_3	32.35	32.28	mV/Volt	689.5	kPa	Full	DIFF	25	mV	Internal	3.3	Volts
	PPT_4	39.03	39.03	mV/Volt	689.5	kPa	Full	DIFF	25	mV	Internal	3.3	Volts
	PPT_5	40.01	39.70	mV/Volt	689.5	kPa	Full	DIFF	25	mV	Internal	3.3	Volts
	PPT_6	34.89	34.89	mV/Volt	689.5	kPa	Full	DIFF	25	mV	Internal	3.3	Volts
	PPT_7	34.19	33.34	mV/Volt	689.5	kPa	Full	DIFF	25	mV	Internal	3.3	Volts
	PPT_8	31.50	-	mV/Volt	689.5	kPa	Full	DIFF	25	mV	Internal	3.3	Volts
	PPT_9	35.71	35.16	mV/Volt	689.5	kPa	Full	DIFF	25	mV	Internal	3.3	Volts
	PPT_{10}	32.41	32.41	mV/Volt	689.5	kPa	Full	DIFF	25	mV	Internal	3.3	Volts

4.2.2 MS54XXX SMD Transducers

The MS54XXX series of sensors from Measurement Specialties™ are surface mountable miniature absolute pressure sensors. The pressure sensors are small, measuring 6.2×6.4 mm and cheap, retailing for approximately US$10/piece (June 2019). The sensing element consists of a micro-machined silicon membrane with borosilicate glass wafer bonded under vacuum. Pressure applied to the membrane is registered using implanted resistors operating by means of the piezo-resistive effect (T E Sensor Solutios 2017). These sensors are typically used for altitude measurements. Their extremely low price makes them a candidate to explore their applicability in centrifuge modeling.

Pertaining to the geotechnical centrifuge modeling, these sensors have been successfully tested only for static tests such as consolidation in soils (Jacobsz 2018).

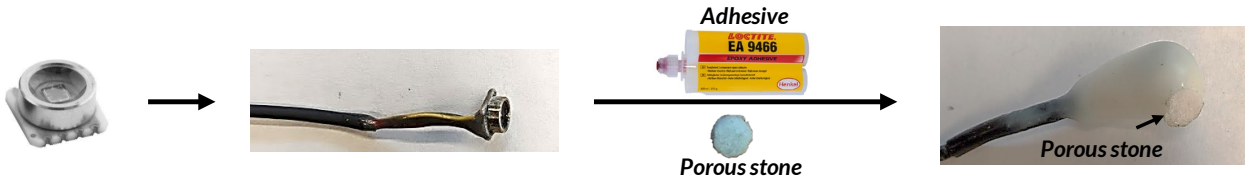

Figure 13. Fabrication of MS54XXX SMD sensor to be able to be used inside soil.

Figure 13 shows the steps required in preparing the sensor to be usable in soil. The first step involves, connecting the wires to the sensor. The second step is to place an appropriate porous stone with its diameter large enough to sit on the outer rim of the sensor and use an adhesive to glue it to the sensor. Loctite Hysol 9466 adhesive was applied in layers to completely seal off and protect the sensor from water when placed in the model.

New Transducers

- PPT_{12}, PPT_{13}, PPT_{15}, PPT_{17}: placed close to the pile.
- PPT_{11}, PPT_{14}, PPT_{16}, PPT_{18}: placed at the center of the model on section E-E.
- PPT_{19} – PPT_{22}: placed below the clay layer to track hydraulic gradient developed during drainage.

Table 10. MS54XXX transducers placed in the model and their location.

	Name	Serial Number	Description	x [mm]	y [mm]	z [mm]	
						Construction Phase	Post Excavation
MS54XXX PPTs	PPT_{11}	MS5407_113	Section F-F, center	825	340	90.60	91.00
	PPT_{12}	MS5407_114	Section E-E, center - 15 cm	675	390	179.40	179.00
	PPT_{13}	MS5407_105	Section E-E, center + 15 cm	975	390	179.10	179.00
	PPT_{14}	MS5407_106	Section F-F, center	825	340	218.00	215.00
	PPT_{15}	MS5407_103	Section E-E, center + 15 cm	975	390	255.20	255.00
	PPT_{16}	MS5407_112	Section F-F, center	825	340	292.70	285.00
	PPT_{17}	MS5407_101	Section E-E, center - 15 cm	675	390	330.50	320.00
	PPT_{18}	MS5407_107	Section F-F, center	825	340	367.50	356.00
	PPT_{19}	MS5407_108	Section E-E, center - 56 cm	265	390	398.40	391.00
	PPT_{20}	MS5407_104	Section E-E, center + 38 cm	1205	390	398.50	385.00
	PPT_{21}	MS5407_111	Section E-E, center + 56 cm	1385	390	399.00	393.00
	PPT_{22}	MS5407_102	Section E-E, center + 74 cm	1565	390	398.50	383.00

Table 11. RESDAQ configuration for all MS54XXX transducers.

	Name	Sensitivity		Sensitivity Units	Xdcr Range	Xdcr units	Bridge Type	Terminal Configuration	DAQ Range	DAQ Range Units	Excitation Source	Excitation Value	Excitation Units
		Construction Phase	Post Excavation										
MS54XXX PPTs	PPT_{11}	74.83	74.43	mV/Volt	689.5	kPa	N/A	DIFF	5	Volts	External	5	Volts
	PPT_{12}	74.45	73.72	mV/Volt	689.5	kPa	N/A	DIFF	5	Volts	External	5	Volts
	PPT_{13}	75.03	74.56	mV/Volt	689.5	kPa	N/A	DIFF	5	Volts	External	5	Volts
	PPT_{14}	73.45	-	mV/Volt	689.5	kPa	N/A	DIFF	5	Volts	External	5	Volts
	PPT_{15}	73.45	72.89	mV/Volt	689.5	kPa	N/A	DIFF	5	Volts	External	5	Volts
	PPT_{16}	75.42	75.60	mV/Volt	689.5	kPa	N/A	DIFF	5	Volts	External	5	Volts
	PPT_{17}	74.84	-	mV/Volt	689.5	kPa	N/A	DIFF	5	Volts	External	5	Volts
	PPT_{18}	73.82	73.26	mV/Volt	689.5	kPa	N/A	DIFF	5	Volts	External	5	Volts
	PPT_{19}	75.63	74.83	mV/Volt	689.5	kPa	N/A	DIFF	5	Volts	External	5	Volts
	PPT_{20}	73.72	75.48	mV/Volt	689.5	kPa	N/A	DIFF	5	Volts	External	5	Volts
	PPT_{21}	73.90	-	mV/Volt	689.5	kPa	N/A	DIFF	5	Volts	External	5	Volts
	PPT_{22}	74.01	-	mV/Volt	689.5	kPa	N/A	DIFF	5	Volts	External	5	Volts

4.3 Instrumentation on Pile

The piles: Pile 1 and 2 were instrumented with 9 full bridge axial strain gages to measure the axial load distribution. Additionally, ICP accelerometers, MEMS accelerometers and settlement sensors were installed to measure the dynamic seismic response and settlement of piles as shown in Figure 14.

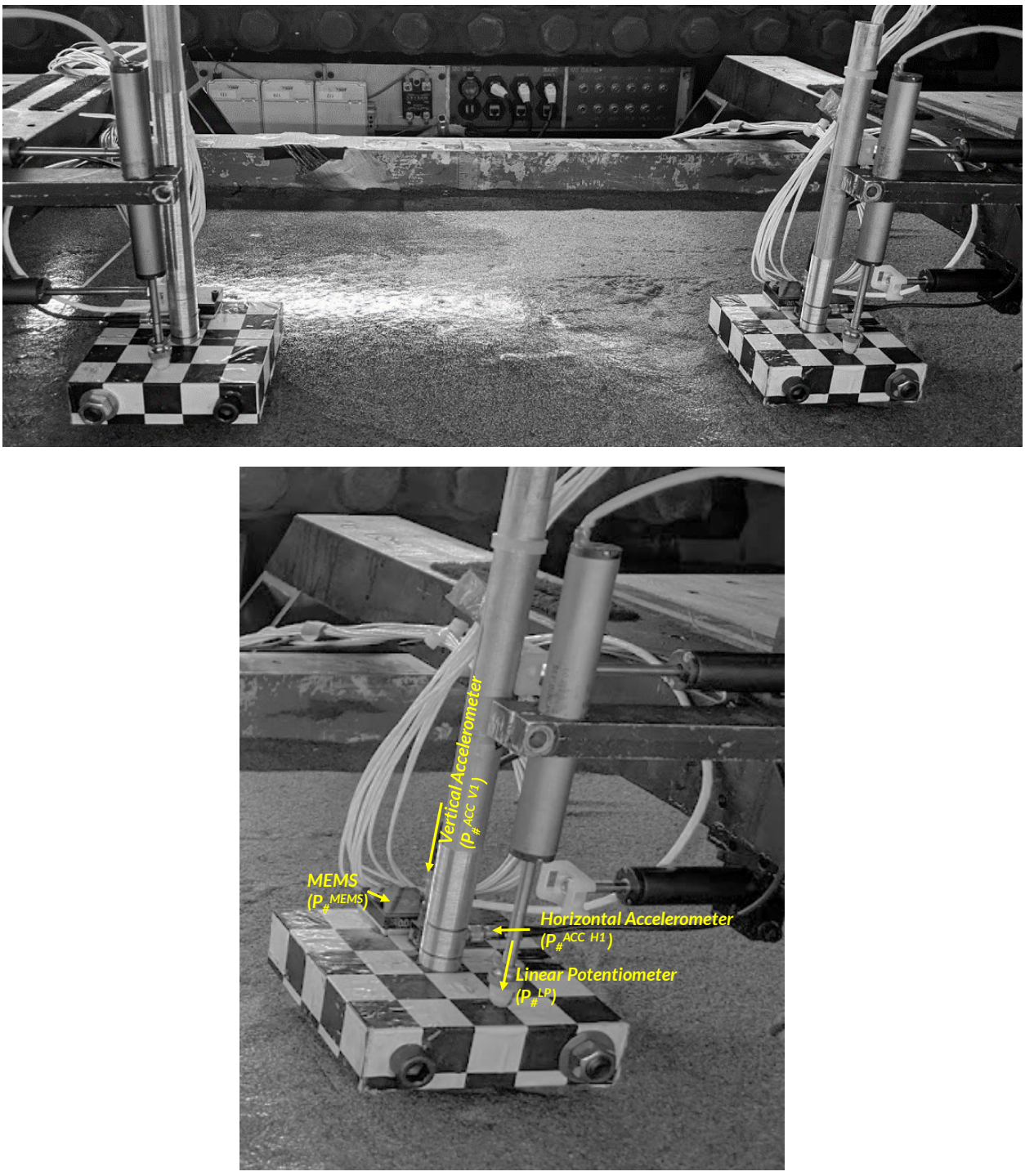

Figure 14 Sensors installed on piles.

4.3.1 Pile 1

The descriptions of instrumentation on pile 1 is shown below. Table 12 and Table 13 shows the location and RESDAQ configuration of the sensors attached to pile 1.

Axial Strain Gages

- $P_1^{G1} – P_1^{G9}$: full bridge axial strain gage array to measure the axial load response.

Sensors Installed on Pile Head Mass

- *ICP Accelerometers*
  - $P_1^{ACC\ H1}$, $P_1^{ACC\ V1}$: records horizontal and vertical response
  - $P_1^{ACC\ H2}$: record horizontal acceleration of the pile 12 cm (model scale) above the pile head to measure dynamic rotation.
- *MEMS Accelerometers*
  - P_1^{MEM}: measures the acceleration normal to the plain of the sensor.
- *Settlement Sensor*
  - P_1^{LP}: linear potentiometer to measure the settlement of the pile.

4.3.2 Pile 2

The descriptions of instrumentation on pile 2 is shown below. Table 14 and Table 15 shows the location and RESDAQ configuration of the sensors attached to pile 2.

Axial Strain Gages

- $P_2^{G1} – P_2^{G9}$: full bridge axial strain gage array to measure the axial load response.

Sensors Installed on Pile Head Mass

- *ICP Accelerometers*
  - $P_2^{ACC\ H1}$, $P_2^{ACC\ V1}$: records horizontal and vertical response
  - $P_2^{ACC\ H2}$: record horizontal acceleration of the pile 12 cm (model scale) above the pile head to measure dynamic rotation.
- *MEMS Accelerometers*
  - P_2^{MEM}: measures the acceleration normal to the plain of the sensor.
- *Settlement Sensor*
  - P_2^{LP}: linear potentiometer to measure the settlement of the pile.

Table 12. Location of sensors installed on Pile 1.

	Name	Serial Number	Location Description	x [mm]	y [mm]	z [mm]	
						Construction Phase	Post Excavation
Pile 1 Strain Gages	P_1^{G1}	J7623-01-01	Section F-F, center - 40 cm	620	390	211.75	204.75
	P_1^{G2}	J7623-01-02	Section F-F, center - 40 cm	620	390	262.55	255.55
	P_1^{G3}	J7623-01-03	Section F-F, center - 40 cm	620	390	313.35	306.35
	P_1^{G4}	J7623-01-04	Section F-F, center - 40 cm	620	390	364.15	357.15
	P_1^{G5}	J7623-01-05	Section F-F, center - 40 cm	620	390	414.95	407.95
	P_1^{G6}	J7623-01-06	Section F-F, center - 40 cm	620	390	465.75	458.75
	P_1^{G7}	J7623-01-07	Section F-F, center - 40 cm	620	390	516.55	509.55
	P_1^{G8}	J7623-01-08	Section F-F, center - 40 cm	620	390	567.35	560.35
	P_1^{G9}	J7623-01-09	Section F-F, center - 40 cm	620	390	618.15	611.15
Pile 1 Sensors	$P_1^{ACC\ H1}$	21060	Pile 1, Head Mass, facing south	620	405	580	573
	$P_1^{ACC\ H2}$	108955	Pile 1, on pipe, facing south	620	390	700	693
	$P_1^{ACC\ V1}$	21051	Pile 1, Head Mass, facing down	620	405	580	573
	P_1^{MEM}	MA00830	Pile 1, Head Mass	620	415	580	573
	P_1^{LP}	LP_308	Pile 1, Head Mass, facing down	620	365	580	573

Table 13. RESDAQ configuration of sensors on Pile 1.

	Name	Sensitivity		Sensitivity Units	Xdcr Range	Xdcr units	Bridge Type	Terminal Configuration	DAQ Range	DAQ Range Units	Excitation Source	Excitation Value	Excitation Units
		Construction Phase	Post Excavation										
Pile 1 Strain Gages	P_1^{G1}	0.335	0.462	mV/Volt	224.8	lbf	Full	DIFF	25	mV	Internal	2.5	Volts
	P_1^{G2}	0.216	0.237	mV/Volt	224.8	lbf	Full	DIFF	25	mV	Internal	2.5	Volts
	P_1^{G3}	0.384	0.372	mV/Volt	224.8	lbf	Full	DIFF	25	mV	Internal	2.5	Volts
	P_1^{G4}	0.305	0.285	mV/Volt	224.8	lbf	Full	DIFF	25	mV	Internal	2.5	Volts
	P_1^{G5}	0.355	0.330	mV/Volt	224.8	lbf	Full	DIFF	25	mV	Internal	2.5	Volts
	P_1^{G6}	0.378	0.367	mV/Volt	224.8	lbf	Full	DIFF	25	mV	Internal	2.5	Volts
	P_1^{G7}	0.376	0.357	mV/Volt	224.8	lbf	Full	DIFF	25	mV	Internal	2.5	Volts
	P_1^{G8}	0.447	0.460	mV/Volt	224.8	lbf	Full	DIFF	25	mV	Internal	2.5	Volts
	P_1^{G9}	0.352	0.393	mV/Volt	224.8	lbf	Full	DIFF	25	mV	Internal	2.5	Volts
Pile 1 Sensors	$P_1^{ACC\ H1}$	52.400	52.400	mV/g	100.0	g	N/A	Pseudo	5	Volts	Internal	2	mA
	$P_1^{ACC\ H2}$	49.600	49.600	mV/g	100.0	g	N/A	Pseudo	5	Volts	Internal	2	mA
	$P_1^{ACC\ V1}$	52.100	52.100	mV/g	100.0	g	N/A	Pseudo	5	Volts	Internal	2	mA
	P_1^{MEM}	800.000	800.000	mV/Volt	100.0	g	N/A	DIFF	5	Volts	External	5	Volts
	P_1^{LP}	994.533	994.533	mV/Volt	76.2	mm	N/A	RSE	5	Volts	External	5	Volts

Table 14. Location of sensors installed on Pile 2.

	Name	Serial Number	Location Description	x [mm]	y [mm]	z [mm]	
						Construction Phase	Post Excavation
Pile 2 Strain Gages	P_2^{G1}	J7623-02-01	Section F-F, center + 40 cm	1020	390	132.38	135.75
	P_2^{G2}	J7623-02-02	Section F-F, center + 40 cm	1020	390	183.18	186.55
	P_2^{G3}	J7623-02-03	Section F-F, center + 40 cm	1020	390	233.98	237.35
	P_2^{G4}	J7623-02-04	Section F-F, center + 40 cm	1020	390	284.78	288.15
	P_2^{G5}	J7623-02-05	Section F-F, center + 40 cm	1020	390	335.58	338.95
	P_2^{G6}	J7623-02-06	Section F-F, center + 40 cm	1020	390	386.38	389.75
	P_2^{G7}	J7623-02-07	Section F-F, center + 40 cm	1020	390	437.18	440.55
	P_2^{G8}	J7623-02-08	Section F-F, center + 40 cm	1020	390	487.98	491.35
	P_2^{G9}	J7623-02-09	Section F-F, center + 40 cm	1020	390	538.78	542.15
Pile 2 Sensors	$P_2^{ACC\ H1}$	131509	Pile 2, Head Mass, facing north	1020	405	580	576.63
	$P_2^{ACC\ H2}$	21319	Pile 2, on pipe, facing north	1020	390	700	703.38
	$P_2^{ACC\ V1}$	99511	Pile 2, Head Mass, facing down	1020	405	580	576.63
	P_2^{MEM}	MA00829	Pile 2, Head Mass	1020	415	580	583.38
	P_2^{LP}	LP_312	Pile 2, Head Mass, facing down	1020	365	580	576.63

Table 15. RESDAQ configuration of sensors on Pile 2.

	Name	Sensitivity		Sensitivity Units	Xdcr Range	Xdcr units	Bridge Type	Terminal Configuration	DAQ Range	DAQ Range Units	Excitation Source	Excitation Value	Excitation Units
		Construction Phase	Post Excavation										
Pile 1 Strain Gages	P_2^{G1}	1.031	1.031	mV/Volt	449.6	lbf	Full	DIFF	25	mV	Internal	2.5	Volts
	P_2^{G2}	0.856	0.856	mV/Volt	449.6	lbf	Full	DIFF	25	mV	Internal	2.5	Volts
	P_2^{G3}	0.707	0.707	mV/Volt	449.6	lbf	Full	DIFF	25	mV	Internal	2.5	Volts
	P_2^{G4}	0.825	0.825	mV/Volt	449.6	lbf	Full	DIFF	25	mV	Internal	2.5	Volts
	P_2^{G5}	0.910	0.910	mV/Volt	449.6	lbf	Full	DIFF	25	mV	Internal	2.5	Volts
	P_2^{G6}	0.900	0.900	mV/Volt	449.6	lbf	Full	DIFF	25	mV	Internal	2.5	Volts
	P_2^{G7}	0.915	0.915	mV/Volt	449.6	lbf	Full	DIFF	25	mV	Internal	2.5	Volts
	P_2^{G8}	0.964	0.964	mV/Volt	449.6	lbf	Full	DIFF	25	mV	Internal	2.5	Volts
	P_2^{G9}	1.003	1.003	mV/Volt	449.6	lbf	Full	DIFF	25	mV	Internal	2.5	Volts
Pile 1 Sensors	$P_2^{ACC\ H1}$	48.100	48.100	mV/g	100.0	g	N/A	Pseudo	5	Volts	Internal	2	mA
	$P_2^{ACC\ H2}$	52.200	52.200	mV/g	100.0	g	N/A	Pseudo	5	Volts	Internal	2	mA
	$P_2^{ACC\ V1}$	50.400	50.400	mV/g	100.0	g	N/A	Pseudo	5	Volts	Internal	2	mA
	P_2^{MEM}	800.000	800.000	mV/Volt	100.0	g	N/A	DIFF	5	Volts	External	5	Volts
	P_2^{LP}	994.533	994.533	mV/Volt	76.2	mm	N/A	RSE	5	Volts	External	5	Volts

4.4 Soil Settlement Sensors

Two surface markers (SM_1 and SM_2) were placed to measure the settlement of the soil. 3-inch linear potentiometers were used to measure the settlement. The linear potentiometers were attached to the rack as shown in Figure 15.

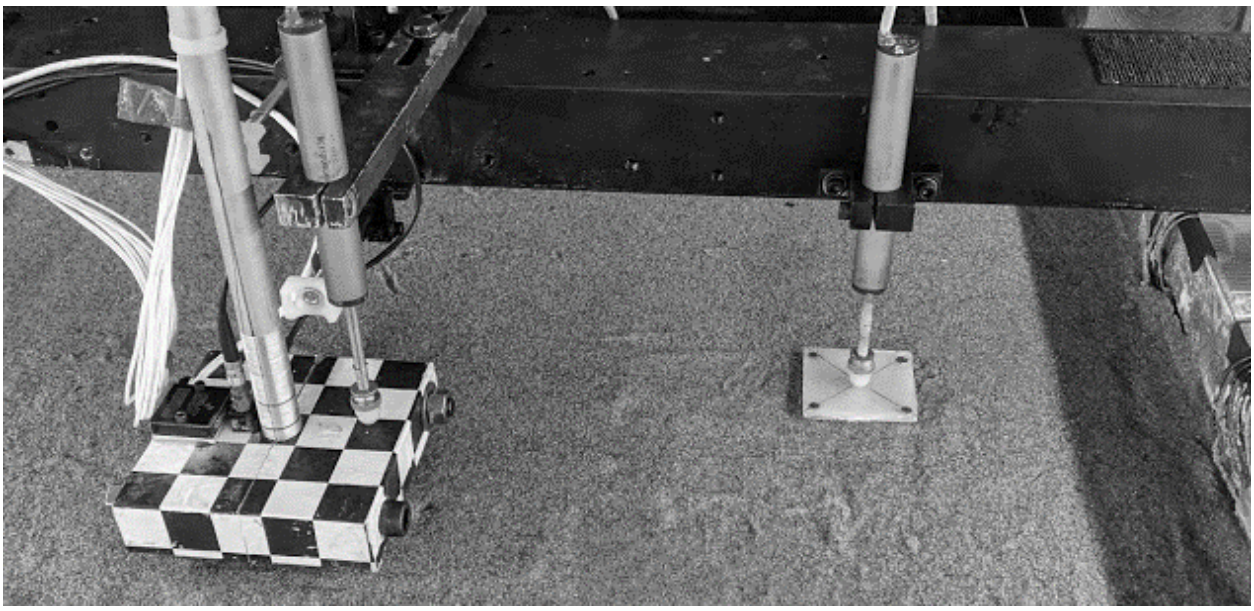

Figure 15. Settlement sensor SM_2 placed near (west of) pile 2.

Table 16. Location of settlement sensors in soil.

	Name	***Serial Number***	***Description***	***x [mm]***	***y [mm]***	***z [mm]***	
						Construction Phase	***Post Excavation***
Settlement Markers	SM_1	LP_307	Free Field Settlement Marker 1	500	140	530	522.55
	SM_2	LP_311	Free Field Settlement Marker 2	1140	140	530	521.85

Table 17. RESDAQ configuration of settlement sensors on soils.

	Name	***Sensitivity***		***Sensitivity Units***	***Xdcr Range***	***Xdcr units***	***Bridge Type***	***Terminal Configuration***	***DAQ Range***	***DAQ Range Units***	***Excitation Source***	***Excitation Value***	***Excitation Units***
		Construction Phase	***Post Excavation***										
Settlement Markers	SM_1	994.53	994.53	mV/Volt	76.2	mm	N/A	RSE	5	Volts	External	5	Volts
	SM_2	994.53	994.53	mV/Volt	76.2	mm	N/A	RSE	5	Volts	External	5	Volts

4.5 Centrifuge Cone Penetration and Pile Load Tests

Two probes (shown in Figure 16) were used to perform cone penetration test (CPT) and pile load test (PLT). Load cells were attached to the probes as shown in Figure 16. CPT had a one load cell attached at its tip and one at its head, to measure both the tip as well as shaft load. The probe for PLT had only an external load cell attached, which measured the total resistance offered by the soil (i.e., the sum of tip and shaft load). Since, the hydraulic actuator could only push 30 cm (model scale), CPT and PLT tests were used to characterize the tip resistance in loose and dense sand, respectively.

Note: The centrifuge cone penetration test and centrifuge pile load test should not be confused with the ASTM standard CPT and pile load test performed in field. The centrifuge cone penetration tests have been extensively used and conducted on centrifuge tests to determine the strength of the soil (Bolton et al. (1999), Gui et al. (1998), Mo et al. (2016), Darby et al. (2016).

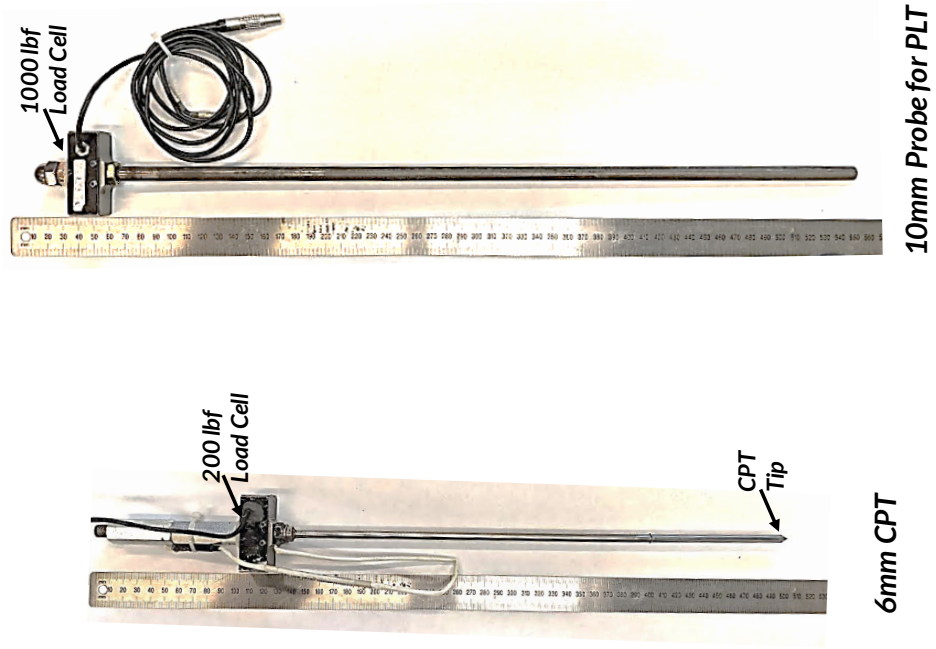

Figure 16. Probes used to perform centrifuge cone penetration test (CPT) and centrifuge pile load test (PLT).

Table 18. RESDAQ configuration of load cells attached to the probes.

	Name	Sensitivity		Sensitivity Units	Xdcr Range	Xdcr units	Bridge Type	Terminal Configuration	DAQ Range	DAQ Range Units	Excitation Source	Excitation Value	Excitation Units
		Construction Phase	Post Excavation										
Load Cells	PLT	1.99	1.99	mV/Volt	1000	lbf	Full	DIFF	25	mV	Internal	10	Volts
	CPT	0.31	0.31	mV/Volt	100	lbf	Full	DIFF	25	mV	Internal	10	Volts
	EXT	0.98	0.98	mV/Volt	500	lbf	Full	DIFF	25	mV	Internal	10	Volts

4.6 Lasers

While linear potentiometers work quite well for static settlement measures, their dynamic response is not reliable. Some other problems related to linear potentiometers is the requirement of a mounting rack which covers the model surface and makes the area unusable for other important tests (like CPT or anything else that any researcher might use it for). At the same time, since these sensors are attached to the structure, they potentially affect their response. Also, during seismic events, these sensors could slip from their original position affecting the settlement measurements.

With the advancement of image processing and availability of high-speed cameras, the use of lasers in centrifuge modeling provides a potential to measure static as well as dynamic settlements. Since there is no physical contact of sensor to the structure, the worry of altering the response is reduced. The accuracy of the measurement depends upon the resolution of the image and thickness of the laser. A high-resolution image and thin laser line could produce an accurate, non-contact settlement measure over a line instead of a point.

The methodology behind the use of lasers to measure settlement is shown in Figure 17. The laser is mounted with a known angle (let us say θ) to a fixed frame. When a line-laser projects light, it makes a straight line on the flat surface. If the flat surface undergoes a vertical settlement (VS), it results in horizontal movement (HM) of the laser. Having measured the horizontal movement of laser, the vertical settlement (VS) can be estimated as $VS = HM \tan \theta$. Sinha et al. (2020) describes the use of line lasers and cameras to measure vertical movements in model.

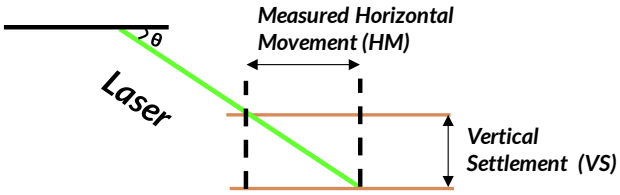

Figure 17. Schematic diagram showing the working of the lasers to measure vertical displacements.

In the model two line lasers (Laser 1 and Laser 2) were attached to the camera beam mounted across the rails of the bucket as shown in Figure 18. The lasers were mounted with an angle of 46° on the east and west side of the model. The lasers were of 532nm 50mW green light line lasers brought from https://www.civillaser.com/ with product id 63 and 33, respectively.

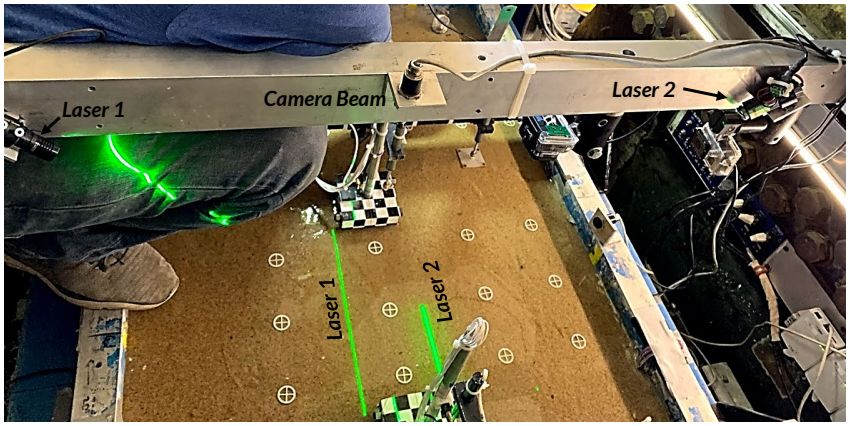

Figure 18. Line-lasers installed on the model.

4.7 Video Recordings

The model was video graphed with 2 high-resolution and 2 high-speed cameras. These cameras recorded top and side view of the model as shown in Figure 19. The description of the cameras is shown below. The log of snapshots and recordings taken by the camera are summarized in Table 19 and Table 20 respectively. The recorded snapshots were later processed to get displacements from laser recordings.

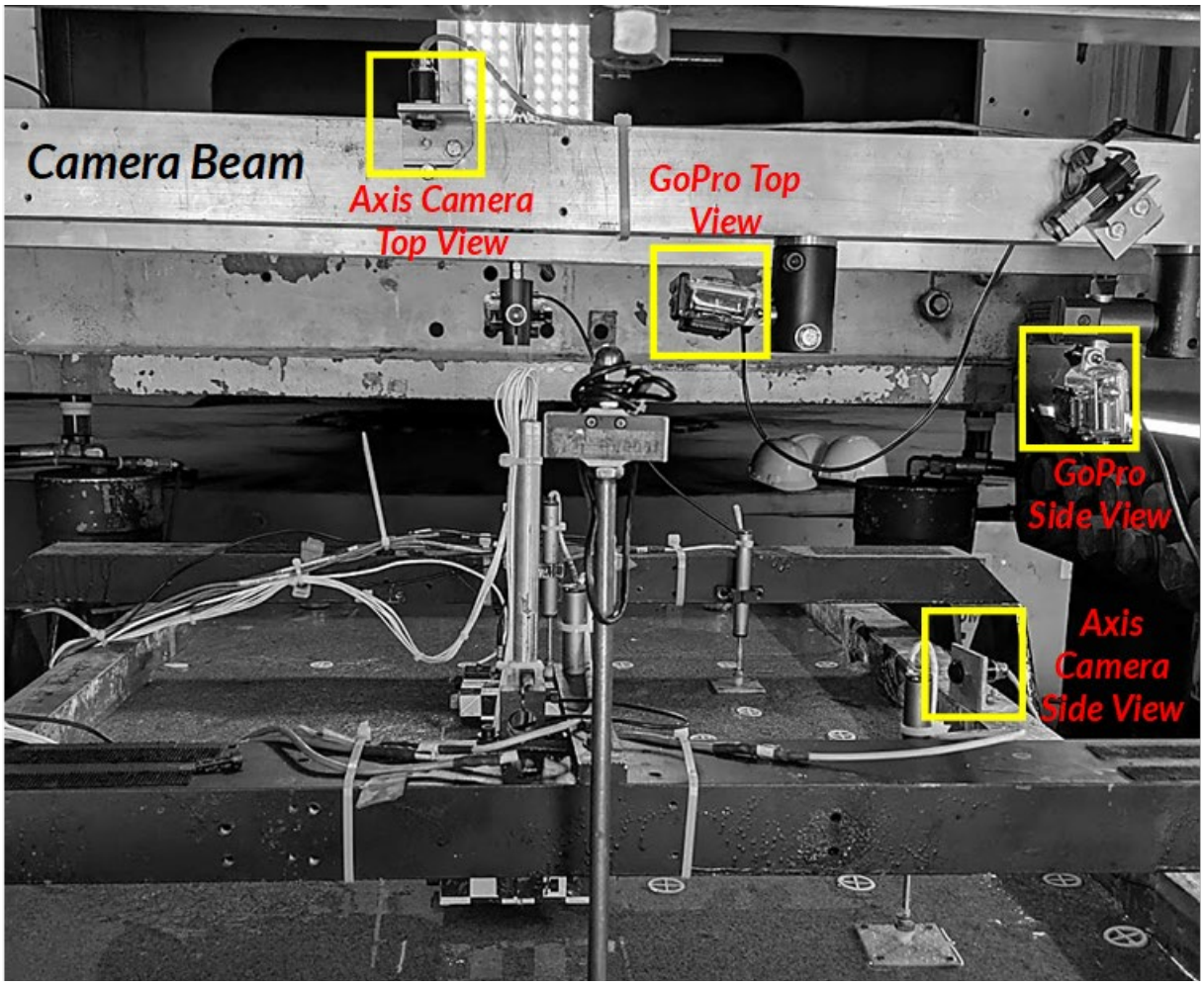

Figure 19. Position of cameras installed on the model.

Hi-Resolution Cameras

- Model: AXIS P1214-E Network Cameras
- Frame Rate: 30 fps
- Resolution: 1280x720

Hi-Speed GoPro

- Model: Hero3 Black Edition
- Frame Rate: 240 fps
- Resolution: 848x480

Table 19. Log of snapshots taken from Axis cameras.

Day	***Time***	***Event***	***Snapshots Filename***
7/10/2019	13:26		Snapshot_Side_View_Day_1_Spin_2_at_12pm.jpg
	15:11		Snapshot_Top_View_Day_1_Spin_2_Spin_Up_at_20g.jpg
	15:14		Snapshot_Side_View_Day_1_Spin_2_Spin_Up_at_20g.jpg
	15:18		Snapshot_Side_View_Day_1_Spin_2_Spin_Up_at_40g.jpg
	15:19		Snapshot_Top_View_Day_1_Spin_2_Spin_Up_at_40g.jpg
	16:26		Snapshot_Top_View_Before_EQM_1_Small_Santa_Cruz.jpg
	16:27	EQM_1	Snapshot_Side_View_Before_EQM_1_Small_Santa_Cruz.jpg
	16:32		Snapshot_Side_View_After_EQM_1_Small_Santa_Cruz.jpg
	16:33		Snapshot_Top_View_After_EQM_1_Small_Santa_Cruz.jpg
	16:56	EQM_2	Snapshot_Top_View_After_EQM_2_Medium_Santa_Cruz.jpg
	16:59		Snapshot_Side_View_After_EQM_2_Medium_Santa_Cruz.jpg
	17:36		Snapshot_Side_View_Before_EQM_3_Large_Santa_Cruz.jpg
	17:37		Snapshot_Top_View_Before_EQM_3_Large_Santa_Cruz.jpg
	17:41	EQM_4	Snapshot_Side_View_After_EQM_3_Large_Santa_Cruz.jpg
	17:42		Snapshot_Top_View_After_EQM_3_Large_Santa_Cruz.jpg
	18:25		Snapshot_Top_View_After_45_minutes_of_EQM_3_Large_Santa_Cruz.jpg
	19:14		Snapshot_Side_View_Day_2_Spin_2_Spin_Down_at_RPM_3_5.jpg
	19:14		Snapshot_Top_View_Day_2_Spin_2_Spin_Down_at_RPM_3_5.jpg
7/12/2019	11:29		Snapshot_Side_View_Day_2_Spin_2_at_1g.jpg
	11:30		Snapshot_Top_View_Day_2_Spin_2_at_1g.jpg
	12:31		Snapshot_Side_View_Day_2_Spin_2_Spin_Up_at_40g.jpg
	12:32		Snapshot_Top_View_Day_2_Spin_2_Spin_Up_at_40g.jpg
	13:08	PLT_2	Snapshot_Side_View_After_Pile_Load_Test_2.jpg
	13:08		Snapshot_Top_View_After_Pile_Load_Test_2.jpg
	13:11	EQM_4	Snapshot_Side_View_After_EQM_4_Medium_Santa_Cruz.jpg
	13:12		Snapshot_Top_View_After_EQM_4_Medium_Santa_Cruz.jpg
	13:39	EQM_5	Snapshot_Side_View_After_EQM_5_Large_Santa_Cruz.jpg.jpg
	13:39		Snapshot_Top_View_After_EQM_5_Large_Santa_Cruz.jpg
	15:27		Snapshot_Top_View_Day_2_Spin_2_at_56_40g_Consolidation.jpg
	15:29		Snapshot_Side_View_Day_2_Spin_2_at_56_40g_Consolidation.jpg
	15:47	EQM_6	Snapshot_Top_View_After_EQM_6_EJM01_Freq_Corrected_38g.jpg
	15:49		Snapshot_Side_View_After_EQM_6_EJM01_Freq_Corrected_38g.jpg

Note: To get the list of the description of the events refer to Table 21 and Table 22.

Table 20. Log of recorded earthquake events EQM_1-EQM_6.

Event	***Video Filename***	***Camera***
EQM_2	Axis_Cam_Side_View_EQM_2_Medium_Santa_Cruz.asf	Axis Camera
	Axis_Cam_Top_View_EQM_2_Medium_Santa_Cruz.asf	
EQM_3	Axis_Cam_Side_View_EQM_3_Large_Santa_Cruz.asf	Axis Camera
	Axis_Cam_Top_View_EQM_3_Large_Santa_Cruz.asf	
	Go_Pro_Side_View_EQM_3_Large_Santa_Cruz.MP4	GoPro
EQM_4	Axis_Cam_Side_View_EQM_4_Medium_Santa_Cruz.asf	Axis Camera
	Axis_Cam_Top_View_EQM_4_Medium_Santa_Cruz.asf	
EQM_5	Axis_Cam_Side_View_EQM_5_Large_Santa_Cruz.asf	Axis Camera
	Axis_Cam_Top_View_EQM_5_Large_Santa_Cruz.asf	
	Go_Pro_Side_View_EQM_5_Large_Santa_Cruz.MP4	GoPro
	Go_Pro_Top_View_EQM_5_Large_Santa_Cruz.MP4	
EQM_6	Axis_Cam_Side_View_EQM_6_EJM01_Freq_Corrected_38g.asf	Axis Camera
	Axis_Cam_Top_View_EQM_6_EJM01_Freq_Corrected_38g.asf	
	Go_Pro_Side_View_EQM_6_EJM01_Freq_Corrected_38g.MP4	GoPro
	Go_Pro_Top_View_EQM_6_EJM01_Freq_Corrected_38g.MP4	

Note: To get the list of the description of the events refer to Table 21 and Table 22.

5 MODEL CONSTRUCTION

Figure 20. Model container.

The model container used was (Flexible Shear Beam) FSB 2.1 of dimensions 165cm x 78 cm x 58 cm. Shear rods on both east and west ends were placed to provide complementary shear. Several paper scales were stick on the container to monitor the soil placement during pluvitaion. The initial weight of the model was recorded and as soil was poured in the total weight and thickness of the soil surface layer was recorded. A depth gage was used to measure the soil surface at was pluviated to an accuracy of 0.1 mm.

5.1 Placement of Sand

Figure 21. Pluviators used to place dense and loose sand layers.

Pluviator with a hose and drum pluviator (shown in Figure 21) were used to place dense and loose layers, respectively. During pluviation, the model container as well as the pluviator was grounded to discharge any electrostatic force developed between the particles. The location of sensors pretty much decided the thickness of each lift. The lift thickness was kept to 2-3 cm and was made smaller in case any sensors were needed to be placed. After placing the soil, each lift was vacuumed to level of the surface. The weight and then the height of the layer was measured to calculate the achieved incremental as well as total relative density. A snapshot of the spreadsheet is shown below in Figure 22. The calibration parameters used for pluviating dense and loose layers, and the achieved relative density is summarized in Section 3-22.

Incremental and Overall Depth of Soil Relative Density Calibration

Lift	Balance Reading [kg]			Dial Gauge Reading at soil surface [cm] North to South									Layer Thickness [cm]		Volume [cm^3]		Density [kg/m^3]		Void Ratio (e)		Relative Density (Dr)[
	Empty Container [kg]	Container With Soil [kg]	Mass of Soil in Container [kg]	Reading 1	Reading 2	Reading 3	Reading 4	Reading 5	Reading 6	Reading 7	Reading 8	Average	Incremental Lift Thickness	Total Layer Thickness	Incremental Lift Volume	Total Volume of Soil	Incremental Lift Density	Total Density of Soil	Incremental Lift Void Ratio	Total Void Ratio of Soil	Incremental Lift Dr	Dr of total soil Layer
0	824	824	0	2.6	2.6	2.55	2.55	2.55	2.55	2.6	2.6	2.65	0	0	0	0						
1	824	880	56	5.2	5.2	5.3	5.2	5.3	5.2	5.1	5.1	5.20	2.55	2.55	33235.48	33235.48	1684.95	1684.95	0.57	0.57	80.39	80.39
2	880	954	74	8.58	8.7	8.58	8.47	8.44	8.59	8.55	8.61	8.57	3.37	5.92	43857.79	77093.27	1687.27	1686.27	0.57	0.57	81.07	80.78
3	954	1031	77	11.96	11.85	11.92	12.01	12.01	11.92	11.99	11.97	11.95	3.39	9.30	44167.34	121260.61	1743.37	1707.07	0.52	0.55	96.86	86.76
4	1031	1080	49	14.17	14.17	14.15	14.11	14.19	14.17	14.24	14.29	14.19	2.23	11.54	29097.33	150357.95	1684.00	1702.60	0.57	0.56	80.12	85.49
5	1080	1123.5	43.5	16.18	16.1	16.04	16.06	16.04	16.07	16.16	16.15	16.10	1.91	13.45	24942.90	175300.84	1743.98	1708.49	0.52	0.55	97.03	87.16
6	1123.5	1180	56.5	18.71	18.71	18.65	18.60	18.59	18.66	18.59	18.68	18.65	2.55	16.00	33219.18	208520.03	1700.82	1707.27	0.56	0.55	84.98	86.82
7	1180	1227	47	20.65	20.6	20.62	20.63	20.83	20.9	20.66	20.64	20.69	2.04	18.04	26620.96	235140.99	1765.53	1713.87	0.50	0.55	102.82	88.68

Figure 22. Snapshot of MS-Excel spreadsheet to record achieved relative density for dense layer.

(a) (b) (c) (d)

Figure 23. Steps involved while pluviating the model (a) pouring sand (b) vacuum the lift layer and remove any sand grains on the container (c) record the surface measurements and weight of the model (d) place sensors and route them.

Figure 23 shows the steps involved while placing the sand layer. Figure 22 shows the placement of sensors and routing of the senor wires through the walls of the container. The accelerometers were placed parallel to the shaking direction (North-South) whereas the pore pressure transducers were placed perpendicular (North-East) to the shaking direction. To track the settlement of the soil layers during excavation, colored sand was placed at the interface of dense and loose sand and at the middle if loose sand layer.

5.2 Saturation

The model was saturated with a viscous fluid mixture of deionized water and 2% methyl cellulose to produce a viscosity 25 times that of water. According to the scaling laws the kinematic viscosity of the fluid should be scaled to the full centrifugal acceleration. However, it has been shown in the previous tests and analyses that use of fluid with very high viscosity dramatically increases the time required for pore pressure dissipation and model saturation (Stewart et al. 2009). The preparation of methyl cellulose mixture followed the standards presented in Stewart et al. (2009).

Figure 24. Preparation of the model for saturation.

A top-down saturation method while maintaining a tilt in the model was used to saturate the model. A trough of 8 cm wide and 5 cm deep was excavated at the north end of the model to act as a small water reservoir in the initial stage of saturation. To prevent soil disturbance while pouring fluid in the model, the

trough was connected to a cup placed on sponge as shown in Figure 24. During saturation, the fluid would slowly overfill the cup and spill on the sponges to the soil and fill the trench at one end of the container.

The model was saturated on the consolidation press, so that after finishing saturation, consolidation can be carried out without further moving the model. Figure 25 shows the saturation set-up. The model was first placed on the consolidation floor with the help of a chain fall attached to its south end. The model was then lifted to about 6 cm (~2º) from south side. The set-up contained two deairing chambers, a HPMC mixer and vacuum cart. The vacuum pumps were connected to the model and the deairing chambers and constantly maintaining a vacuum of ~97 kPa.

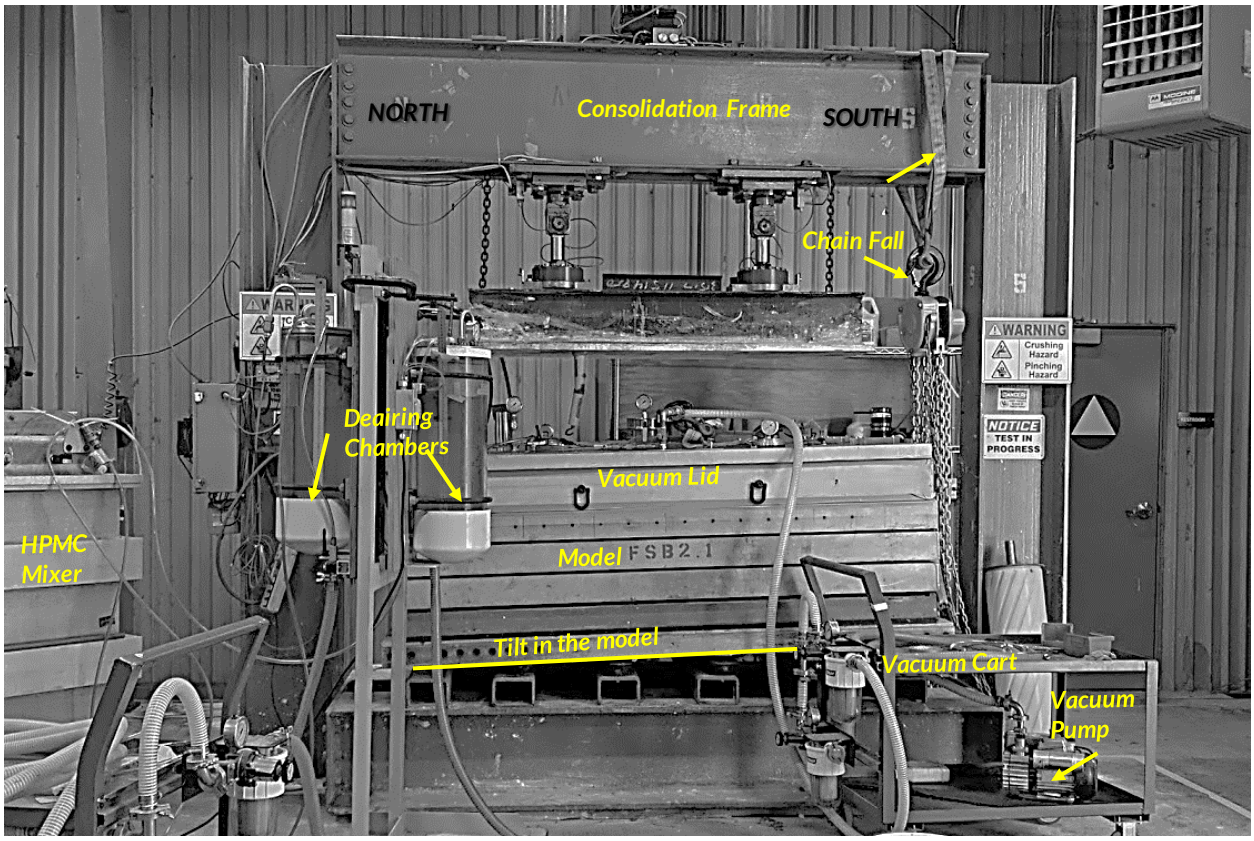

Figure 25. Set-up for saturating the model.

Before the start of saturation, the model was pulled under vacuum and then flushed with CO_2 three times in a row to remove about 99.9% of the air voids. Then, the deaired viscous fluid was pumped to the model (from the north side of the container) slowly saturating the model from north to south direction. Saturation of the model was continuously monitored through portals in the vacuum lid. The speed of the fluid injection was controlled such that the saturation front was always ahead of the waterfront (see Figure 26), to minimize the entrapment of air under the wet sand. The saturation was completed in 48 hours. Figure 26 shows the model at the end of saturation. Once saturation was complete, the model was lowered down to the horizontal position.

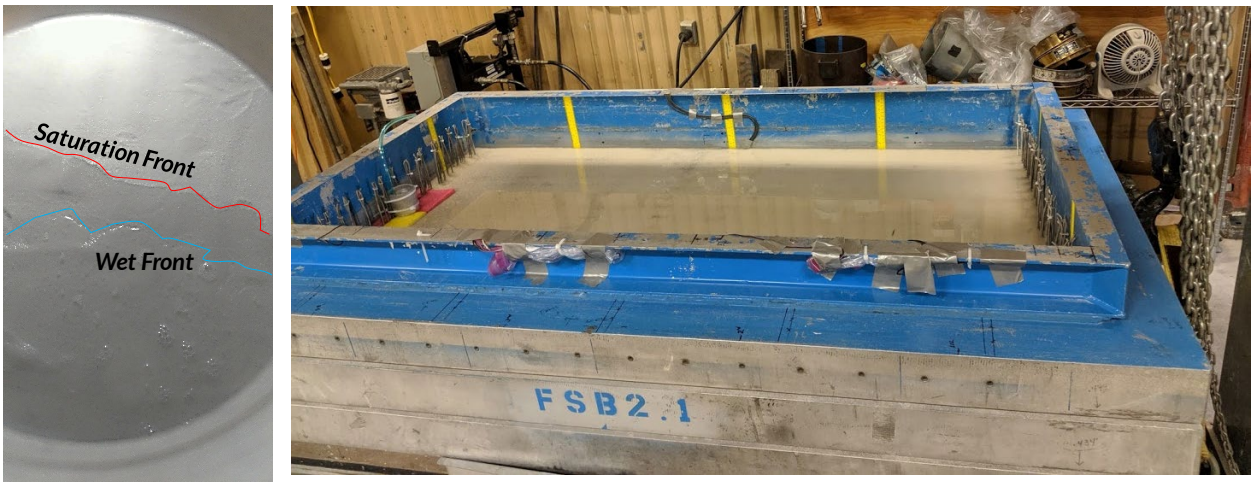

Figure 26. Model (a) during and (b) at end of saturation.

5.3 Clay Layer and Consolidation

To place the clay layer, a slurry of coarse Kaolin with de-ionized water was prepared in a mixer at a water content of w=80%. The slurry was mixed under vacuum of 45 kPa. The slurry was then placed in the model and consolidated at 1-g using the consolidation press up to a load equivalent to 100 kPa. The clay layer was placed in two lifts, each with an initial slurry thickness of 7 cm (which reduced to 5 cm after consolidation).

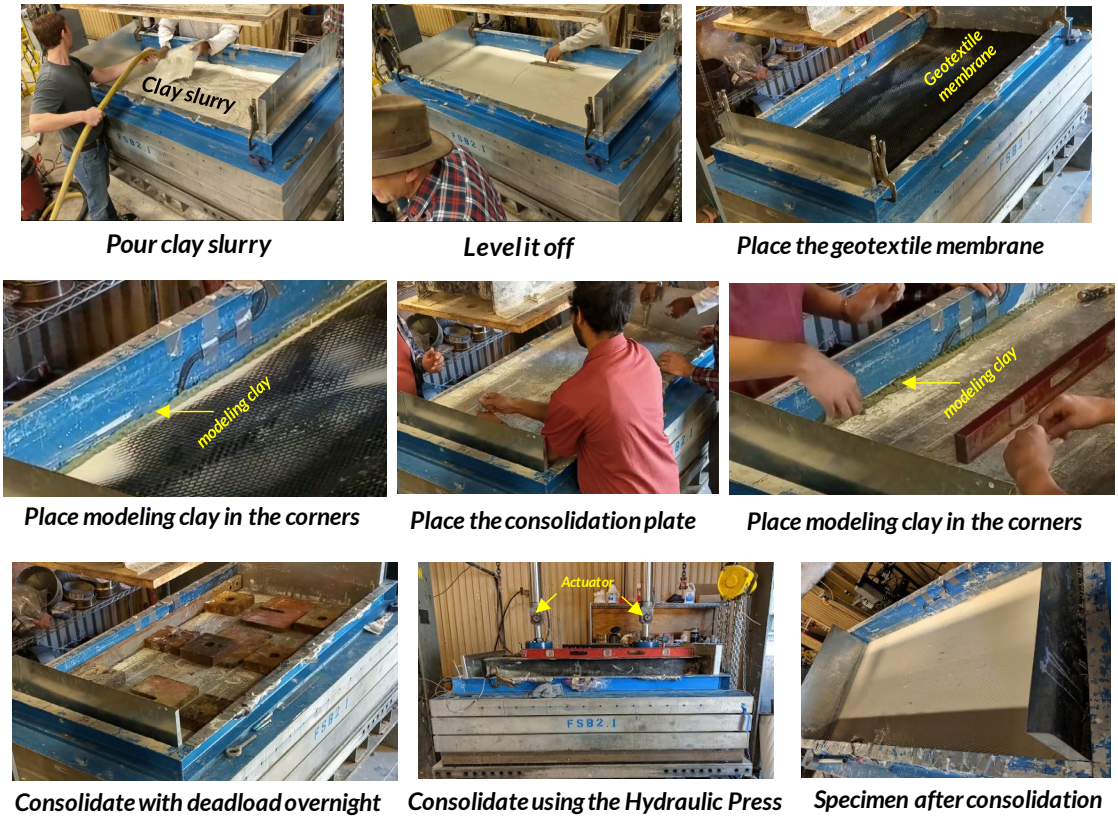

Figure 27. Steps involved while placing the clay layer and its consolidation.

The preparation for placing the clay layer involved putting a vertical sheet metal end plates on north and south side of the container separated by 5 cm from the walls. The end plates protected the shear rods from the consolidation press. The soil behind the end plate (around the shear rods) was filled with 10% Bentonite-Monterey sand mixtures to provide a stiff, low permeability confinement and to prevent drainage from the ends. Preventing drainage around the sides of the clay would also prevent drainage of pure water from the bottom of clay that could dilute the concentration and viscosity of the methyl cellulose mixture in the sand.

Figure 27 show steps involved in placing the clay layer and its consolidation. It involved placing the clay slurry and leveling it off. A geotextile membrane was then placed while applying a modeling clay on all the corners to prevent any drainage and squeezing of slurry from the sides during consolidation. The consolidation plate was then placed on the model with further application of modeling clay to fill in the gaps between the plate and the sides of the container. Dead load of 200 to 500 lbf (i.e 100-250 kg) was then applied to the model and left overnight to consolidate under self-weight.

	Load Increment					Lift Thickness [cm]			7
	Force [lbf]	*Load command to the press [lbf]*	*Force [N]*	*Stress [kPa]*	*Day*	*Time Start*	*Time End*	*Duration*	Height
Loading	0	-	0	0.00	12th June, 2019	11:29	11:40	0:11	28.64
	215	-	956	0.74		11:40	14:01	2:21	29.17
	215	-	956	0.74		14:01	16:30	2:29	29.43
	479.6	-	2133	1.65		16:30	8:49	16:19	29.90
	479.6	-	2133	1.65	13th June, 2019	8:49	9:20	0:31	29.88
									29.88
		-							29.88
Unloading	215	-	956	0.74		9:20	10:02	0:42	29.94
	0	-	0	0.00		10:02	10:20	0:18	29.85
	1000	500	4448	3.43		11:03	12:12	1:09	#DIV/0!
	2000	1000	8896	6.87		12:12	13:49	1:37	#DIV/0!
	3000	1500	13345	10.30		13:49	14:39	0:50	#DIV/0!
	4000	2000	17793	13.74		14:39	15:23	0:44	#DIV/0!
	5000	2500	22241	17.17		15:23	16:28	1:05	#DIV/0!
	6000	3000	26689	20.61		16:28	17:26	0:58	#DIV/0!
	7000	3500	31138	24.04		17:26	18:15	0:49	#DIV/0!

Figure 28. Load schedule applied during consolidation.

Figure 28 shows the load schedule applied during consolidation. The initial dead load applied to the model was 215 lbf which was increased to 480 lbf after 5 hours and then left overnight. In the morning, the model was slowly unloaded by removing the deadload and then loaded again with the hydraulic press. To continuously monitor the consolidation, two LP sensors (each on the north and south of the consolidation plate) and one pore pressure transducer (at the bottom of the clay layer) were placed. The load increment with the hydraulic press was kept to 1000 lbf (~3.43 kPa). The load was increased only when 90% of the excess pore pressures dissipated. The model was fully consolidated slowly with an equivalent load of 110 kPa. Once full consolidation was achieved, the load was slowly decreased to zero again in the decrements of 1000 lbf.

5.4 Monterey Sand Layer

Once consolidation was complete the model was carefully moved from the consolidation press and placed on the ground. Coarser sand (Monterey sand, D_{50} 0.95 mm) was pluviated using the drum pluviator on top of the clay layer. The relative density achieved was D_r=95%. The layer was then saturated to the top with methyl cellulose mixture. Figure 29 shows the model with Monterey sand layer.

Figure 29. Model with Monterey sand layer.

5.5 Vacuum Transportation

Since, saturated loose models are more vulnerable to vibration caused during transportation, a vacuum transportation methodology was developed. In this method, the model was pulled under vacuum of 30-50 kPa while a geotextile, a gravel layer, and membrane covered the top surface of the soil as shown in Figure 30. The vacuum confinement stress was intended to develop enough effective stress in the sand to prevent any densification from the vibrations caused during transportation.

5.5.1 Preparation

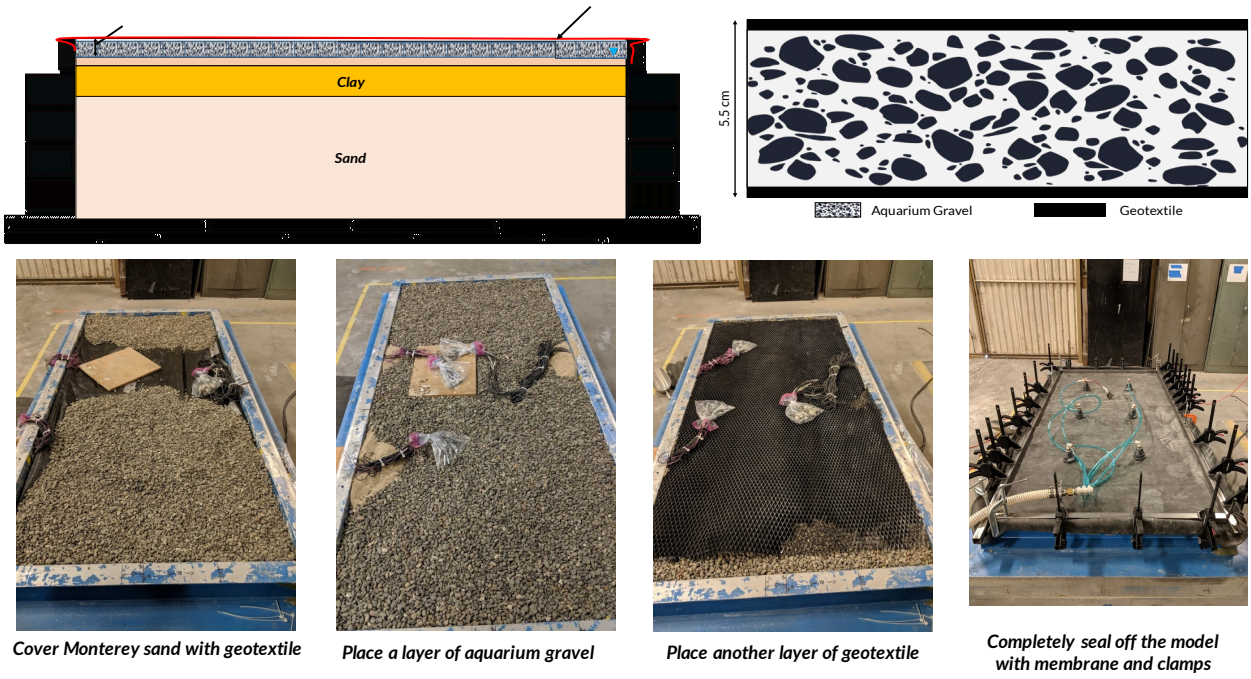

Figure 30. Preparation of the model for vacuum transportation.

Six bulkhead fittings in the top membrane were connected to the vacuum pump with gages attached to monitor the suction developed. The wires of the sensors were rested on the wooden plywood away from the bulk heads.

5.5.2 Transportation

The sealed model was slowly pulled under vacuum equivalent to overburden stress of 50 kPa and was left overnight. A mobile generator was used to provide power to the vacuum pump. Figure 31 shows the vacuum transportation of the model. In the morning, a forklift was used to move the model from the preparation room to the centrifuge. During that process and until the model was placed on the centrifuge arm, the model was constantly under vacuum confinement. At the centrifuge, the model was gently lifted with a chainfall and then slowly lowered on the arm.

Model transportation from prep room to the centrifuge

Model at the centrifuge arm

Placing the model on the arm

Figure 31 Vacuum transportation of the model and placement on the centrifuge arm.

Removing the geotextile membrane and gravel layer

Model after removal of geotextile membrane

Use of Monterey sand to give a nice surface finish

Figure 32. Model after vacuum transportation.

Once the model was fully sitting on the arm, the vacuum was slowly decreased to zero. The preparation for the vacuum transportation was removed as shown in Figure 32. Measurements of the soil surface was taken to check any settlement during the process. The vacuum transportation worked extremely well. No surface settlement was observed during model transportation. At the end, the surface layer was leveled with Monterey sand to give a nice finish as shown in Figure 32.

5.6 Pile Installation

5.6.1 Preparation

Since jacking the pile directly from the ground surface would smear the clay layer along the pile's interface to the soil beneath, small smooth guide pipe with diameter 90% of the model pile were installed to the depth of 12.5 cm (to the bottom of clay layer) as shown in Figure 33. These piles were used to remove the clay from the installation depth and provided a guidance during pile installation. Hand-held surveyor's level was used ensure the verticality of pile during installation. To allow drainage from beneath the clay layer to surface, four drainage wells of diameter 3.8 cm were installed on the four corners of the model (Figure 33).

Figure 33. Installation of guide piles to remove the clay layer and provide guide to jacking of piles.

5.6.2 Installation

For installing piles, a hand-held surveyor's level, 1000 lbs dead load, spirit level attached to the pile mass and a pile cap with ball-bearing was used. Figure 34 shows the steps involved in the installation of piles. Spirit levels were attached to the pile mass in the two directions to ensure verticality of the pile head mass. The first step involved the manual installation of the pile, to the bottom of clay layer. This was done to ensure the verticality of the pile before it is pushed into the sand. For this, the guide pile was removed, and the model pile was slowly pushed in the same hole using a hand-held surveyor's level as shown in Figure 34. The pile was then pushed using a 1000lbs dead load. A ball-bearing was attached to the pile cap to prevent any transfer of moment when in contact with the dead weight (see Figure 34).

Removing the guide pile *Manual installation to the bottom of clay layer* *Preparation for installation using 1000lbf load*

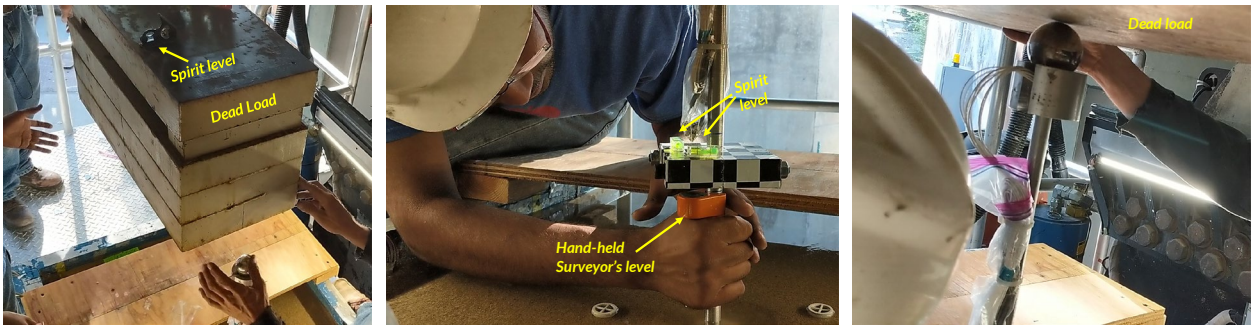

1000 lbs dead load | View near the soil surface during pile installation | View at the dead load during pile installation

Figure 34. Steps involved in installation of pile.

Figure 35. View of model with installed piles.

A chainfall was used to slowly lower the dead load such that its center of the mass was just in contact with the ball-bearing. The dead load was initially levelled off with the spirit level attached at its top surface (see Figure 34).

Each installation took almost 20-30 minutes involving three persons. One operating the chain fall, second balancing the dead load and third guiding the pile's vertically in the soil. Figure 35 shows the view of the model with the installed piles.

5.7 Work on the Arm

Work on the arm involved placing the rack to support the displacement transducers on the piles, routing all the sensor cables to the data acquisition system (DAQ) and installing cameras. During this process, the model was occasionally sprinkled with water at regular intervals to prevent desiccation of the clay surface from drying. Figure 36 and Figure 37 show model view while working on the arm.

Figure 36. Views of the model while working on the arm.

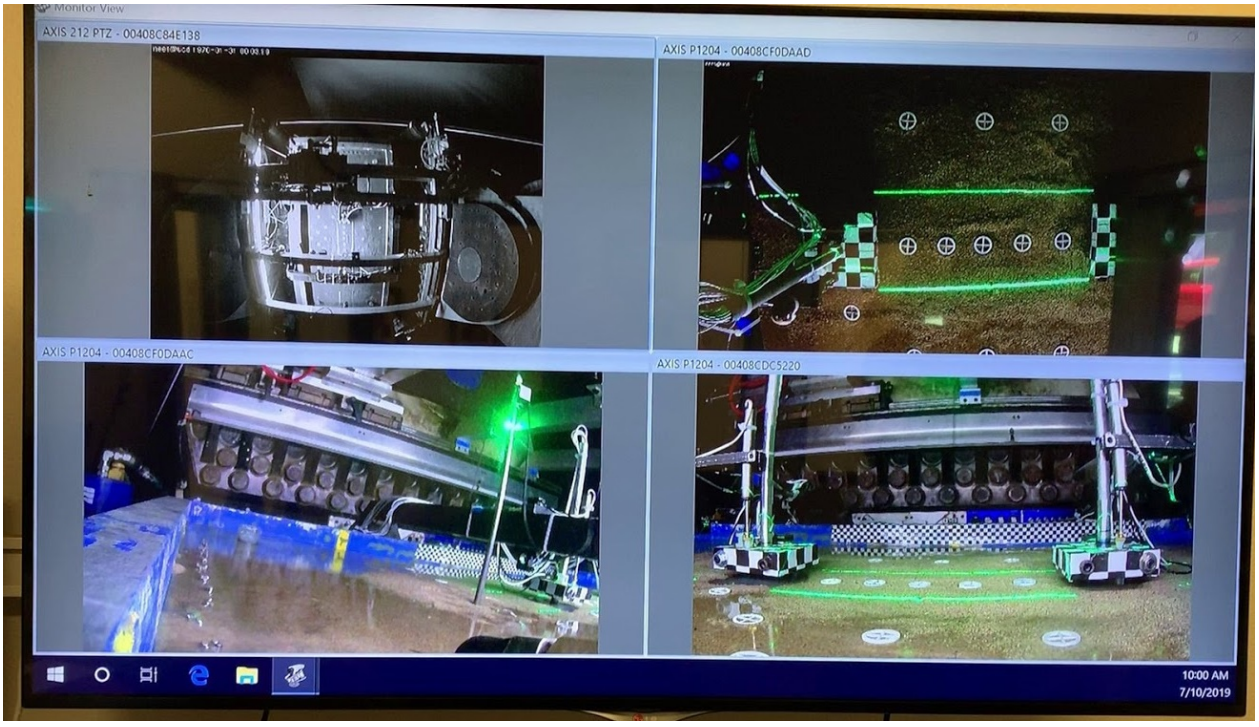

Figure 37. View of the model from the control room.

6 CENTRIFUGE TEST

6.1 Test Chronology and Log Details

The test was conducted on 10th and 12th July 2019. Table 21 and Table 22 outlines the details of different events during and in between those days.

Table 21. Log of events and their description on Day 1 (10th of July).

Date	*Spin*	*Time*	*Event*	*Event Description*	*Fast Data*	*Slow Data*
6th July	-	11:53	VS_1 - VS_3	Motorized Vane Shear Test	-	-
	-	15:00	VS_4 - VS_5	Hand Vane Shear Test, 19 mm blade	-	-
	-	15:15	VS_6	Hand Vane Shear Test, 33 mm blade	-	-
10th July	1	7:16	-	Slow Data started	-	07102019@071632.bin
		9:25	-	Started Spinning	-	
		10:06	PLT_1	Pile Load Test	07102019@071632@101132@64.3rpm.bin	
	-	11:45	-	Hand measurement of soil surface	-	
	-	12:32	VS_7-VS_8	Hand Vane Shear Test, 33mm blade	-	
	2	13:05	-	Slow Data started	-	07102019@130544.bin
		14:56	-	Started Spinning	-	
		15:23	SWM_1	Step Wave (AF=1.0, IF=4000, P-P=1.8g)	07102019@130544@152140@64.5rpm.bin	
		16:00	CPT_1	CPT Pushed	07102019@130544@155837@64.4rpm.bin	
		16:12		CPT Retracted	07102019@130544@155929@64.4rpm.bin	
		16:32	EQM_1	Small Santa Cruz (AF =1.5, IF=2000, P-P=2.1g)	07102019@130544@163104@64.5rpm.bin	
		16:53	EQM_2	Medium Santa Cruz (AF=5, IF=2000, P-P=10g)	07102019@130544@165238@64.2rpm.bin	
		17:25	CPT_2	CPT Pushed	07102019@130544@172549@64.5rpm.bin	
		17:28		CPT Retracted	07102019@130544@172708@64.5rpm.bin	
		17:35	EQM_3	Large Santa Cruz (AF=7.5, IF=2000, P-P=17g)	07102019@130544@173810@64.6rpm.bin	
	-	19:43	VS_9-VS_{10}	Hand Vane Shear Test, 33mm blade	-	-
	-	20:10	-	Hand measurement of soil surface	-	-

Event Description: VS: Vane Shear Test, PLT: Centrifuge Pile Load Test, SWM: Step Wave Motion, CPT: Centrifuge Cone Penetration Test, EQM: Earthquake Motion
Earthquake Motion Terminologies: AF: Amplification Factor, IF: Input Frequency, P-P: Peak to Peak
Slow Data Filename Description: Date@Time.bin
Fast Data Filename Description: SlowDataDate@SlowDataTime@FastDataTime.bin

Table 22. Log of events and their description on Day 2 (12th of July).

Date	Spin	Time	Event	Event Description	Fast Data	Slow Data
11th July		-	-	Mass of Pile 1 increased to 1.569 Kg	-	-
12th July, 2019	1	7:26		Slow Data started	-	07122019@072613.bin
		9:12		Started Spinning	-	
		9:31	PLT_2	Pile Load Test	07122019@072613@093119@64.4rpm.bin	
	-	10:59	-	Hand measurement of soil surface	-	
	-	10:59	VS_{11}	Hand Vane Shear Test, 33mm blade	-	
	2		-	Slow Data started	-	07122019@121326.bin
			-	Started Spinning	-	
		12:52	SWM_2	Step Wave (AF=1.0, IF=4000, P-P=1.8g)	07122019@121326@125214@64.4rpm.bin	
		13:02	CPT_3	CPT Pushed	07122019@121326@130218@64.4rpm.bin	
		13:03		CPT Retracted	07122019@121326@130325@64.4rpm.bin	
		13:09	EQM_4	Medium Santa Cruz (AF=5, IF=2000, P-P=10g)	07122019@121326@130934@64.3rpm.bin	
		13:38	EQM_5	Large Santa Cruz (AF=10, IF=2000, P-P=24g)	07122019@121326@133831@64.4rpm.bin	
		14:12	-	Spinning attempt to 60 g - Throttle fall down close to 60 g - Three attempts performed - Only 57 g was able to be achieved		
		14:53	-	Spinning down to 40g		
		15:25	-	Clay consolidation completed	-	
		15:25	CPT_4	CPT pushed in same spot as CPT_3	07122019@121326@152510@64.4rpm.bin	
		15:26		CPT retracted	07122019@121326@152604@64.4rpm.bin	
		15:27	CPT_5	CPT pushed in a new spot	07122019@121326@152726@64.4rpm.bin	
		15:28		CPT Retracted	07122019@121326@152819@64.4rpm.bin	
		15:45	EQM_6	EJM01_Freq_Corrected_38g(IF=1428, AF=0.65, P-P=24g)	07122019@121326@154548@64.4rpm.bin	
		16:17	CPT_6	CPT pushed in same spot as CPT_5	07122019@121326@161718@64.5rpm.bin	
		16:18		CPT Retracted	07122019@121326@161809@64.5rpm.bin	
	-	17:47	VS_{12} - VS_{13}	Hand Vane Shear Test, 33mm blade	-	-
	-	18:00	-	Hand measurement of soil surface	-	-

Event Description: VS: Vane Shear Test, PLT: Centrifuge Pile Load Test, SWM: Step Wave Motion, CPT: Centrifuge Cone Penetration Test, EQM: Earthquake Motion
Earthquake Motion Terminologies: AF: Amplification Factor, IF: Input Frequency, P-P: Peak to Peak
Slow Data Filename Description: Date@Time.bin
Fast Data Filename Description: SlowDataDate@SlowDataTime@FastDataTime.bin

6.2 Vane Shear Tests

Vane shear tests were performed at 1 g at multiple stages of the centrifuge experiment as listed in Table 23. The table also shows the excess pore pressure (Δu) in the clay layer measured during these tests. Water content samples were also taken at the depths of 1.6 m, 3 m, and 4.4 m after the vane shear test (Table 24). The vane shear tests were performed in middle of the clay layer i.e., at the depth of 3 m (prototype scale).

Table 23. Vane shear test performed during the test.

Date	*Time*	*Test #*	*Description*	s_u^{pk} *[kPa]*	s_u^{res} *[kPa]*	Δu *[kPa]*
7/6/2019	3:00 PM	VS_4	Hand Vane Shear, 19mm blade	7	3	0
	3:10 PM	VS_5	Hand Vane Shear, 19mm blade	7	3	0
	3:15 PM	VS_6	Hand Vane Shear, 33mm blade	10	2	0
7/10/2019	12:21 PM	VS_7	Hand Vane Shear, 33mm blade	13	4	-1
	12:32 PM	VS_8	Hand Vane Shear, 33mm blade	12	3	-1
	7:43 PM	VS_9	Hand Vane Shear, 33mm blade	15	3	-2
	7:49 PM	VS_{10}	Hand Vane Shear, 33mm blade	17	3	-2
7/12/2019	10:59 AM	VS_{11}	Hand Vane Shear, 33mm blade	17	4	-2
	5:47 PM	VS_{12}	Hand Vane Shear, 33mm blade	20	5	-1
	5:58 PM	VS_{13}	Hand Vane Shear, 33mm blade	20	4	-1
Motorized vane shear test (VS1-VS3) results are not shown here because of their sensitivity to bending.						

Table 24. Water content samples taken during the vane shear test.

Date	*Time*	*Depth [m]*	*w (%)*	*e*
7/6/2019	2:00 PM	1.6	44	1.13
		3	42	1.09
		4.4	42	1.07
7/10/2109	7:49 PM	1.6	45	1.16
		3	43	1.11
		4.4	43	1.10
7/12/2109	6:15 PM	1.6	42	1.08
		3	42	1.08
		4.4	39	1.01

6.2.1 Undrained Shear Strength Evaluation

Vane shear and water content tests presented in Table 23 and Table 24 were used to determine the undrained shear strength of the clay layer. The effective friction angle of the clay was taken as $\phi' = 22^o$ (i.e. critical state parameter q/p=M=0.856) (Upadhyaya et al. 2016). From Figure 6, the compression index (C_c) and recompression index (C_r) was estimated to be C_c=0.185 and C_r=0.041, respectively. The undrained shear strength was estimated from the strength normalizing concept

$$s_u/\sigma'_{vc} = 0.30\ OCR^m$$

Where, 0.30 is the undrained shear strength ratio for normally consolidated clay (Khosravi et al. 2015) and the over consolidation ratio (OCR) parameter m is defined as $m = \frac{C_c - C_r}{C_c}$ (Roscoe and Burland 1968). For C_c=0.185 and C_r=0.041, the OCR parameter m came to be 0.76. Table 25 shows the measured and estimated undrained shear strength of the clay using the above normalized shear strength method. It must be noted that the estimated and the measured shear strength are for the middle of the clay layer (i.e, at the depth of 3 m).

Table 25. Estimated undrained shear strength at the middle of the clay layer.

Test #	*Δu [kPa]*	*σ'v [kPa]*	*e*	*Consolidation Stress [kPa]*	*OCR*	*Measured s_u^{pk} [kPa]*	*Estimated s_u [kPa] at 1g*	*Estimated s_u [kPa] at 40g*
VS4	0	0.6	1.11	103	172	7	10	22
VS5	0	0.6	1.11	103	172	7	10	22
VS6	0	0.6	1.11	103	172	10	10	22
VS7	-1	1.6	1.11	103	65	13	12	22
VS8	-1	1.6	1.11	103	65	12	12	22
VS9	-2	2.6	1.1	121	47	15	16	25
VS10	-2	2.6	1.1	121	47	17	16	25
VS11	-2	2.6	1.1	121	47	17	16	25
VS12	-1	1.6	1.07	196	122	20	20	37
VS13	-1	1.6	1.07	196	122	20	20	37

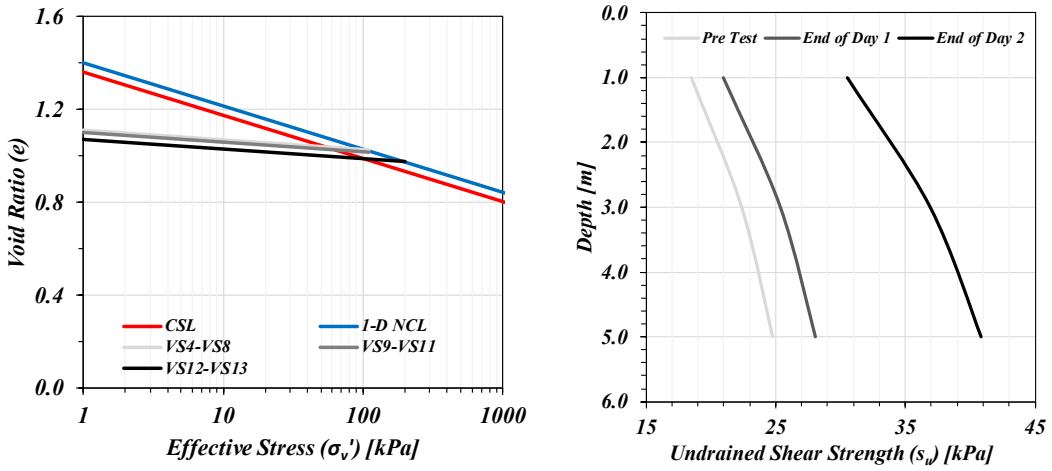

Figure 38. Undrained shear strength (s_u) profile of clay layer estimated from vane shear test.

6.3 Centrifuge Cone Penetration Tests

Centrifuge cone penetration tests were performed with a 6 mm diameter probe with tip angle of 60 degrees and length of 300 mm (12 m in prototype scale) (see Figure 12) at different stages of centrifuge test (see Table 21 and Table 22). The cone was pushed at the rate of 1 cm/s. On Day 1, the connection of the CPT probe with the Data Acquisition System (DAQ) was little loose which resulted in a noisy data. For sake of reference, the raw result from the first CPT test conducted on day 2 (CPT_3) is shown in Figure 214. It must be noted that CPT_4 and CPT_6 were conducted in the same hole as CPT_3 and CPT_5 respectively and hence their results have not been shown in the report. The tests CPT_4 and CPT_6 were performed to check whether CPTs conducted in the same spot (once the soil is fully reconsolidated after liquefaction) can predict the soil state correctly. The analysis of CPTs in the same spot will be performed later as we gather more data in future tests.

Inspection of raw CPT results showed an effect of temperature on the recorded measurements. As a result, all the centrifuge cone penetration tests were corrected for temperature effects (see Appendix L). Interpretations from CPTs are shown in Figure 39. Normalized cone tip resistance (qc1N) and relative density (D_r) was estimated based on Idriss and Boulanger (2008) CPT correlation with constants C_1=3.09 and C_2=0.514 as calibrated by Darby et al. (2019) for Ottawa sand using a 6-mm-diamter cone on large centrifuge. In these plots, the qc1N and relative density is not shown for the clay layer and above it.

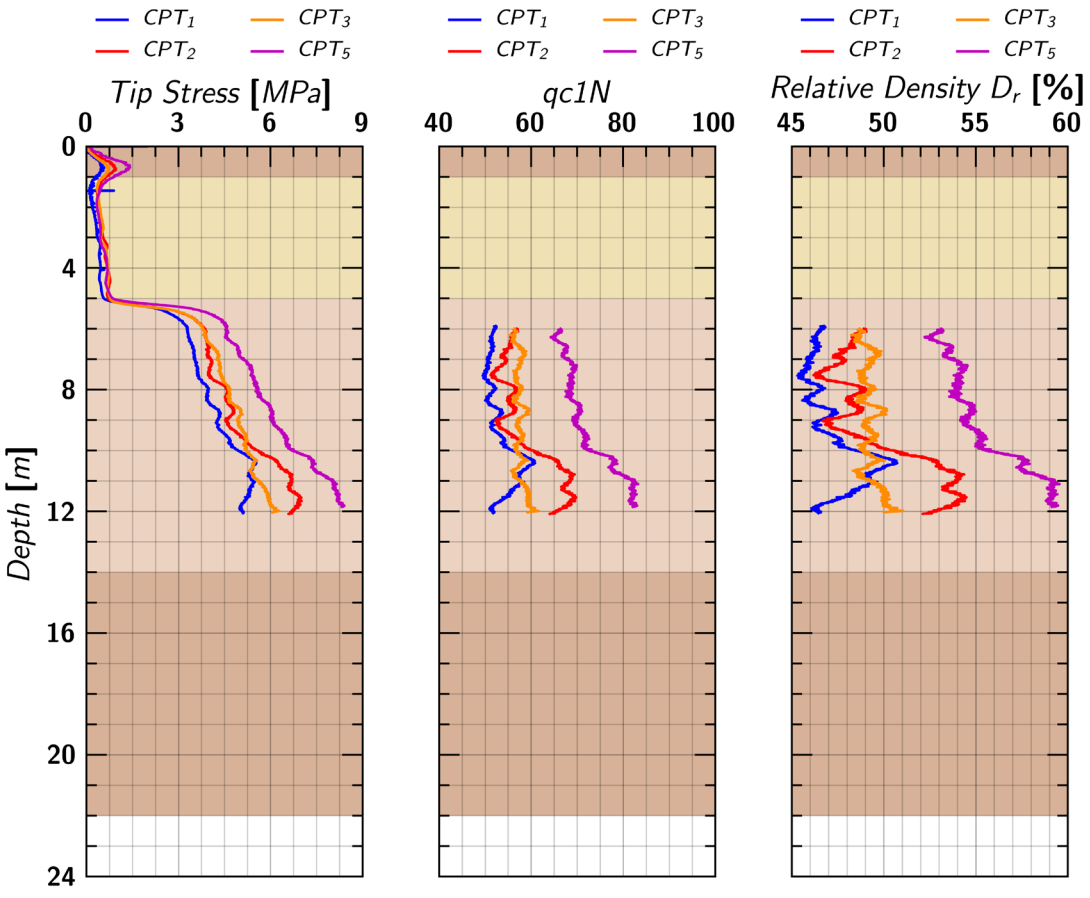

Figure 39. Temperature corrected centrifuge cone penetration tests (CPT_1, CPT_2, CPT_3 and CPT_5), showing the tip stress, normalized cone tip resistance qc1N and estimated relative density (D_r) in the sand layer.

6.4 Centrifuge Pile Load Test

Because the stroke of the actuator was limited, CPT tests could not extend beyond 12 m. As a result, a pile load test was devised to characterize the deeper dense layer. A 10 mm diameter (model scale), 48 cm long solid steel rod with a tip angle of 120 degrees was inserted at 1 g up to a depth of 17 cm (model scale) and was then pushed into the dense sand at 40g using a hydraulic actuator advancing at 1cm/s. The total axial load at the pile head was measured. Appendix M describes the process for interpreting the results from the centrifuge pile load test.

Figure 40 plots the raw pile load test results and the interpreted tip load for cone tip load factor α=0.8 and pile tip apex angle factor β=1.4 (see Appendix M.1). The results show a clear delineation of the boundary between the loose sand and the dense sand at a depth of 14 m. The interpreted tip loads were consistent with the intended density of the dense sand. The results show a very small increase of penetration resistance in PLT_2, presumably due to the seismic shaking between PLT_1 and PLT_2.

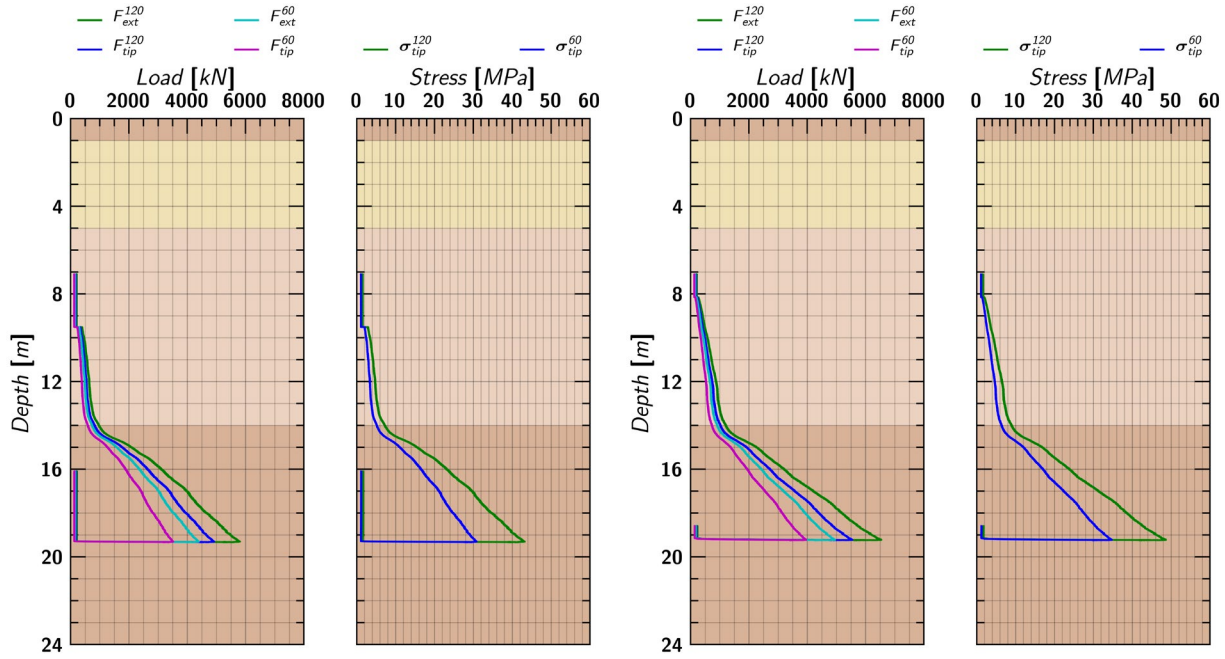

Figure 40. Interpreted results from centrifuge pile load test PLT_1 (left) and PLT_2 (right), for cone tip load factor α=0.8 and pile tip apex angle factor β=1.4 (see Appendix M.1).

6.5 Pile Capacity

Figure 41 show the pile load curve estimated from the axial load distribution in Pile 2 at the end of the centrifuge test (i.e., after EQM_6, see Figure 207). From the load curve, a shaft friction capacity of 2300 kN and 1200 kN was estimated for Pile 1 and Pile 2 which were embedded 0D and 5D in dense sand layer. The pile tip stress obtained from the centrifuge pile load test was used to estimate the tip capacity. Figure 40 shows a tip stress of 8 MPa and 24 MPa for a 60-degree cone tip at a depth of 0D and 5D in the dense sand layer. Figure 42 and Figure 43 show the static pile capacity calculated using different methods based on the estimated cone tip resistance of 8 MPa and 24 MPa and skin resistance of 1200 kN and 2300 kN for Pile 1 (0D embedment) and Pile 2 (5D embedment) respectively. The median pile load capacity was found to be about 2700 kN and 6200 kN for Pile 1 and Pile 2, respectively. The piles (Pile 1 and Pile 2) initially loaded

with 500 kN resulted in a static factor of safety of 5.4 and 12.4, respectively. From the total pile capacity, the tip capacities came to be 1500 kN and 3900 kN for Pile 1 and Pile 2, respectively.

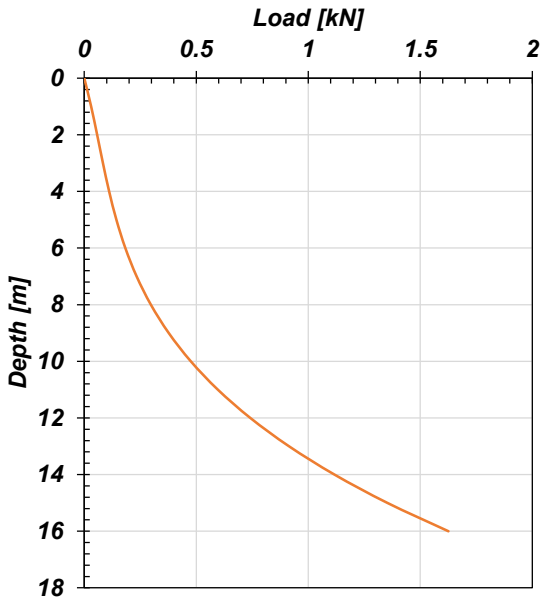

Figure 41. Pile load curve estimated from the axial load profile of Pile 2 at the end of EQM$_6$ shaking (Figure 207).

Soil Drained Critical Friction Angle [Degrees]		30
Scale Factor		40
Pile Properties		*At 40 g*
Outer Dia [mm]	15.88	635
Inner Dia [mm]	14.10	564
Length [mm]	660.40	26416
Crossectional Area [mm^2]	41.85	66966
Base Area [mm^2]	197.93	316692
Pile Self Weight [kN]	0.00146	2
I [mm^4]	1179.08	3018453162
Young's Modulus, E [Pa]	70000000000.00	70000000000
Bending Stiffness EI [Pam^4]	82.54	211291721.35
Skin Friction Capacity [kN]		1200
Drag Load [kN]		800
$N_{1\prime60}$ @ 0D in Dense Sand (Dr=80%))		40
Cone Tip Resistance @ 0D in Dense Sand (Dr=80%) [MPa]		8
Effective Stress [kPa]		128

Design Method	*Pile Base Stress [MPa]*	*Pile Base Resistance [kN]*	*Total Pile Resistance [kN]*	*Base Resistance Factor*	*Nominal Pile Resistance [kN]*
Based on Cone Tip Resistance	8.0	2533.5	3733.5	0.50	1807
Norddlund/Thurman Method	8.6	2736.2	3936.2	0.45	1771
Nottingham and Schmertmann method	6.0	1900.2	3100.2	0.50	1490
Dutch Method (qc average over 8D above and 4D below tip)	6.0	1900.2	3100.2	0.50	1490
Aoki and Velloso's method	4.6	1447.7	2647.7	0.50	1264
LCPC Method	3.2	1013.4	2213.4	0.50	1047
FHWA/IN/JTRP-99/8 (Rodrigo Salgado,Junhwan Lee) s/d=10%	3.2	1013.4	2213.4	0.50	1047
ICP-05	3.2	1013.4	2213.4	0.50	1047
Lehane, Scheider and Xu (2005)	3.6	1140.1	2340.1	0.50	1110
Kenneth Gavina, Meho Sasa Kovacevic, David Igoec	4.8	1520.1	2720.1	0.50	1300
Mean	5.1	1621.8	2821.8	0.50	1351
Median	4.7	1483.9	2683.9	0.50	1282
Max	8.6	2736.2	3936.2	0.50	1908
Minimum	3.2	1013.4	2213.4	0.50	1047

Figure 42. Determination of static pile capacity for Pile 1 (0D embedment) using different methods of pile tip stress.

Soil Drained Critical Friction Angle [Degrees]		30
Scale Factor		40
Pile Properties		*At 40 g*
Outer Dia [mm]	15.88	635
Inner Dia [mm]	14.10	564
Length [mm]	660.40	26416
Crossectional Area [mm^2]	41.85	66966
Base Area [mm^2]	197.93	316692
Pile Self Weight [kN]	0.00146	2
I [mm^4]	1179.08	3018453162
Young's Modulus, E [Pa]	70000000000.00	70000000000
Bending Stiffness EI [Pam^4]	82.54	211291721.35
Skin Friction Capacity [kN]		2300
Drag Load [kN]		1200
$N_{1,60}$ @ 5D in Dense Sand (Dr=80%))		40
Cone Tip Resistance @ 0D in Dense Sand (Dr=80%) [MPa]		24
Effective Stress [kPa]		158

Design Method	*Pile Base Stress [MPa]*	*Pile Base Resistance [kN]*	*Total Pile Resistance [kN]*	*Base Resistance Factor*	*Nominal Pile Resistance [kN]*
Based on Cone Tip Resistance	24.0	7600.6	9900.6	0.50	4835
Norddlund/Thurman Method	10.7	3377.5	5677.5	0.45	2555
Nottingham and Schmertmann method	15.0	4750.4	7050.4	0.50	3410
Dutch Method (qc average over 8D above and 4D below tip)	15.0	4750.4	7050.4	0.50	3410
Aoki and Velloso's method	13.7	4343.2	6643.2	0.50	3207
LCPC Method	9.6	3040.2	5340.2	0.50	2555
FHWA/IN/JTRP-99/8 (Rodrigo Salgado,Junhwan Lee) s/d=10%	9.6	3040.2	5340.2	0.50	2555
ICP-05	9.6	3040.2	5340.2	0.50	2555
Lehane, Scheider and Xu (2005)	9.0	2850.2	5150.2	0.50	2460
Kenneth Gavina, Meho Sasa Kovacevic, David Igoec	14.4	4560.4	6860.4	0.50	3315
Mean	13.1	4135.3	6435.3	0.50	3103
Median	12.2	3860.4	6160.4	0.50	2965
Max	24.0	7600.6	9900.6	0.50	4835
Minimum	9.0	2850.2	5150.2	0.50	2460

Figure 43. Determination of static pile capacity for Pile 2 (5D embedment) using different methods of pile tip stress.

6.6 Step Wave Motion Test

Step wave motion tests SWM_1 and SWM_2 were performed on Day 1 and Day 2, respectively to characterize the natural period of the piles. Section 6.6.1 and Section 6.6.2 shows the response of piles during those tests. The estimated natural period of the piles in horizontal and vertical direction are summarized in Table 26.

Table 26. Natural period of piles evaluated from the step wave motion tests.

Test	*Natural Period (s)*			
	Pile 1		*Pile 2*	
	Horizontal	*Vertical*	*Horizontal*	*Vertical*
SWM_1	1	1.5	1.1	1.2
SWM_2	0.8	1.5	1	1.2

6.6.1 Step Wave Motion SWM_1

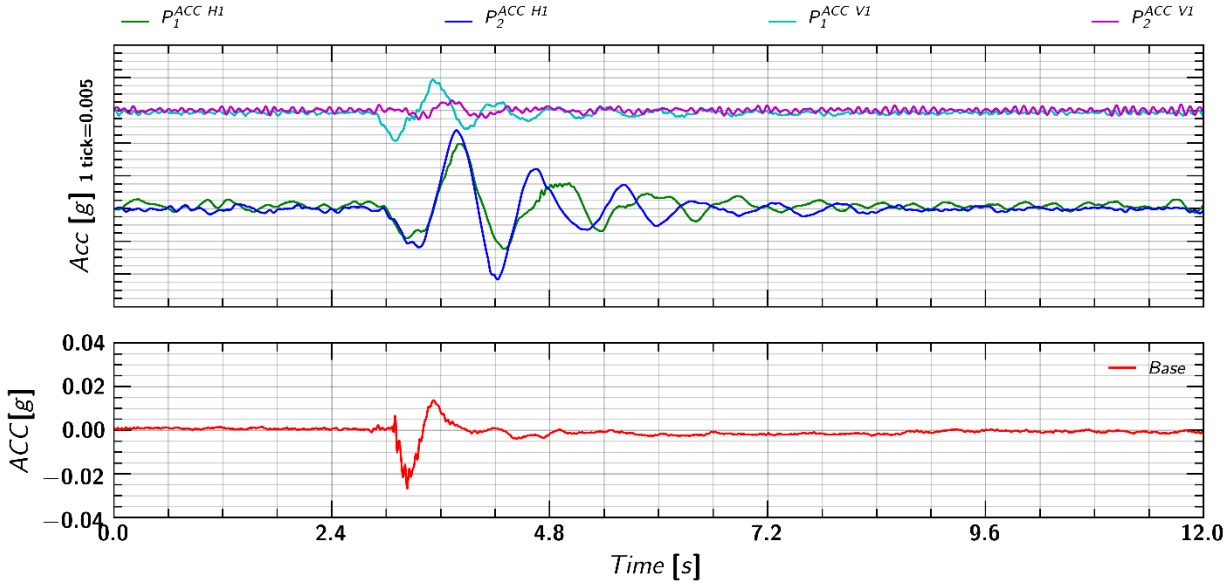

Note: Base refers to the average of acceleration measured by EAST and WEST sensors.

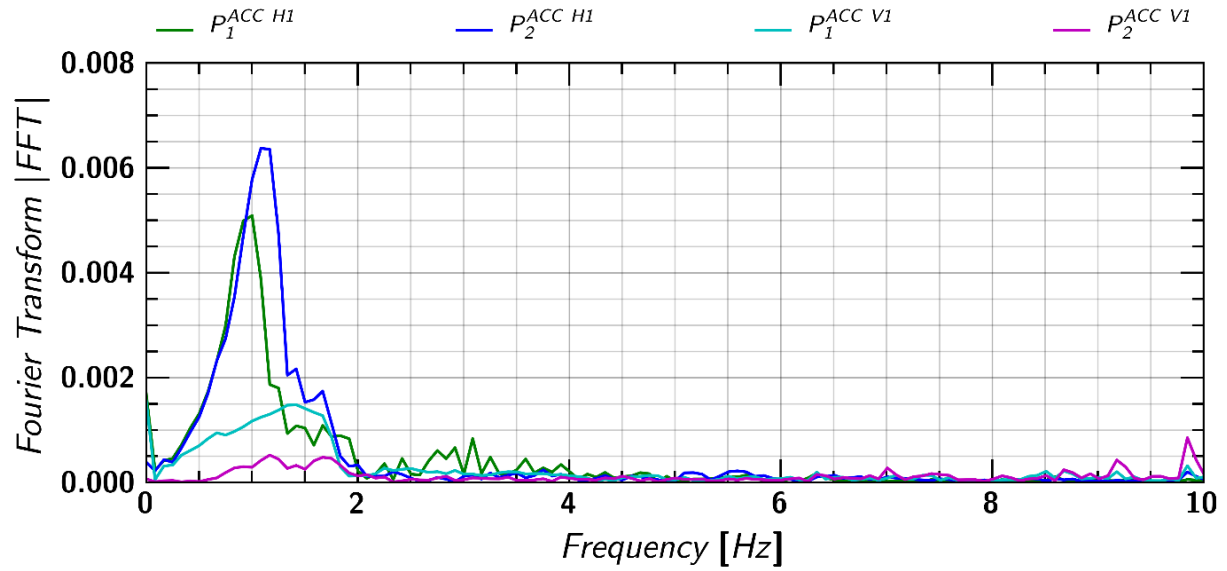

Figure 44. Dynamic response of piles during step wave motion SWM_1.

6.6.2 Step Wave Motion SWM₂

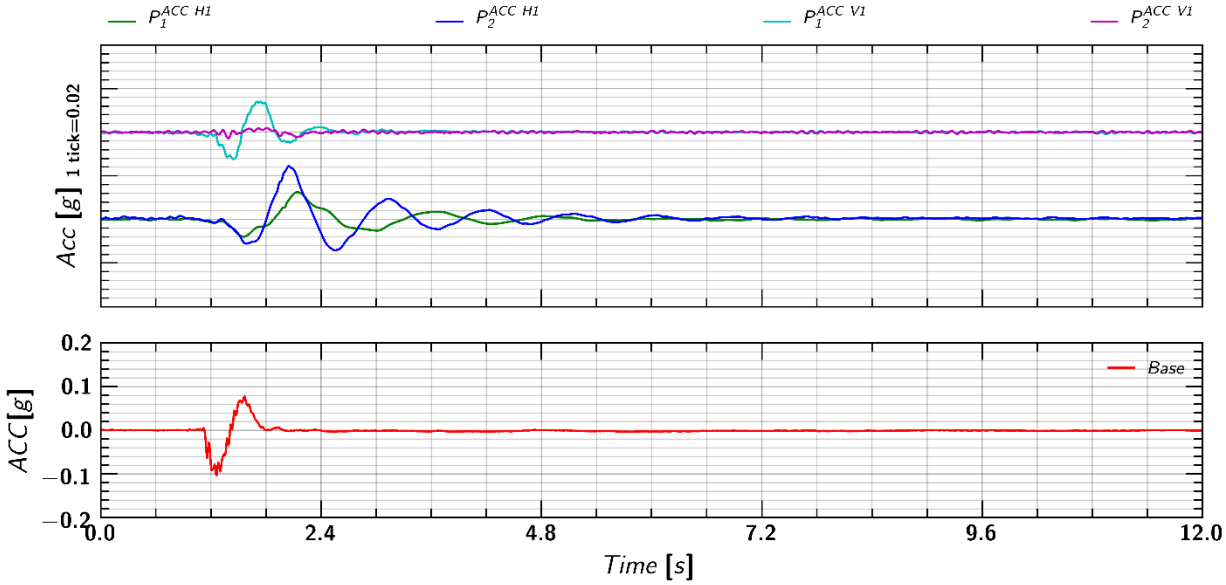

Note: Base refers to the average of acceleration measured by EAST and WEST sensors.

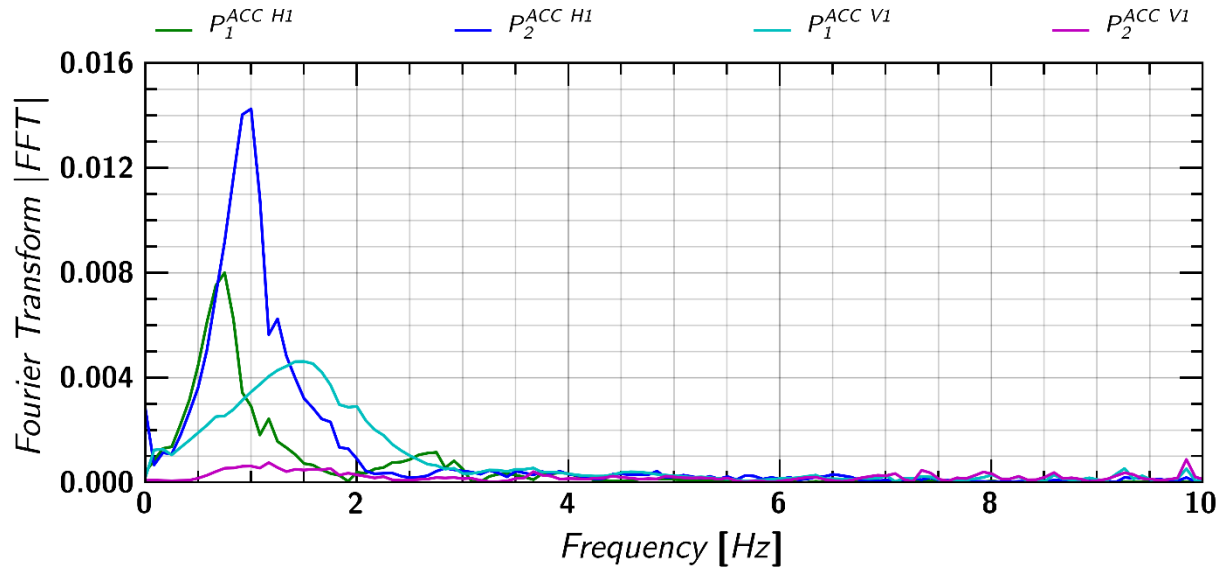

Figure 45. Dynamic response of piles during step wave motion SWM₂.

6.7 Soil and Pile Settlement

6.7.1 Estimated from Linear Potentiometers

Figure 46 and Figure 47 plots the settlement in soil and pile measured with linear potentiometers across different events.

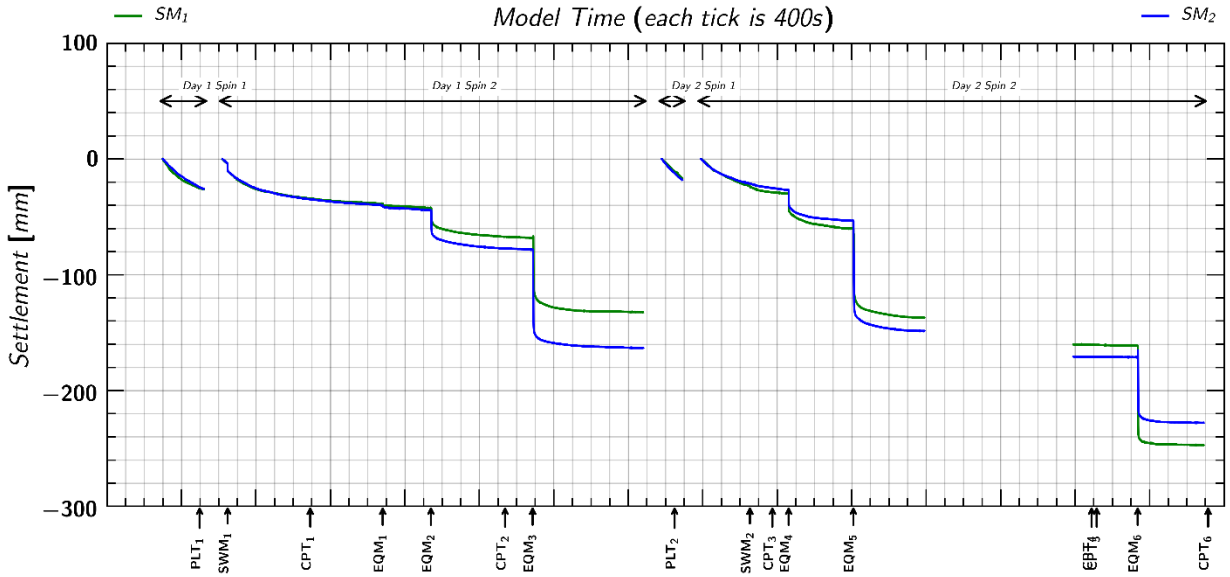

Figure 46. Soil settlement measured with surface markers SM_1 and SM_2 across different events.

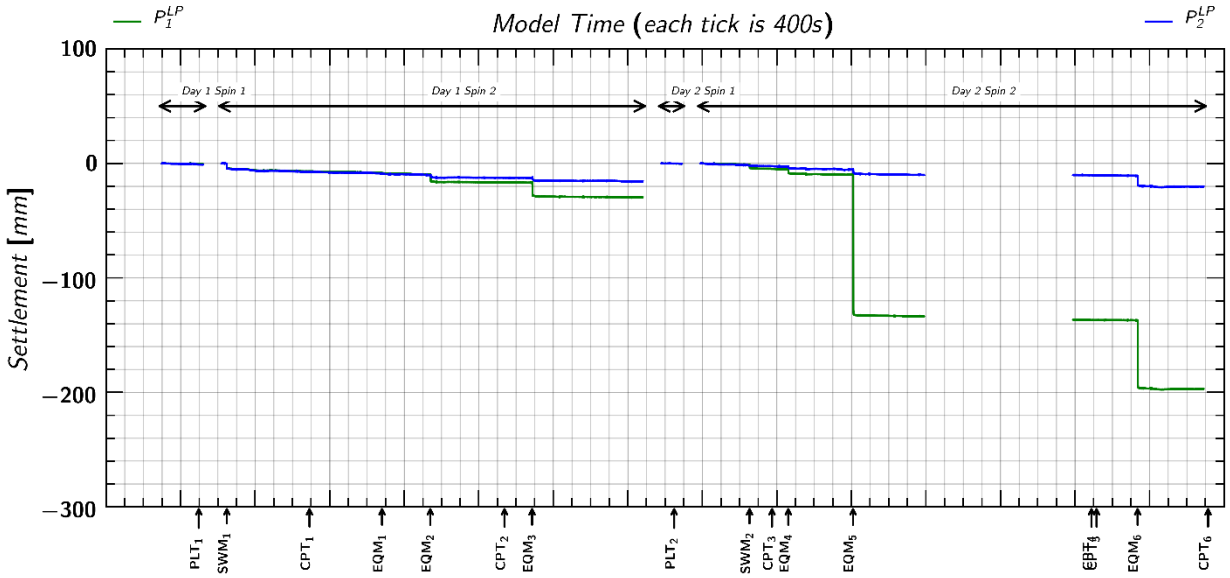

Figure 47. Pile settlement measured with linear potentiometers P_1^{LP} and P_2^{LP} across different events.

6.7.2 Estimated from Processing Lasers in Snapshots

The laser position in the snapshots taken from Axis cameras (see Table 19) were processed to find out the settlement of soil and pile as per the theory discussed in Section 4.6 (Sinha et al. 2020). Figure 48 show the change in laser position (from the settlement in soil and the pile) in the snapshots taken before and after the earthquake event EQM_6.

Figure 49 and Figure 50 plots the average settlement in soil and pile estimated from processing the lasers lines in the snapshots (see Table 19) taken at different times during the test. The estimated settlement can be seen to be matching quite well with the linear potentiometer recordings.

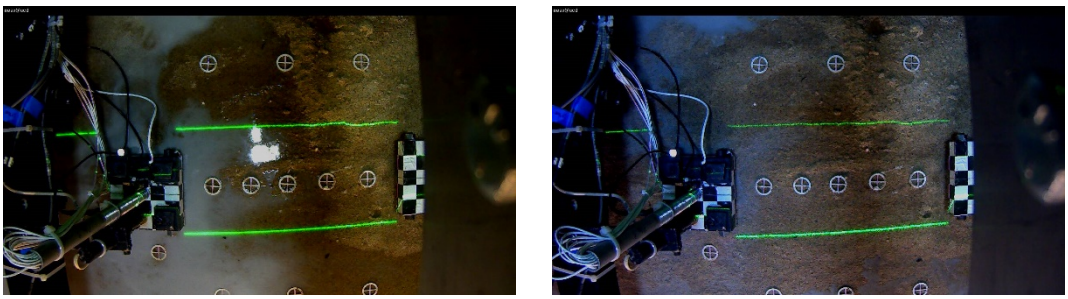

Figure 48. A view (in north-south direction) of change in laser position due to settlement of soil and piled as recorded in the snapshot taken from the Axis cameras before (left) and after (right) the earthquake event EQM_6.

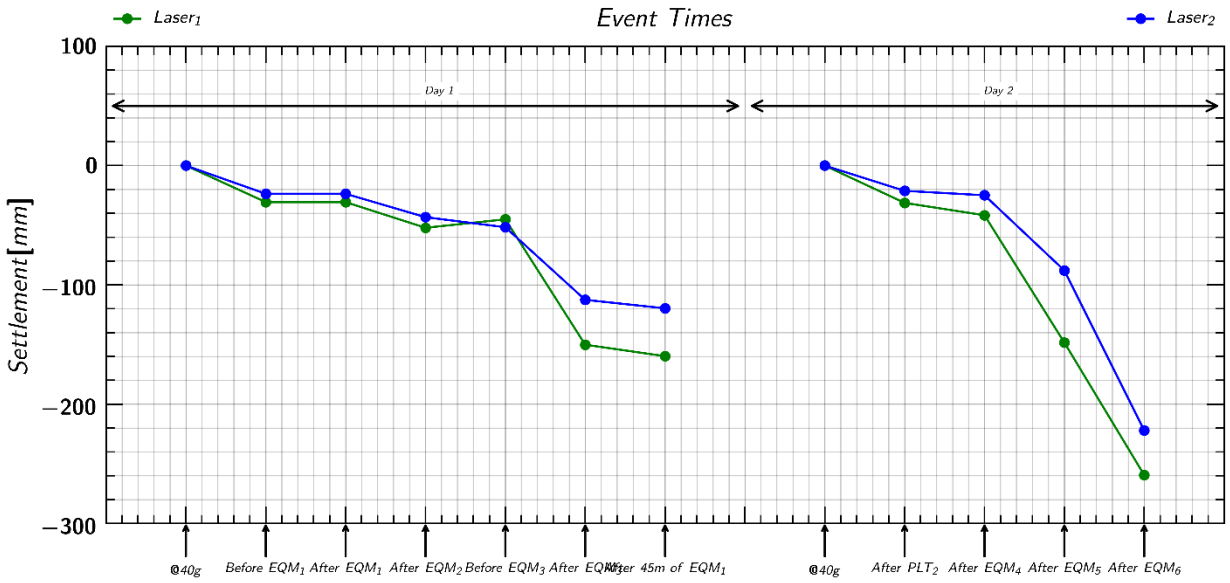

Figure 49. Soil settlement measured with Laser 1 and Laser 2 across different events.

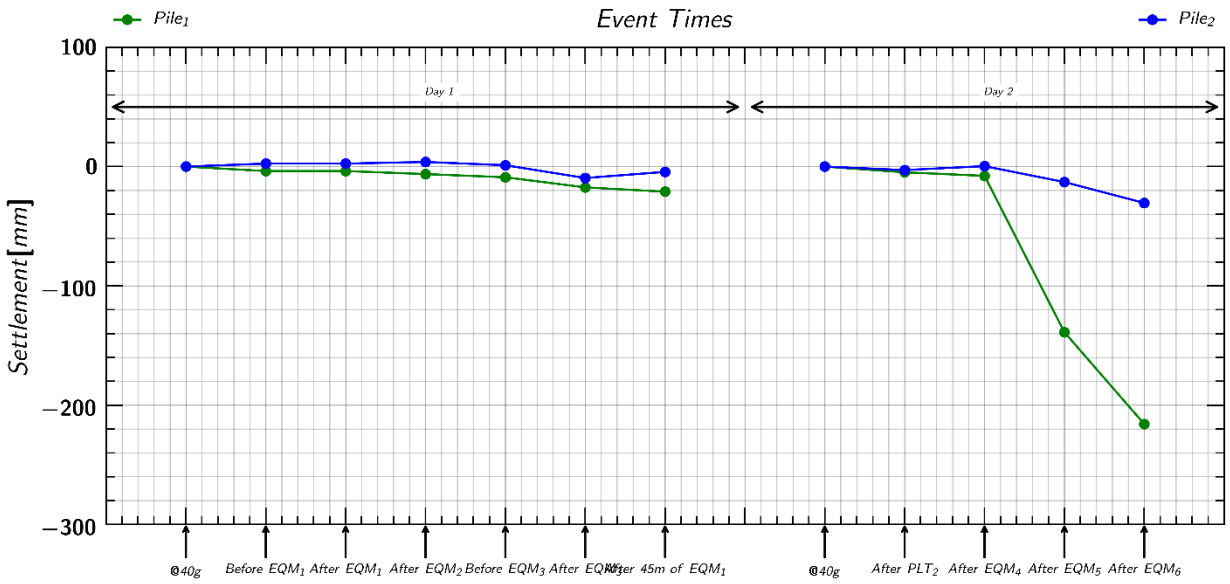

Figure 50. Pile settlement measured with lasers lines on pile head across different events.

6.8 Shaking Events

In total six earthquake shaking events were applied to the model with five Santa Cruz motions and one EJM01 motion. Table 27 lists these motions.

Table 27. Applied earthquake motions.

Motion	***Recording***	***Filename***
Santa Cruz	1989 Loma Prieta earthquake - UCSC/Lick Lab, Ch. 1 - 90 degrees	SC60696.txt
EJM01	Modified Northridge Motion (Malvick et al. 2002)	EJM01.txt

The chronological application of all the six motions EQM_1-EQM_6 are summarized in Table 21 and Table 22. The details on these motions and the achieved peak ground acceleration (PGA) are shown below as well as in the APPENDIX sections[1] where the results are plotted.

- EQM_1 : Small Santa Cruz Earthquake (PGA=0.026g): see APPENDIX C
- EQM_2 : Medium Santa Cruz Earthquake (PGA=0.14g): see APPENDIX D
- EQM_3 : Large Santa Cruz Earthquake (PGA=0.24g): see APPENDIX E
- EQM_4 : Medium Santa Cruz Earthquake (PGA=0.14g): see APPENDIX H
- EQM_5 : Large Santa Cruz Earthquake (PGA=0.32g): see APPENDIX I
- EQM_6 : Large EJM01 Modified Northridge Motion (PGA=0.40g): see APPENDIX J

[1] To plot the response of each sensors, an initial offset reading was applied for each centrifuge spin as described below.
- PPT_1- $PPT2_1$ – offset reading at 1g, corrections made for pore pressure at 1g
- Accelerometers ($ACC_{\#}$)– offset reading is taken as just before the start of event
- SM_1, SM_2, P_1^{LP}, P_2^{LP} – offset reading at 40 g
- Axial strain gages – offset reading at 1 g
- Laser Recordings – offset reading at 1 g

6.8.1 EQM Event Plots

Appendix A, B, F and, G plot the slowly sampled data throughout the course of each spin. These long duration plots are useful for understanding the sequence of the test and for observing slow processes such as consolidation of the clay. The high-speed data is shown for each earthquake motion in the sections listed above.

For each EQM event the following plots are shown.

- *Input motion:* The applied motion measured by EAST and WEST senor. An average of these motions is represented as BASE motion, where BASE=0.5(EAST+WEST).
- *Container Acceleration:* Response of accelerometers attached to the container.
- *Soil Acceleration:* Response of accelerometers placed in soil.
- *Pile Mass Acceleration:* Response of accelerometers placed on pile.
- *Pore pressure:* Measured pore pressure in soil by Keller and MS54XXX transducers
- *Excess Pore pressure Ratio (r_u):* The excess pore pressure ratio (r_u) in soil was estimated using the formula $r_u(t) = (u(t) - u_o)/\sigma'_{vo}$, where u_o and σ'_{vo} is the hydrostatic and initial vertical effective stress respectively before the start of EQM event and u is the pore pressure at any given time (t) during the event. To compute the effective stress (σ'_{vo}), the total stress (σ_{vo}) was computed based on the initial densities and layer depth as summarized in Table 2.
- *Axial Load :* Axial load measured by the strain gages installed in the pile. To remove/reduce the effect of moment on the axial load measurements during shaking, a moving mean with a window of 6 and 3 seconds is taken for pile 1 and pile 2 strain gages respectively (shown as dashed line).
- *Pore pressure and Axial Load Profile:* Plot of axial load profiles for pile 1 and pile 2 and pore pressure profiles in soil. It must be noted that the axial load used in these plots were taken from the moving mean data of the axial measurements (shown as dashed line in Axial Load plots).

Note : Unless specified, raw data measured from the sensors are shown in the plots. During the event, some of the sensors failed and might show erratic responses. Especially the MS54XXX transducers seemed to be very unstable. The reader should take caution while reading these plots. Although, the response of MS54XXX transducers was not very good, they do contain some useful information and hence they are included in this data report.

7 MODEL DISSECTION

Upon completion of the test, the model was moved to the model prep room and dissected. Figure 51 shows the tools used in model dissection.

Figure 51. Tool used for dissecting the model.

Figure 52. A view of model during dissection.

The model was cut carefully longitudinally from the east to west side of the container as shown in Figure 52. Measurements of the sensors and colored sand layers were taken. Additionally, the model was investigated for evidence of sand boils, soil and pile settlement and tilting of pile. The observations are discussed in the sections below.

7.1 Ejecta

Several manifestations of ejecta were observed on the surface of the model as shown in Figure 53.

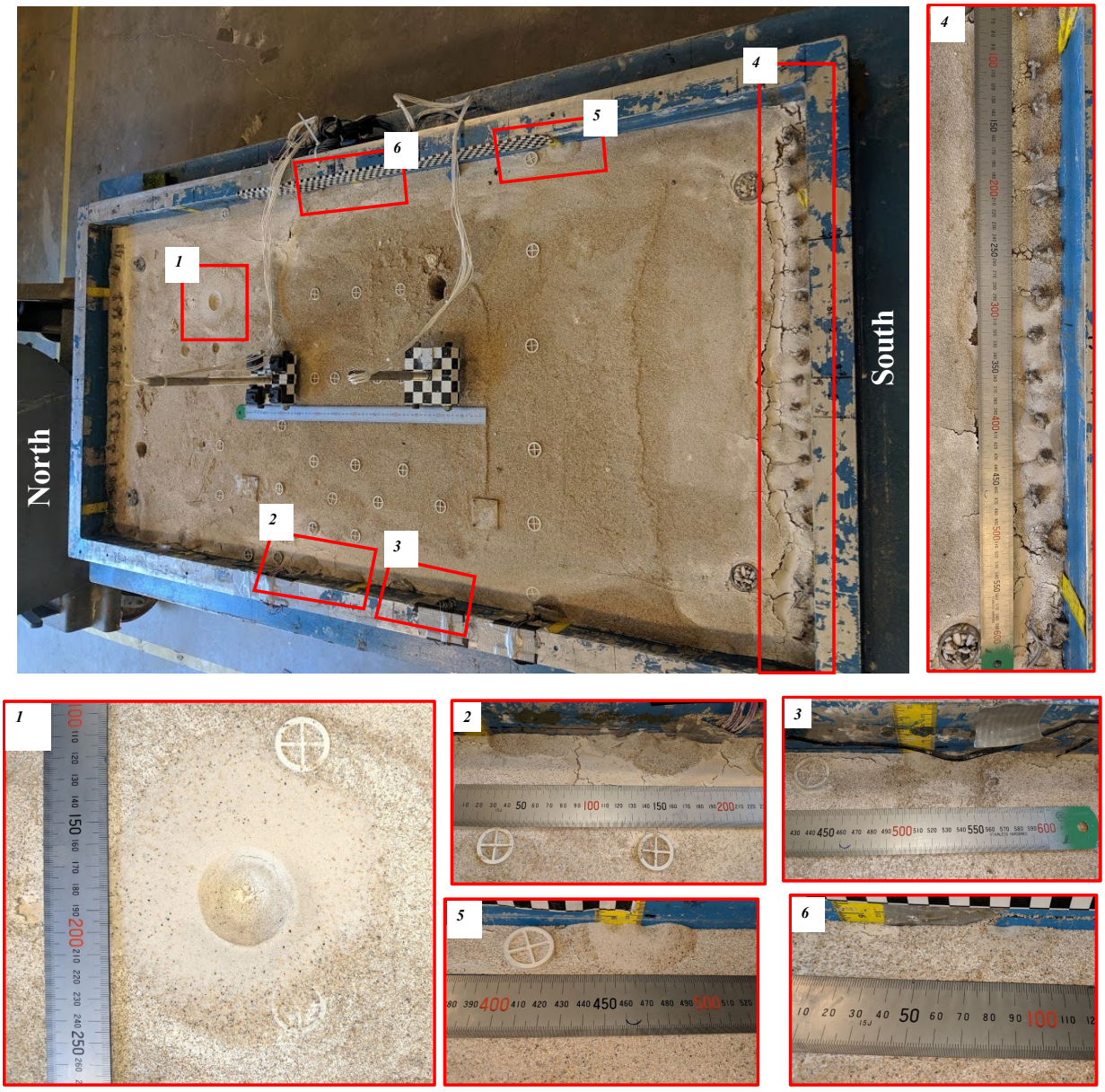

Figure 53. Surface ejecta observed in the model.

Among them, Ejectum 1 was the biggest that occurred during shaking event EQM_6 and appeared at the location of the CPT_3 hole. Upon dissecting the model, it was found that the Ejectum 1 came through the route created by the insertion of CPT_3, crossing the clay layer all the way to the surface. A cross-section view of Ejectum 1 is shown in Figure 54. Several smaller ejecta were also observed in the middle of the east-west edge of the container (Ejectum 2, 3, 5, and 6). Sand boils were also observed near the shear rods on the south side of the container. The recorded videos from Axis and GoPro cameras during shaking events confirmed the emergence of water from the sides (east/west) of the container, which might have led to ejecta on the edges.

Figure 54. Cross-section view (south-north direction) of the Ejectum 1 observed during event EQM6.

7.2 Soil Settlement

Several measurements were taken during model dissection to measure the position of the different soil layers and colored sand placed during model construction. The measurements were taken at different longitudinal (North-South) and (East-West) sections, summarized in Table 28. A view of the model cross-section during dissection is shown in Figure 55.

Table 28. Coordinates of soil layers (model scale) measured on different sections during model dissection.

x [cm]	***y [cm]***	***z coordinate [mm]***					
		Top of Dense Layer	***2/3 of Loose layer***	***1/3 of Loose Layer***	***Top of Loose Layer***	***Top of Clay Layer***	***Model Surface***
320	305	179.5	247	320	390	485	515
925	305	179	247	323	387	492	518
1340	305	179	245	320	388.5	492	518
320	390	181	249	320	386	489	520
825	390	179	249	320	389	491	520
1330	390	179	248	320	391	491	520
320	485	179	247	322	387	498	520.5
825	485	179	249.5	321.5	389.5	494.5	520
1330	485	180	248.5	320.5	390	496	520.5
320	540	179.5	250	324	389.5	495.5	521
825	540	180	250	322	390	495	520
1330	540	179.5	250.5	323.5	389.5	495.5	521
320	680	179	249.5	324	395	495.5	521
825	680	179	248.5	324	394	495	521
1330	680	179	248.5	324	397	494	519
During Model Dissection		179.4	248.5	321.9	390.2	493.3	519.7
During Model construction		180.4	254	332.1	406.7	508.8	535.2
Average Settlement [mm]		1.0	5.5	10.2	16.5	15.5	15.5
Standard Deviation		0.6	1.4	1.7	2.9	3.2	1.6

Figure 55. Measuring soil settlement during model dissection (model scale).

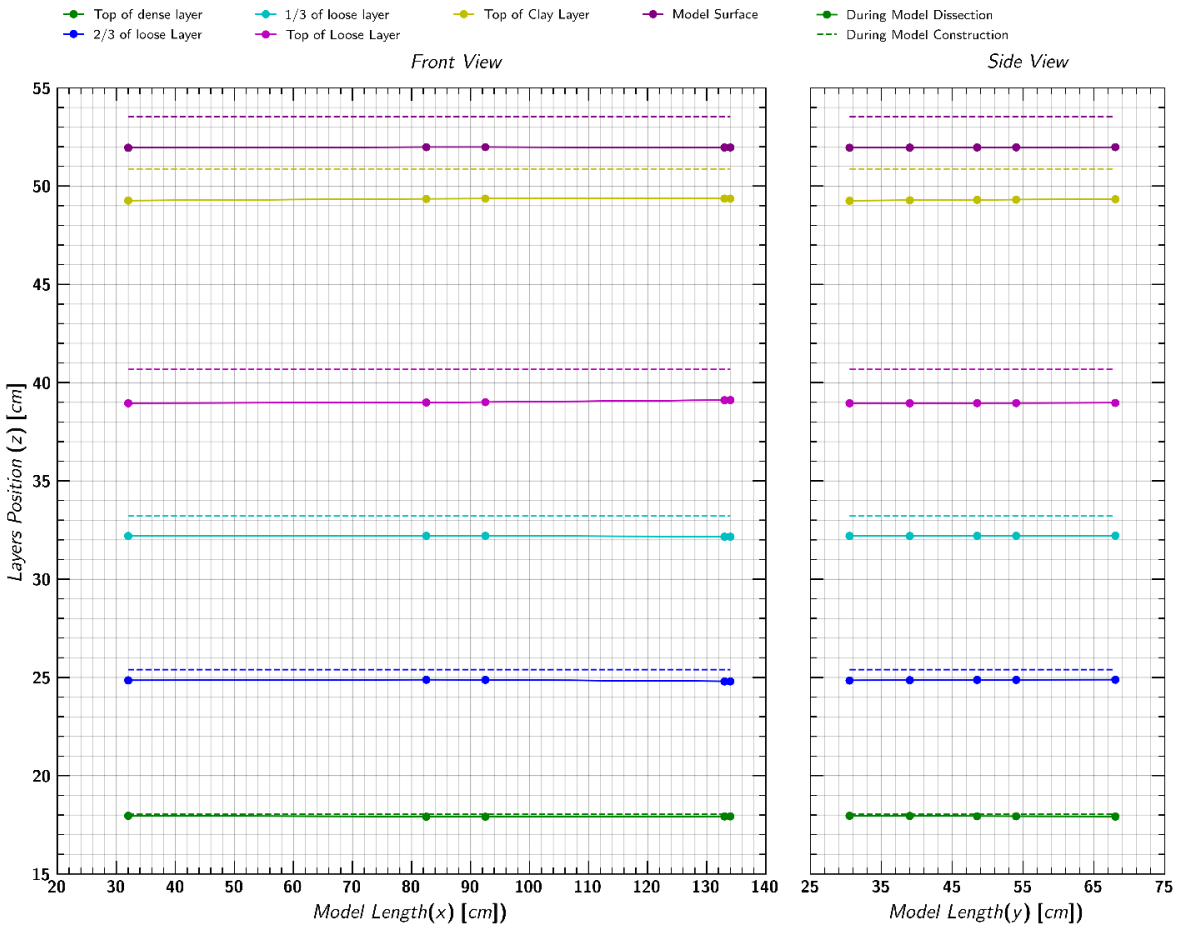

Figure 56. Front view (south-north direction) and side view (east-west direction) of average soil layers position in model scale before and after the centrifuge test.

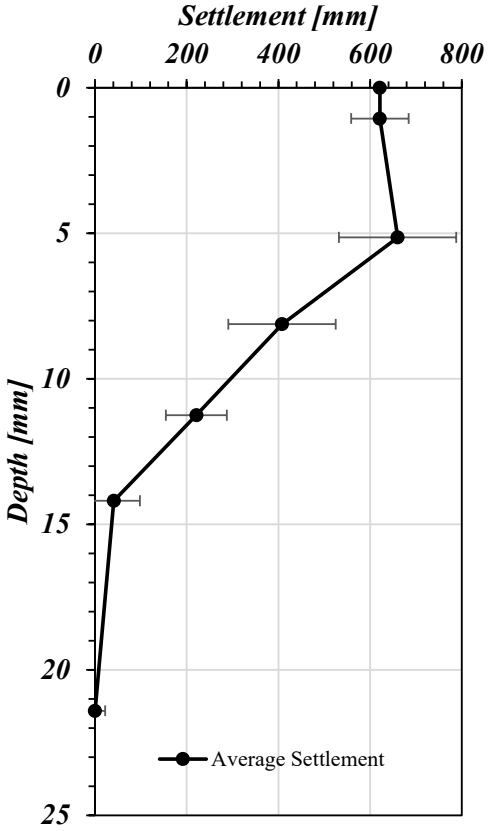

Figure 57. Average settlement profile (with ± one standard deviation) measured in the soil at prototype scale.

Post-excavation position of soil layers was measured with standard ruler with least count of 0.5 millimeters. In Figure 55, the black line denotes the position of model surface before the test. Figure 56 plots the average position of soil layers in the model scale as seen from the front view (North-South section) and side view (East-West section) of the model. Figure 57 shows the average settlement profile.

7.3 Settlement of Piles

Surface measurements were taken to evaluate the position of the pile and tilting relative to the model surface. During model dissection the tilting was further investigated by looking at the cross-section view. The summary of the observed tilt in north and south direction in the piles is show in Table 29.

Table 29. Summary of pile tip position and tilt measured (at model scale) during model dissection.

		Distance of pile head mass from the soil surface [mm]				***Distance of tip from model base [mm]***
		pile head block position				
		North	***South***	***East***	***West***	
Pile 1	Reading	18	15.5	15.5	16.5	168
	Tilt (Degrees)	1.4		-0.6		
Pile 2	Reading	22	22	23	21.5	102
	Tilt (Degrees)	0		0.9		

Figure 58 and Figure 60 shows the measurement of tilt in north-south and east west direction for pile 1 and pile 2, respectively. Figure 59 and Figure 61 shows the cross-section view (north-south direction) and the shearing of the sand layers during installation of pile 1 and pile 2, respectively. The shearing at the interface is maximum at shallow depth (red color sand) as compared to deeper soils (blue colored sand). At the same time, since pile 2 is installed deeper, shearing is larger in pile 2 as compared to pile 1. The red color sand layer is shared ~3 cm in pile 2 as compared to ~2 cm in pile 1. It can also be observed that pile 1 is more tilted in north-south (shaking) direction by approximately 1.5 degrees, whereas pile 2 is almost vertical with a negligible tilt of ~0.3 degrees. Both piles were tilted almost the same magnitude in east-west direction but in opposite direction (Table 29).

7.3.1 Pile 1

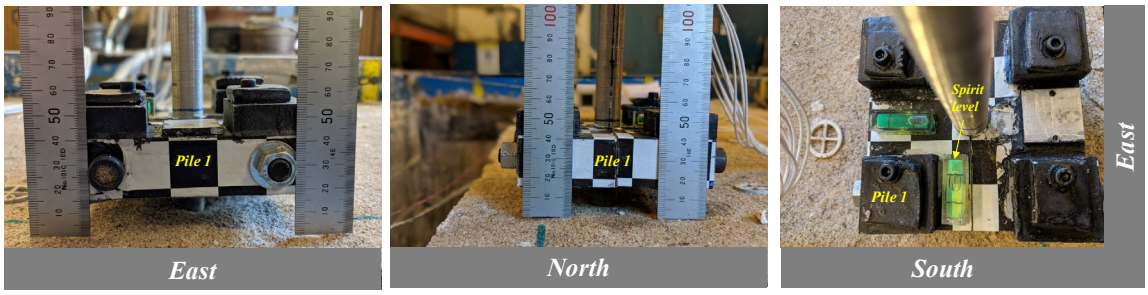

Figure 58. Measurement of tilt in north-south and east-west direction for pile 1 (model scale).

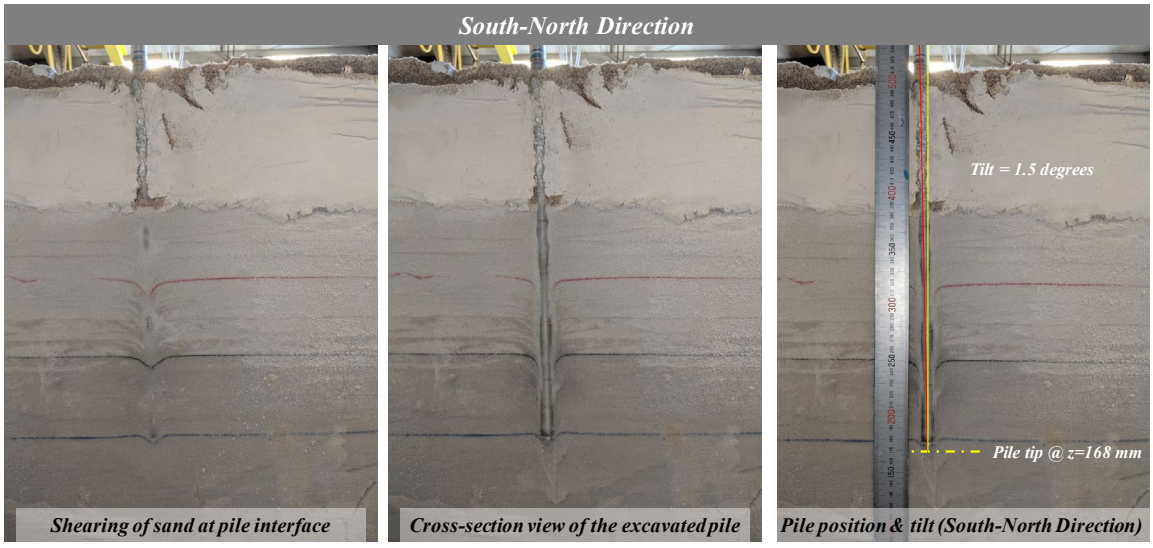

Figure 59. Cross-section view near pile 1 showing shearing of soil layers and measurement of tilt and tip position.

7.3.2 Pile 2

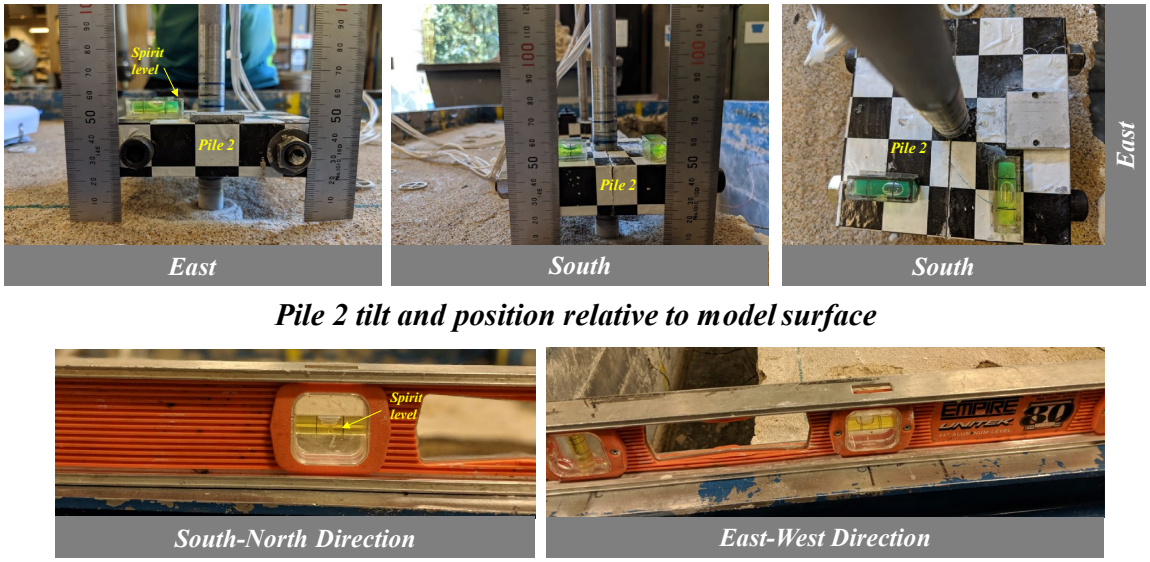

Figure 60. Measurement of tilt in north-south and east-west direction for pile 1 (model scale).

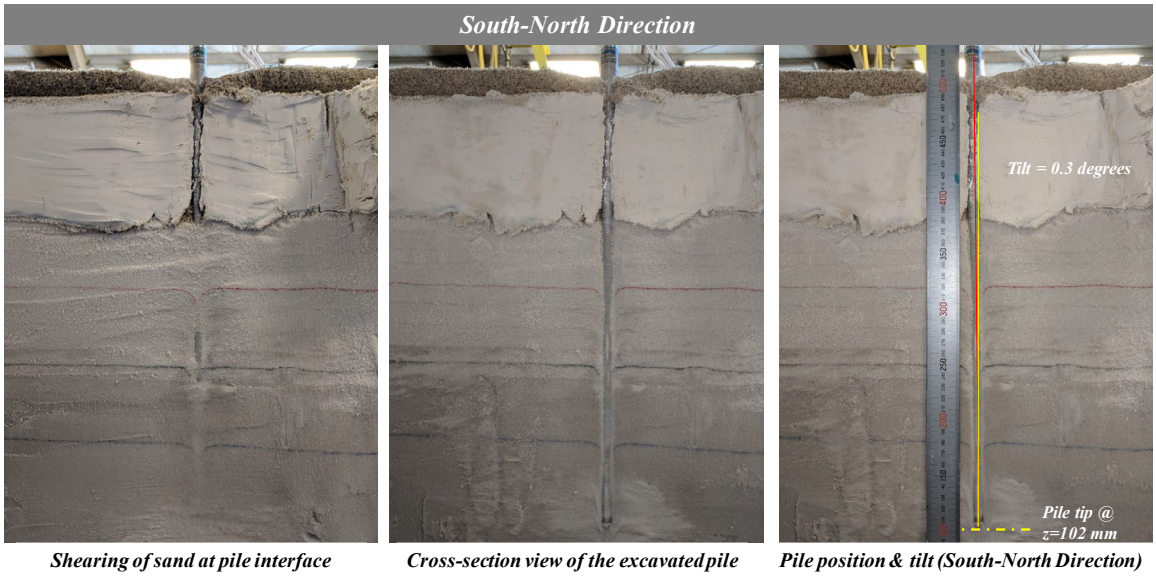

Figure 61. Cross-section view near pile 2 showing shearing of soil layers and measurement of tilt and tip position.

7.4 Sensor Position and Recalibration

During model dissection, the new positions of the sensors were recorded. The sensors were also recalibrated to check the change in sensitivities. The position and sensitivity of the sensors post excavation is recorded in Table 6 through Table 16. Figure 62 shows the view of the sensors during model dissection.

Figure 62. View of the sensors during model dissection.

7.5 Pile Load Test

Figure 63 show the cross-section view of the pile load test PLT_2. In the left image of the figure, a large zone of disturbance can be seen just below the clay layer due to the intrusion of soil from the surface.

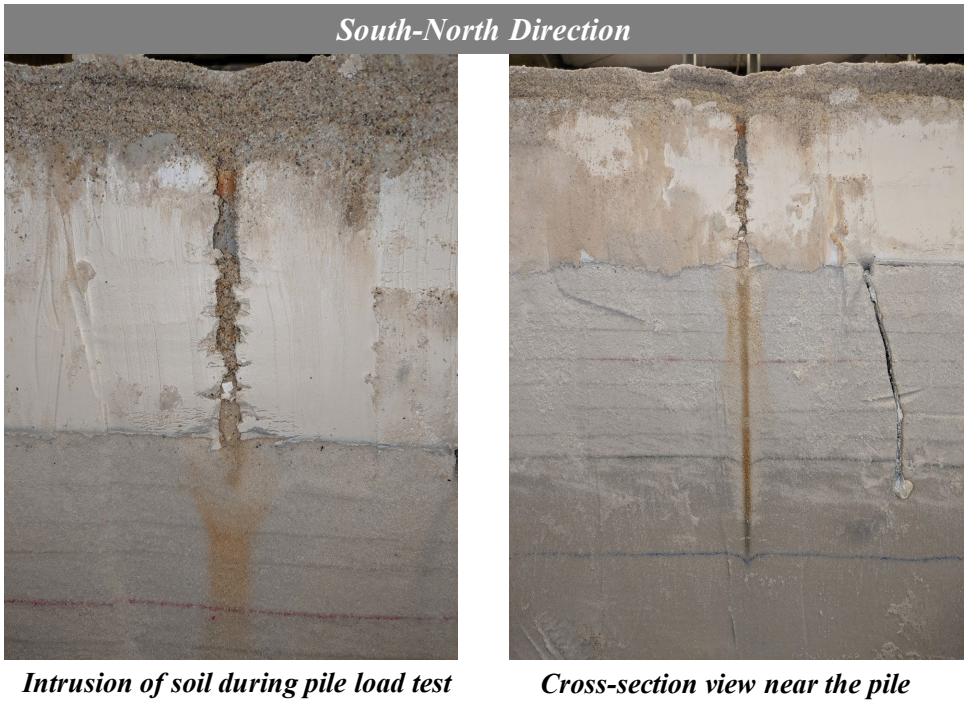

Figure 63. Cross-section view near the PLT probe during pile load test PLT_2.

8 REFERENCES

AASHTO. (2014). *AASHTO LRFD Bridge design specifications*.

Ashford, S. A., Rollins, K. M., and Lane, J. D. (2004). "Blast-induced liquefaction for full-scale foundation testing." *Journal of Geotechnical and Geoenvironmental Engineering*, 130(8), 798–806.

Bolton, M. D., Gui, M. W., Garnier, J., Corte, J. F., Bagge, G., Laue, J., and Renzi, R. (1999). "Centrifuge cone penetration tests in sand." *Géotechnique*, 49(4), 543–552.

Carey, T. J., Stone, N., and Kutter, B. L. (2020). "Grain size analysis and maximum and minimum dry density of ottawa F-65 sand for LEAP-UCD-2017." *Model Tests and Numerical Simulations of Liquefaction and Lateral Spreading,* 31-44.

Coelho, P. A. L. F., Haigh, S. K., and Madabhushi, S. P. G. (2004). "Centrifuge modelling of earthquake effects in unifrom deposits of saturated sand." *5th International Conference on Case Histories in Geotechnical Engineering, New York, April 13-17*, (36).

Darby, K. M., Boulanger, R. W., DeJong, J. T., and Bronner, J. D. (2019). "Progressive changes in liquefaction and cone penetration resistance across multiple shaking events in centrifuge tests." *Journal of Geotechnical and Geoenvironmental Engineering*, 145(3), 1–13.

Darby, K. M., DeJong, J. T., Parra Bastidas, A. M., Boulanger, R. W., and Bronner, J. D. (2016). "Effect of shaking history on the cone penetration resistance and cyclic strength of saturated sand." *Geotechnical and Structural Engineering Congress*, 1460–1471.

Durgunoglu, H. T., and Mitchell, J. K. (1973). *Static penetration resistance of soils*. Space Sciences Laboratory, University of California, Berkeley, 14(24).

Gui, M. W., Bolton, M. D., Garnier, J., Corte, J. F., Bagge, G., Laue, J., and Renzi, R. (1998). "Guidelines for cone penetration tests in sands." *In Centrifuge,* 98, 155-160.

Idriss, I. M., and Boulanger, R. W. (2008). *Soil liquefaction during earthquakes*. Earthquake Engineering Research Institute.

Jacobsz, S. W. (2018). "Low cost tensiometers for geotechnical applications." *In Proceedings of 9th International Conference on Physical Modelling in Geotechnics*, 1, 305–310.

Johnson, J. B. (2003). *A statistical micromechanical theory of cone penetration in granular materials*. Engineer Research and Development Center, Cold Regions Research and Engineering Laboratory, ERDC/CRREL TR-03-3.

Khosravi, M., Wilson, D. W., Boulanger, R. W., and Olgun, C. G. (2015). *Reduction of seismic shaking intensity on soft soil sites using stiff ground reinforcement: Data Report for 2: Test MKH01*. Report No. UCD/CGMDR – 15/02, Center for Geotechnical Modeling, University of California Davis.

Knappett, J. A., and Madabhushi, S. P. G. (2006). "Modeling of liquefaction-induced instability in pile groups." *Seismic Performance and Simulation of Pile Foundations*, 255–267.

Kutter, B. L. (1992). "Dynamic centrifuge modeling of geotechnical structures." *Transportation research record*, (1336), 24–30.

Lunne, T., Powell, J. J. M., and Robertson, P. K. (1997). *Cone Penetration Testing in Geotechnical Practice*. Taylor & Francis Group.

Malvick, E. J., Kulasingam, R., Boulanger, R. W., and Kutter, B. L. (2002). *Effects of void redistribution*

on liquefaction flow of layered soil – centrifuge data report for EJM01. Report No. UCD/CGMDR – 02/02, Center for Geotechnical Modeling, University of California Davis.

Martinez, A., and Frost, J. D. (2017). "The influence of surface roughness form on the strength of sand–structure interfaces." *Géotechnique Letters*, 7(1), 104–111.

Mo, P.-Q., Marshall, A. M., and Yu, H.-S. (2016). "Centrifuge modelling of cone penetration tests in layered soils." *Geotechnique*, 6, 468–481.

Nowatzki, E. A., and Karafiath, L. L. (1972). *The effect of cone angle on penetration resistance*. Grumman Research Department, Grumman Aerospace Corporation.

Price, A. B. (2018). *Cyclic Strength and Cone Penetration Resistance for Mixtures of Silica Silt and Kaolin*. Doctoral Dissertation, University of California Davis.

Rollins, K., and Hollenbaugh, J. (2015). "Liquefaction Induced Negative Skin Friction from Blast-induced Liquefaction Tests with Auger-cast Piles." *6th International Conference on Earthquake Geotechnical Engineering*, New Zealand Geotechnical Society.

Rollins, K. M., Clayton, R. J., Mikesell, R. C., and Blaise, B. C. (2005). "Drilled Shaft Side Friction in Gravelly Soils." *Journal of Geotechnical and Geoenvironmental Engineering*, 131(8), 987–1003.

Rollins, K. M., and Strand, S. R. (2006). "Downdrag forces due to liquefaction surrounding a pile." *In Proceedings of 8th U.S. National Conference on Earthquake Engineering, Earthquake Engineering Research Institute.*

Roscoe, K. H., and Burland, J. B. (1968). "On the generalized stress-strain behaviour of wet clay." *Engineering plasticity*, 535–609.

Sinha, S. K., Kutter, B. L., and Ziotopoulou, K. (2020). "Measuring Vertical Displacement Using Laser lines and Cameras." *International Journal of Physical Modelling in Geotechnics*. (in review)

Sinha, S. K., Ziotopoulou, K., and Kutter, B. L. (2019). "Parametric study of liquefaction induced downdrag on axially loaded piles." *In 7th lnternational Conference on Earthquake Geotechnical Engineering*.

Stewart, D., Chen, Y.-R., and Kutter, B. (2009). "Experience with the Use of Methylcellulose as a Viscous Pore Fluid in Centrifuge Models." *Geotechnical Testing Journal*, 21(4), 365.

Stringer, M. E., Kutter, B. L., Wilson, D. W., Zhou, Y. G., and Zheng, B. L. (2013). *Steel pile jacket seismic soil structure interaction study : Phase 2 Data Report*. Report No. - UCD/CGMDR-12/02 12/02, Center for Geotechnical Modeling, University of California Davis.

T E Sensor Solutios. (2017). *MS54XX miniature SMD pressure sensor*. Measurement Specialties, Inc., a TE Connectivity Company.

Upadhyaya, S., Tiwari, B., and Olgun, G. (2016). "Static and Dynamic Properties of Compacted Soil-Cement Mixtures." *In Geotechnical and Structural Engineering Congress 2016*, 1646–1654.

APPENDIX

A. Day 1 Spin 1

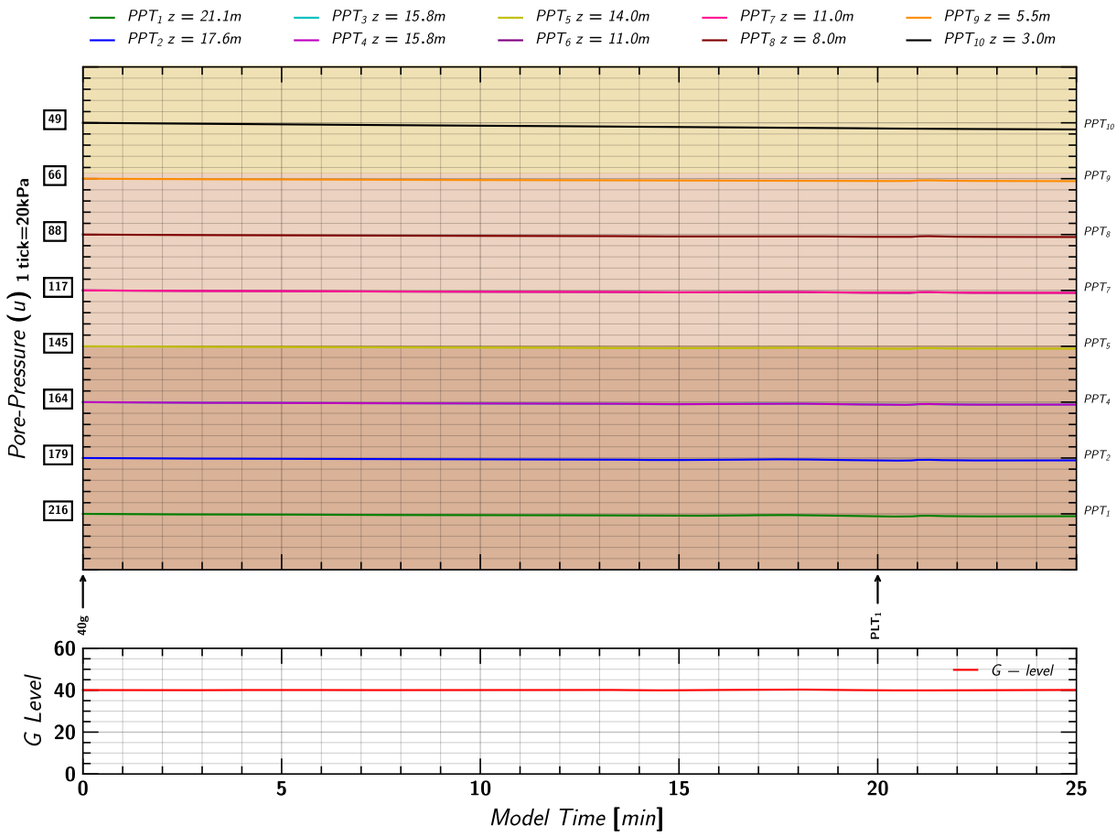

Figure 64. Day 1 Spin 1: Pore pressures measurements in soil from Keller transducers.

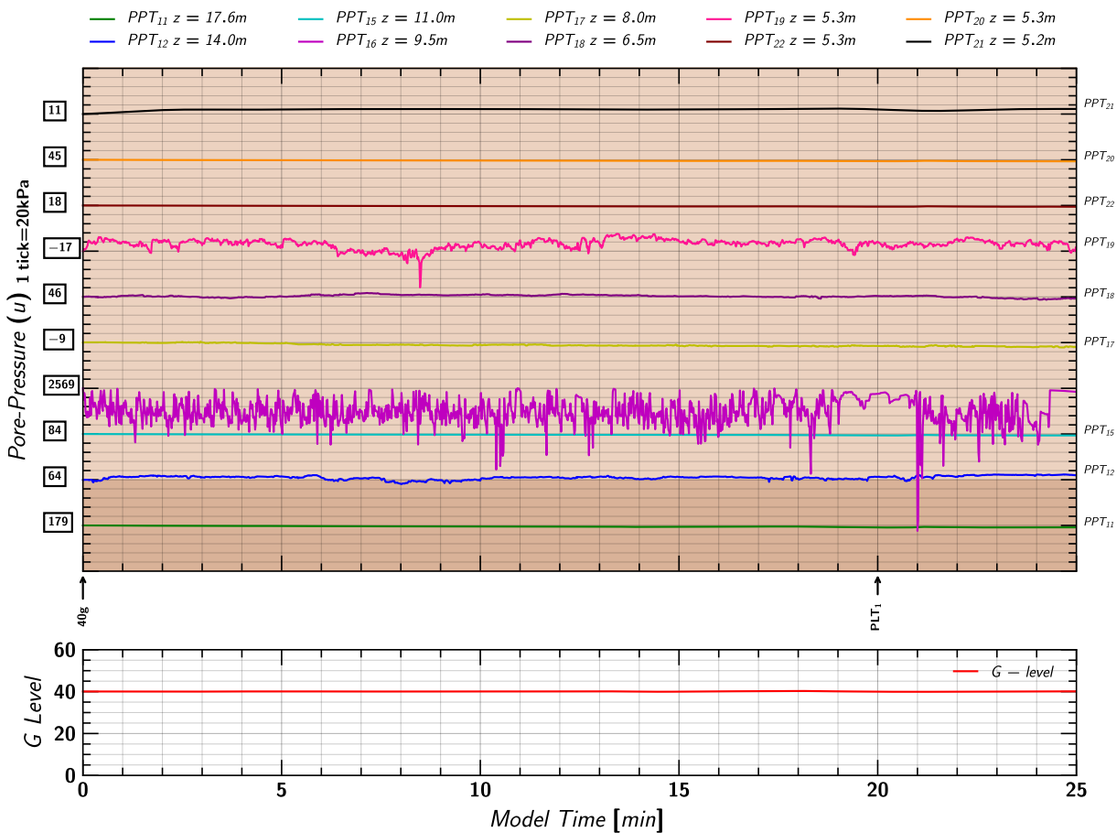

Figure 65. Day 1 Spin 1: Pore pressures measurements in soil from MS54XXX transducers.

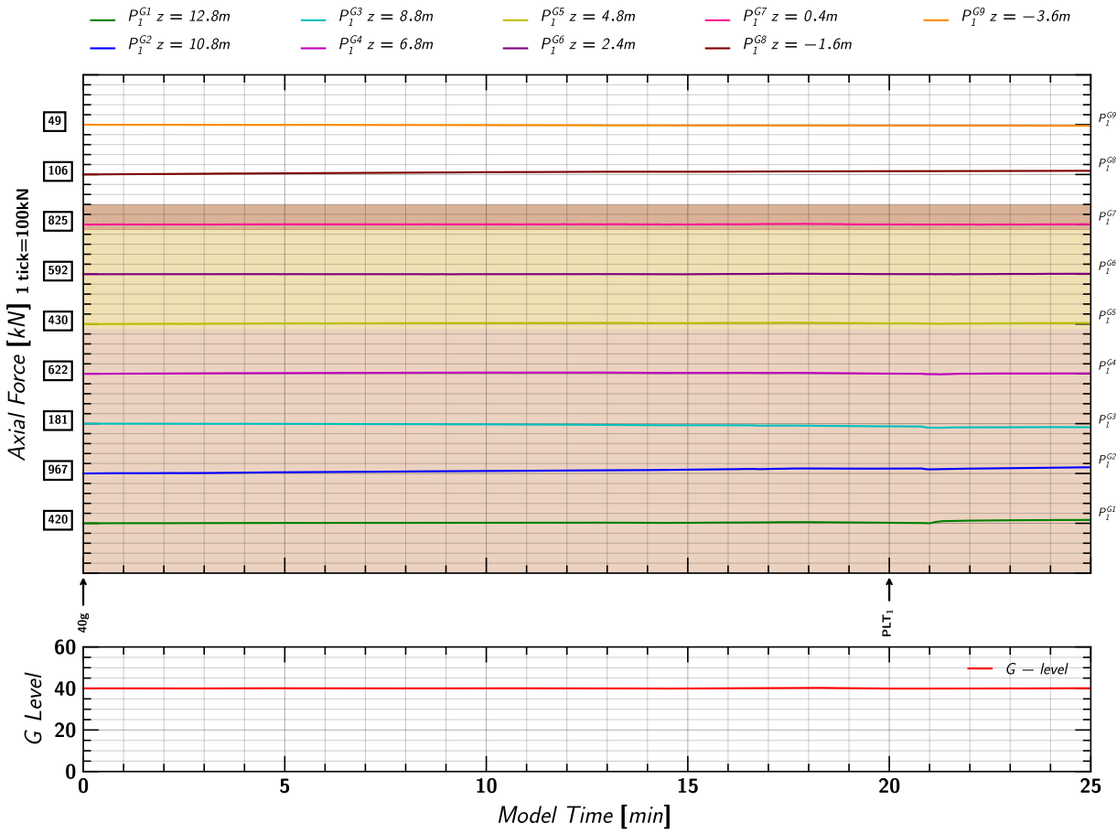

Figure 66. Day 1 Spin 1: Axial load measurements in Pile 1.

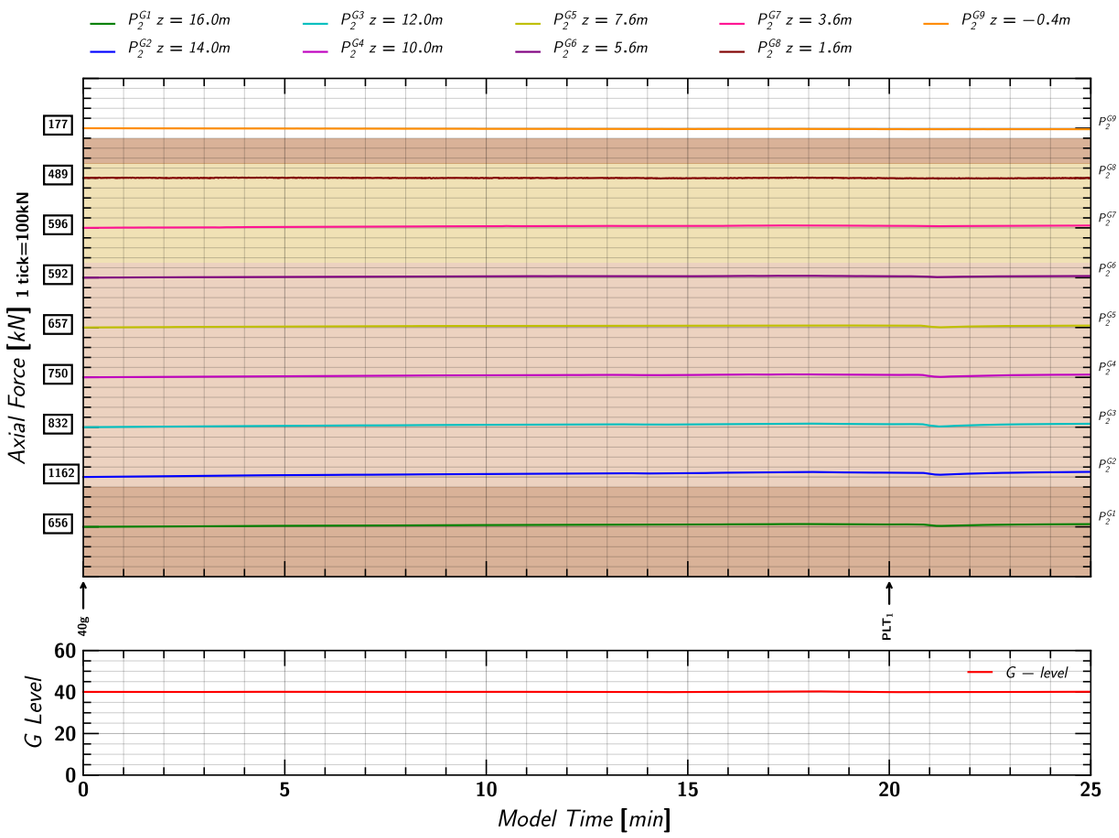

Figure 67. Day 1 Spin 1: Axial load measurements in Pile 2.

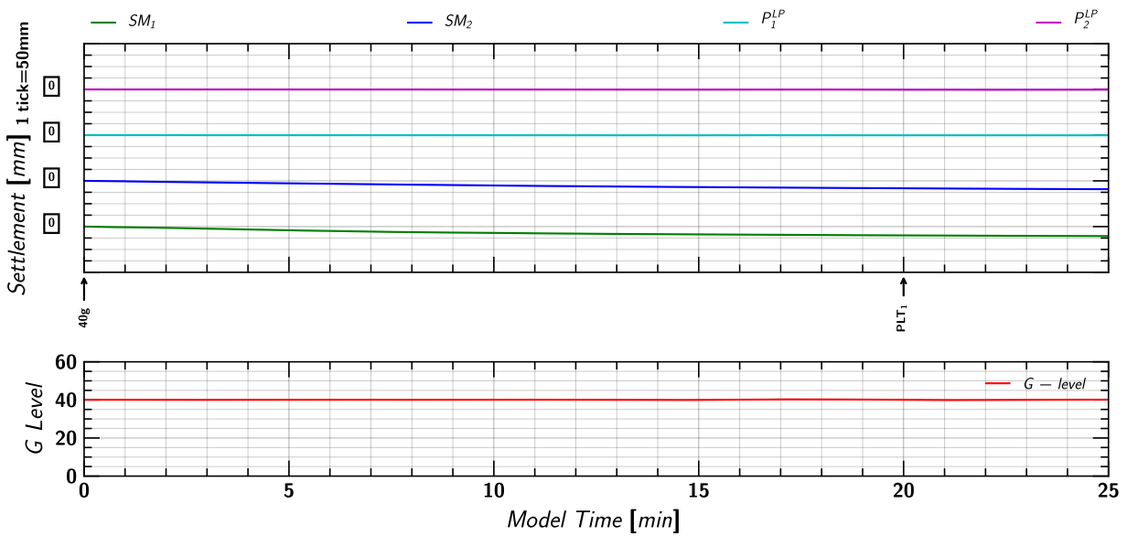

Figure 68. Day 1 Spin 1: Settlement measurements of soil and pile from linear potentiometers.

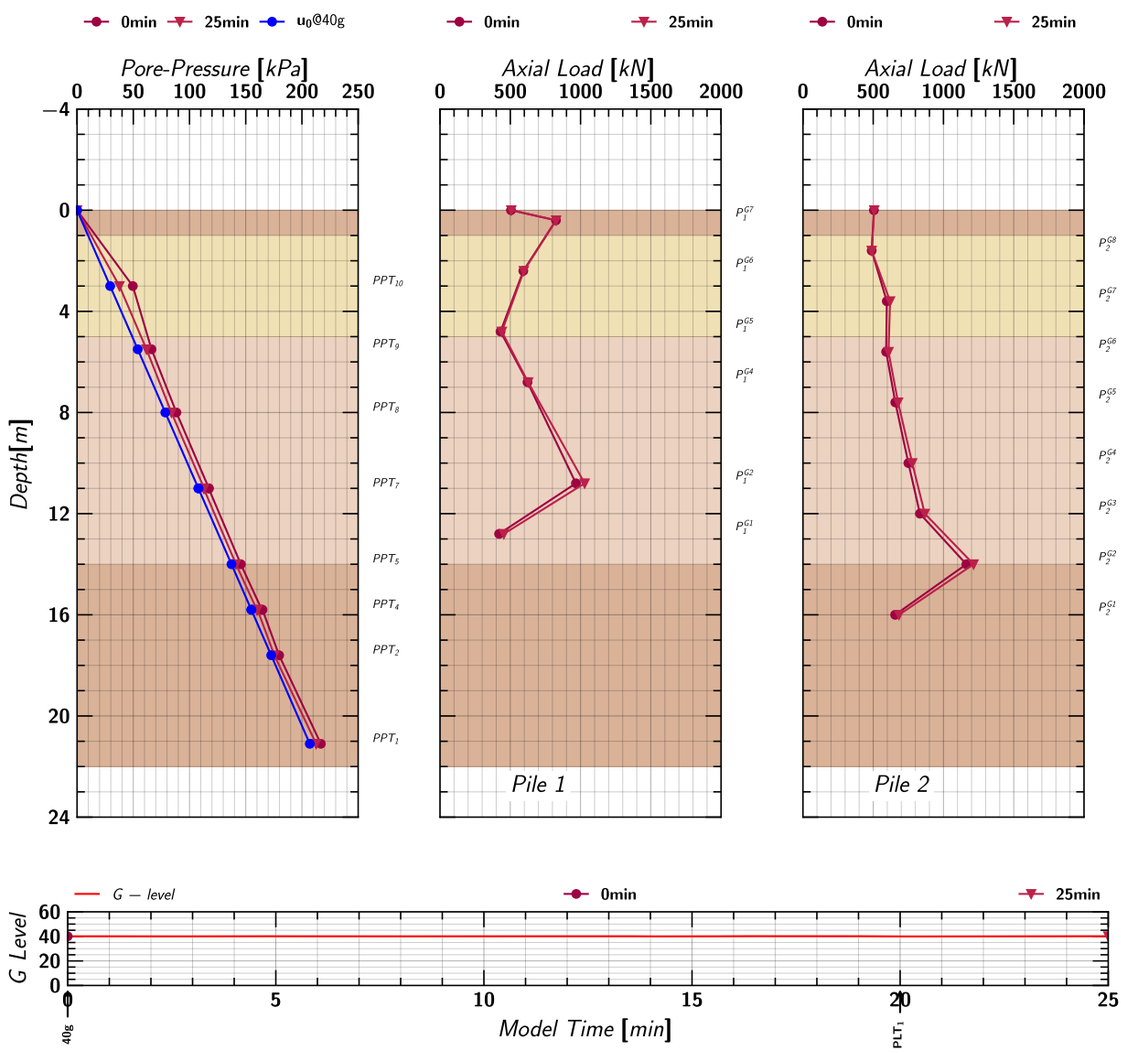

Figure 69. Day 1 Spin 1: Axial load profile of pile 1 and pile 2 at different times during the test.

B. Day 1 Spin 2

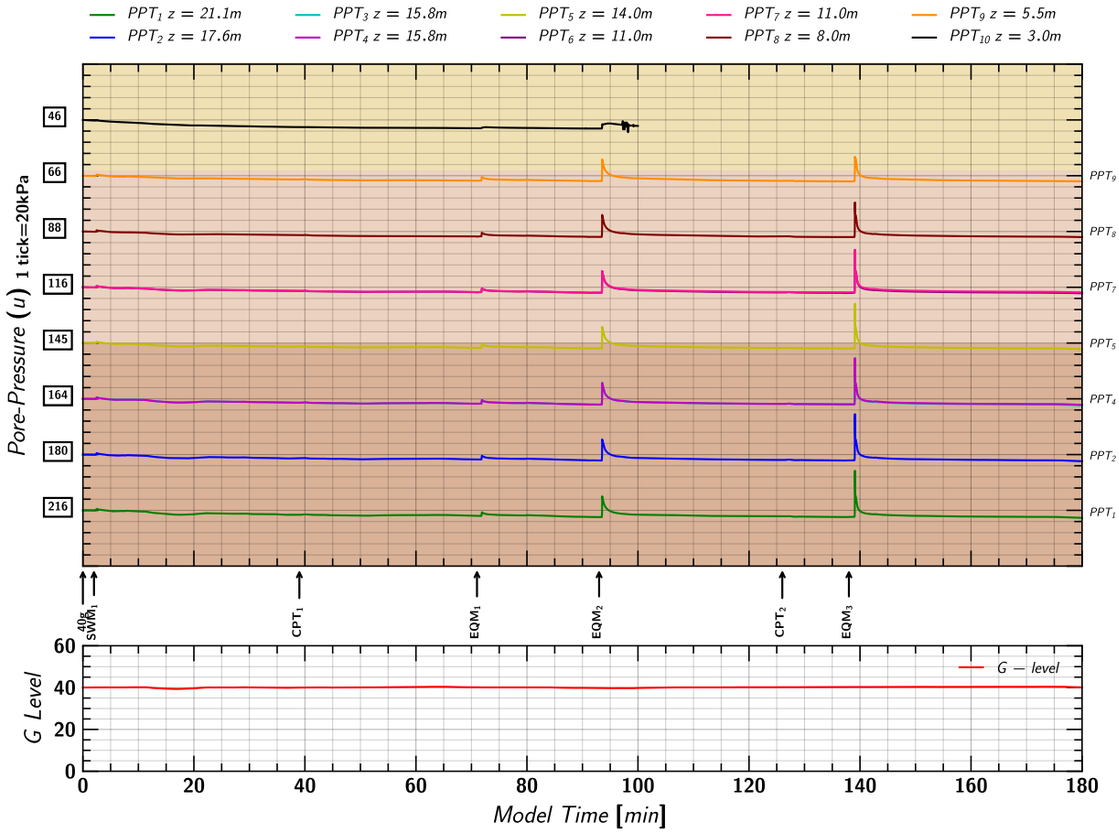

Figure 70. Day 1 Spin 2: Pore pressures measurements in soil from Keller transducers.

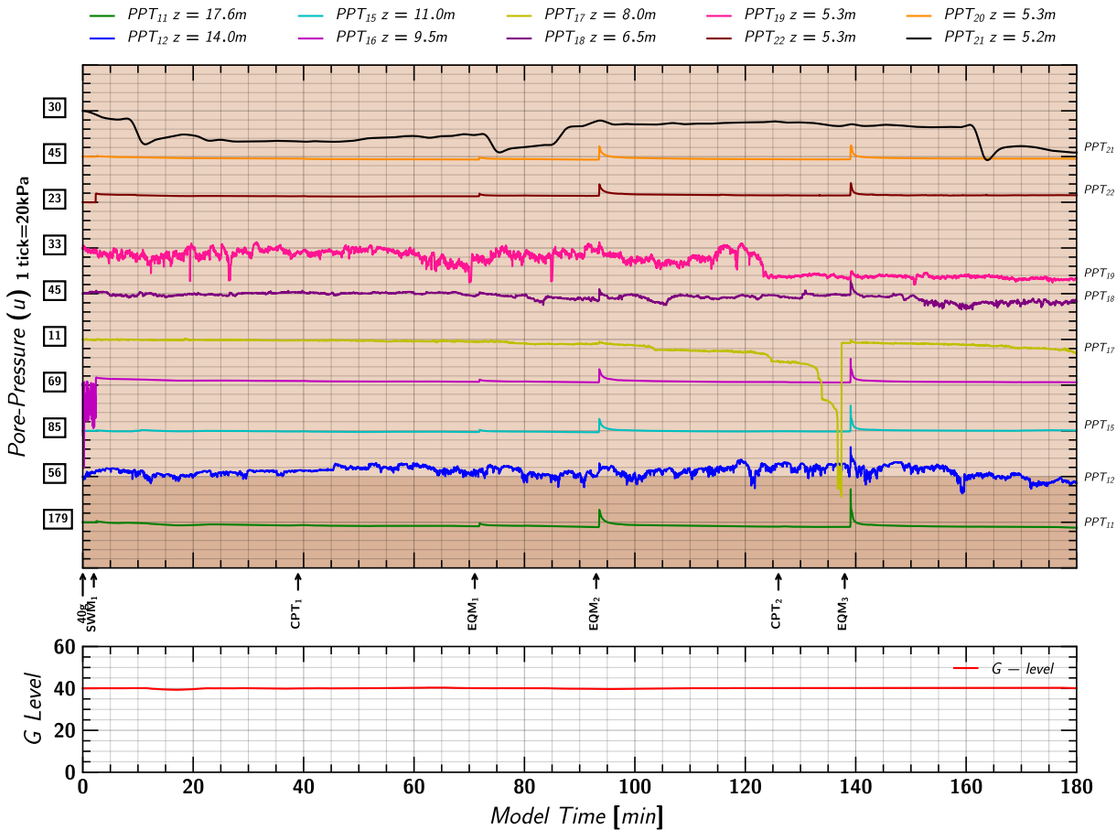

Figure 71. Day 1 Spin 2: Pore pressures measurements in soil from MS54XXX transducers.

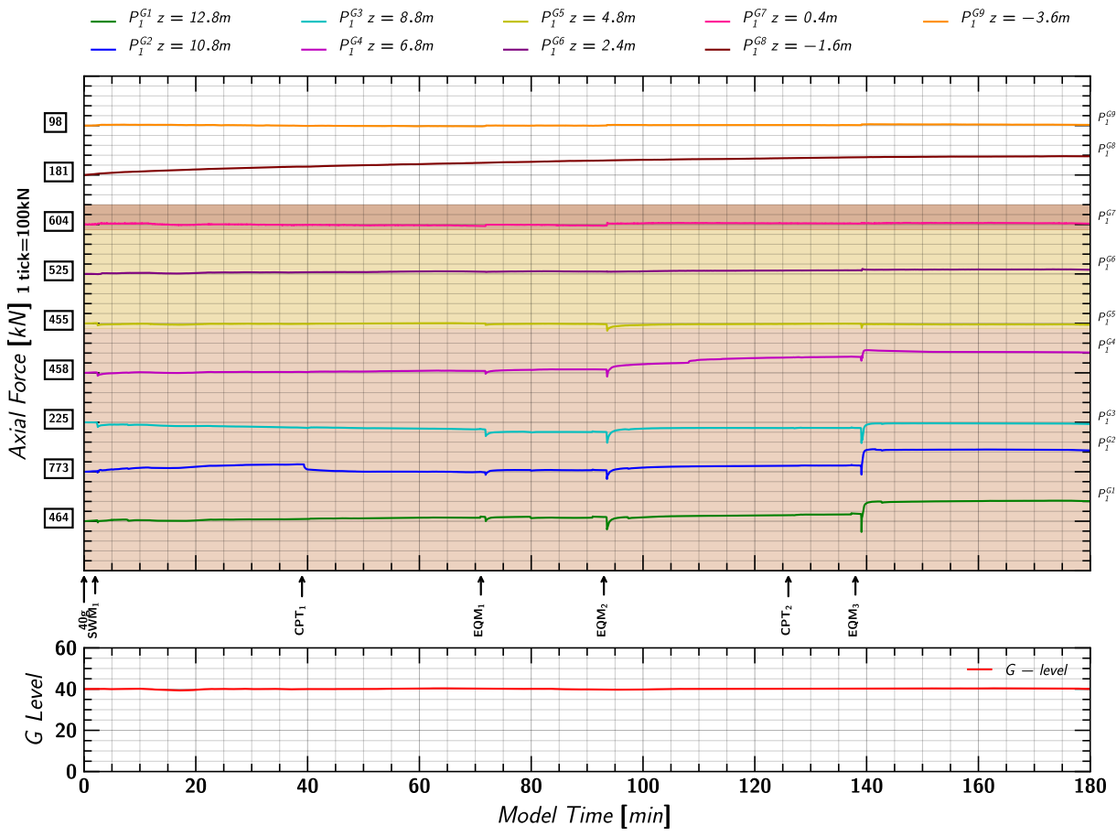

Figure 72. Day 1 Spin 2: Axial load measurements in Pile 1.

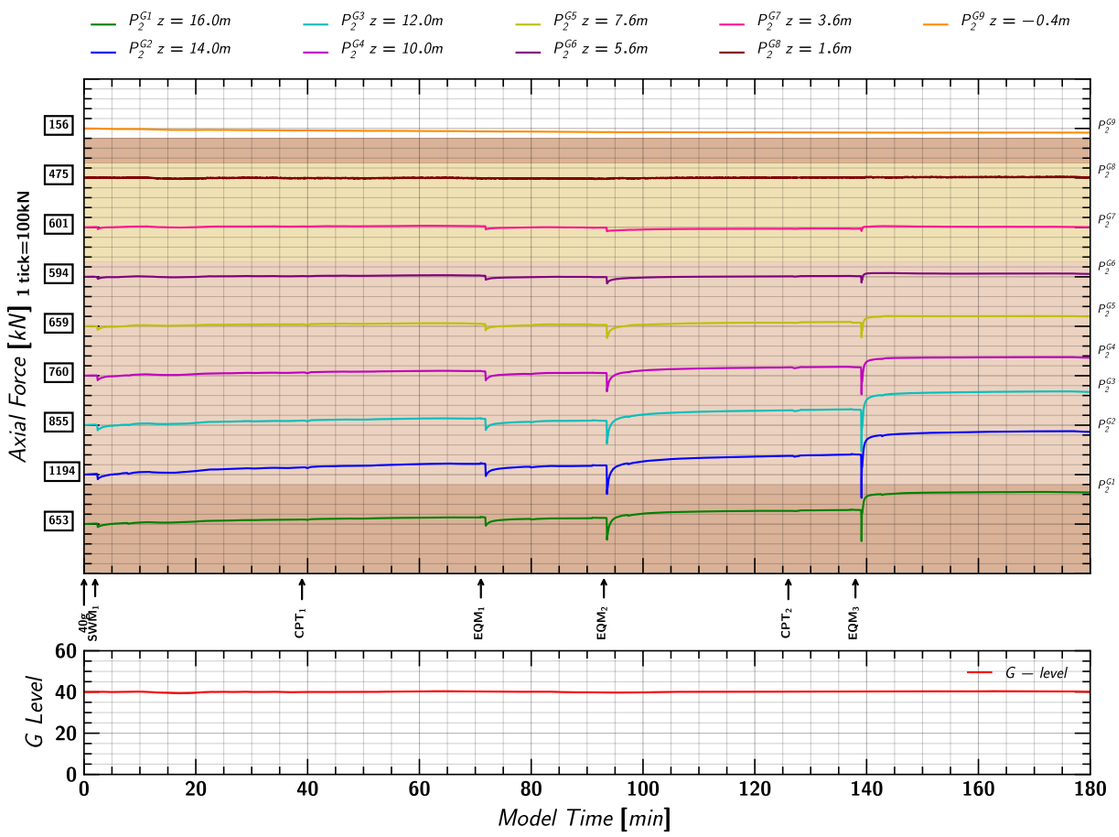

Figure 73. Day 1 Spin 2: Axial load measurements in Pile 2.

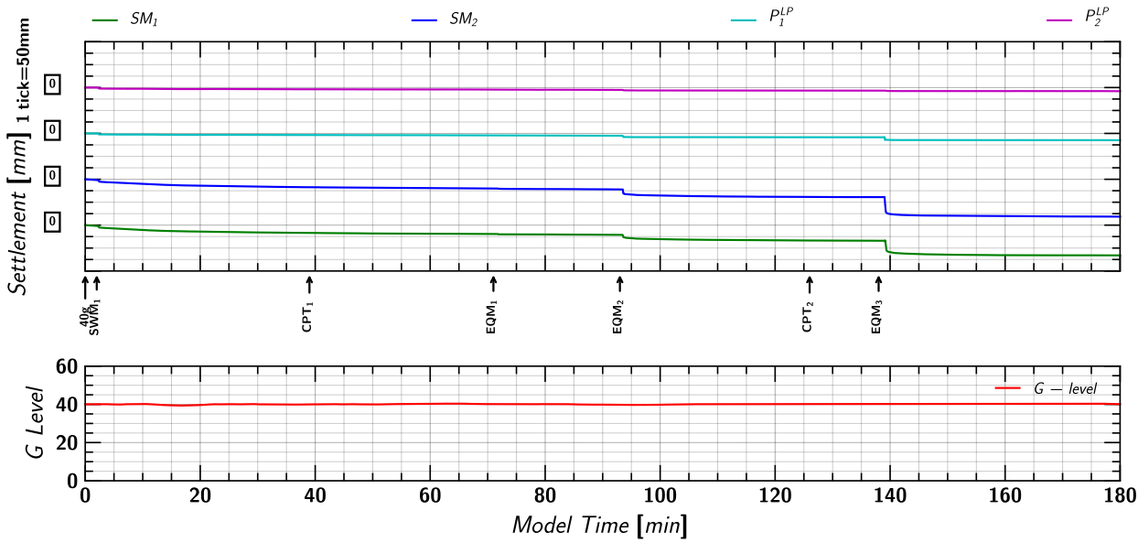

Figure 74. Day 1 Spin 2: Settlement measurements of soil and pile from linear potentiometers.

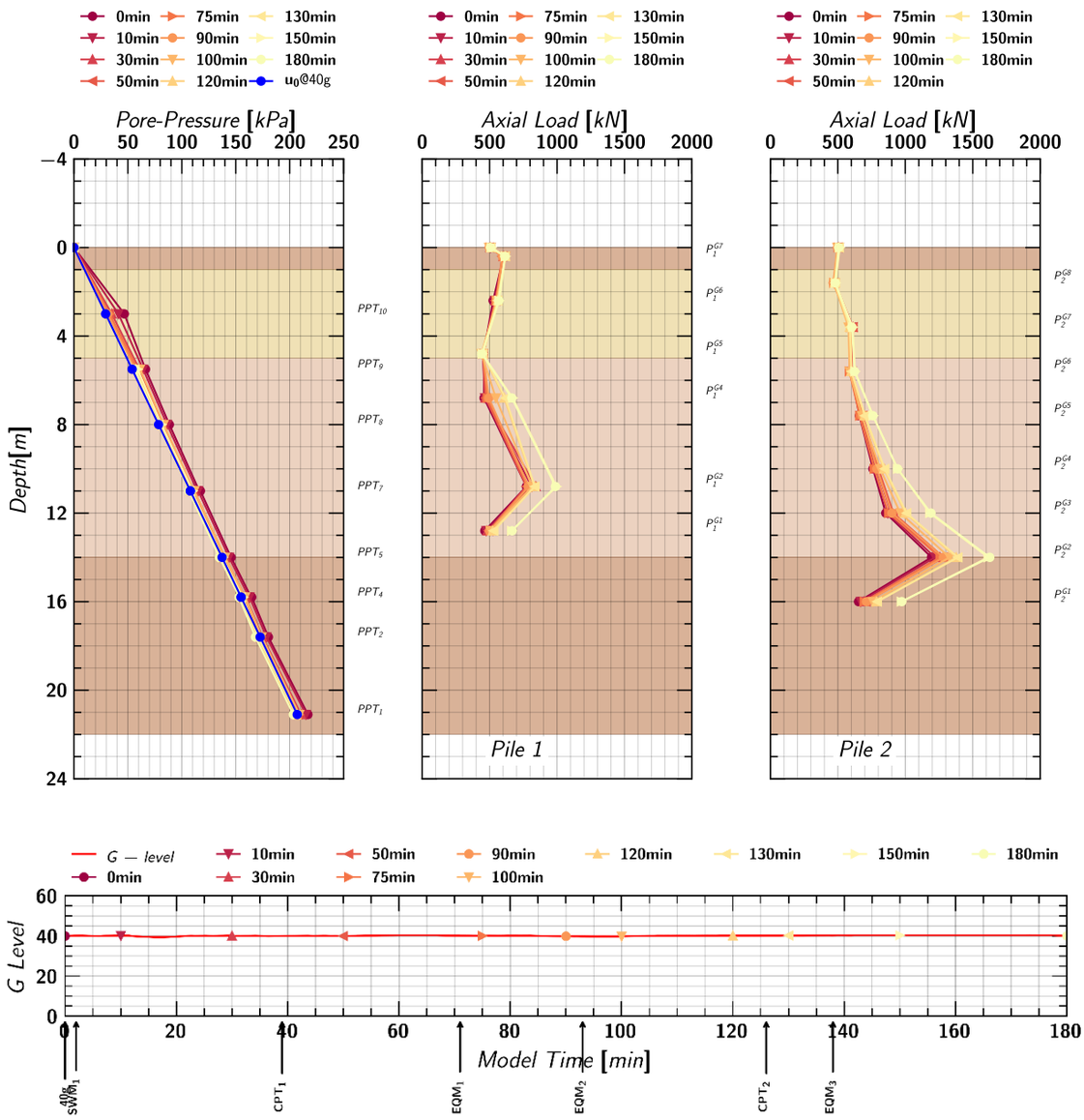

Figure 75. Day 1 Spin 2: Axial load profile of pile 1 and pile 2 at different times during the test.

C. EQM$_1$ - Small Santa Cruz Earthquake Motion (PGA = 0.025g)

C.1 Input Motion

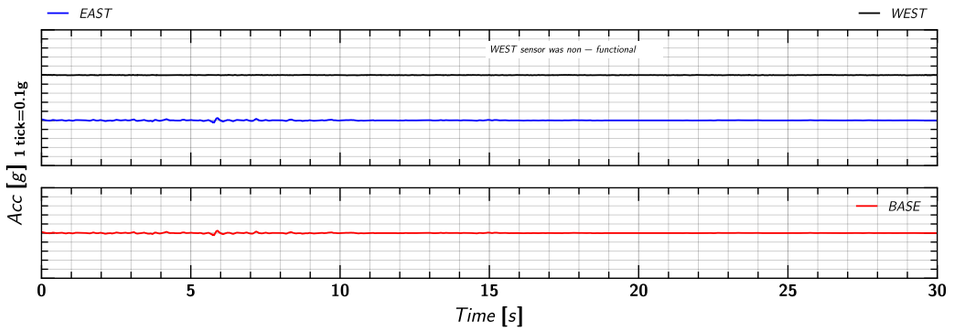

Figure 76. EQM$_1$: Input motion.

C.2 Acceleration in Container

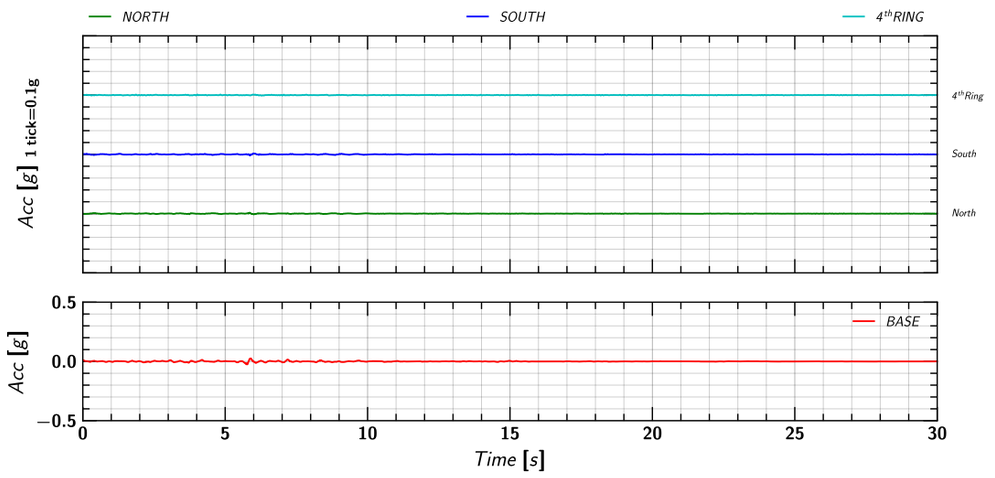

Figure 77. EQM$_1$: Acceleration measurement on container.

C.3 Acceleration in Soil

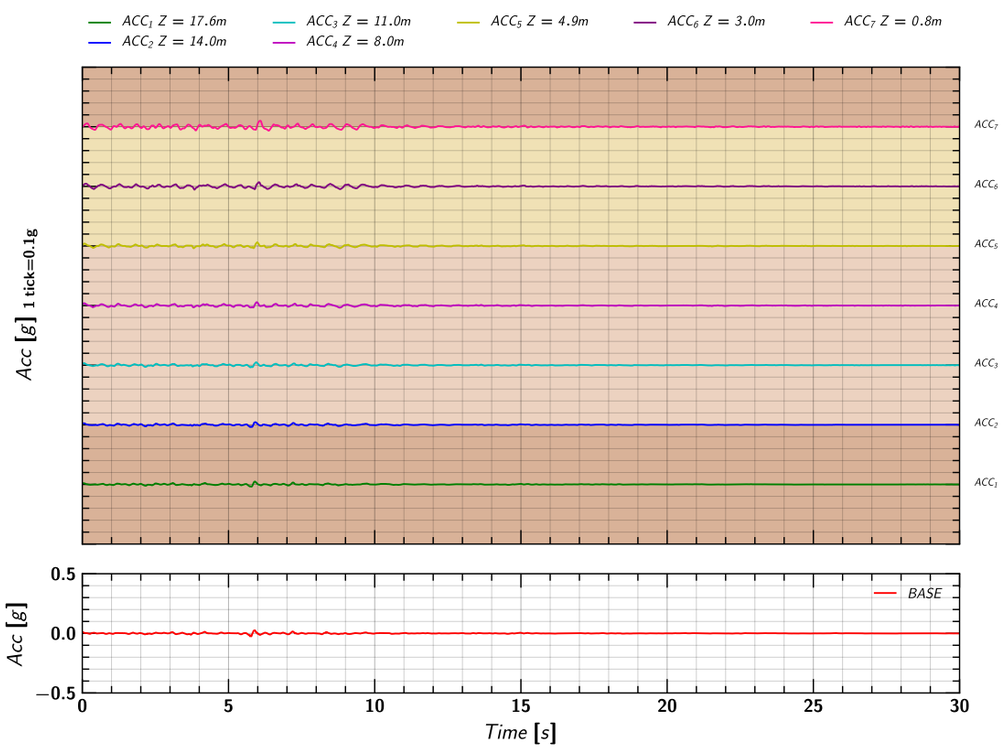

Figure 78. EQM$_1$: Acceleration measurement in soil.

C.4 Acceleration in Pile

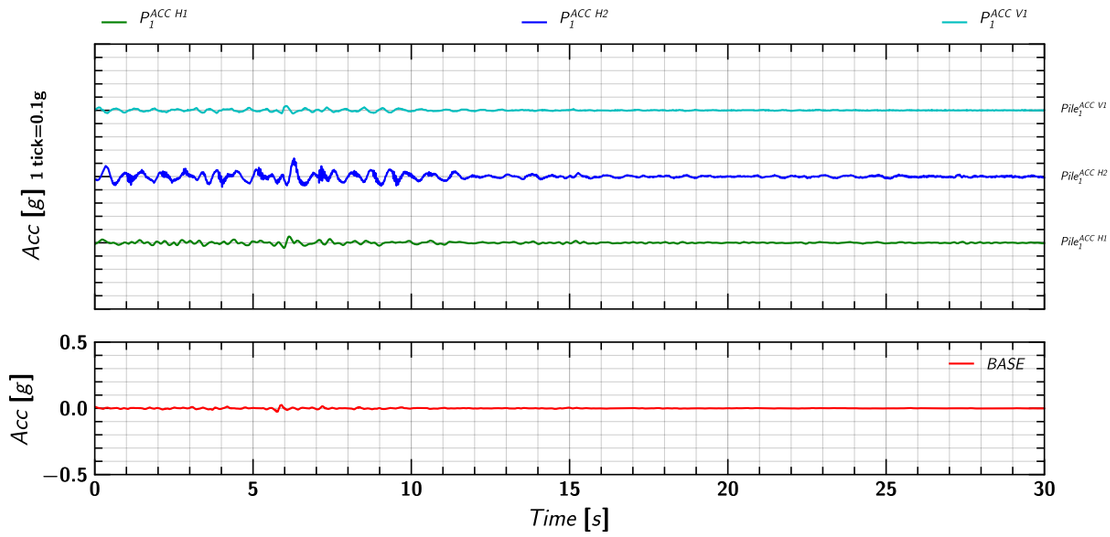

Figure 79. EQM1: Acceleration measurement on pile 1.

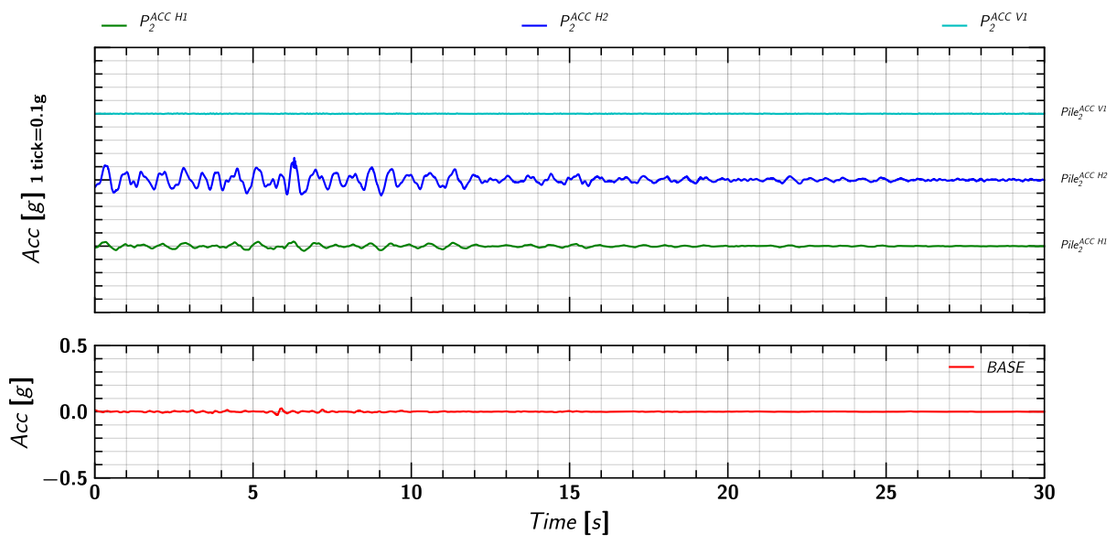

Figure 80. EQM1: Acceleration measurement on pile 2.

C.5 Soil and Pile Settlement

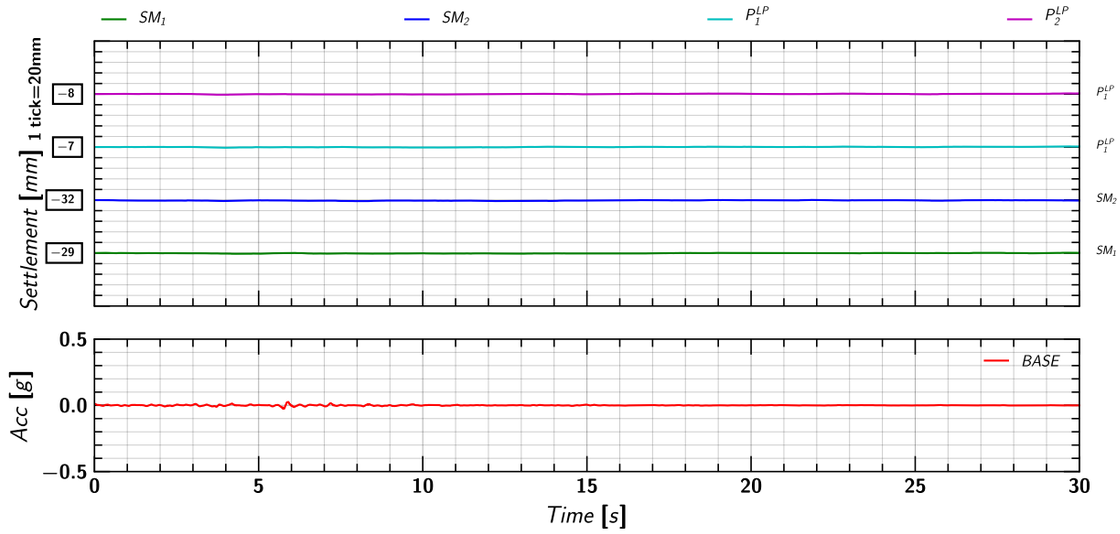

Figure 81. EQM1: Settlement measurement in soil and pile during the applied earthquake motion.

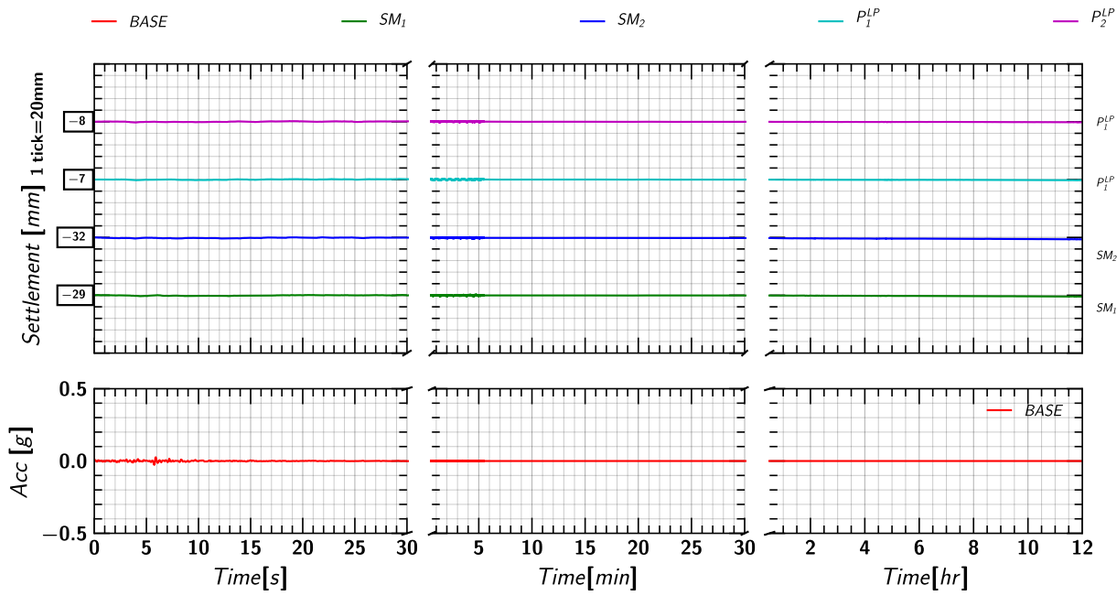

Figure 82. EQM1: Settlement measurement in soil and pile during and post applied earthquake motion.

C.6 Pore pressure measurements in Soil (Keller Transducers)

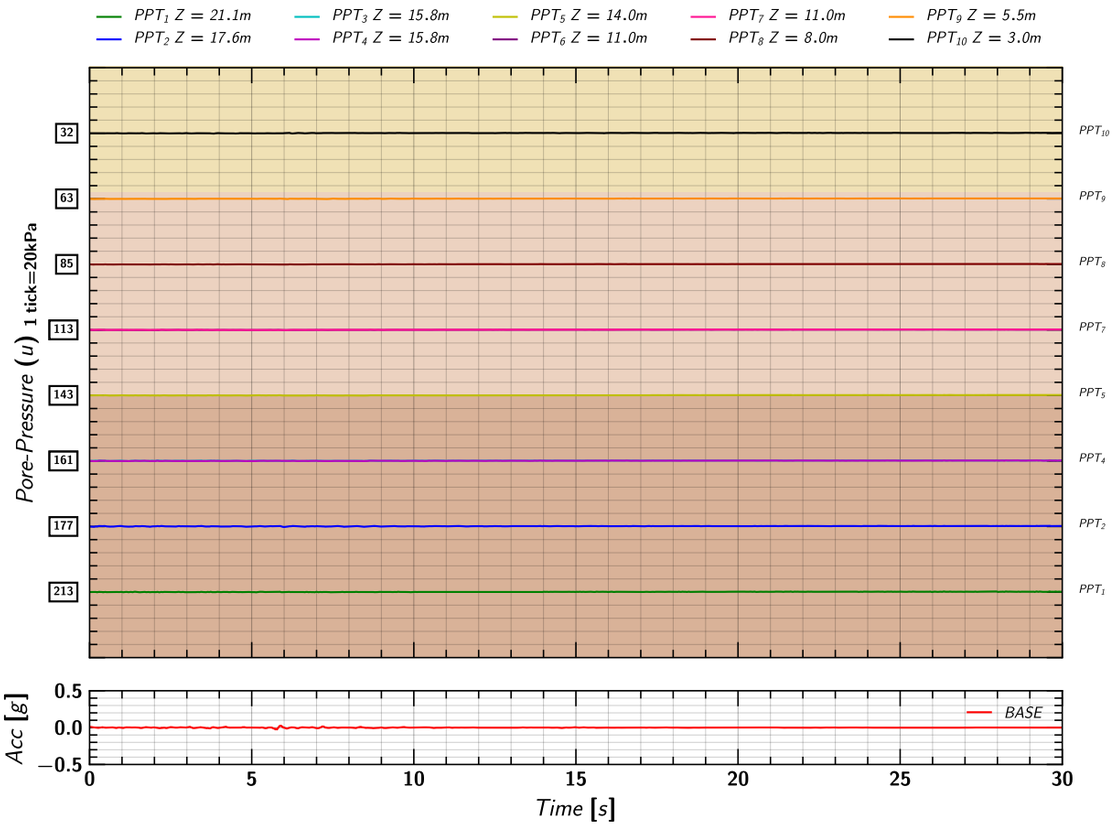

Figure 83. EQM$_1$: Pore pressure measurements in soil from Keller transducers during the applied earthquake motion.

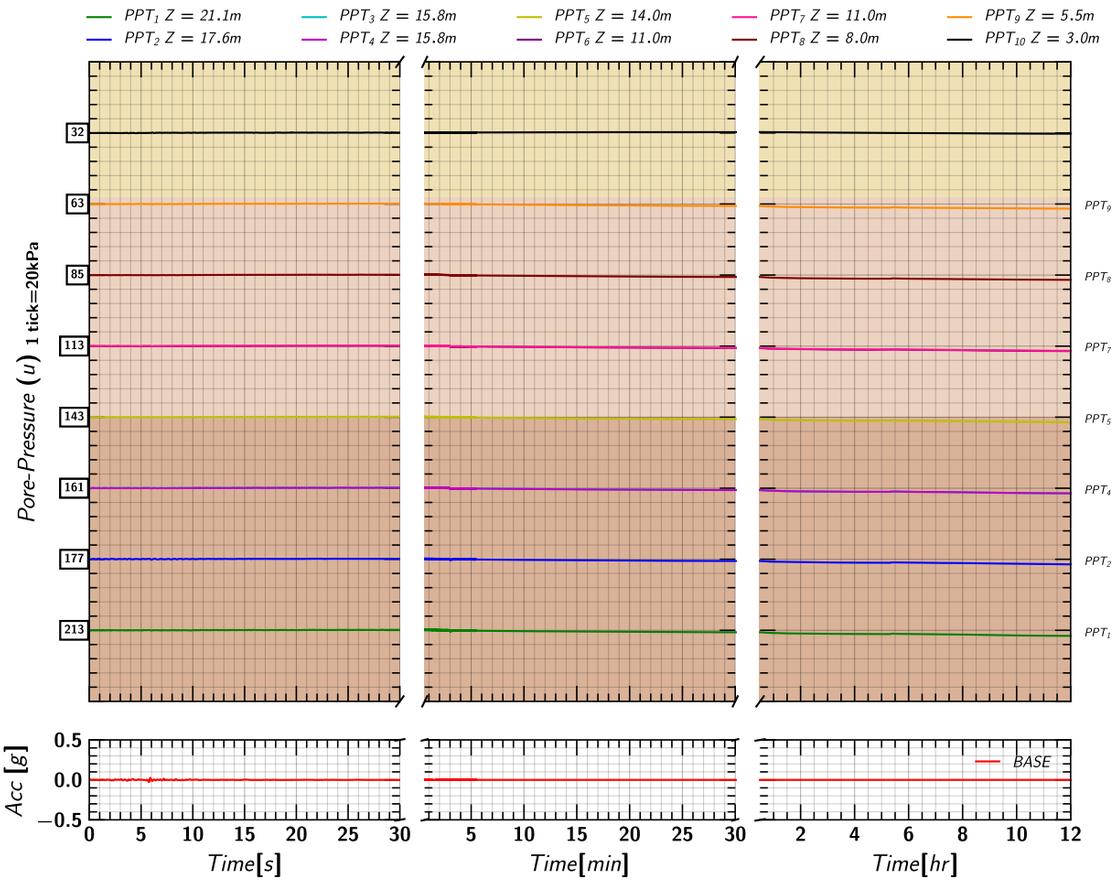

Figure 84. EQM$_1$: Pore pressure measurements in soil from Keller transducers during and post the applied earthquake motion.

C.7 Pore pressure measurements in Soil (MS54XXX Transducers)

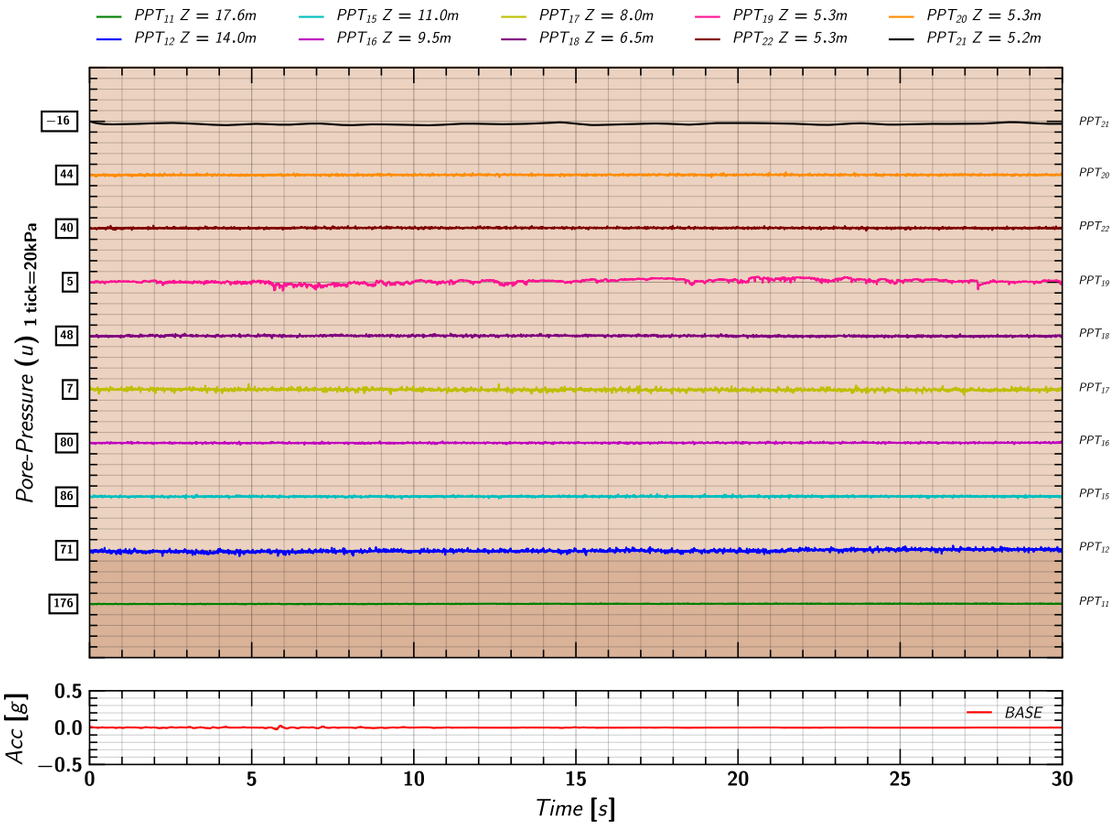

Figure 85. EQM$_1$: Pore pressure measurements in soil from MS54XXX transducers during the applied earthquake motion.

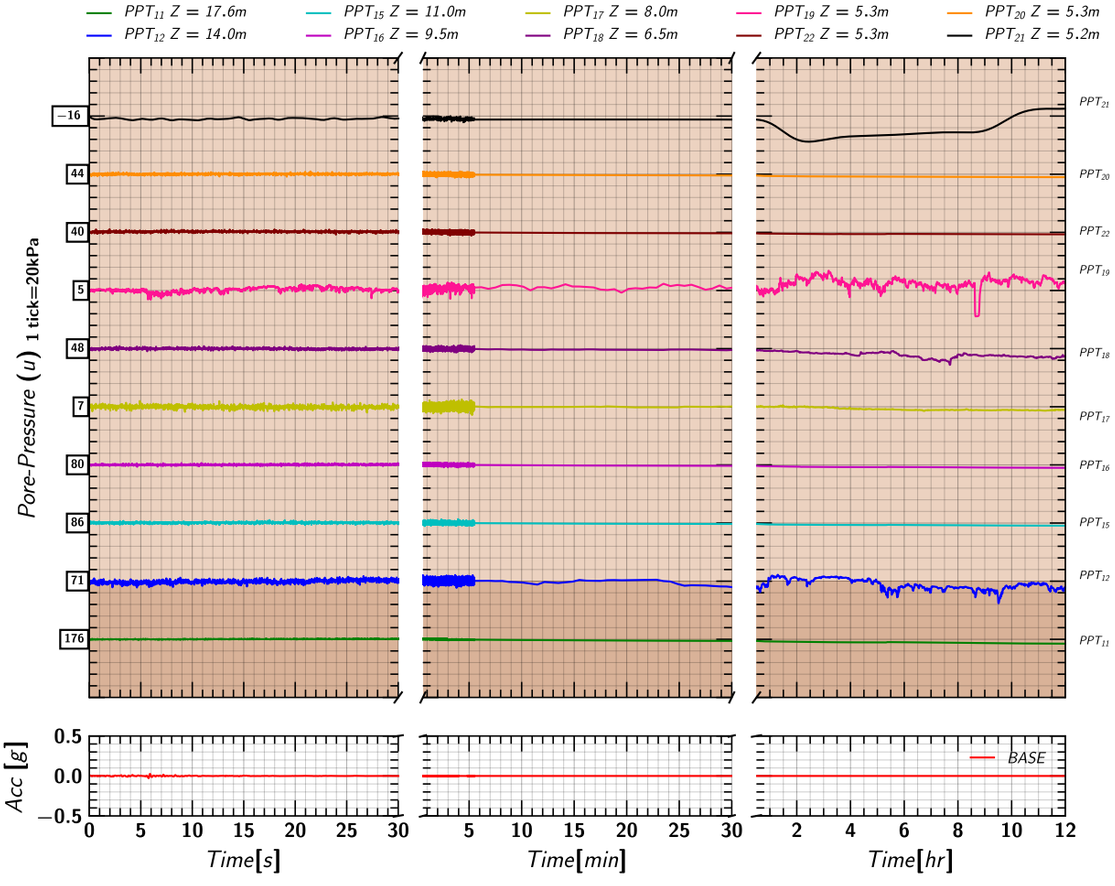

Figure 86. EQM$_1$: Pore pressure measurements in soil from MS54XXX transducers during and post the applied earthquake motion.

C.8 Excess Pore pressures Ratio (r_u) Estimated from Keller Transducers

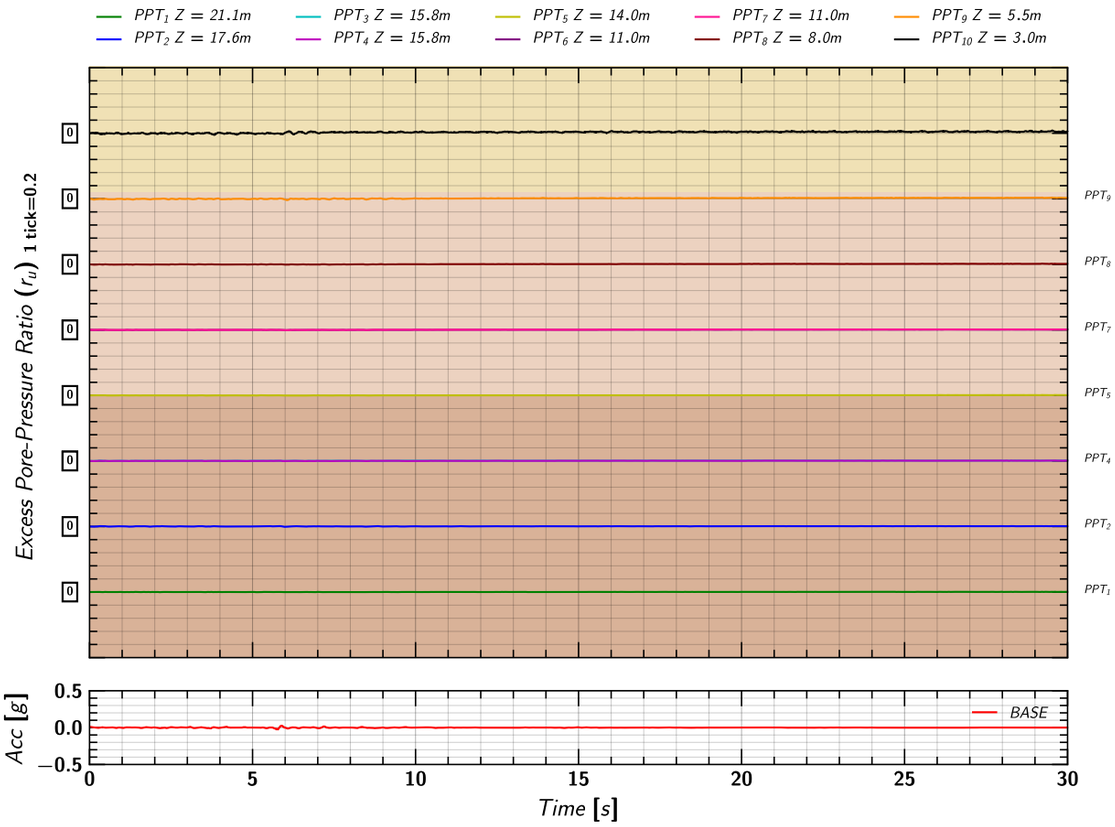

Figure 87. EQM1: Excess pore pressure ratio (r_u) estimated from measurements by Keller transducers during the applied earthquake motion.

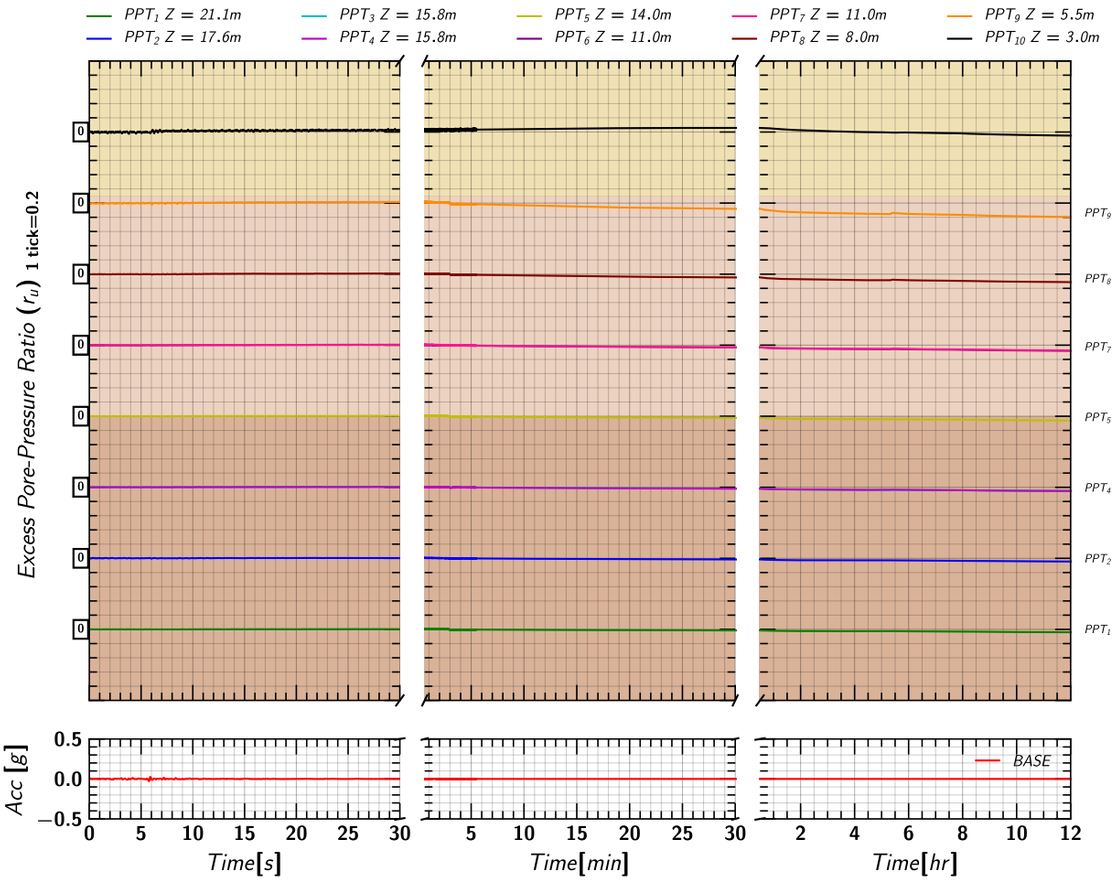

Figure 88. EQM1: Excess pore pressure ratio (r_u) estimated from measurements by Keller transducers during and post the applied earthquake motion.

C.9 Excess Pore pressure Ratio (r_u) Estimated from MS54XXX Transducers

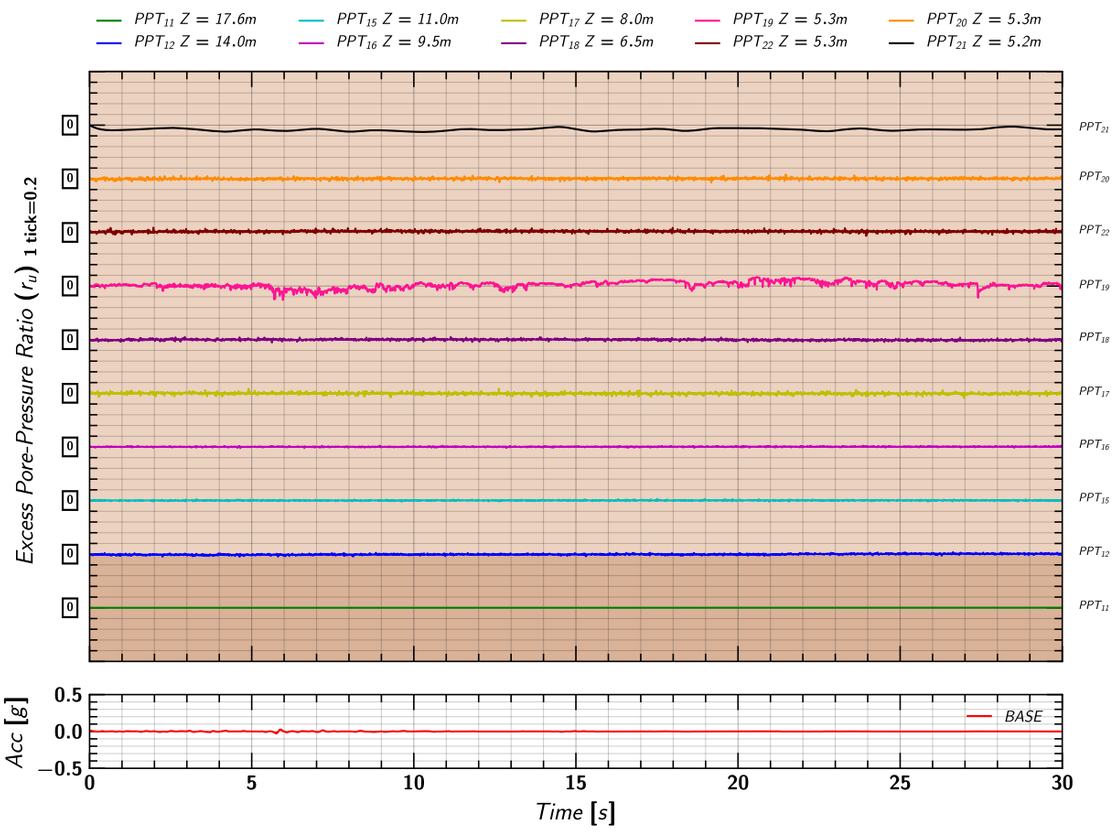

Figure 89. EQM1: Excess pore pressure ratio (r_u) estimated from measurements by MS54XXX transducers during the applied earthquake motion.

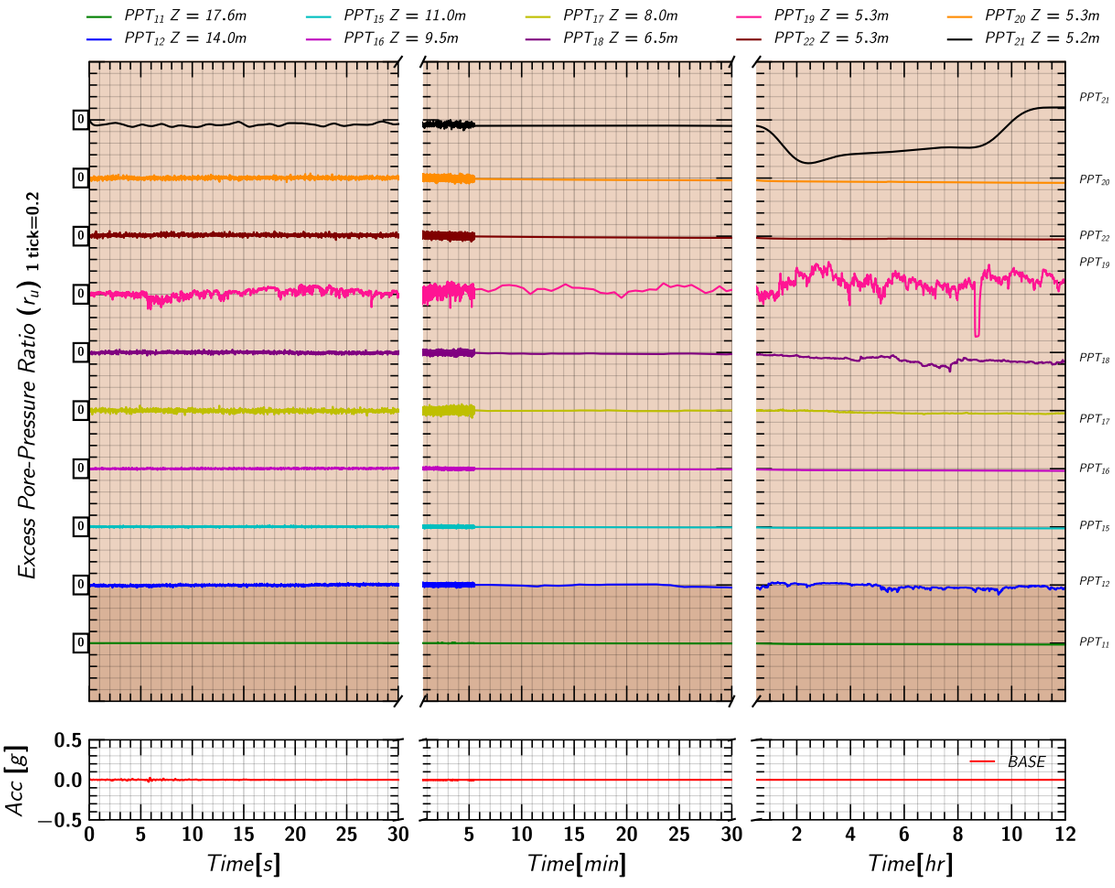

Figure 90. EQM1: Excess pore pressure ratio (r_u) estimated from measurements by MS54XXX transducers during and post the applied earthquake motion.

C.10 Axial Load in Pile 1

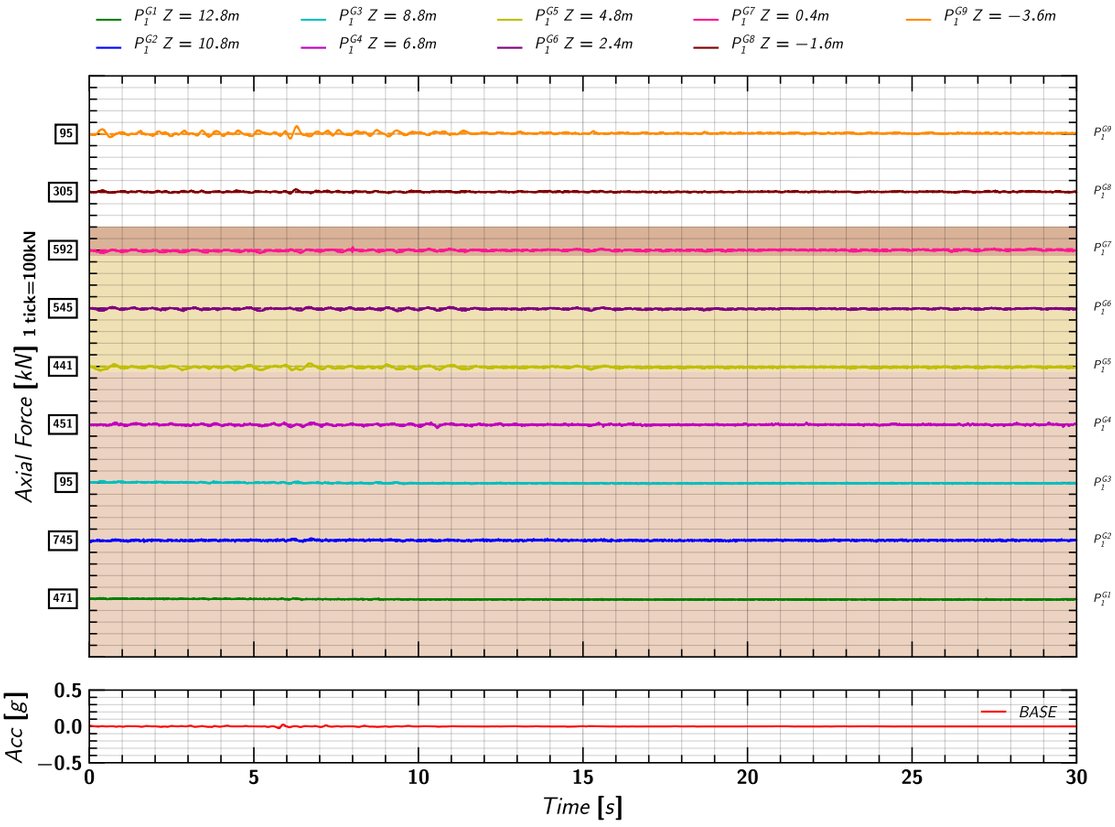

Figure 91. EQM1: Axial load measurements from pile 1 strain gages during the applied earthquake motion.

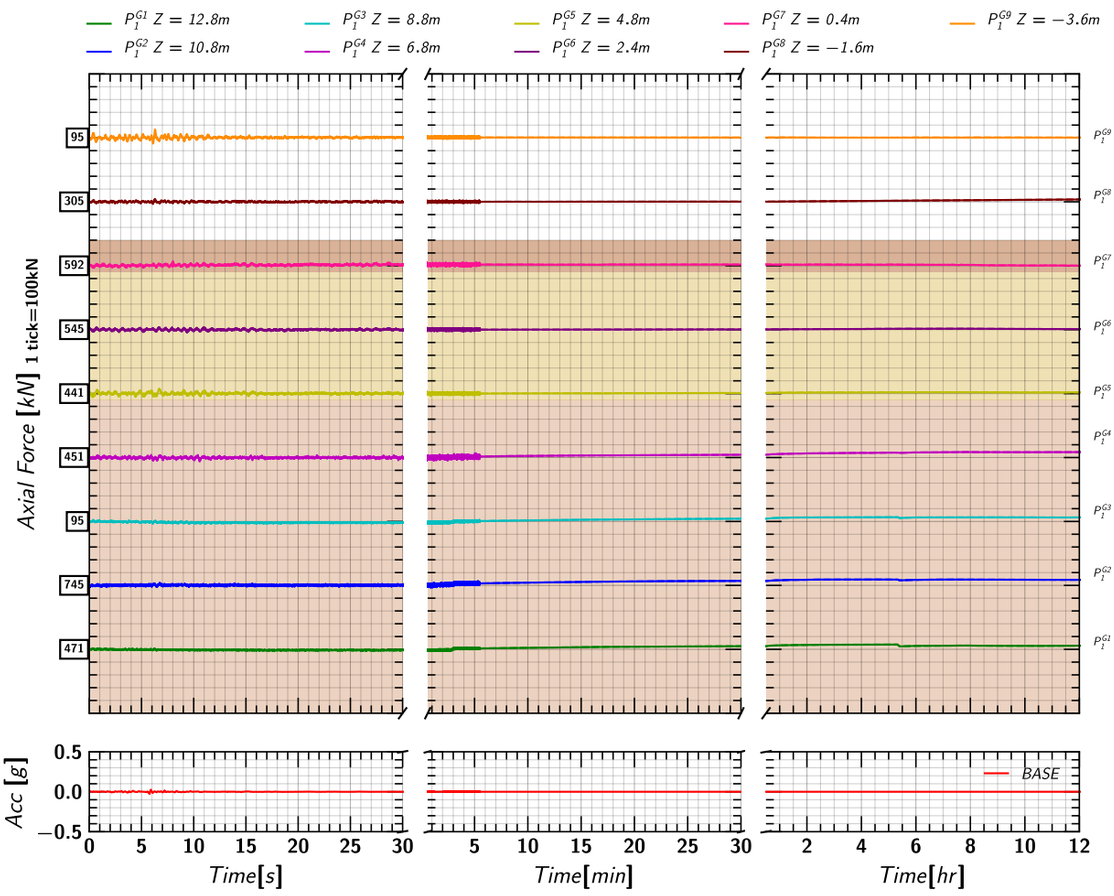

Figure 92. EQM1: Axial load measurements from pile 1 strain gages during and post the applied earthquake motion.

C.11 Axial Load in Pile 2

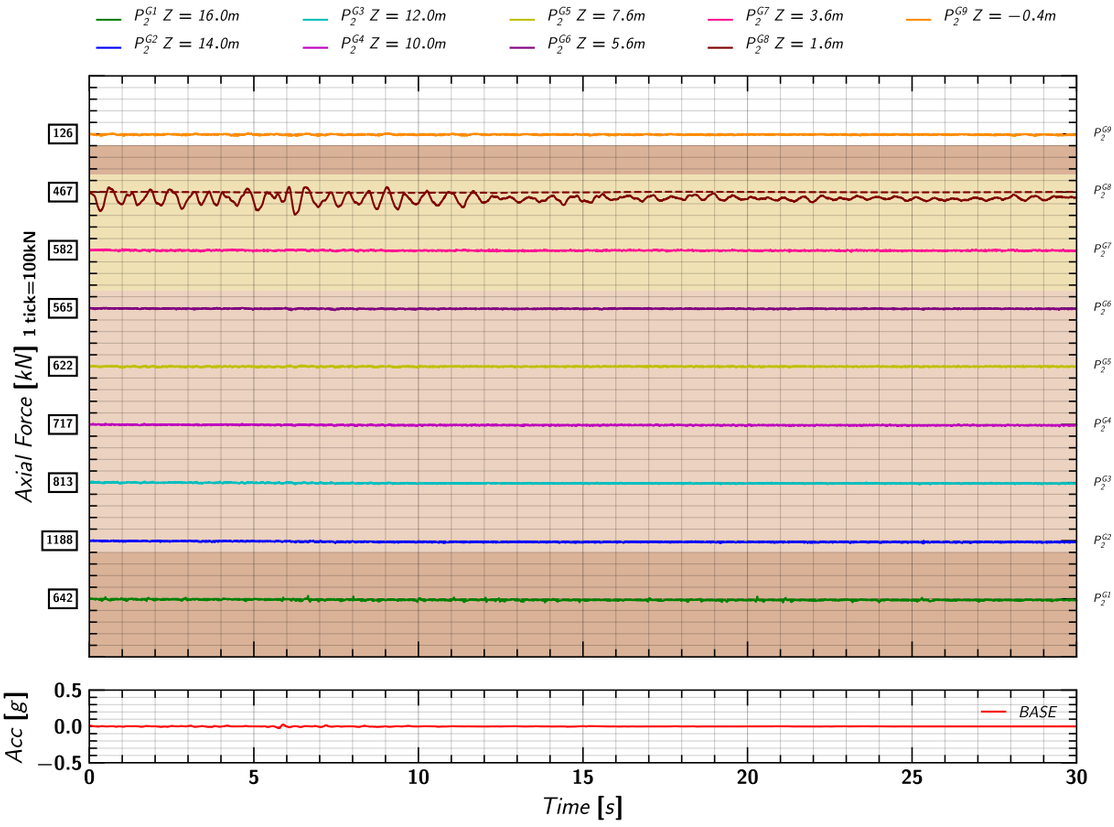

Figure 93. EQM1: Axial load measurements from pile 2 strain gages during the applied earthquake motion.

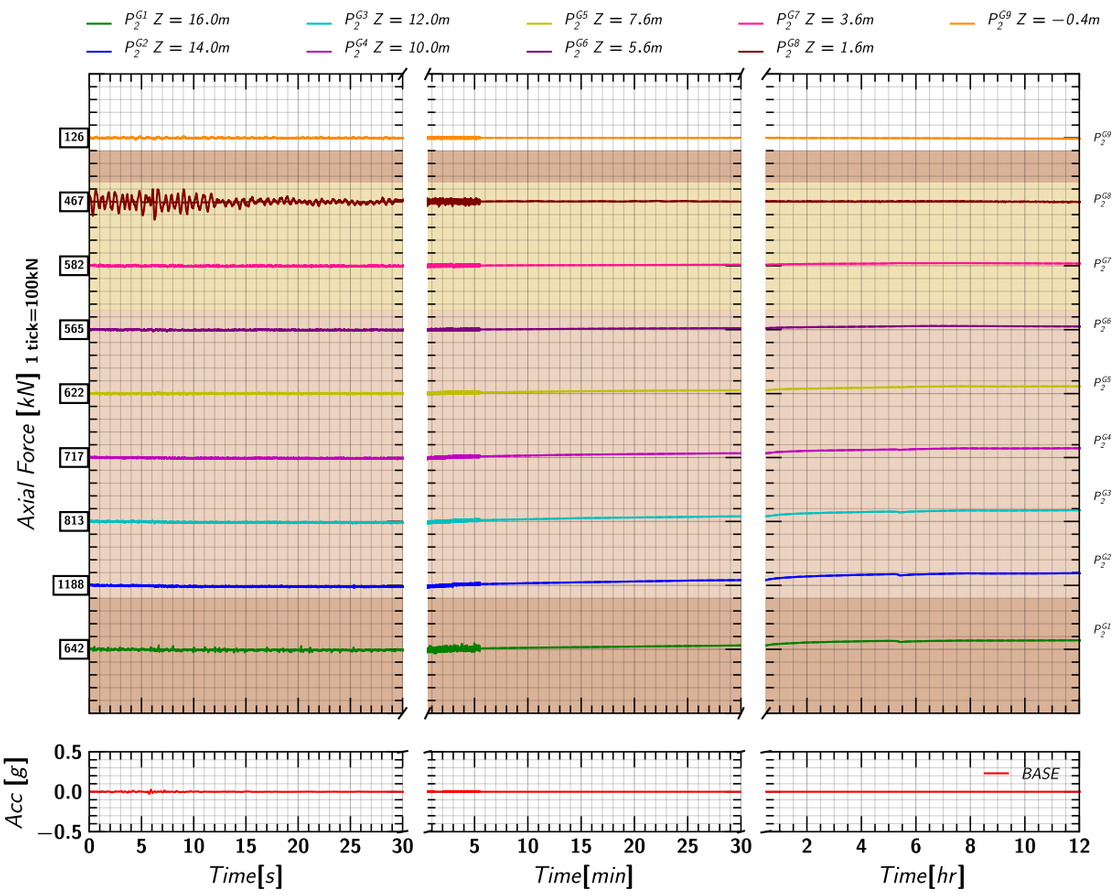

Figure 94. EQM1: Axial load measurements from pile 2 strain gages during and post the applied earthquake motion.

C.12 Pore pressure and Axial Load Profile

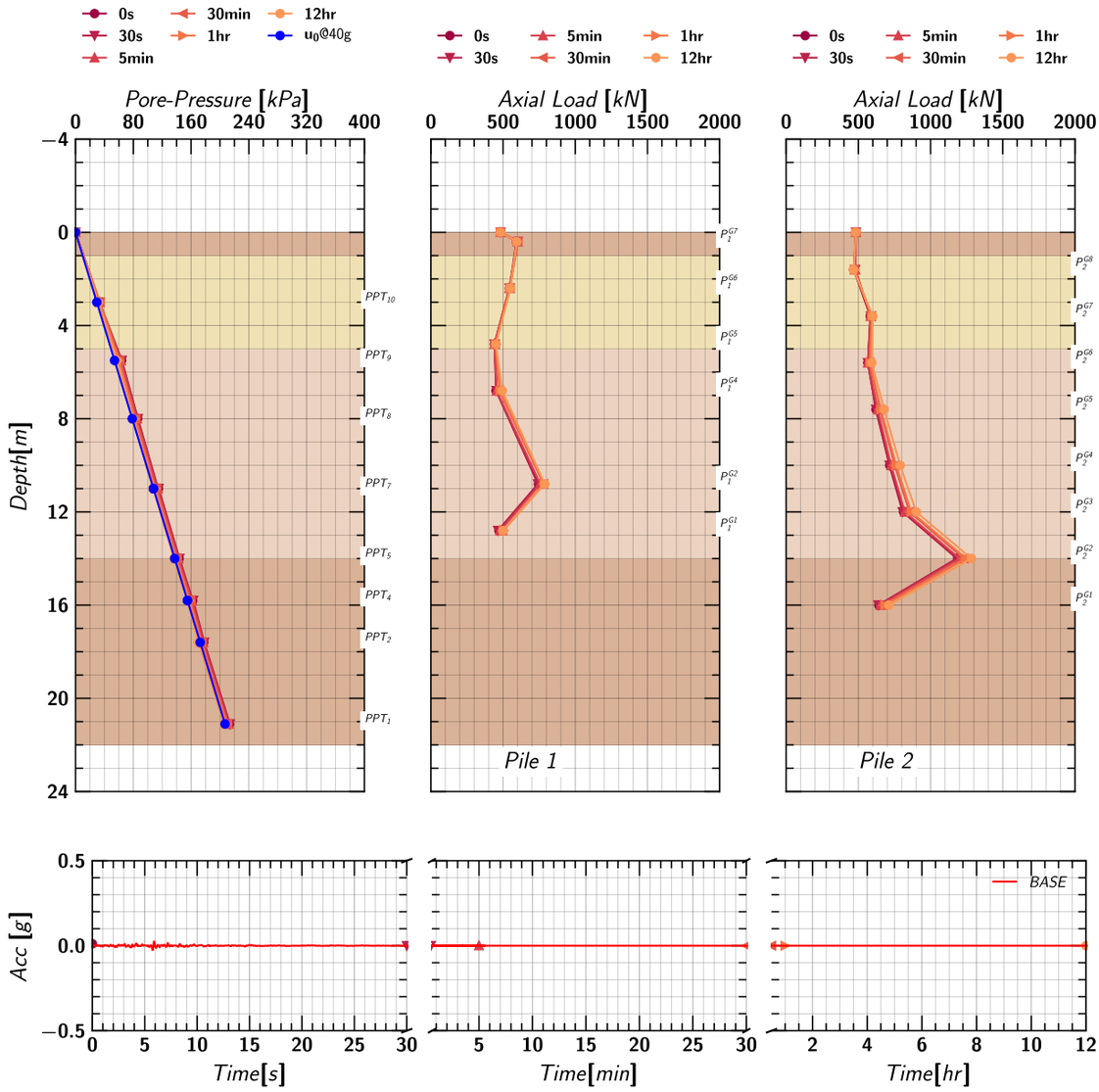

Figure 95. EQM1: Pore pressure and axial load profile in pile 1 and pile 2 at different times during and post the applied earthquake motion.

D. EQM$_2$ - Medium Santa Cruz Earthquake Motion (PGA = 0.14g)

D.1 Input Motion

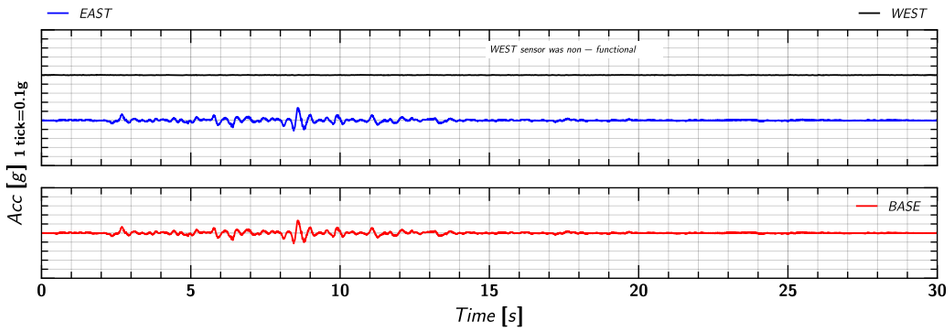

Figure 96. EQM$_2$: Input motion.

D.2 Acceleration in Container

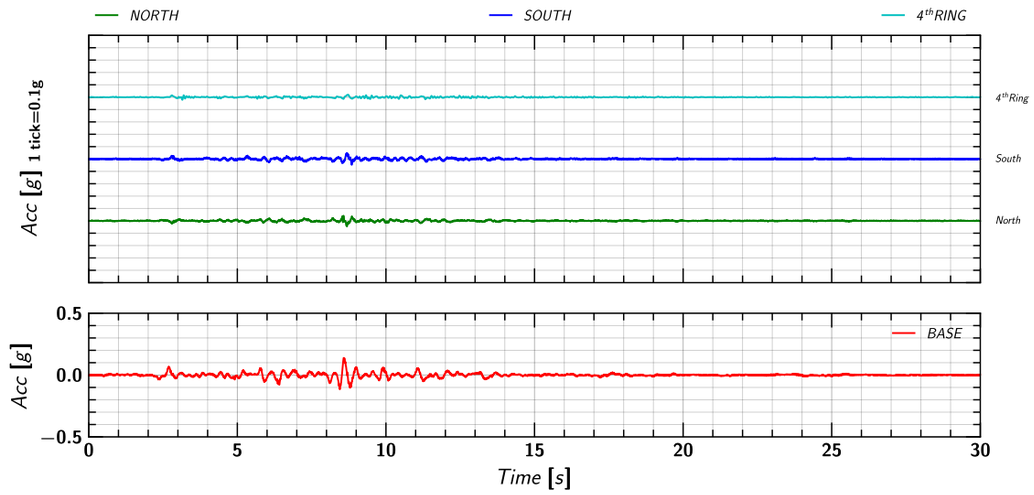

Figure 97. EQM$_2$: Acceleration measurement on container.

D.3 Acceleration in Soil

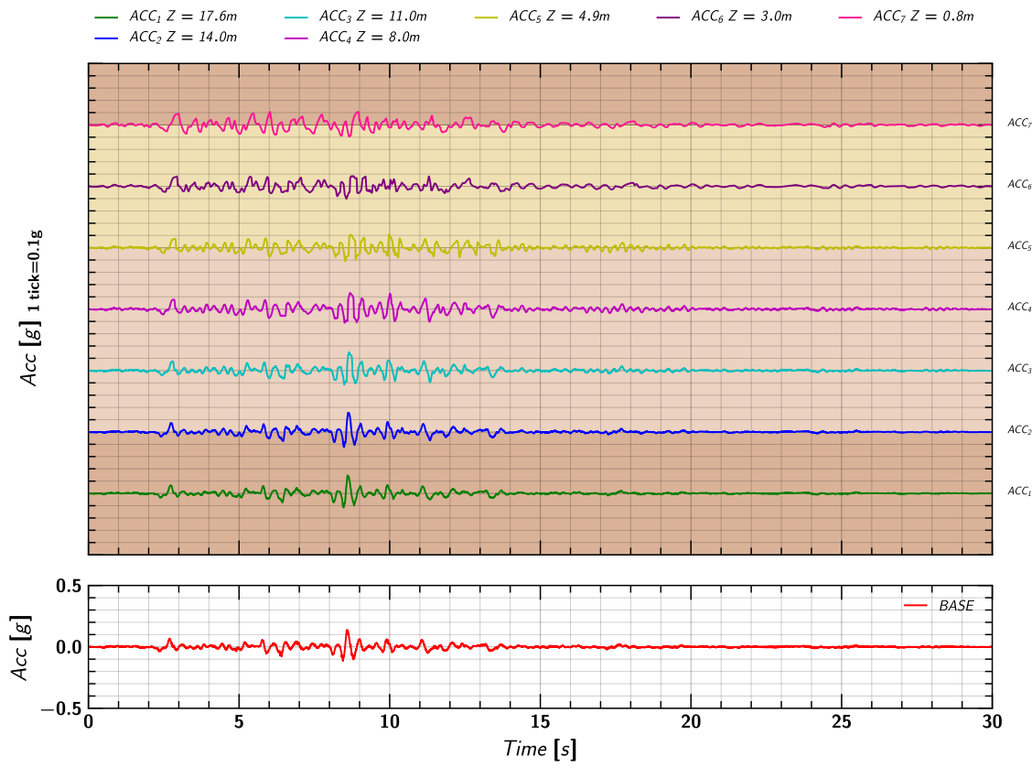

Figure 98. EQM$_2$: Acceleration measurement in soil.

D.4 Acceleration in Pile

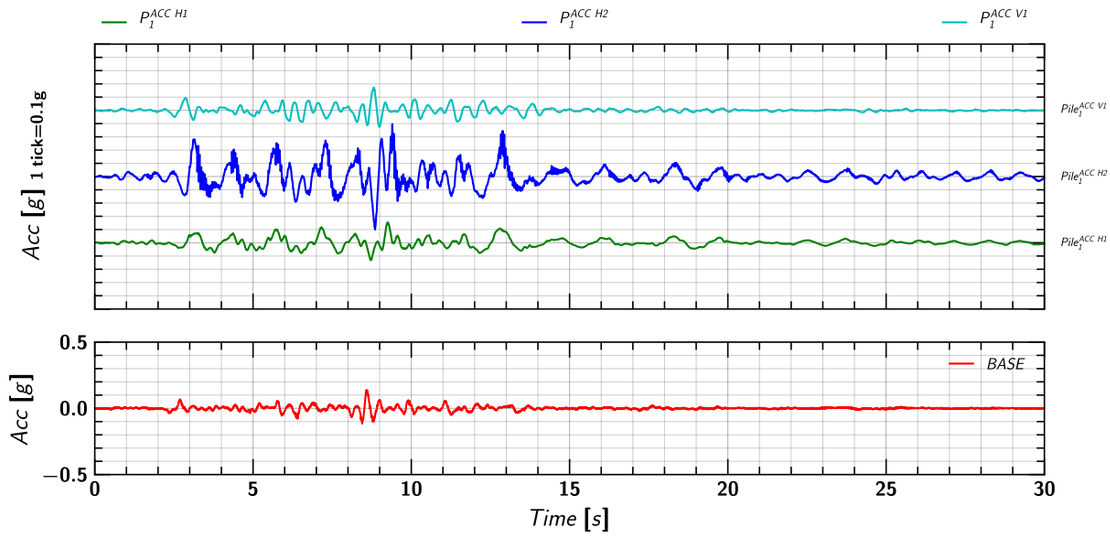

Figure 99. EQM₂: Acceleration measurement on pile 1.

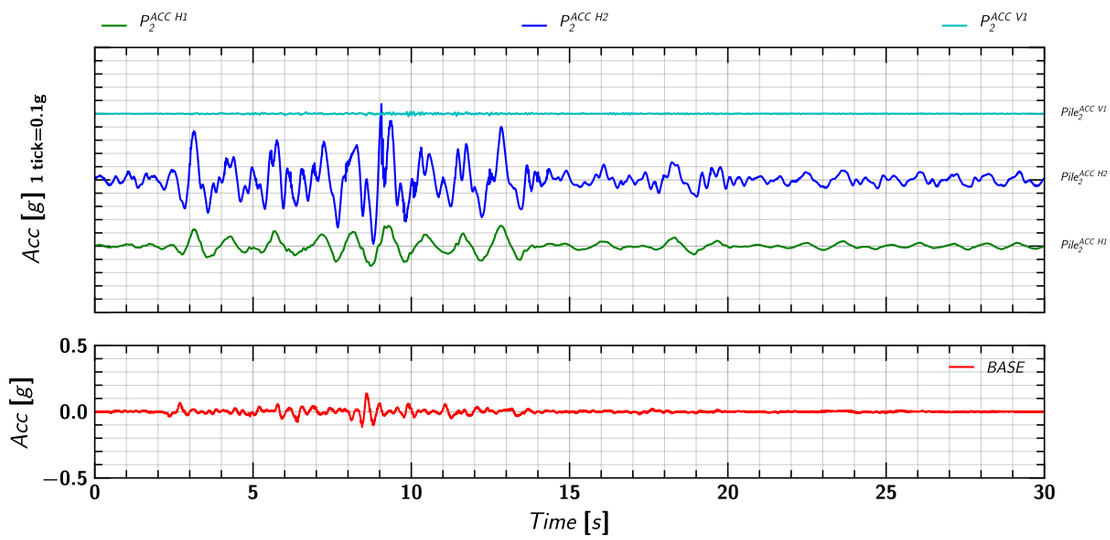

Figure 100. EQM₂: Acceleration measurement on pile 2.

D.5 Soil and Pile Settlement

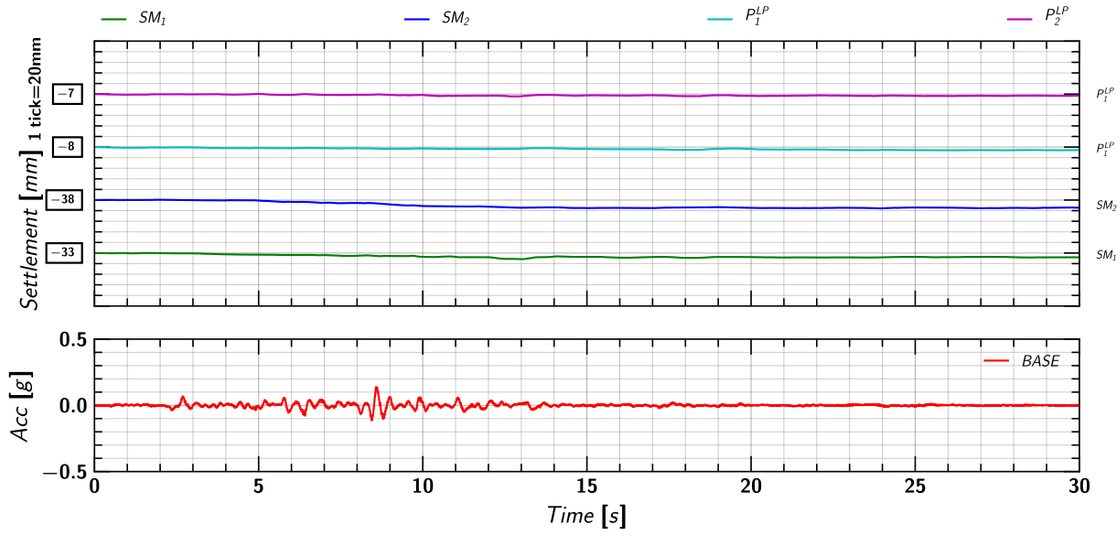

Figure 101. EQM₂: Settlement measurement in soil and pile during the applied earthquake motion.

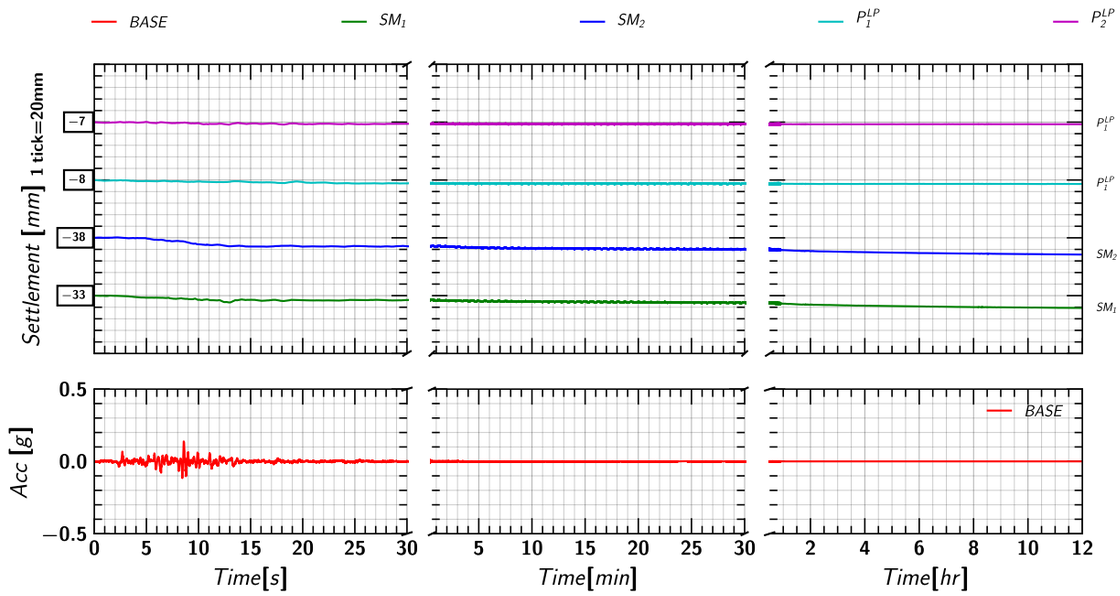

Figure 102. EQM₂: Settlement measurement in soil and pile during and post applied earthquake motion.

D.6 Pore pressure measurements in Soil (Keller Transducers)

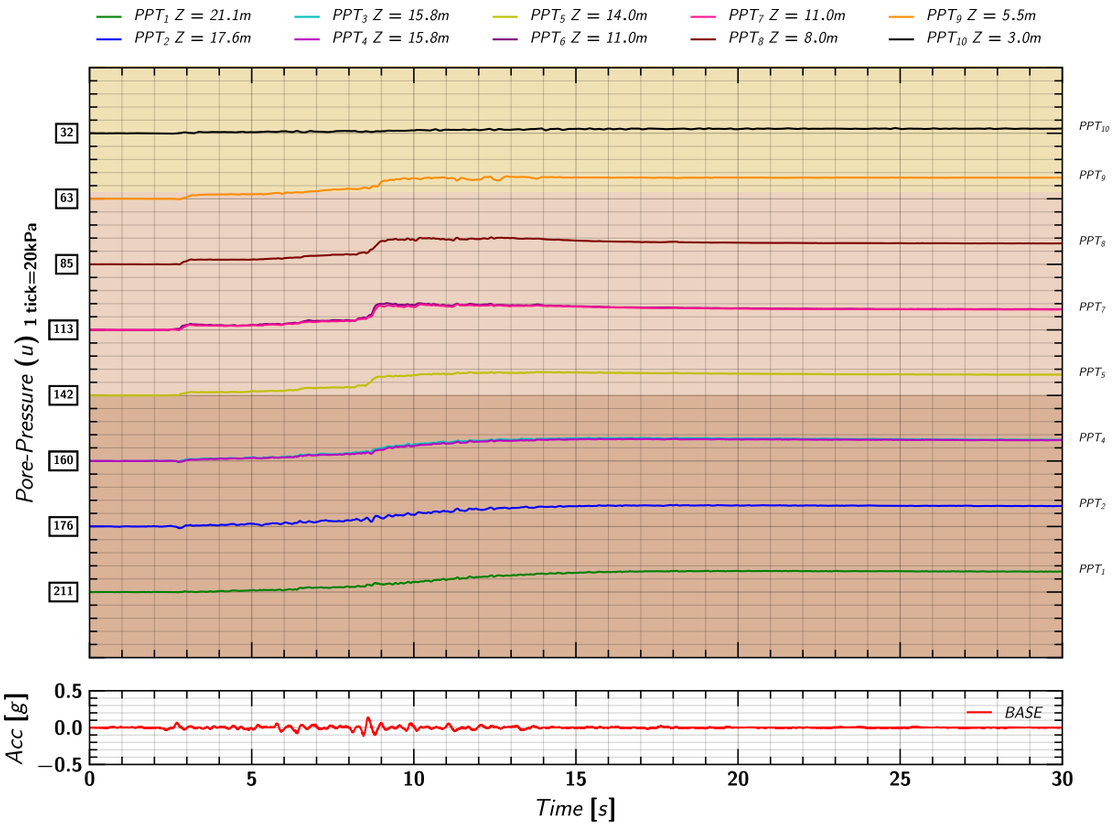

Figure 103. EQM₂: Pore pressure measurements in soil from Keller transducers during the applied earthquake motion.

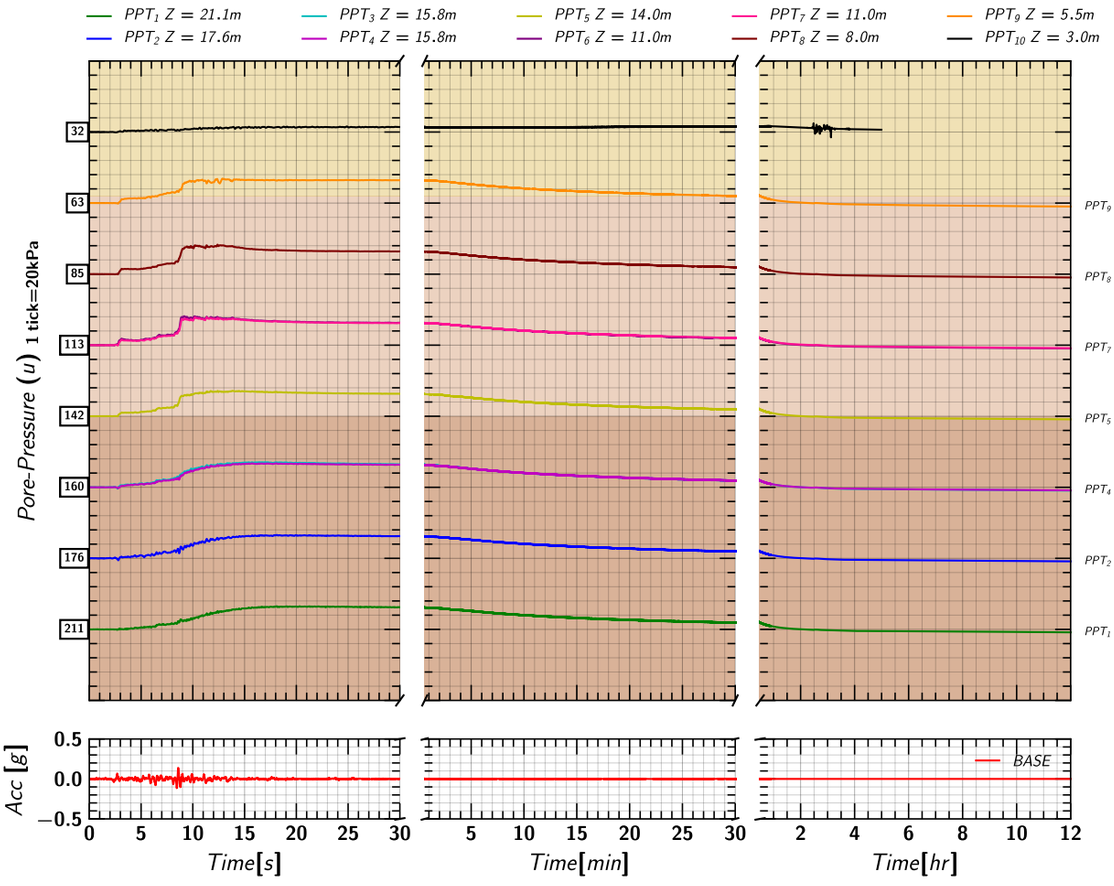

Figure 104. EQM₂: Pore pressure measurements in soil from Keller transducers during and post the applied earthquake motion.

D.7 Pore pressure measurements in Soil (MS54XXX Transducers)

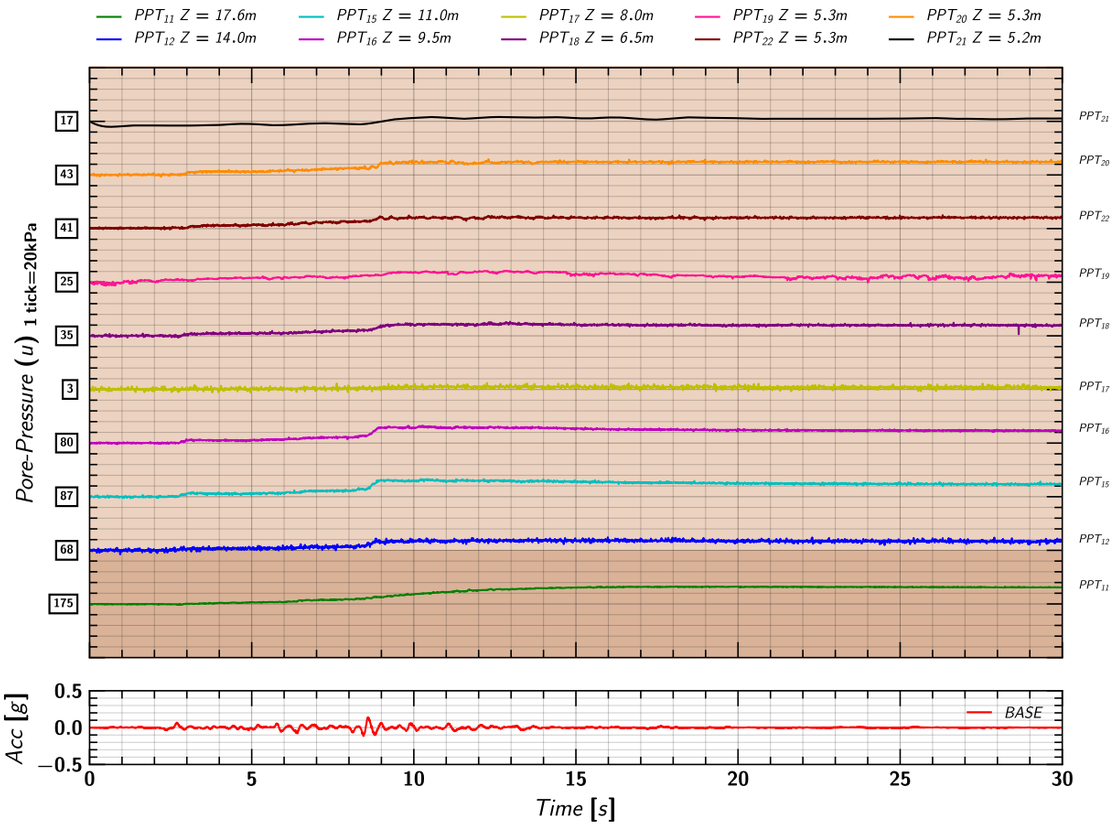

Figure 105. EQM$_2$: Pore pressure measurements in soil from MS54XXX transducers during the applied earthquake motion.

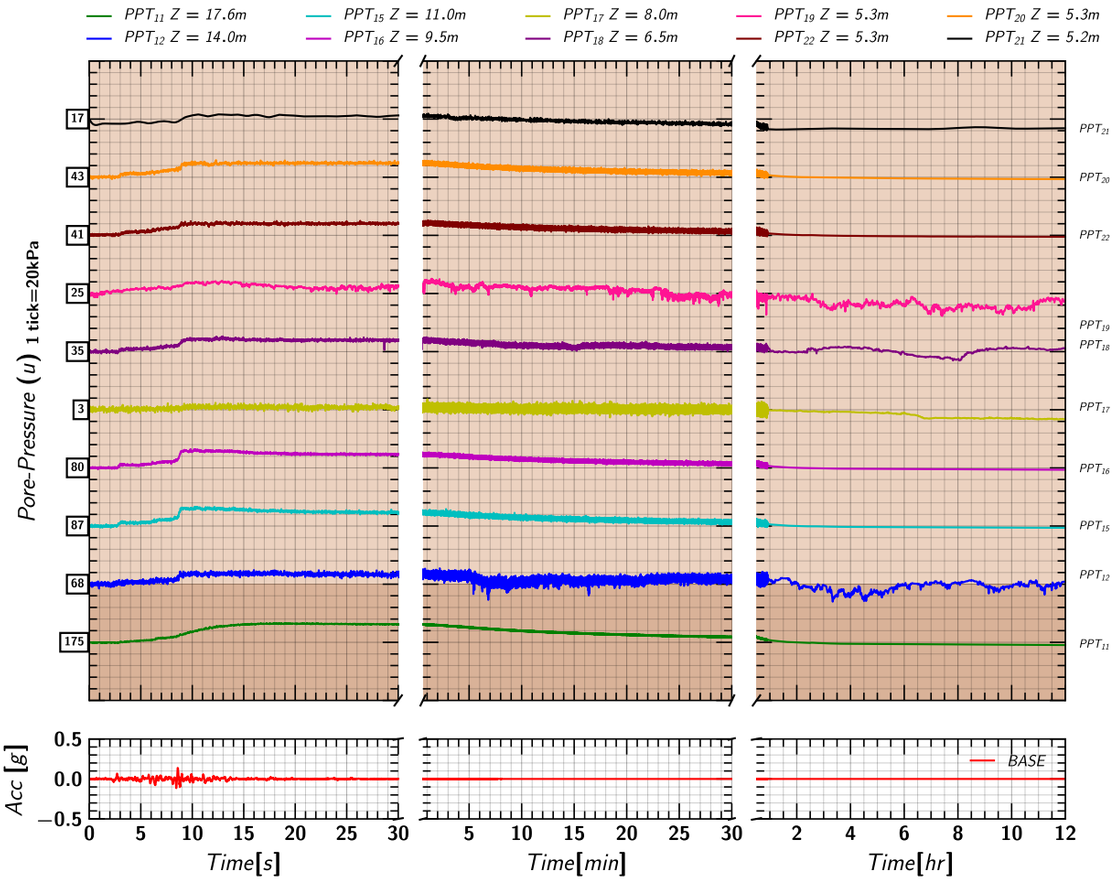

Figure 106. EQM$_2$: Pore pressure measurements in soil from MS54XXX transducers during and post the applied earthquake motion.

D.8 Excess Pore pressures Ratio (r_u) Estimated from Keller Transducers

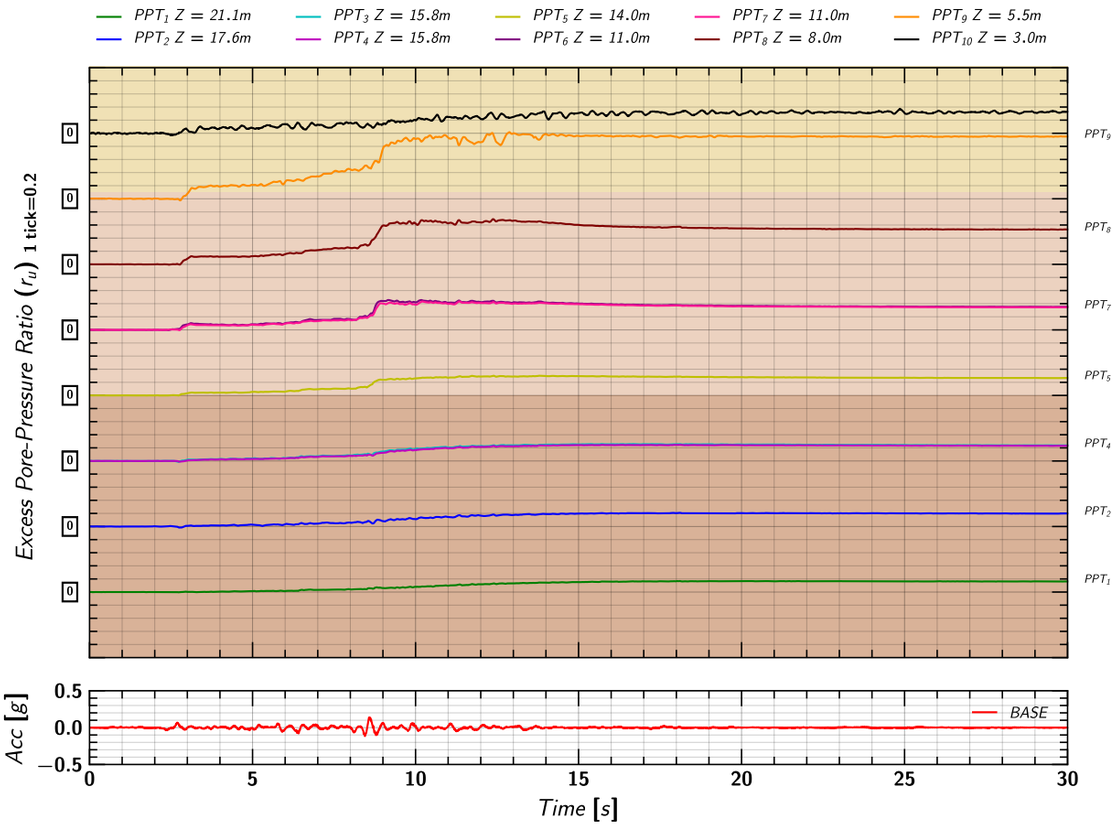

Figure 107. EQM$_2$: Excess pore pressure ratio (r_u) estimated from measurements by Keller transducers during the applied earthquake motion.

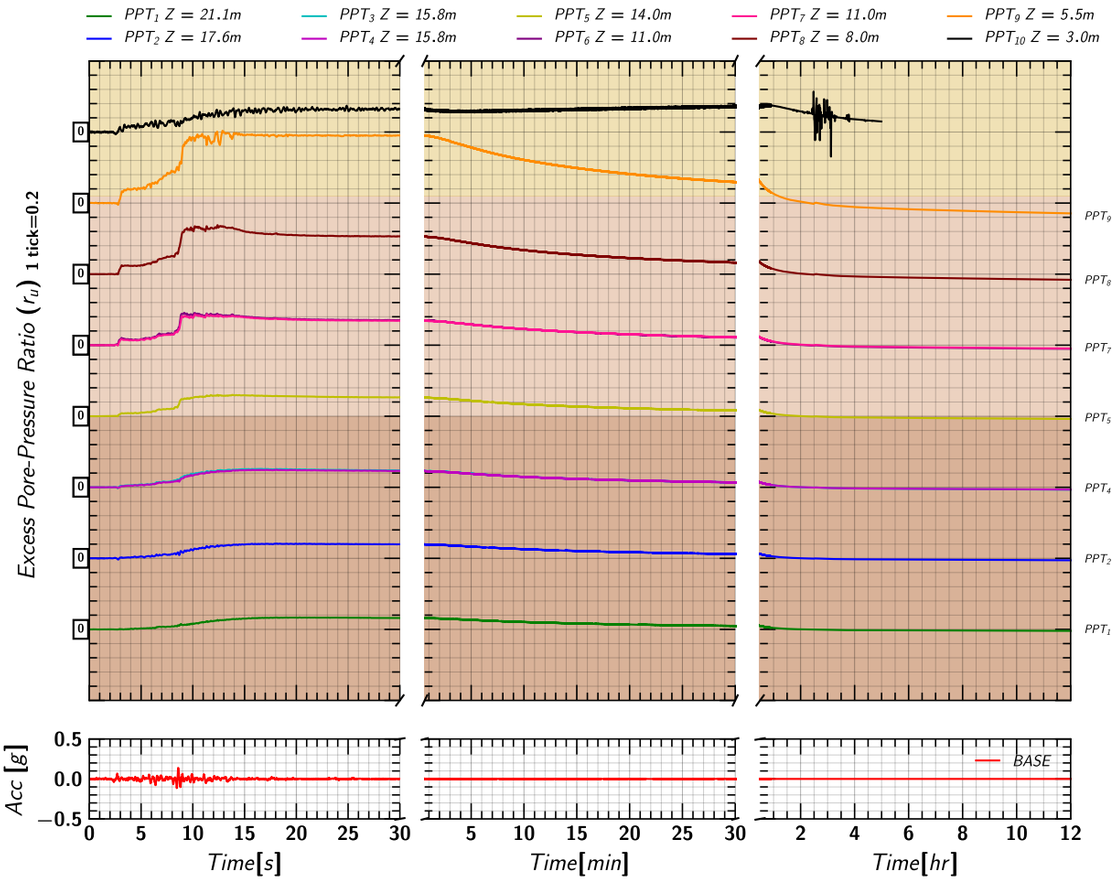

Figure 108. EQM$_2$: Excess pore pressure ratio (r_u) estimated from measurements by Keller transducers during and post the applied earthquake motion.

D.9 Excess Pore pressure Ratio (r_u) Estimated from MS54XXX Transducers

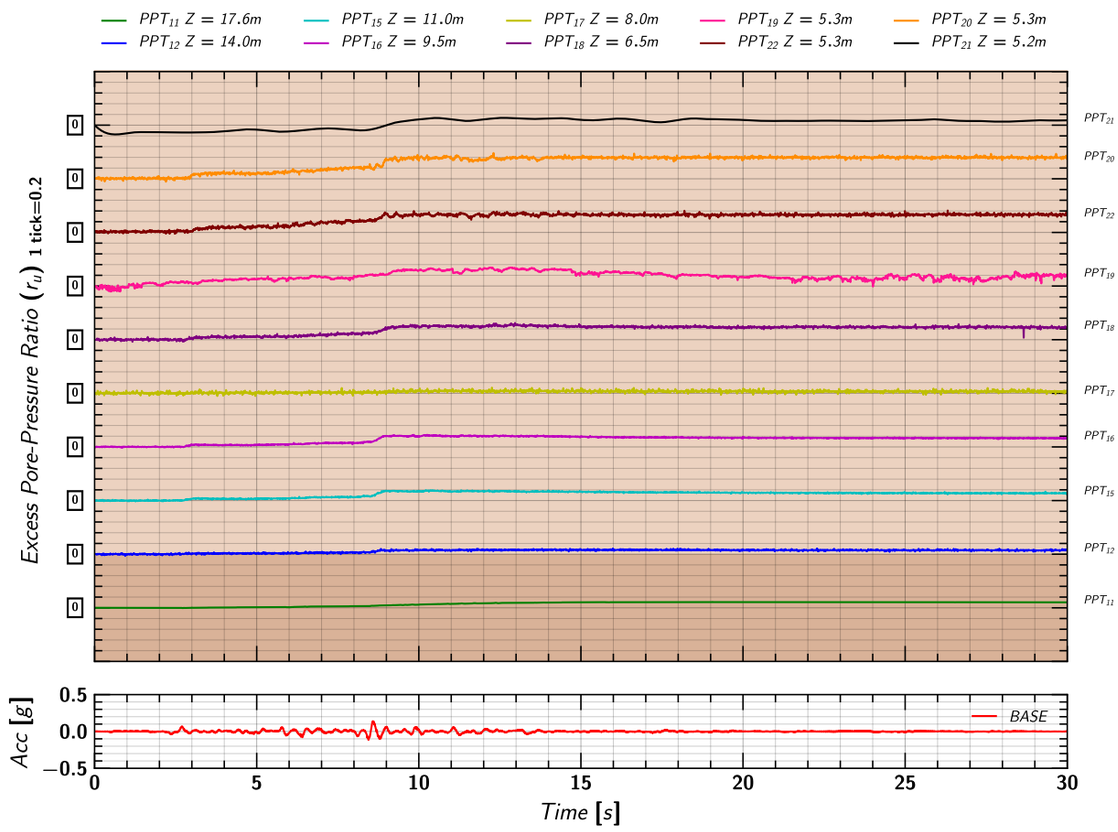

Figure 109. EQM$_2$: Excess pore pressure ratio (r_u) estimated from measurements by MS54XXX transducers during the applied earthquake motion.

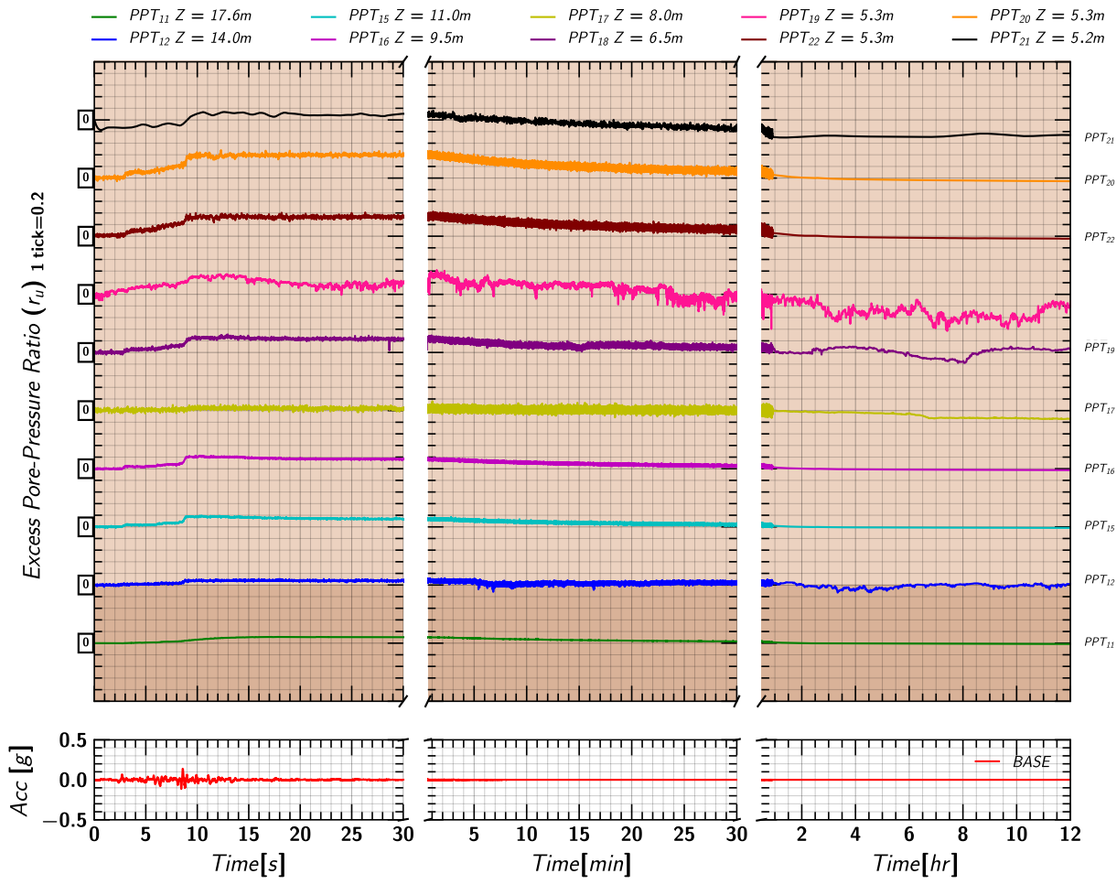

Figure 110. EQM$_2$: Excess pore pressure ratio (r_u) estimated from measurements by MS54XXX transducers during and post the applied earthquake motion.

D.10 Axial Load in Pile 1

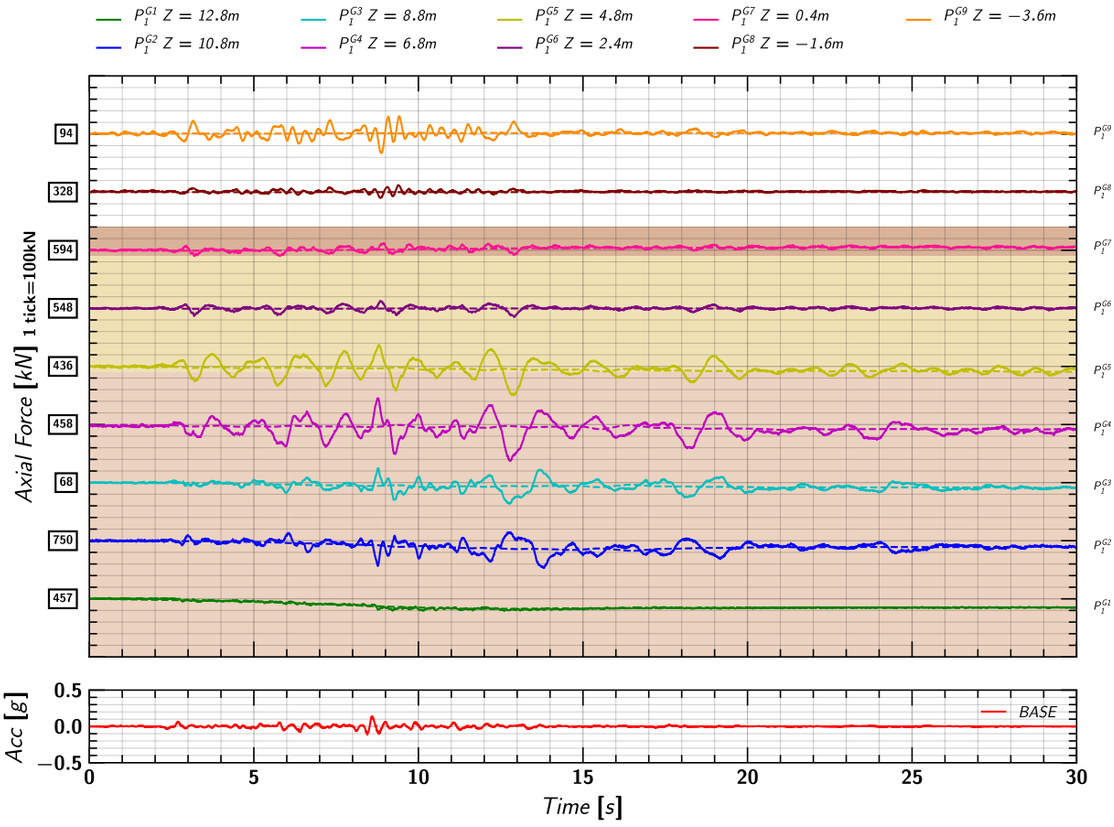

Figure 111. EQM₂: Axial load measurements from pile 1 strain gages during the applied earthquake motion.

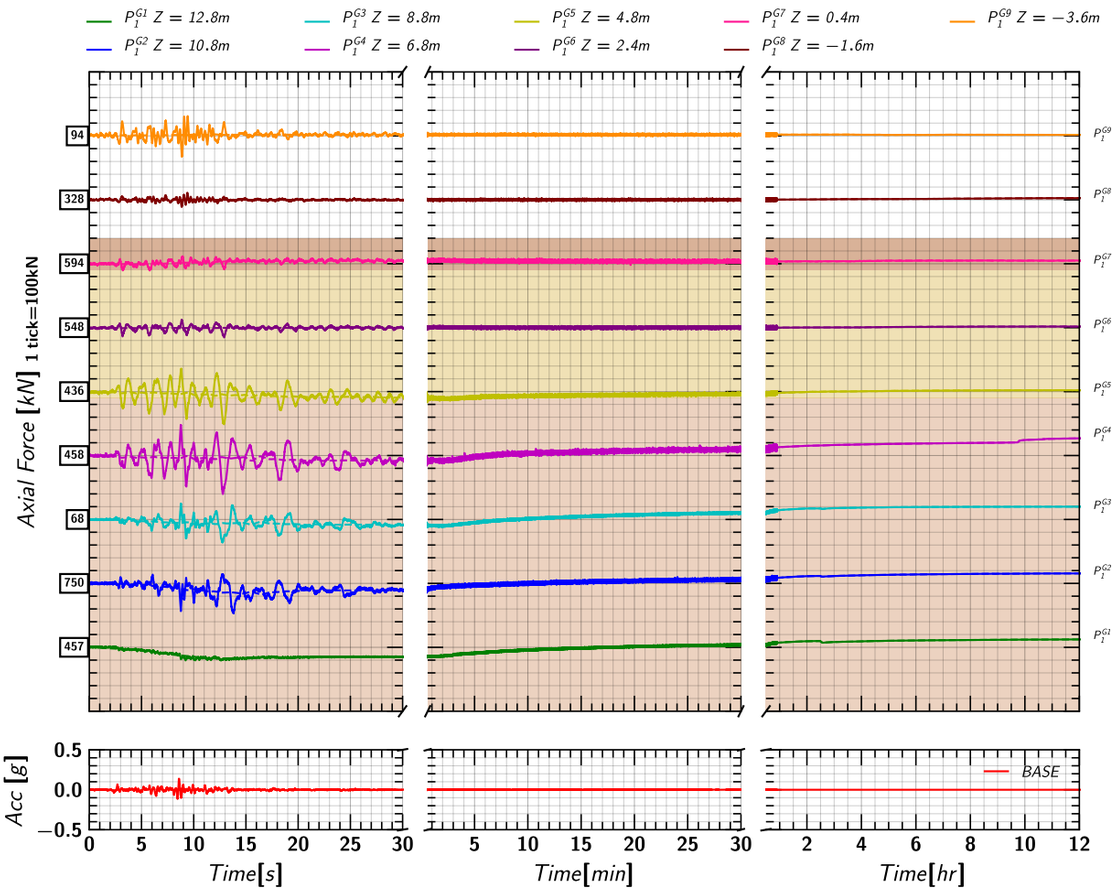

Figure 112. EQM₂: Axial load measurements from pile 1 strain gages during and post the applied earthquake motion.

D.11 Axial Load in Pile 2

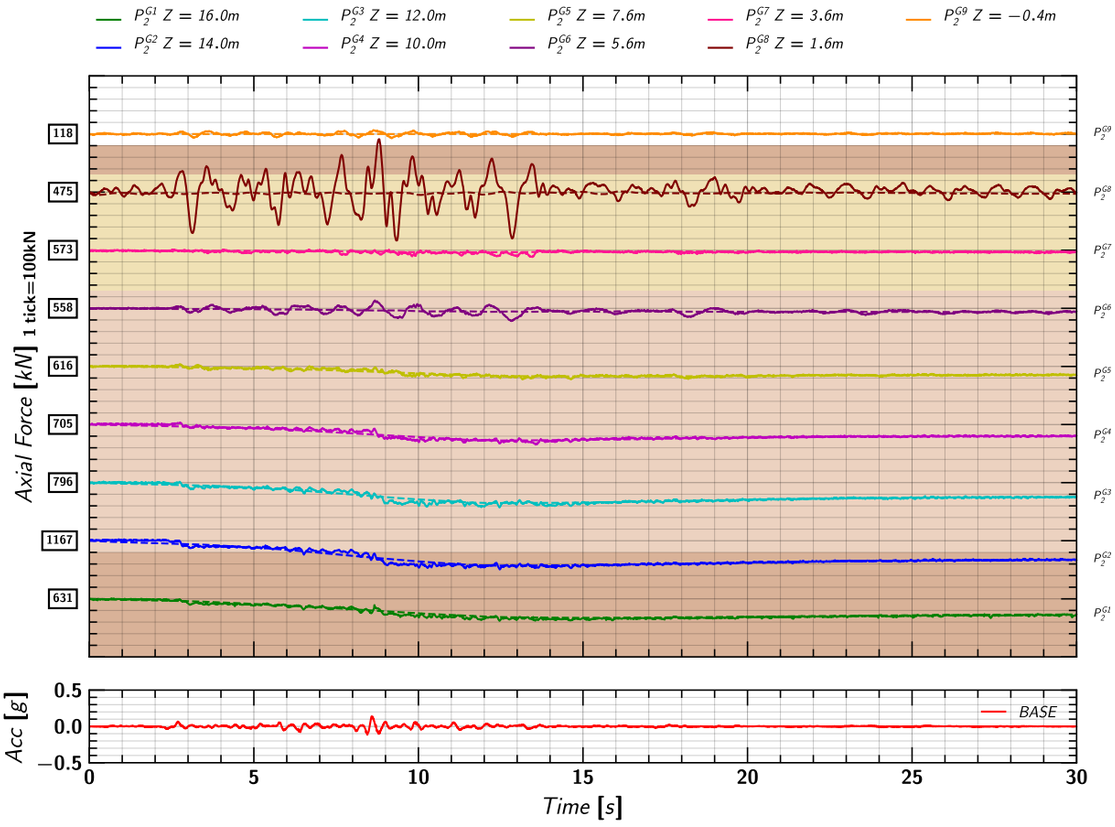

Figure 113. EQM$_2$: Axial load measurements from pile 2 strain gages during the applied earthquake motion.

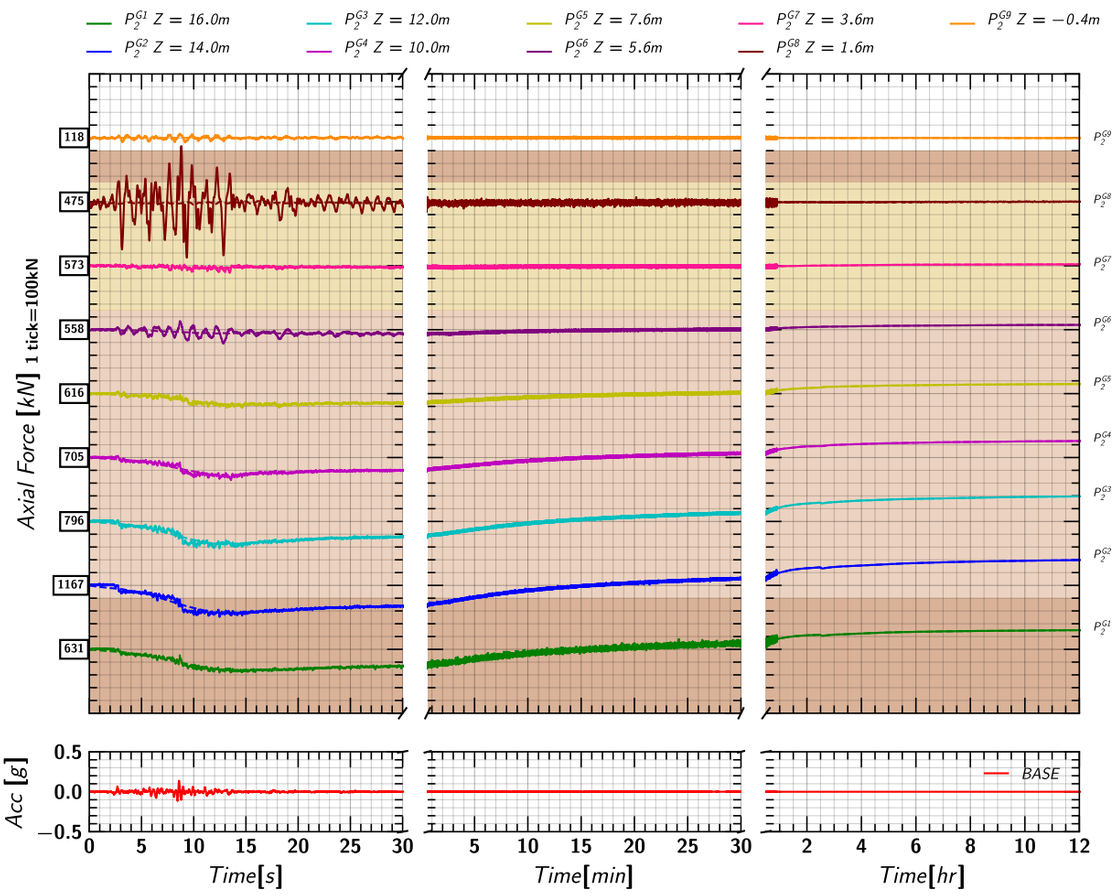

Figure 114. EQM$_2$: Axial load measurements from pile 2 strain gages during and post the applied earthquake motion.

D.12 Pore pressure and Axial Load Profile

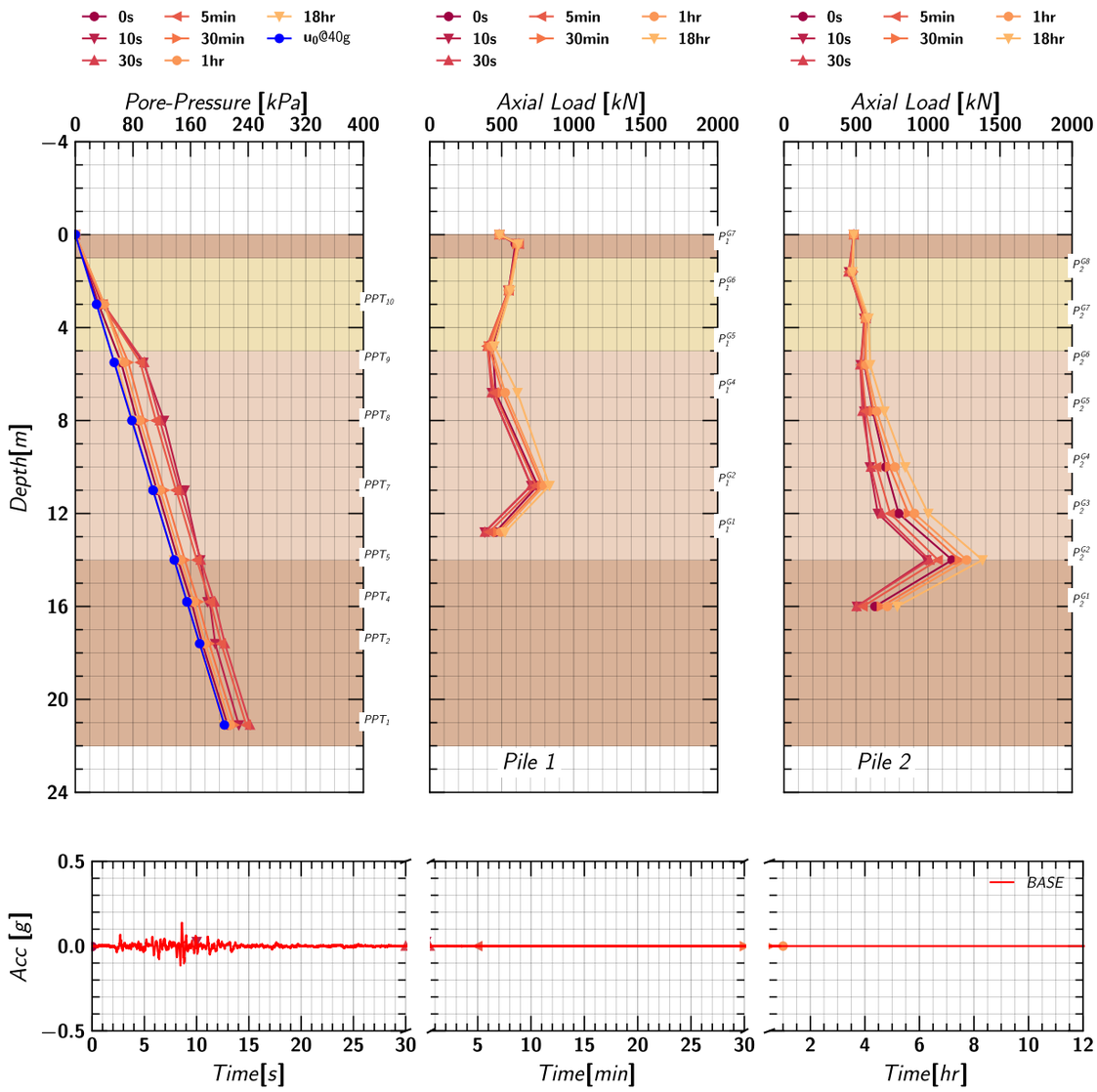

Figure 115. EQM₂: Pore pressure and axial load profile in pile 1 and pile 2 at different times during and post the applied earthquake motion.

E. EQM₃ - Large Santa Cruz Earthquake Motion (PGA = 0.24g)

E.1 Input Motion

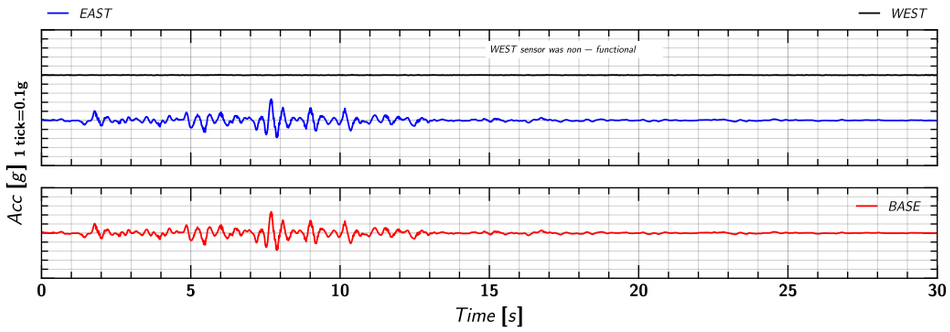

Figure 116. EQM₃: Input motion.

E.2 Acceleration in Container

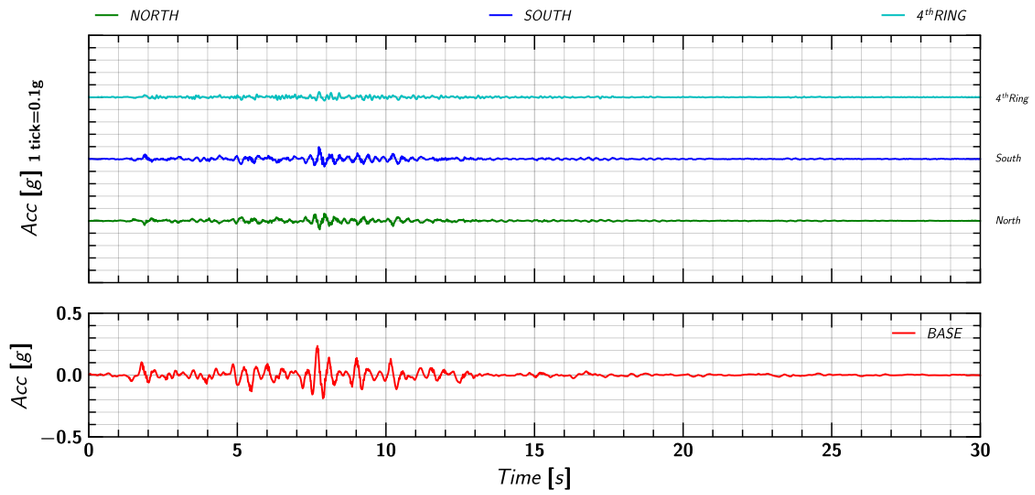

Figure 117. EQM₃: Acceleration measurement on container.

E.3 Acceleration in Soil

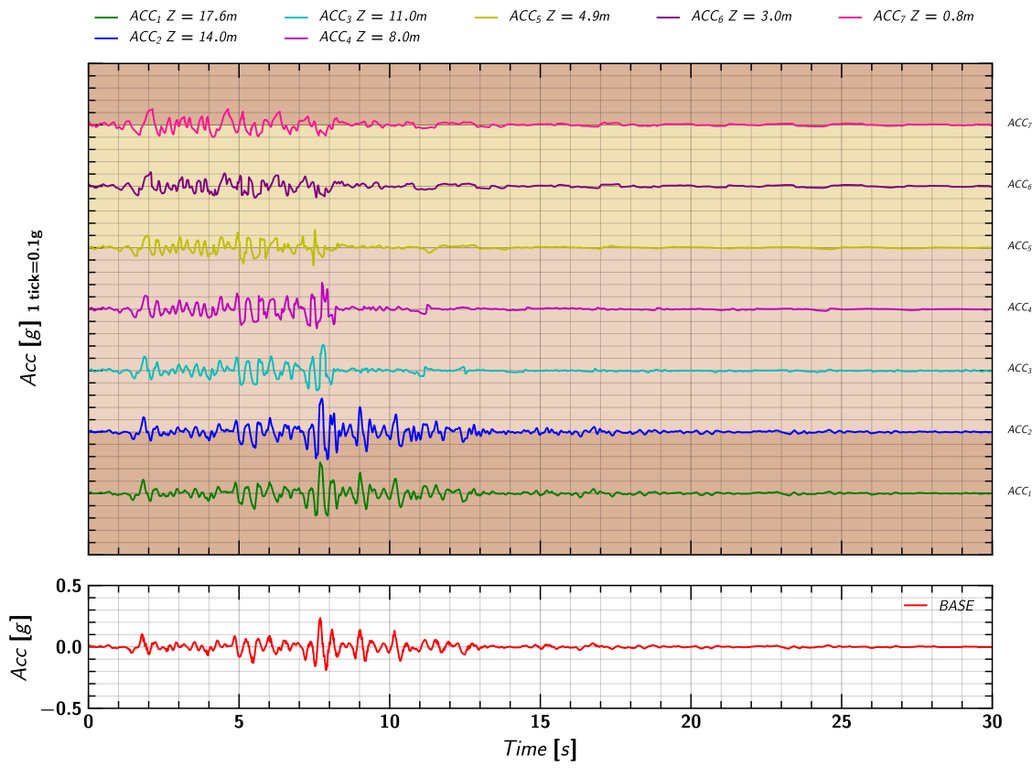

Figure 118. EQM₃: Acceleration measurement in soil.

E.4 Acceleration in Pile

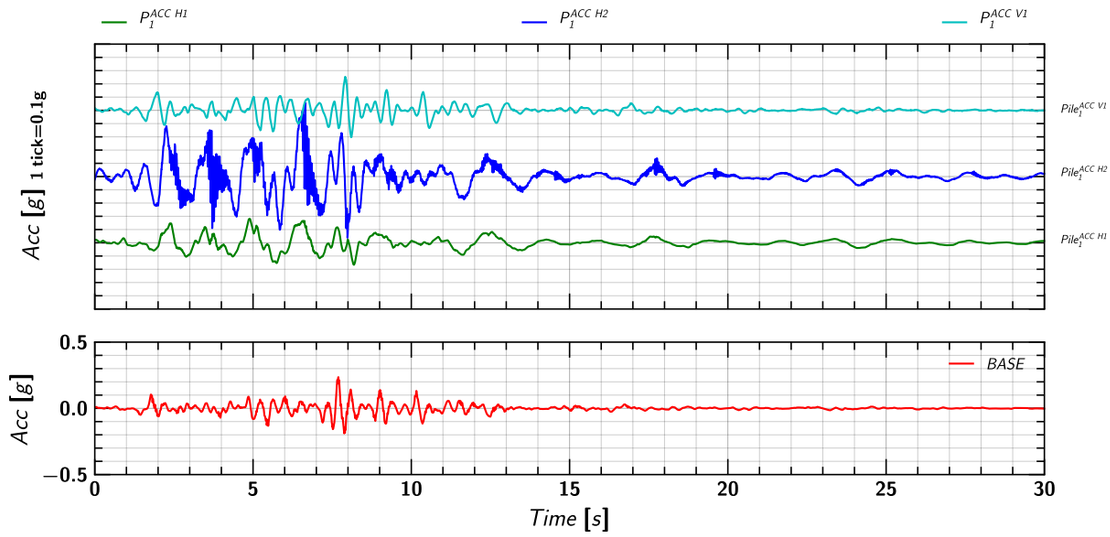

Figure 119. EQM₃: Acceleration measurement on pile 1.

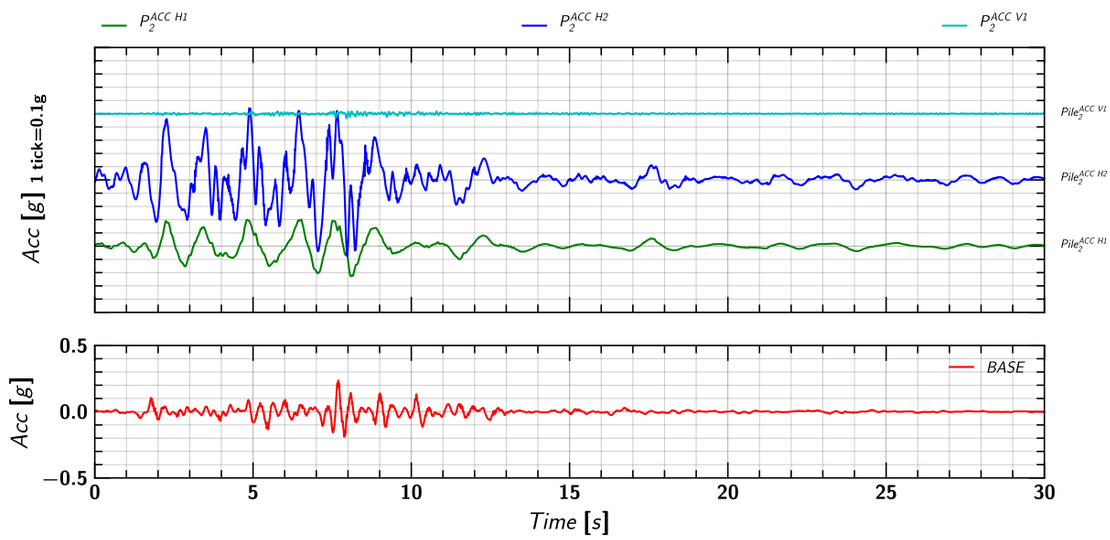

Figure 120. EQM₃: Acceleration measurement on pile 2.

E.5 Soil and Pile Settlement

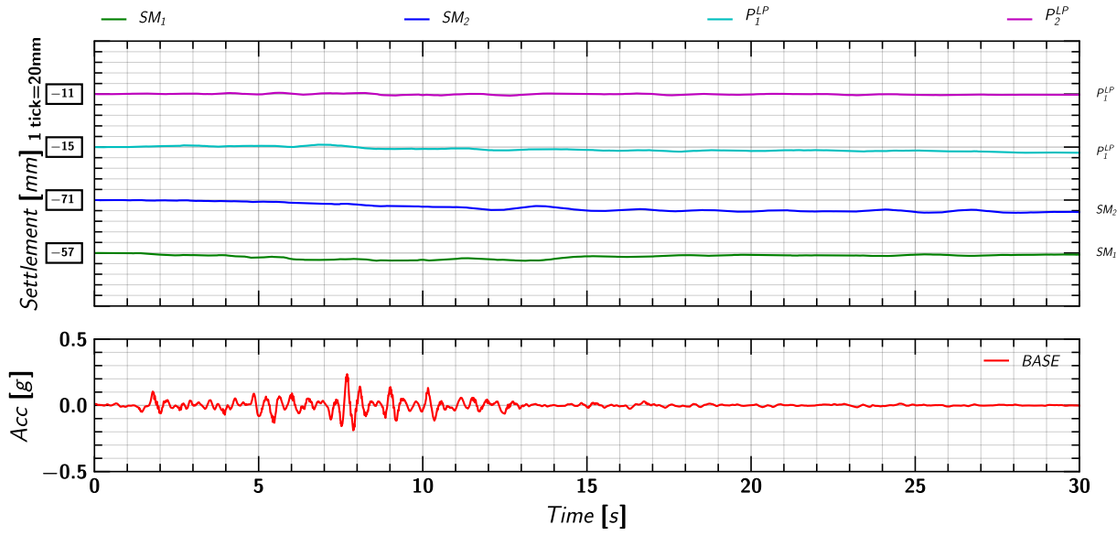

Figure 121. EQM3: Settlement measurement in soil and pile during the applied earthquake motion.

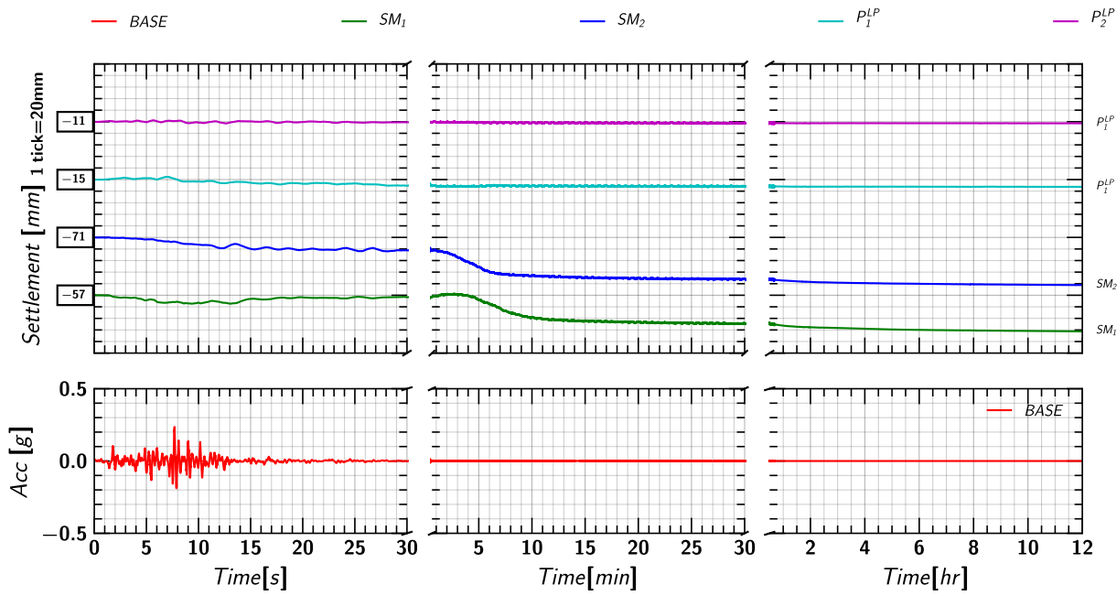

Figure 122. EQM3: Settlement measurement in soil and pile during and post applied earthquake motion.

E.6 Pore pressure measurements in Soil (Keller Transducers)

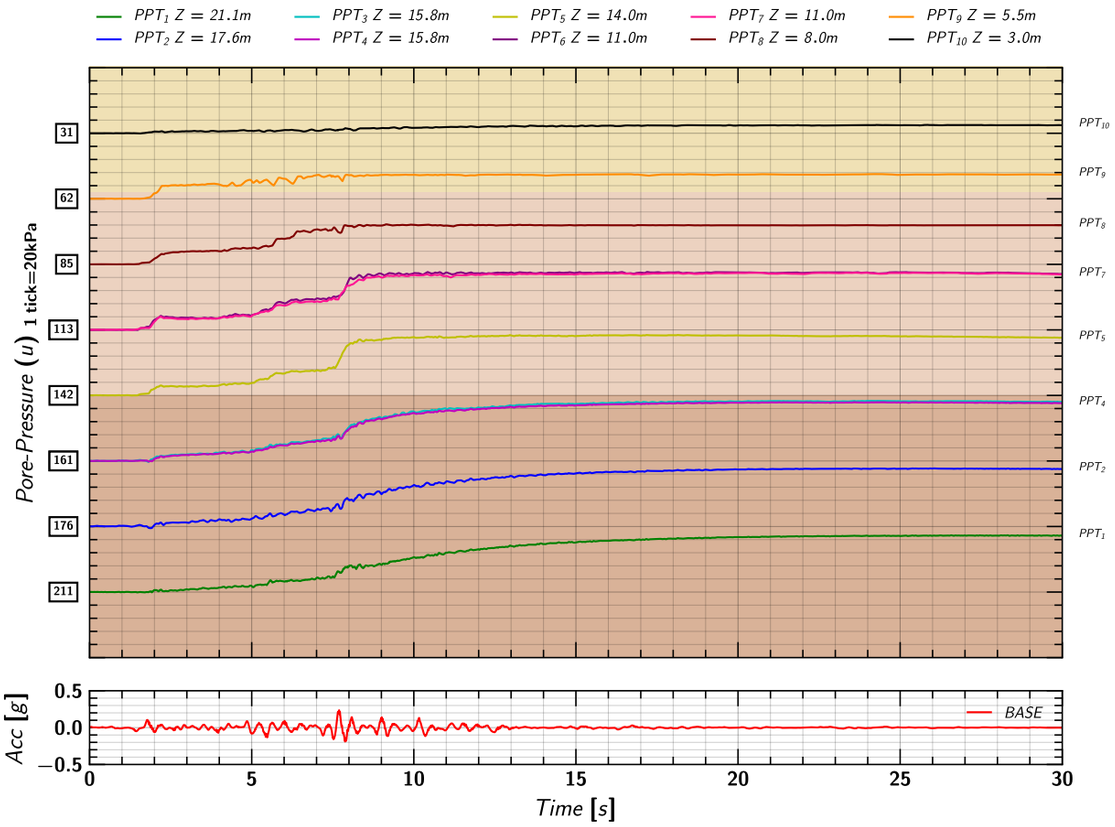

Figure 123. EQM3: Pore pressure measurements in soil from Keller transducers during the applied earthquake motion.

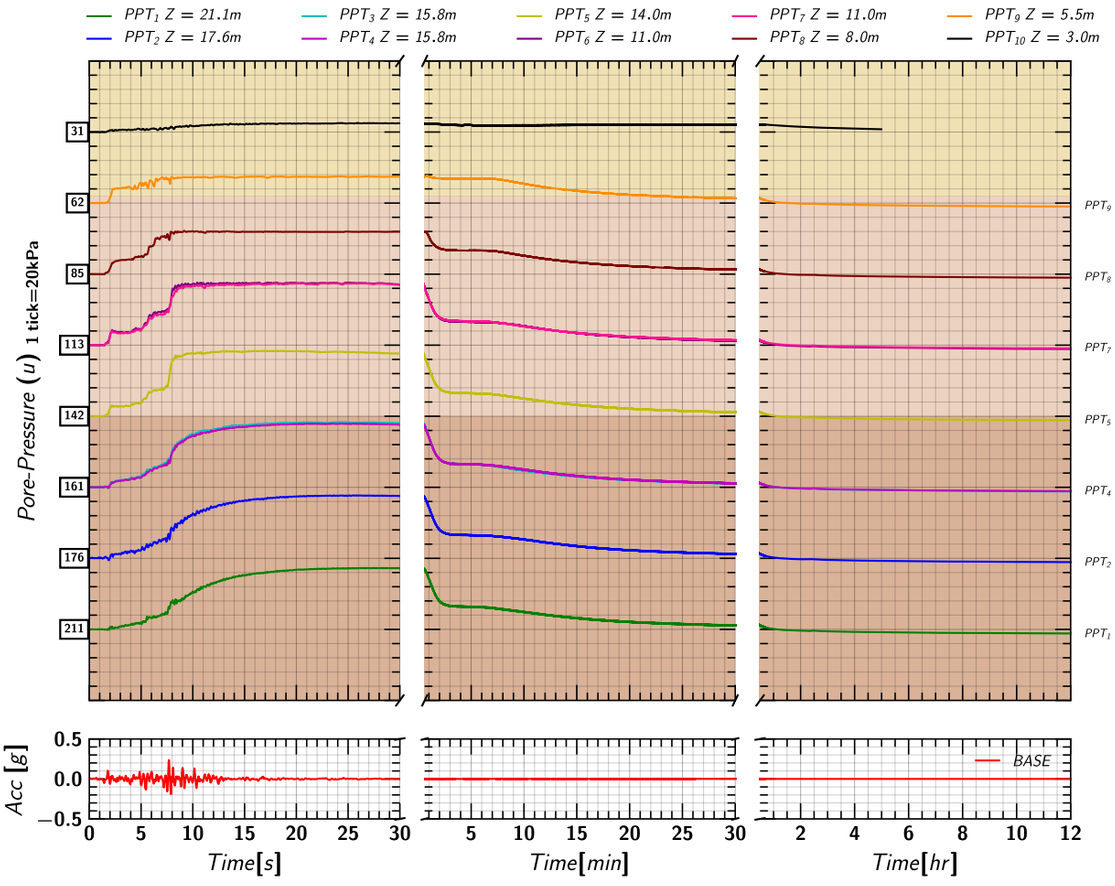

Figure 124. EQM3: Pore pressure measurements in soil from Keller transducers during and post the applied earthquake motion.

E.7 Pore pressure measurements in Soil (MS54XXX Transducers)

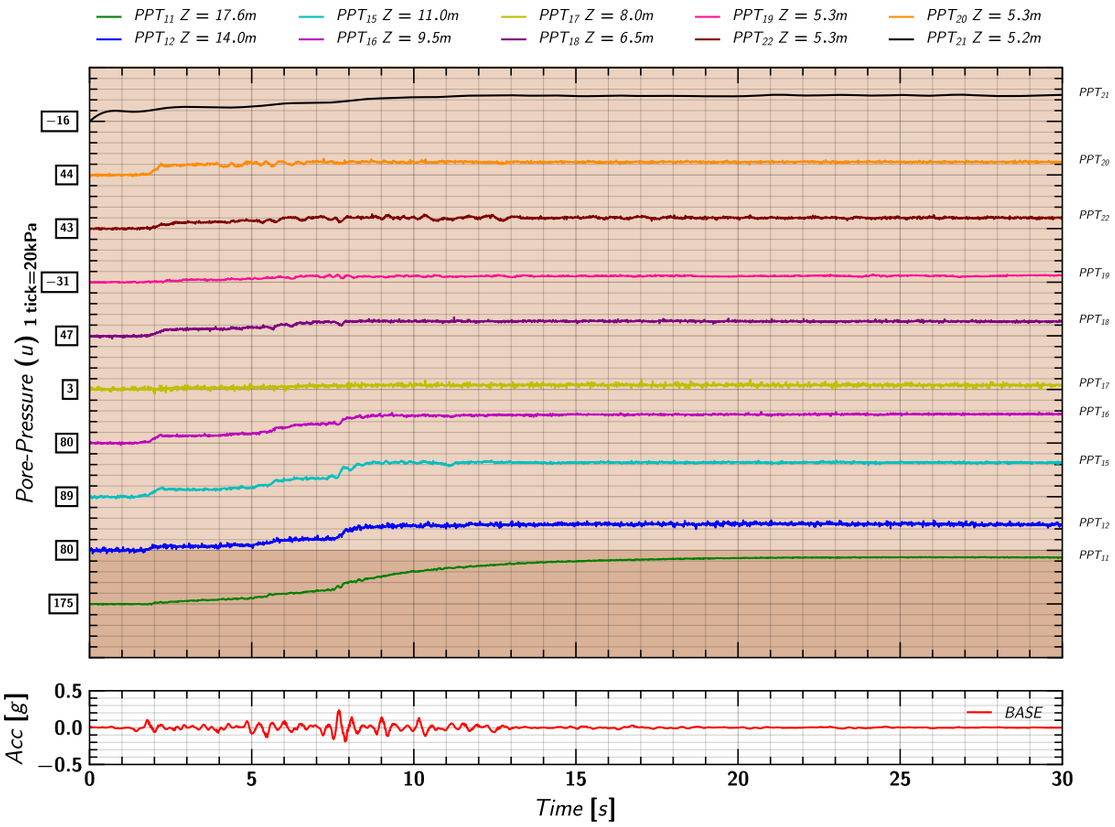

Figure 125. EQM₃: Pore pressure measurements in soil from MS54XXX transducers during the applied earthquake motion.

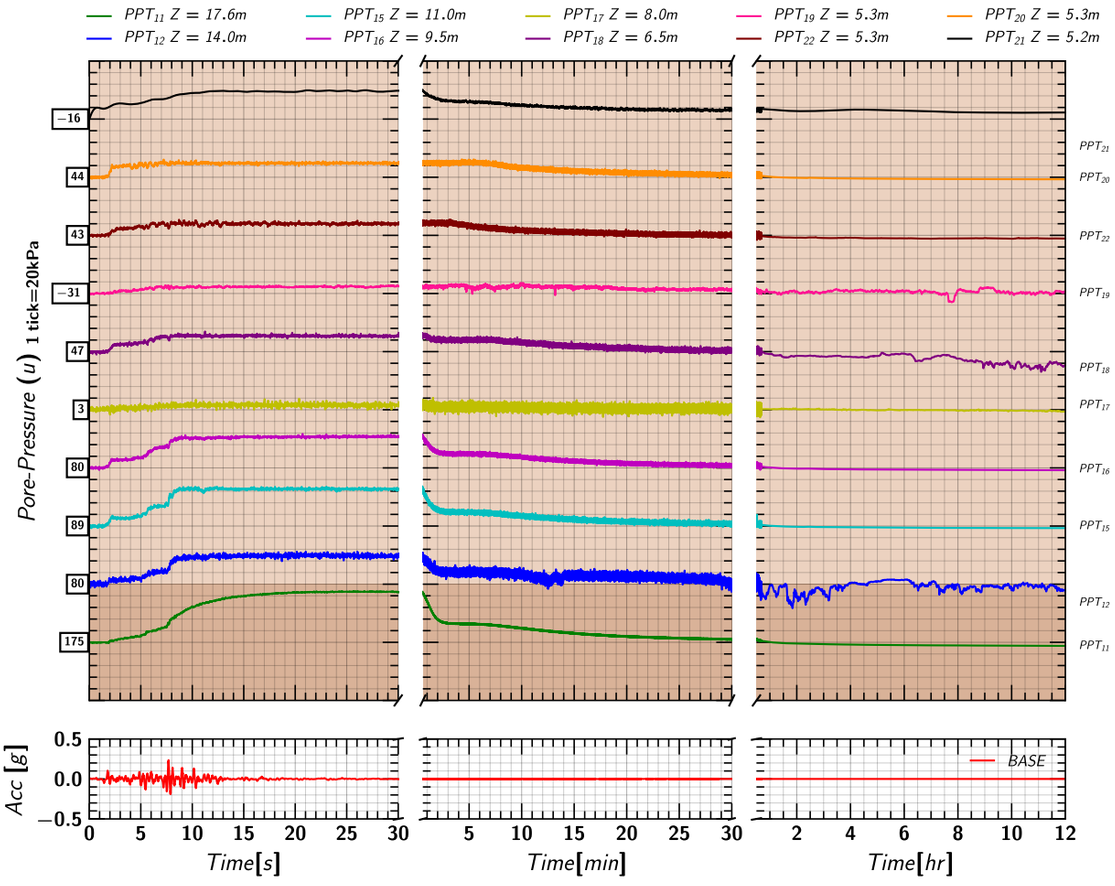

Figure 126. EQM₃: Pore pressure measurements in soil from MS54XXX transducers during and post the applied earthquake motion.

E.8 Excess Pore pressures Ratio (r_u) Estimated from Keller Transducers

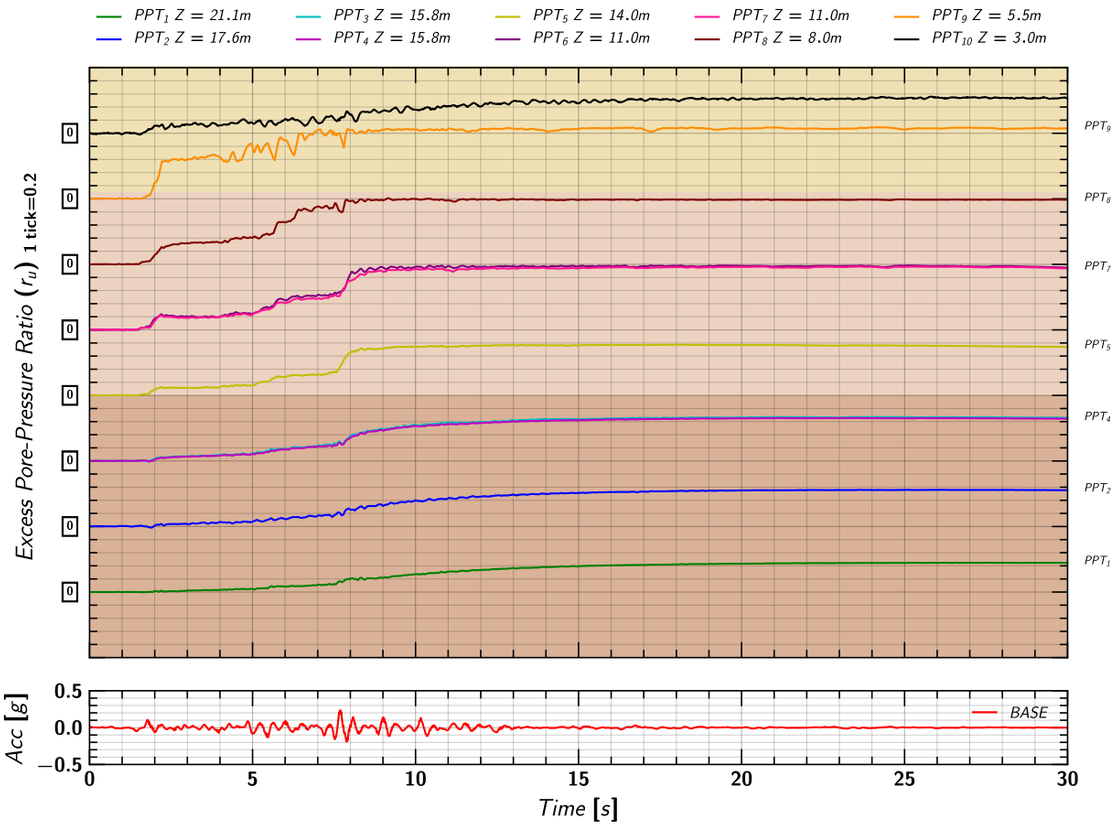

Figure 127. EQM3: Excess pore pressure ratio (r_u) estimated from measurements by Keller transducers during the applied earthquake motion.

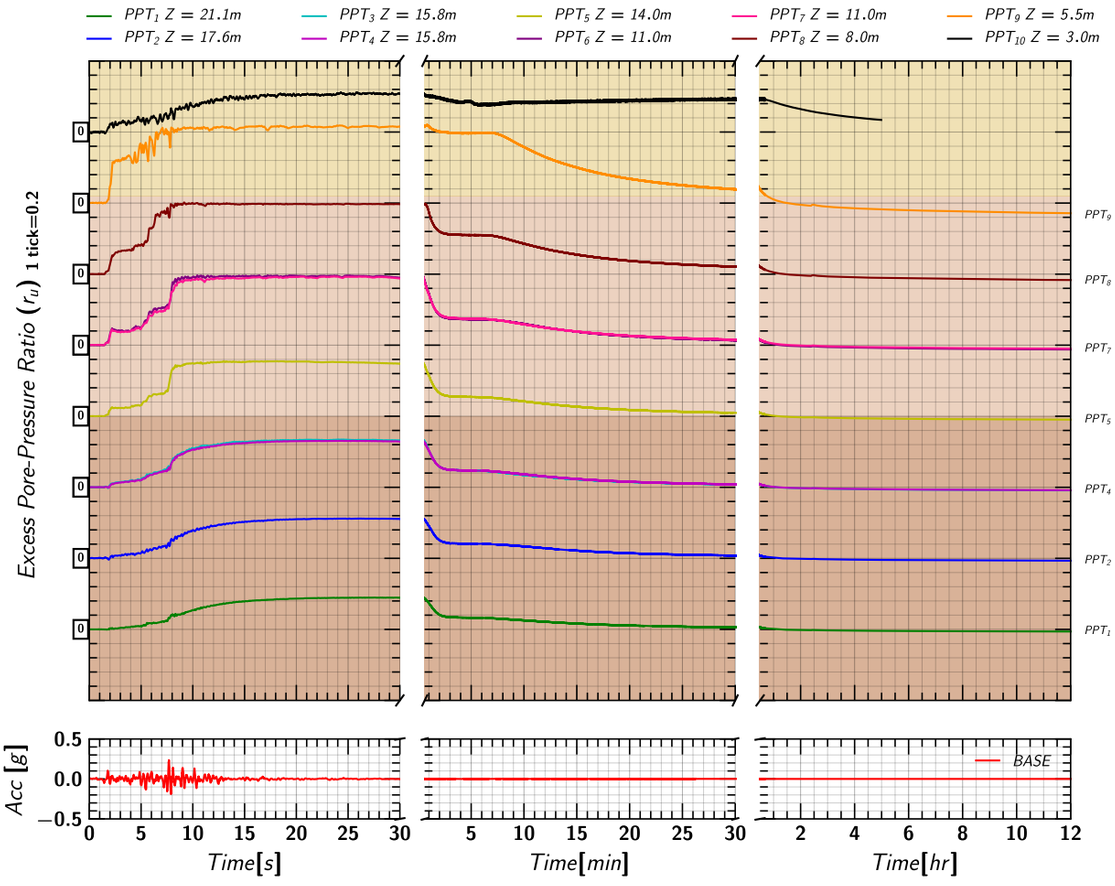

Figure 128. EQM3: Excess pore pressure ratio (r_u) estimated from measurements by Keller transducers during and post the applied earthquake motion.

E.9 Excess Pore pressure Ratio (r_u) Estimated from MS54XXX Transducers

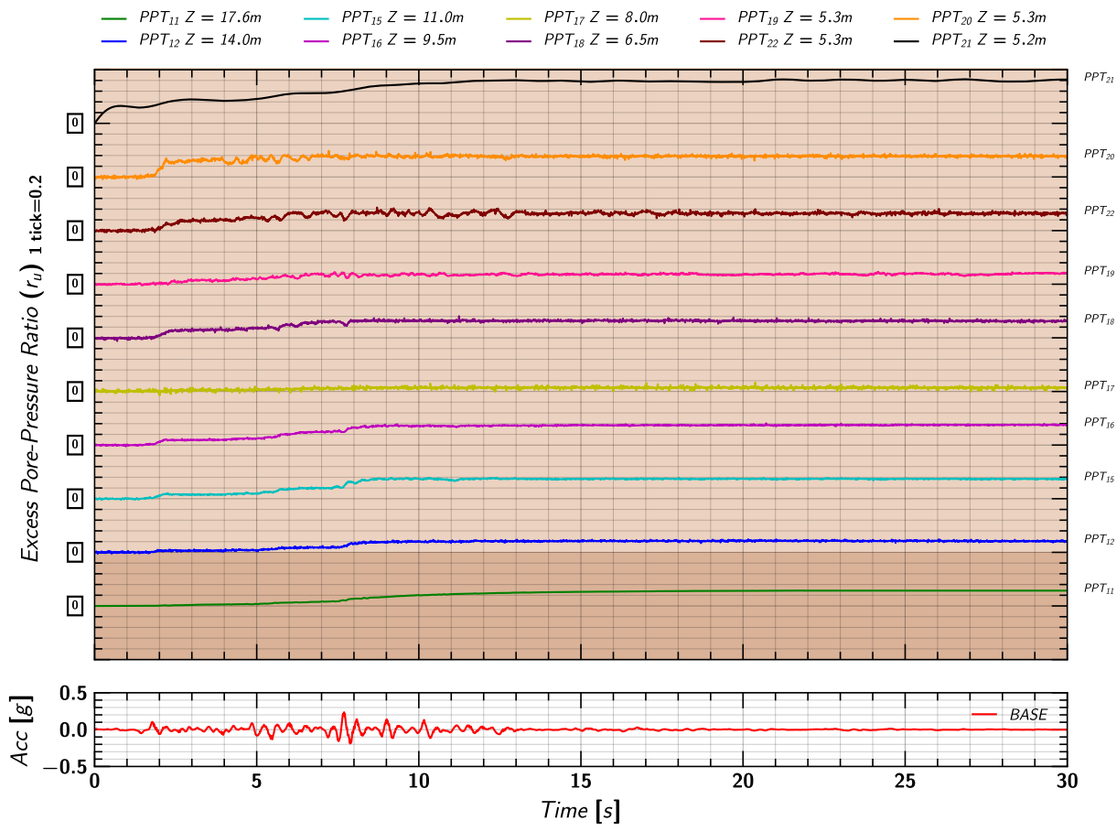

Figure 129. EQM3: Excess pore pressure ratio (r_u) estimated from measurements by MS54XXX transducers during the applied earthquake motion.

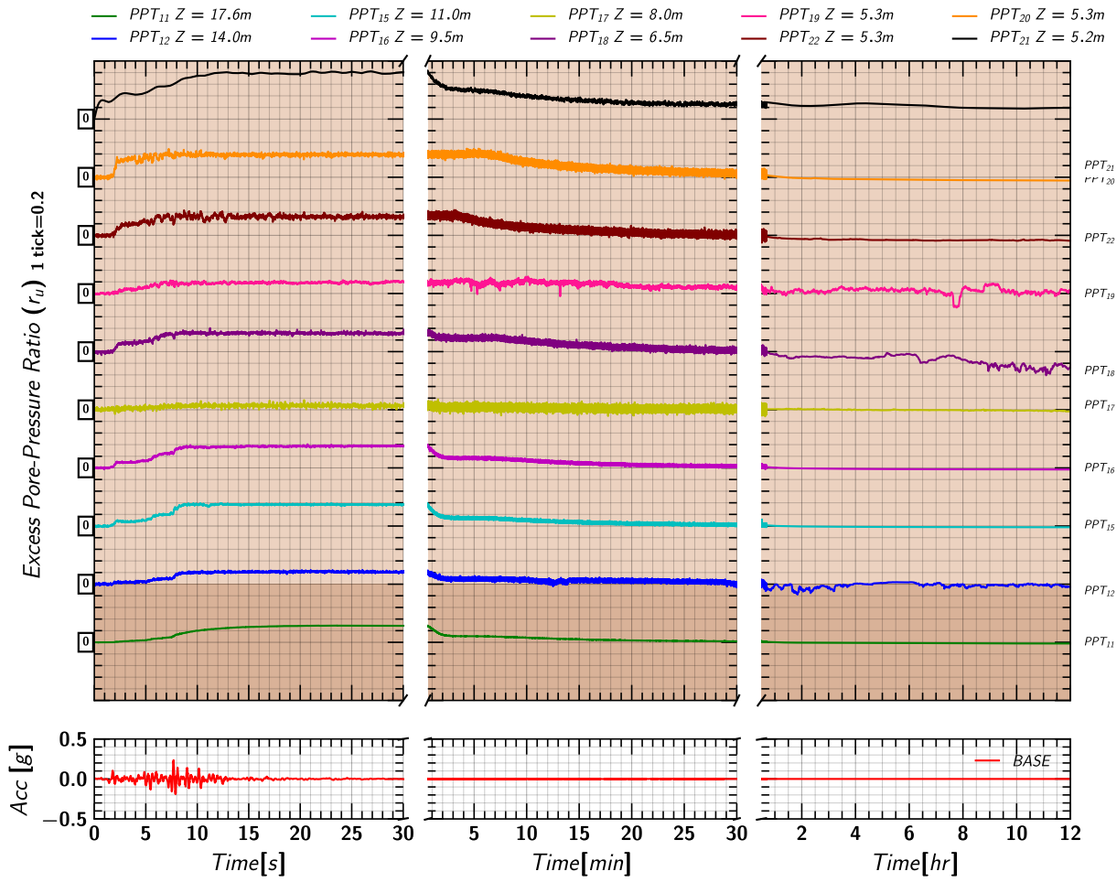

Figure 130. EQM3: Excess pore pressure ratio (r_u) estimated from measurements by MS54XXX transducers during and post the applied earthquake motion.

E.10 Axial Load in Pile 1

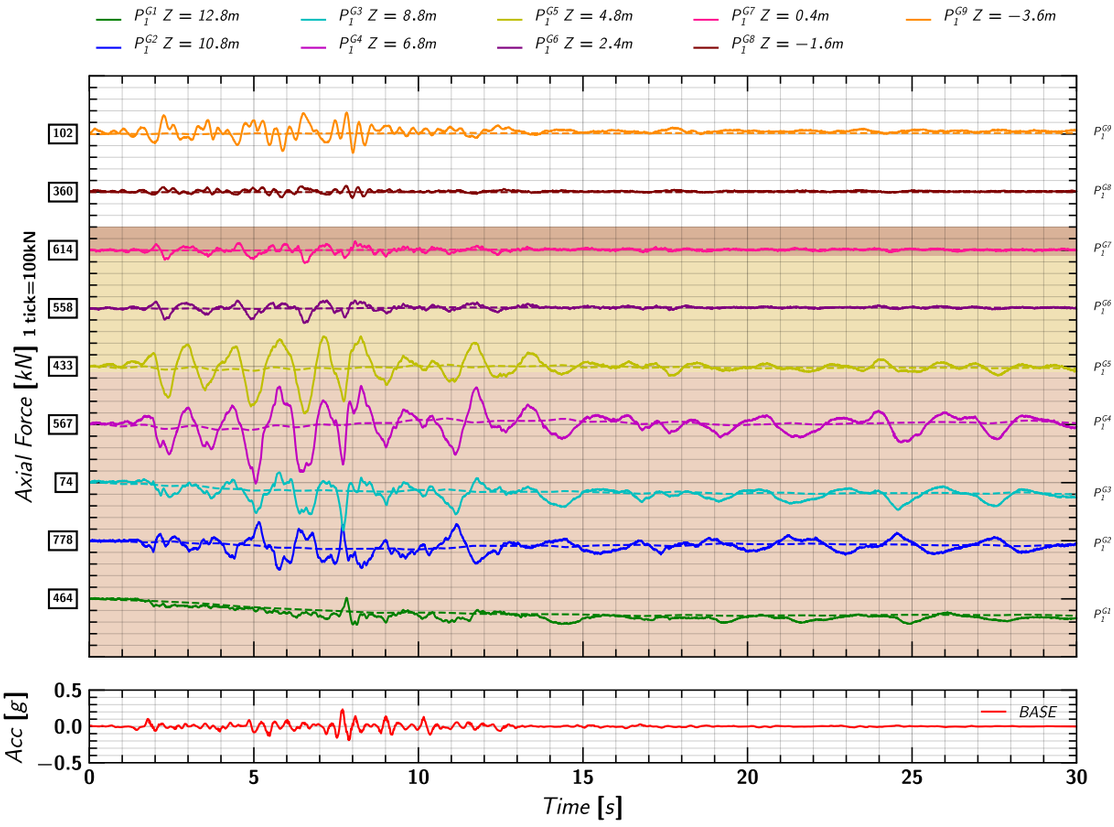

Figure 131. EQM3: Axial load measurements from pile 1 strain gages during the applied earthquake motion.

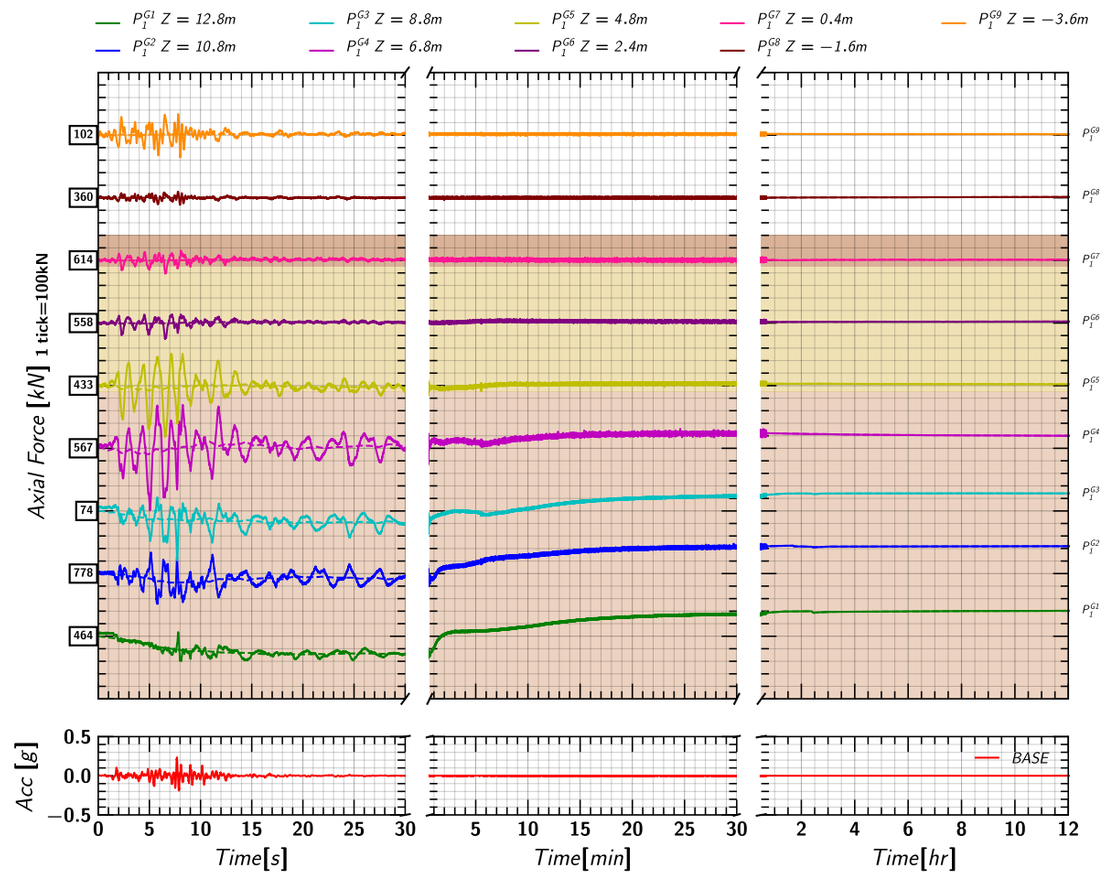

Figure 132. EQM3: Axial load measurements from pile 1 strain gages during and post the applied earthquake motion.

E.11 Axial Load in Pile 2

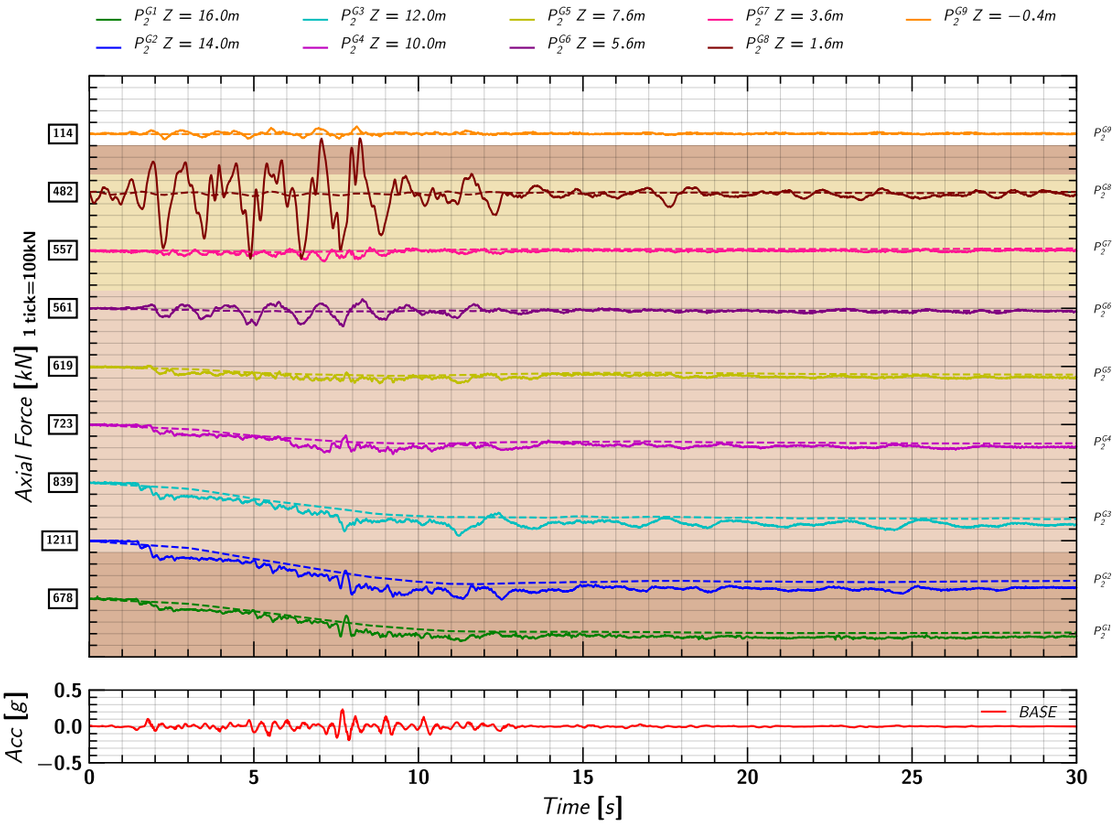

Figure 133. EQM3: Axial load measurements from pile 2 strain gages during the applied earthquake motion.

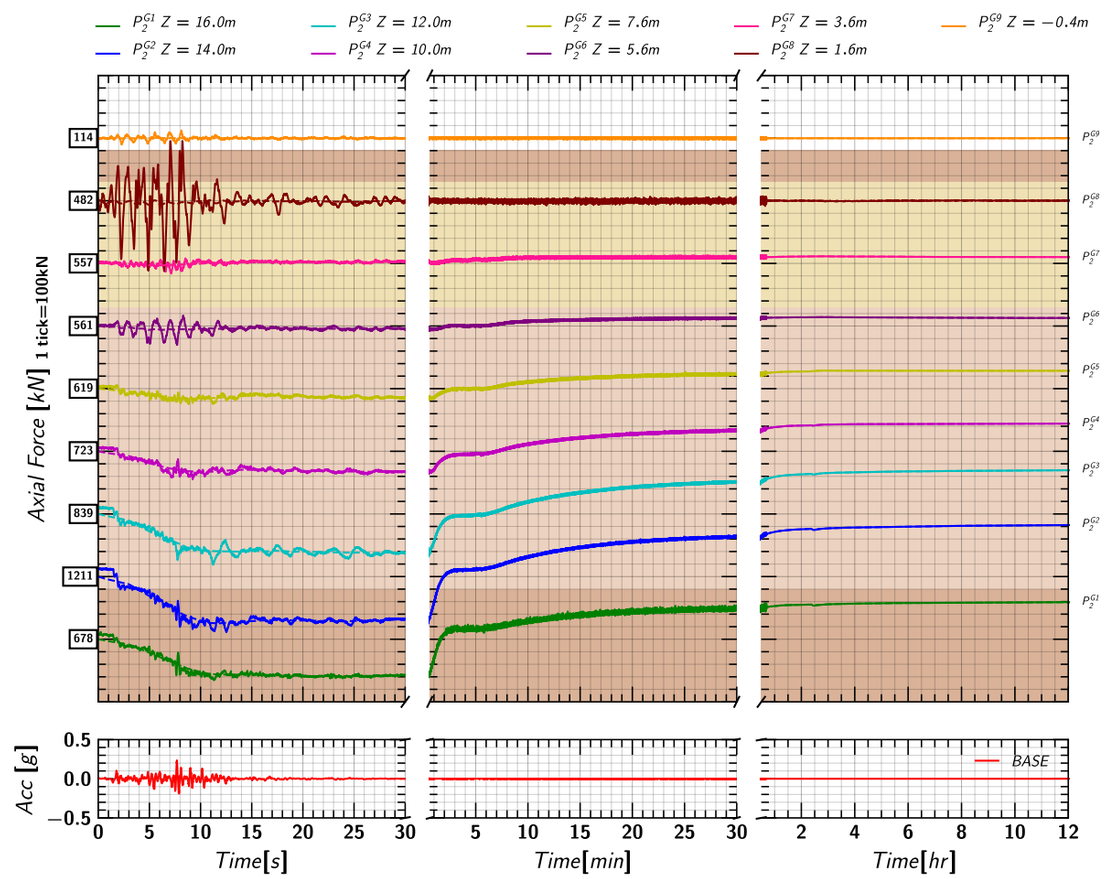

Figure 134. EQM3: Axial load measurements from pile 2 strain gages during and post the applied earthquake motion.

E.12 Pore pressure and Axial Load Profile

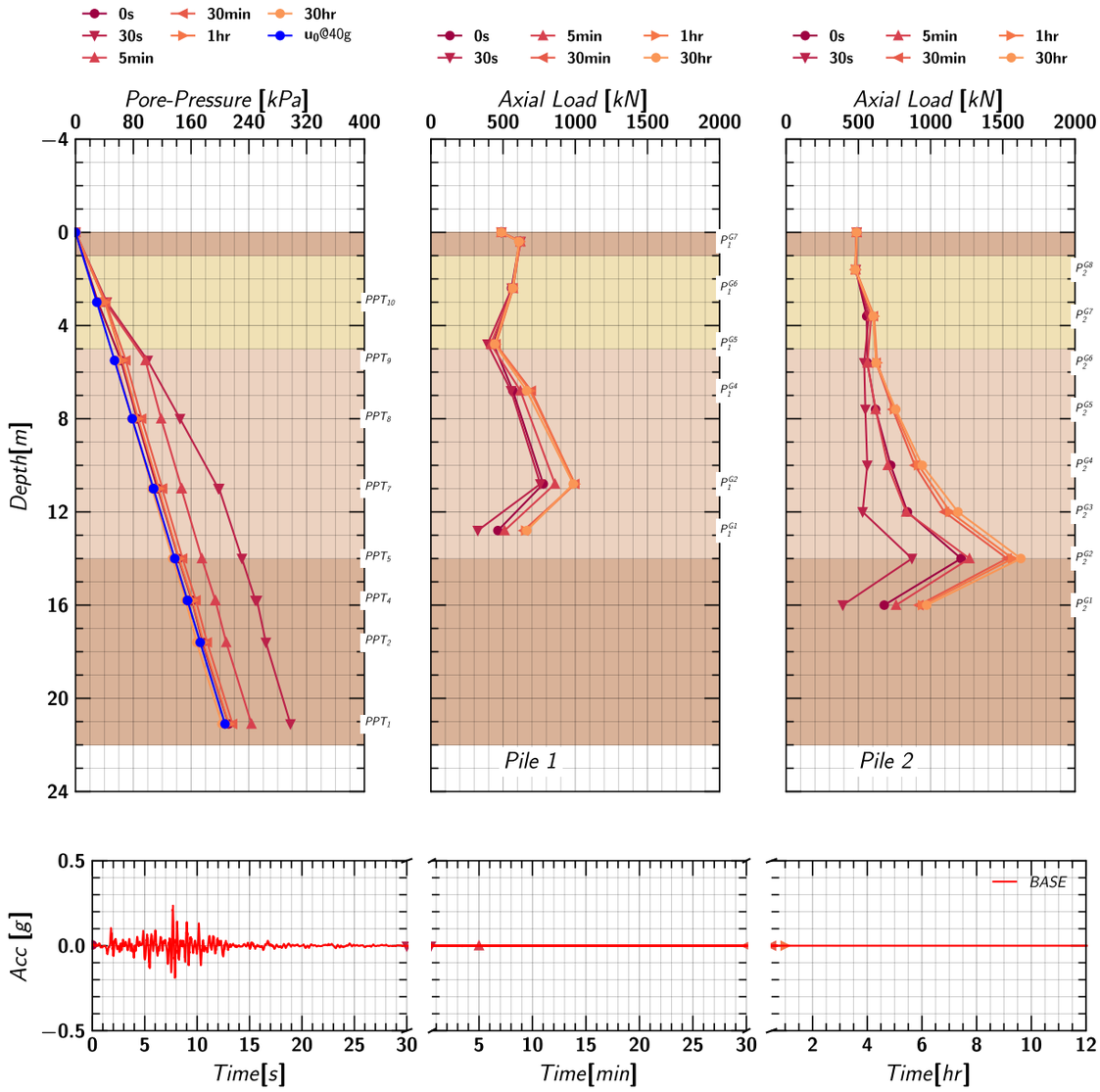

Figure 135. EQM3: Pore pressure and axial load profile in pile 1 and pile 2 at different times during and post the applied earthquake motion.

F. Day 2 Spin 1

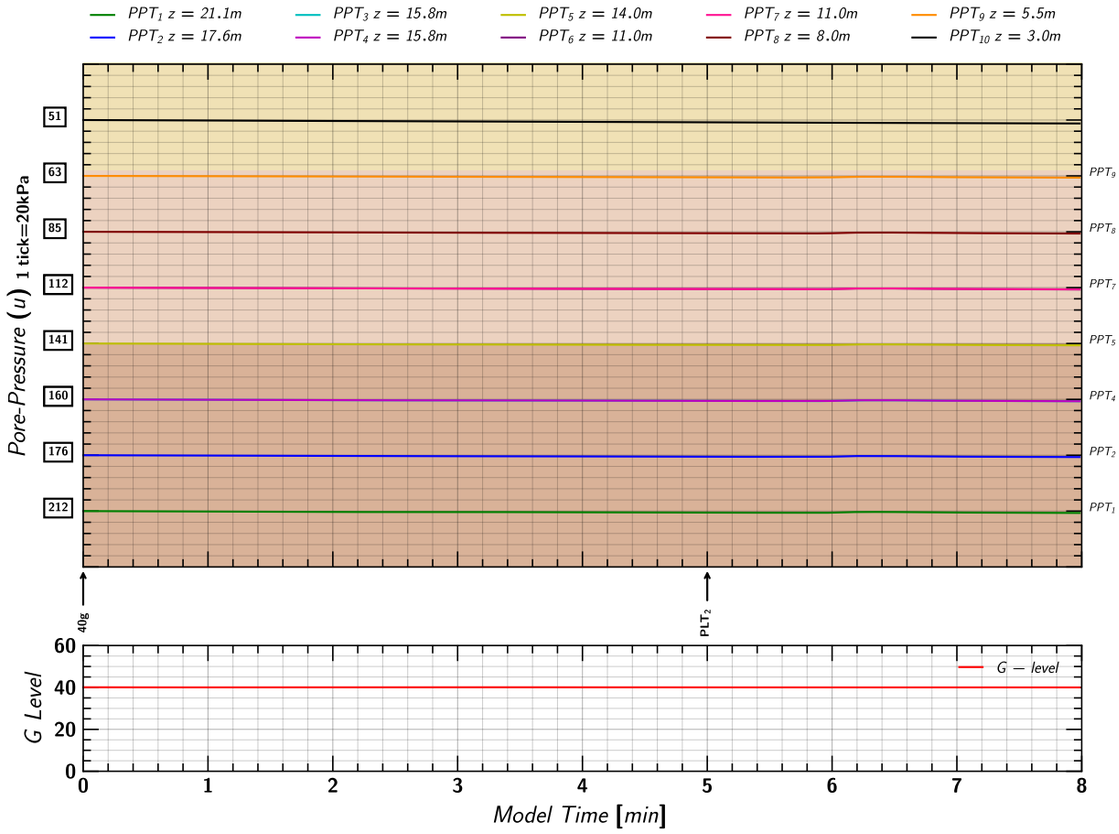

Figure 136. Day 2 Spin 1: Pore pressures measurements in soil from Keller transducers.

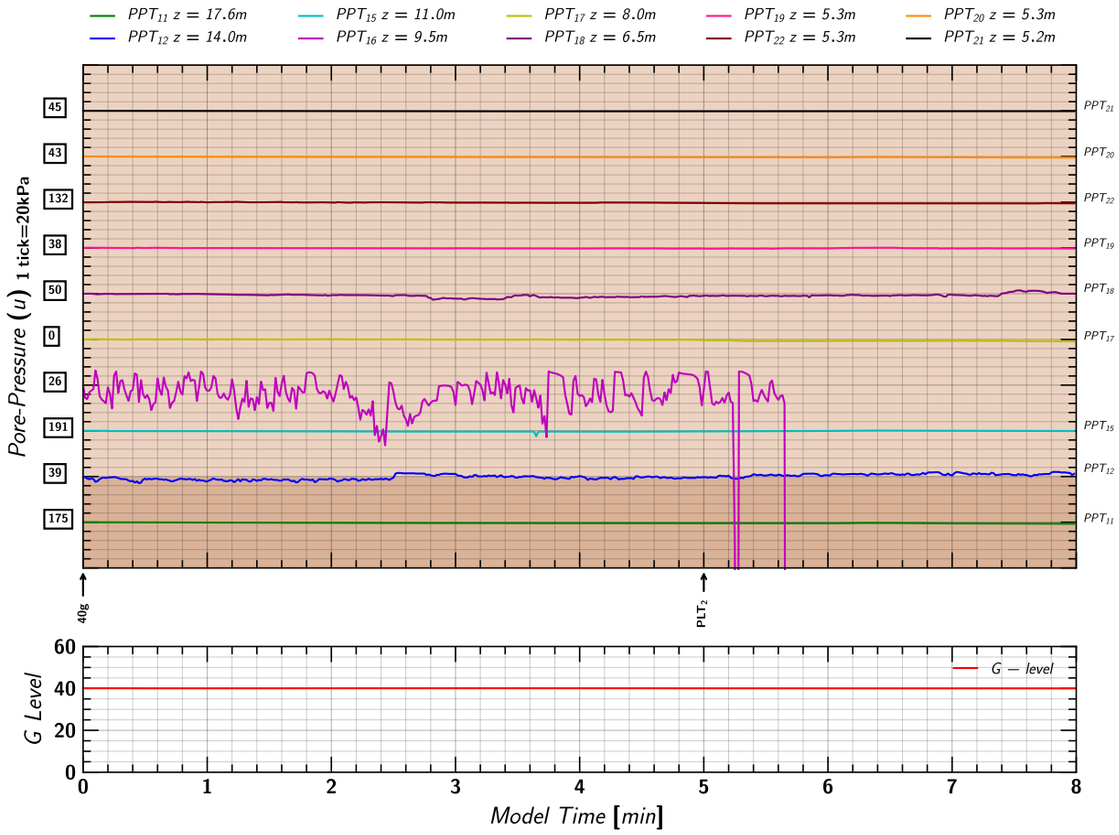

Figure 137. Day 2 Spin 1: Pore pressures measurements in soil from MS54XXX transducers.

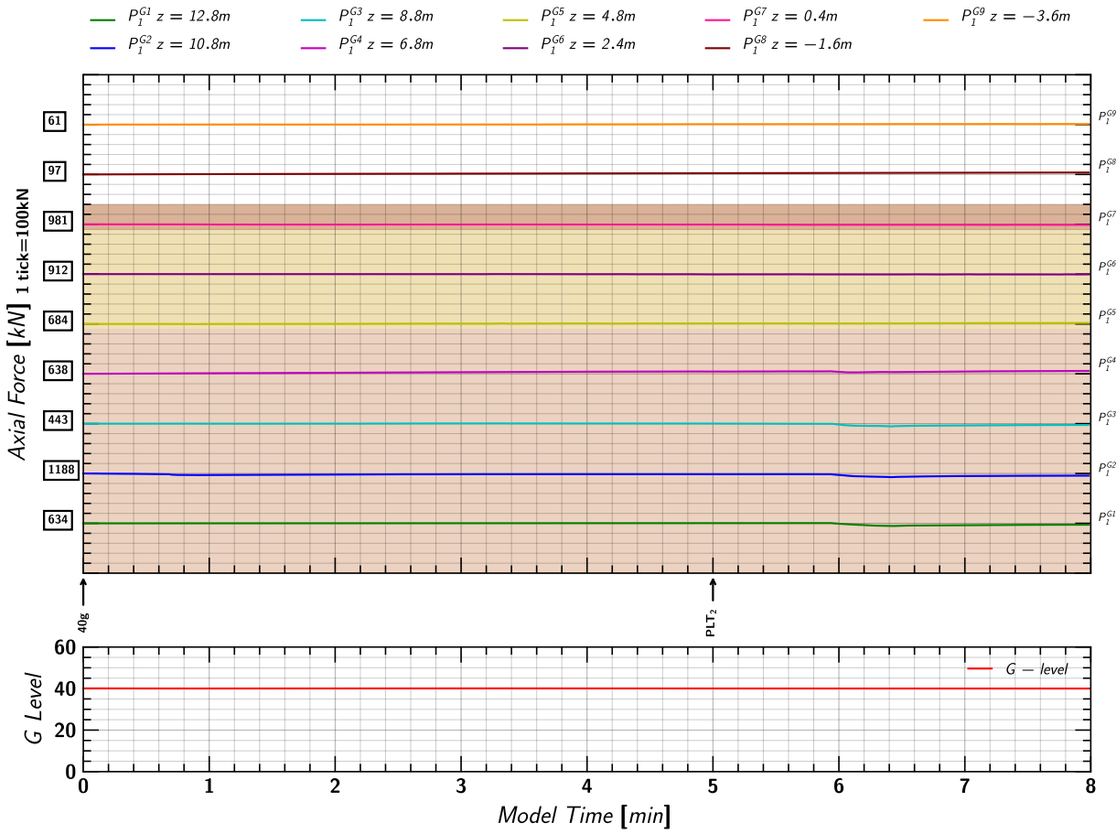

Figure 138. Day 2 Spin 1: Axial load measurements in Pile 1.

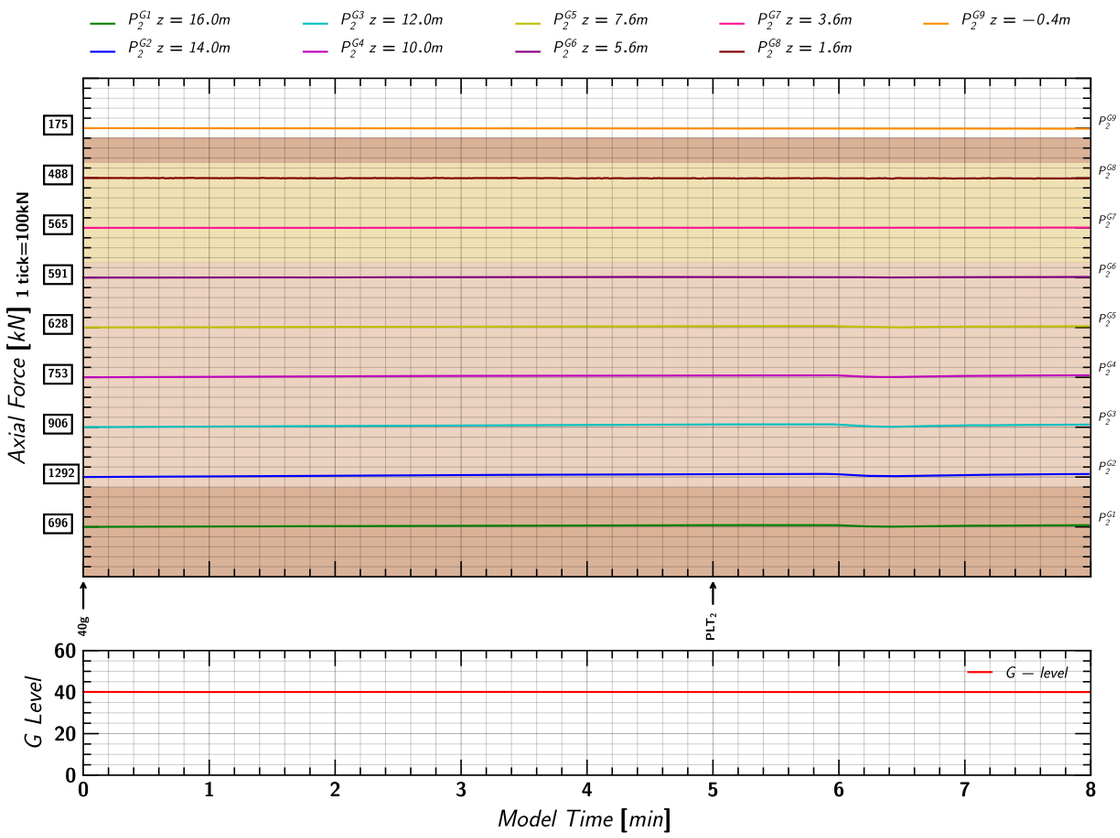

Figure 139. Day 2 Spin 1: Axial load measurements in Pile 2.

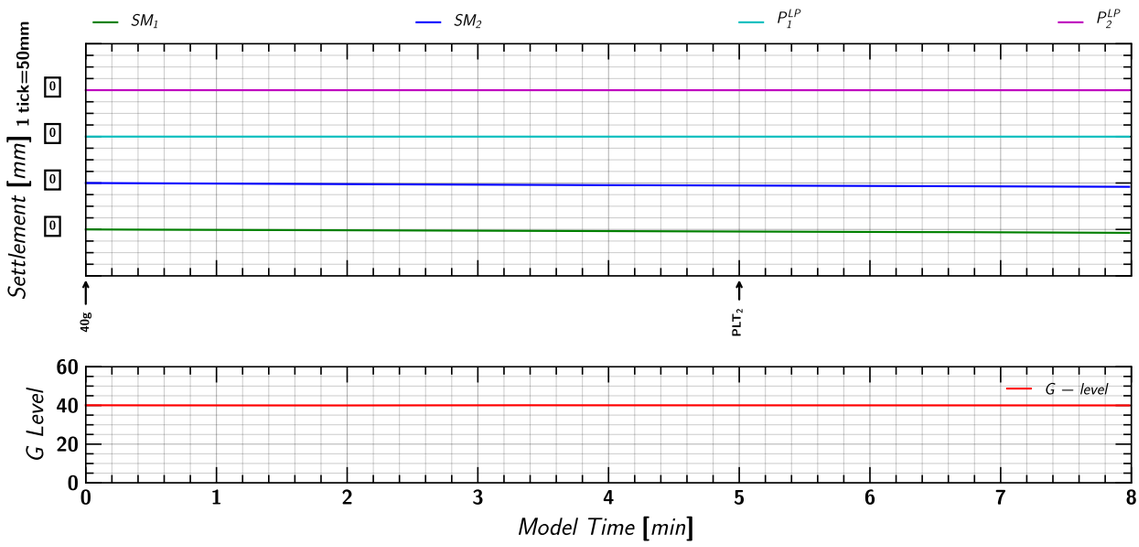

Figure 140. Day 2 Spin 1: Settlement measurements of soil and pile from linear potentiometers.

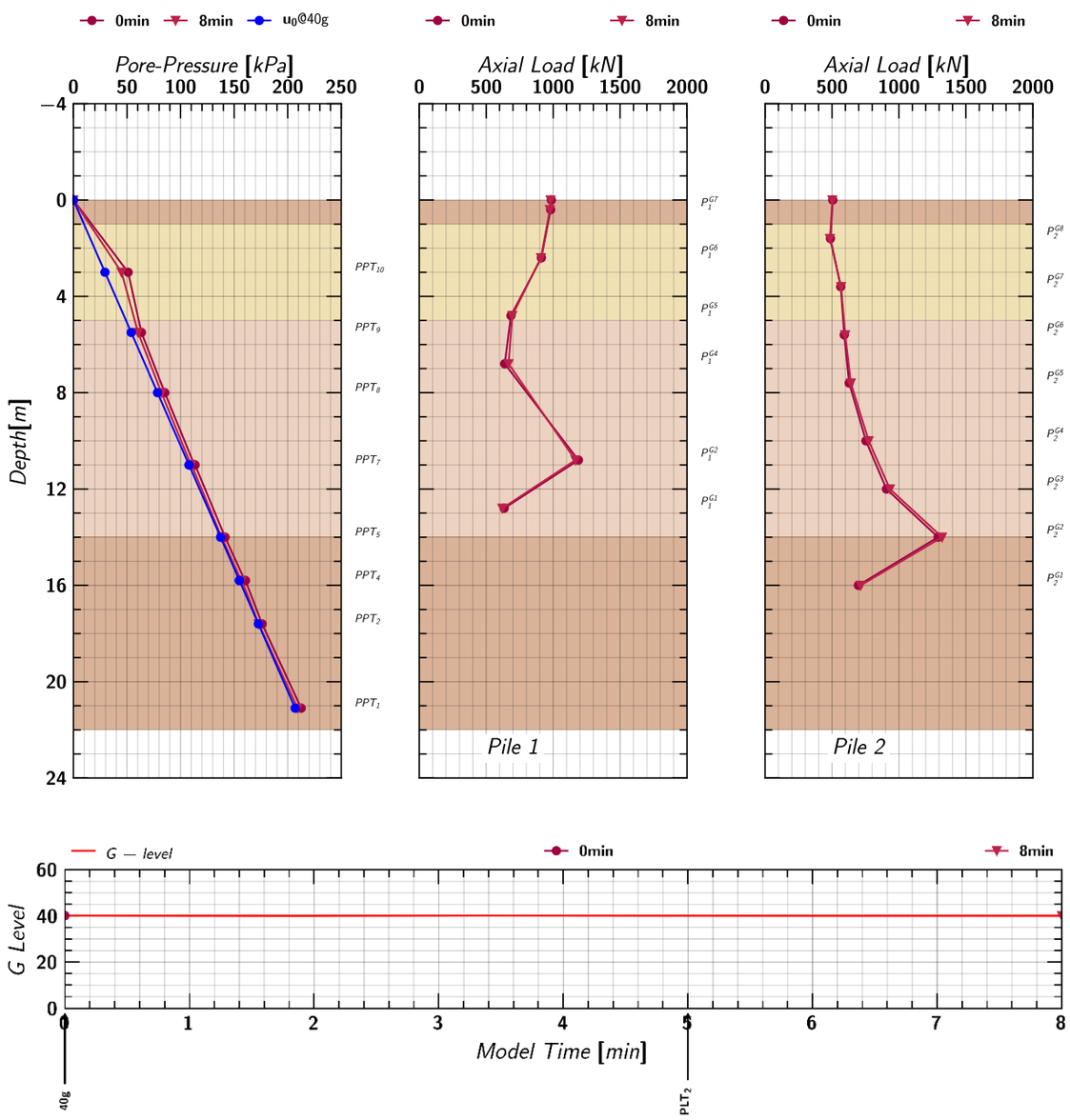

Figure 141. Day 2 Spin 1: Axial load profile of pile 1 and pile 2 at different times during the test.

G. Day 2 Spin 2

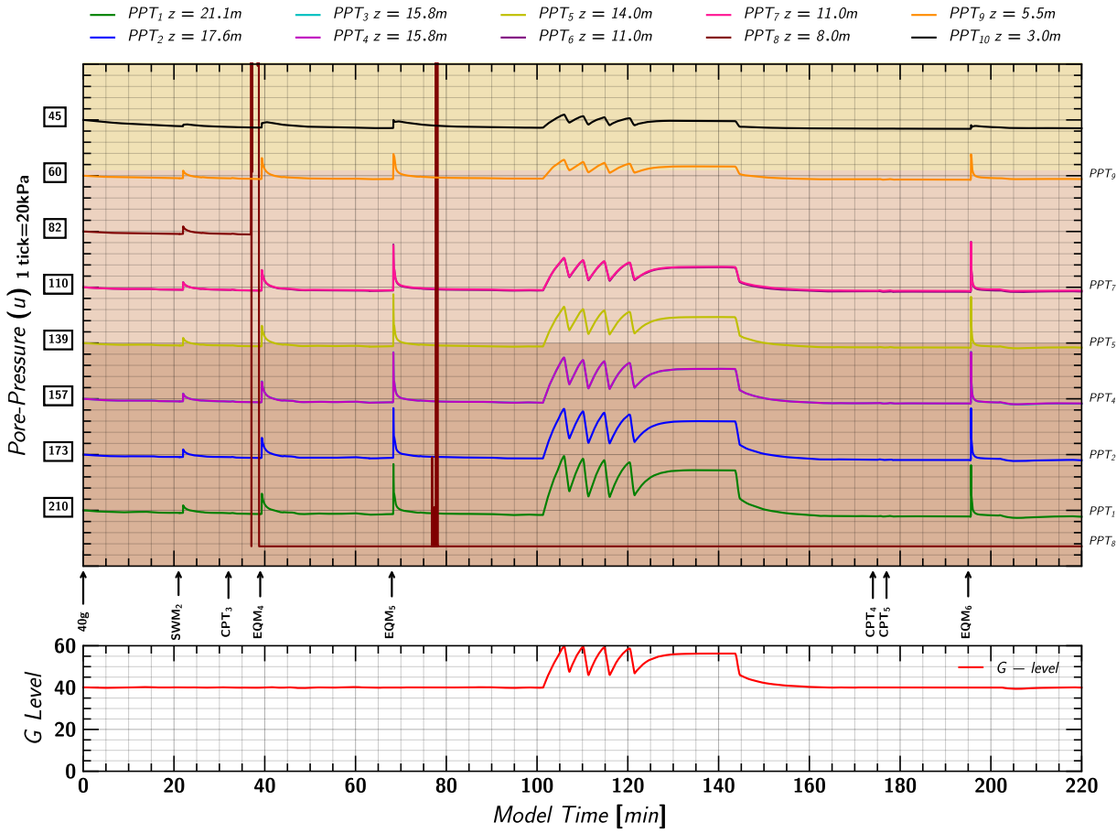

Figure 142. Day 2 Spin 2: Pore pressures measurements in soil from Keller transducers.

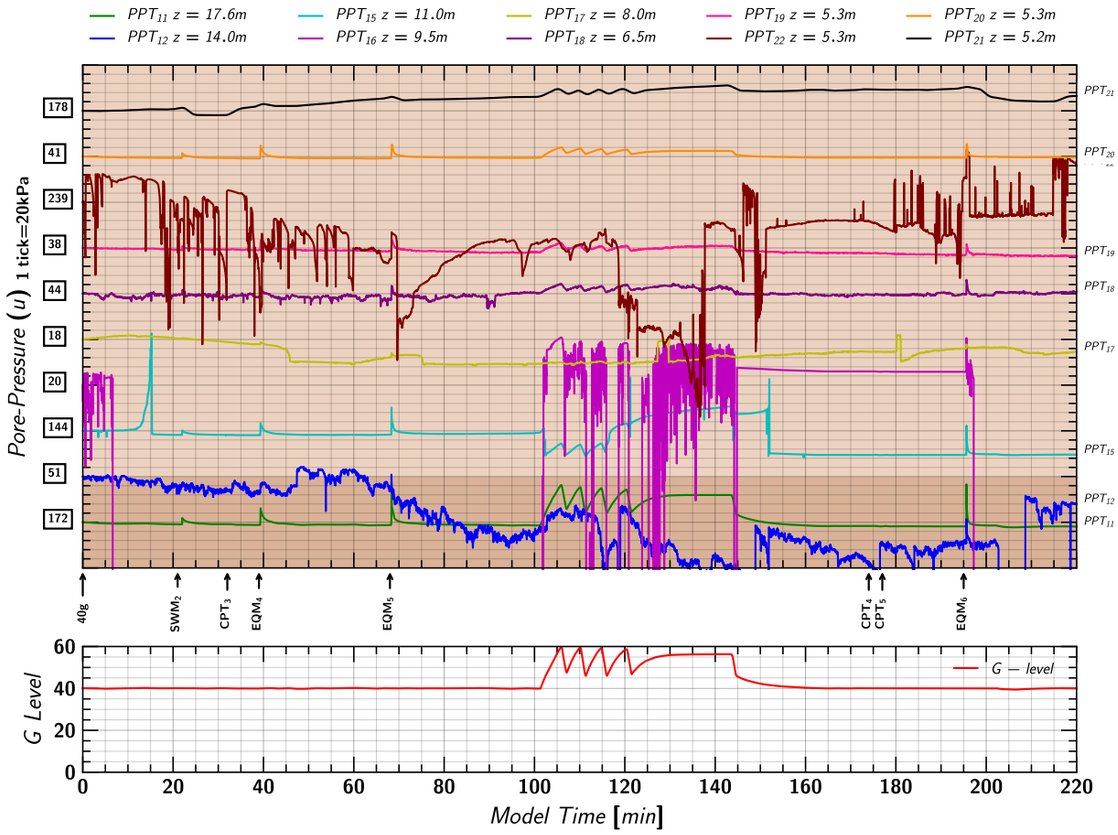

Figure 143. Day 2 Spin 2: Pore pressures measurements in soil from MS54XXX transducers.

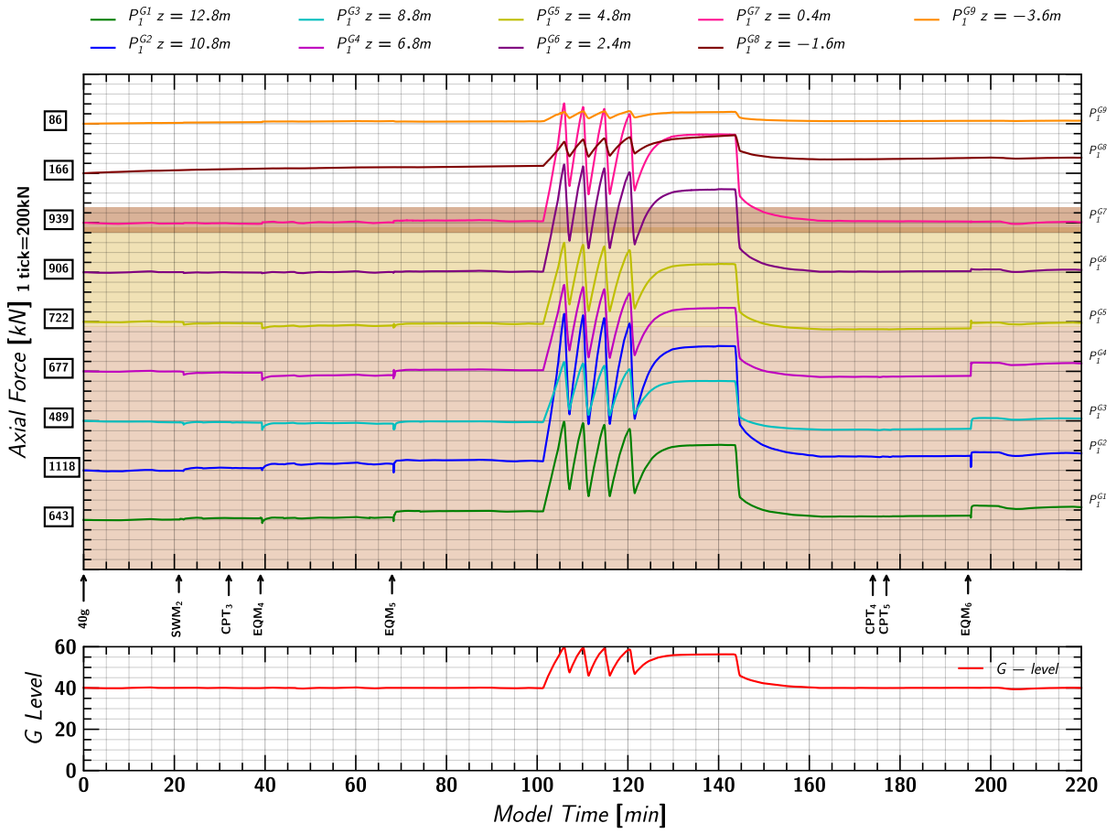

Figure 144. Day 2 Spin 2: Axial load measurements in Pile 1.

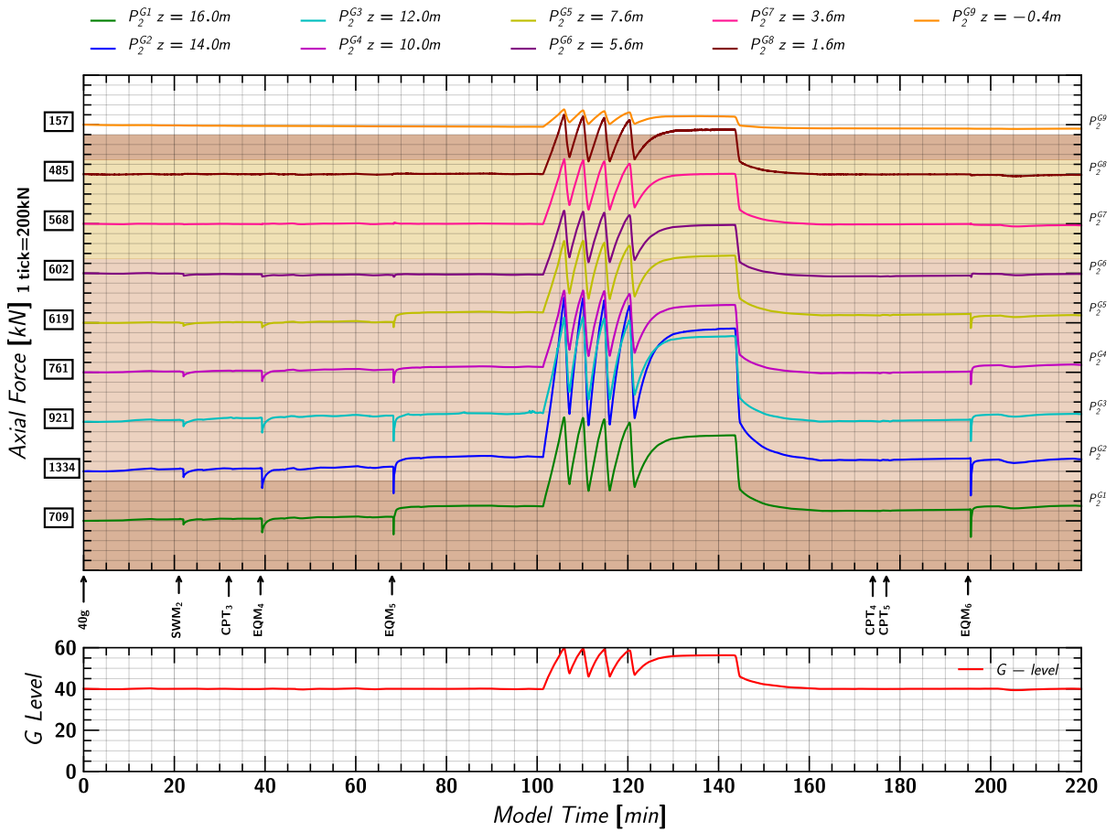

Figure 145. Day 2 Spin 2: Axial load measurements in Pile 2.

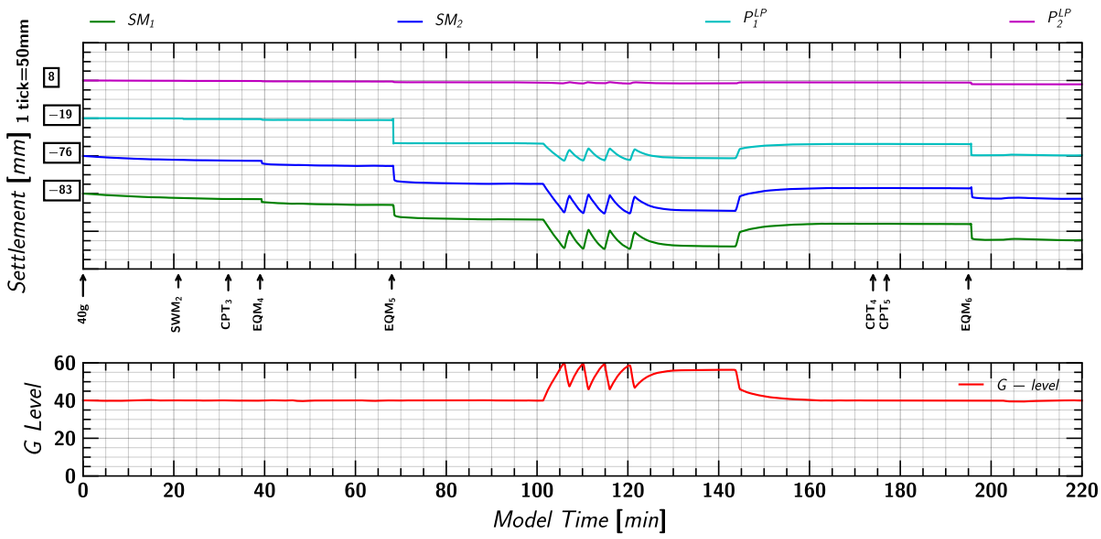

Figure 146. Day 2 Spin 2: Settlement measurements of soil and pile from linear potentiometers.

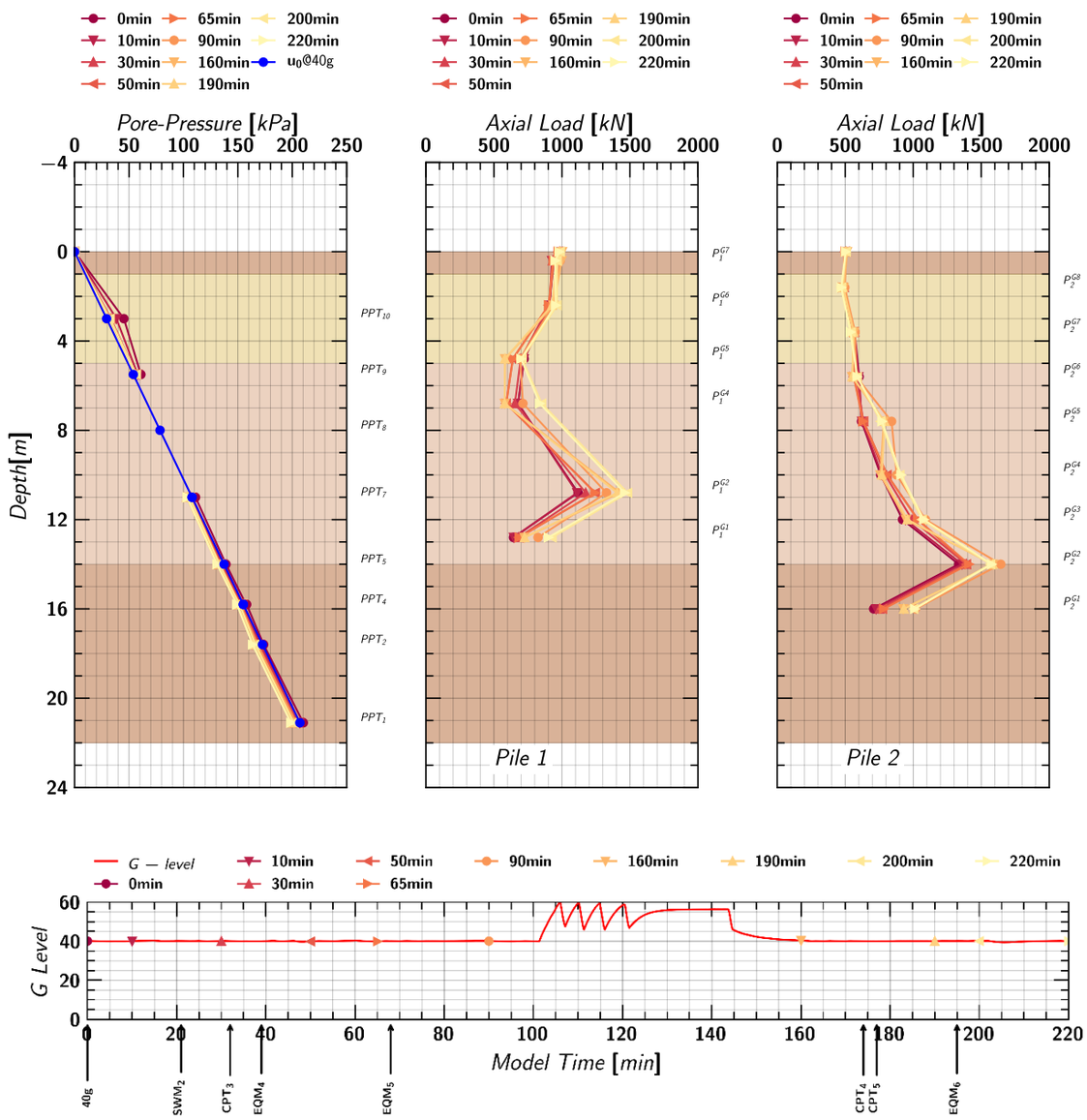

Figure 147. Day 2 Spin 2: Axial load profile of pile 1 and pile 2 at different times during the test.

H. EQM4 - Medium Santa Cruz Earthquake Motion (PGA = 0.14g)

H.1 Input Motion

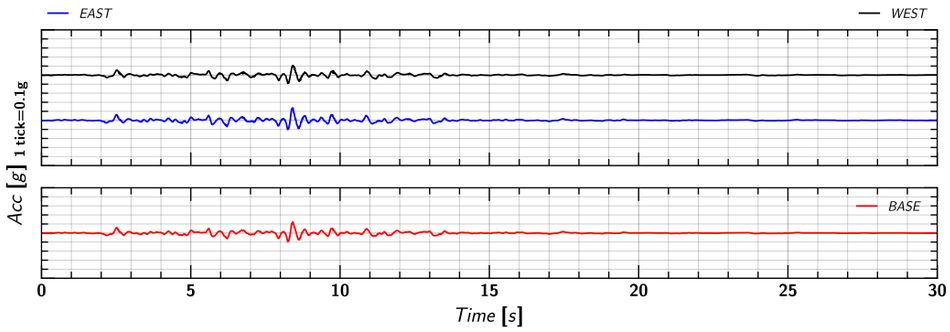

Figure 148. EQM4: Input motion.

H.2 Acceleration in Container

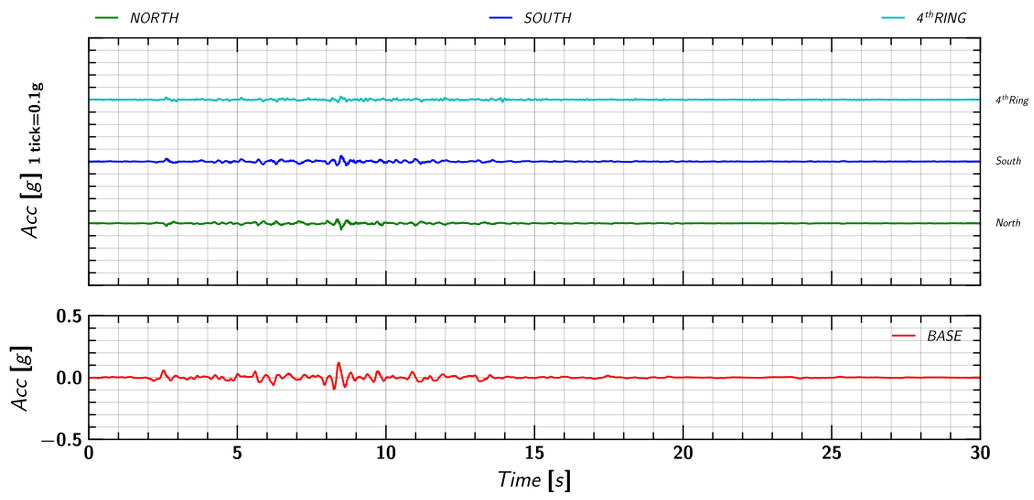

Figure 149. EQM4: Acceleration measurement on container.

H.3 Acceleration in Soil

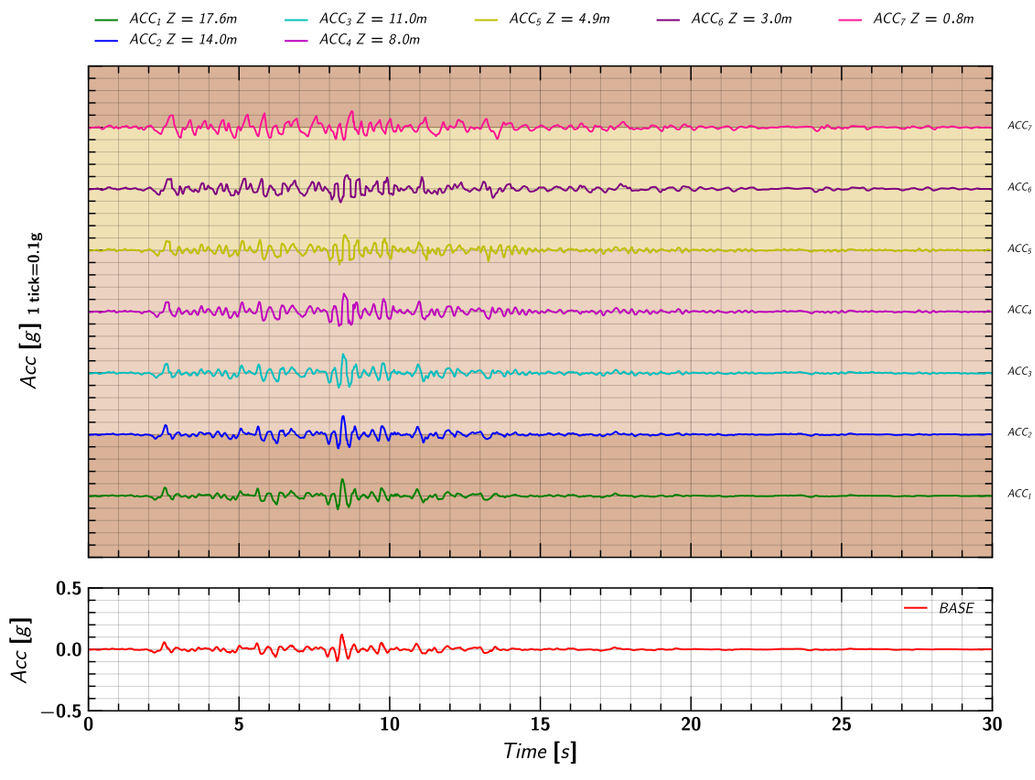

Figure 150. EQM4: Acceleration measurement in soil.

H.4 Acceleration in Pile

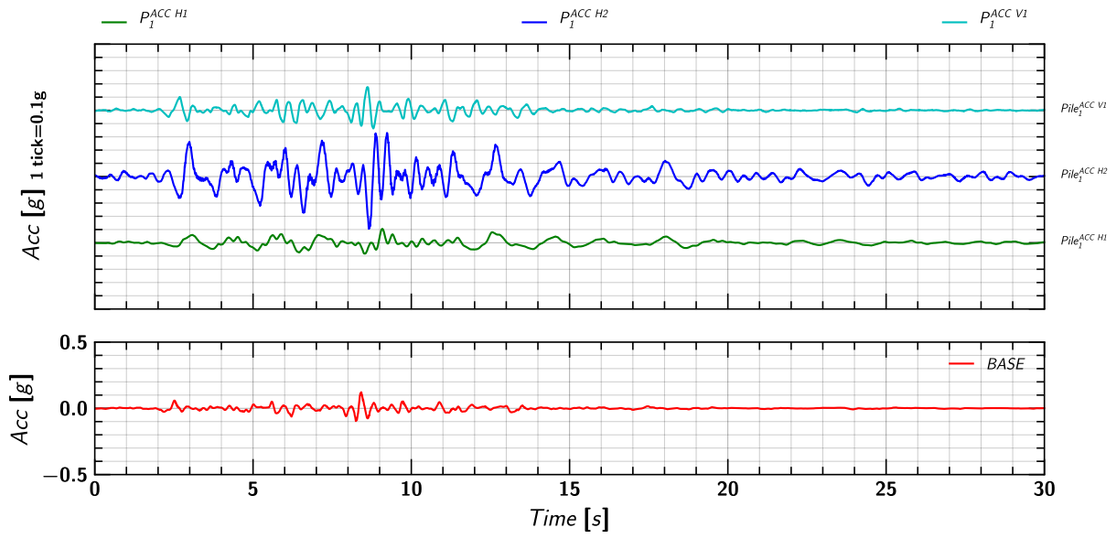

Figure 151. EQM₄: Acceleration measurement on pile 1.

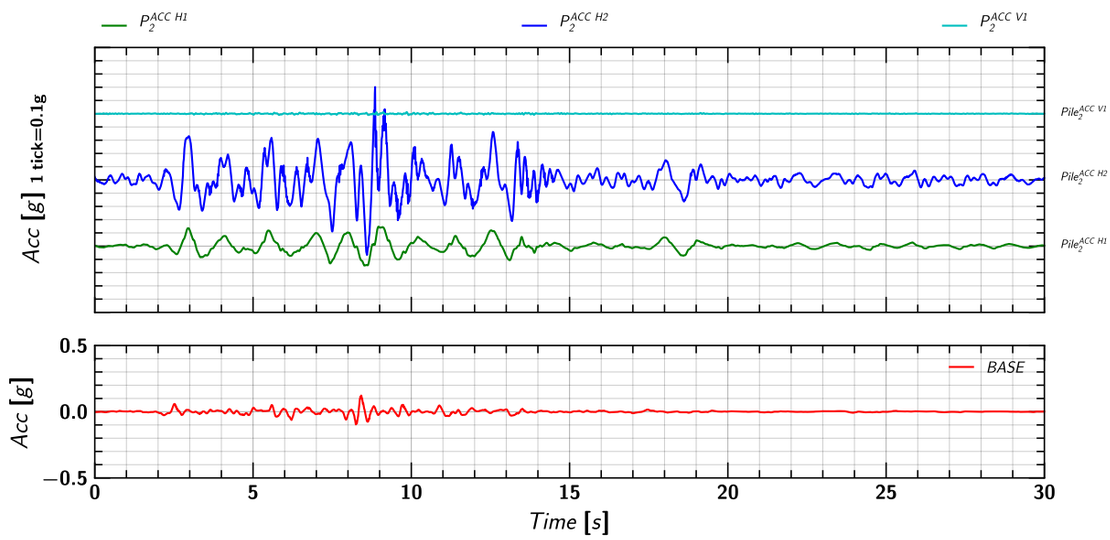

Figure 152. EQM₄: Acceleration measurement on pile 2.

H.5 Soil and Pile Settlement

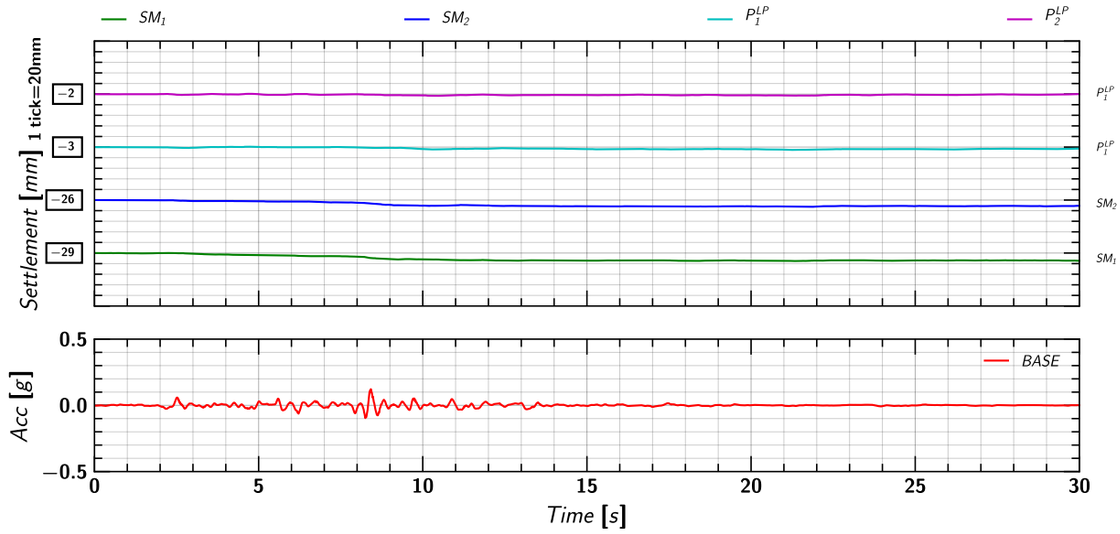

Figure 153. EQM4: Settlement measurement in soil and pile during the applied earthquake motion.

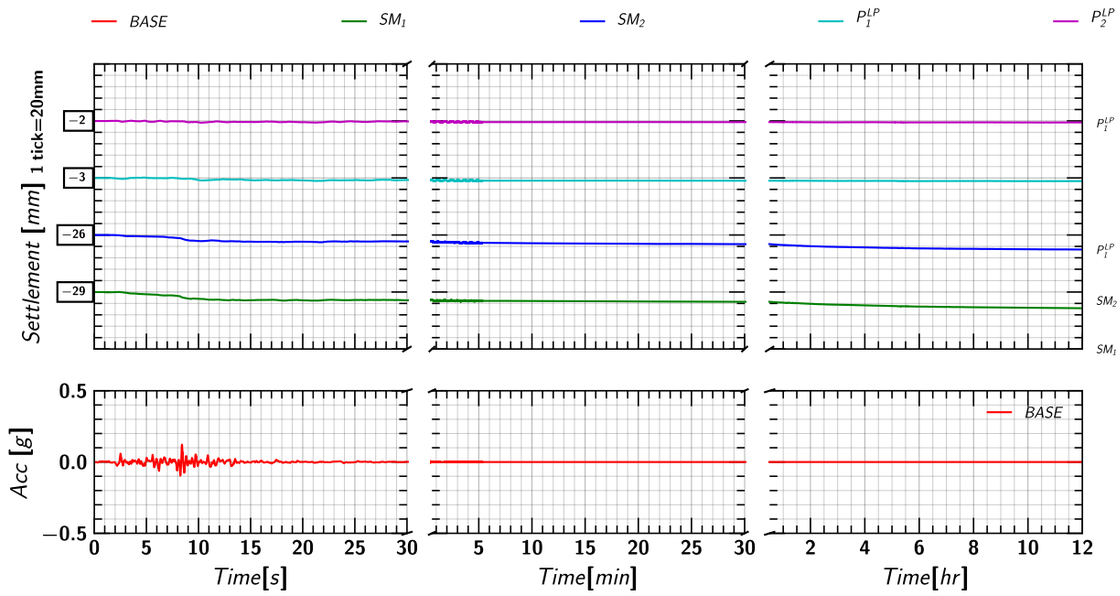

Figure 154. EQM4: Settlement measurement in soil and pile during and post applied earthquake motion.

H.6 Pore pressure measurements in Soil (Keller Transducers)

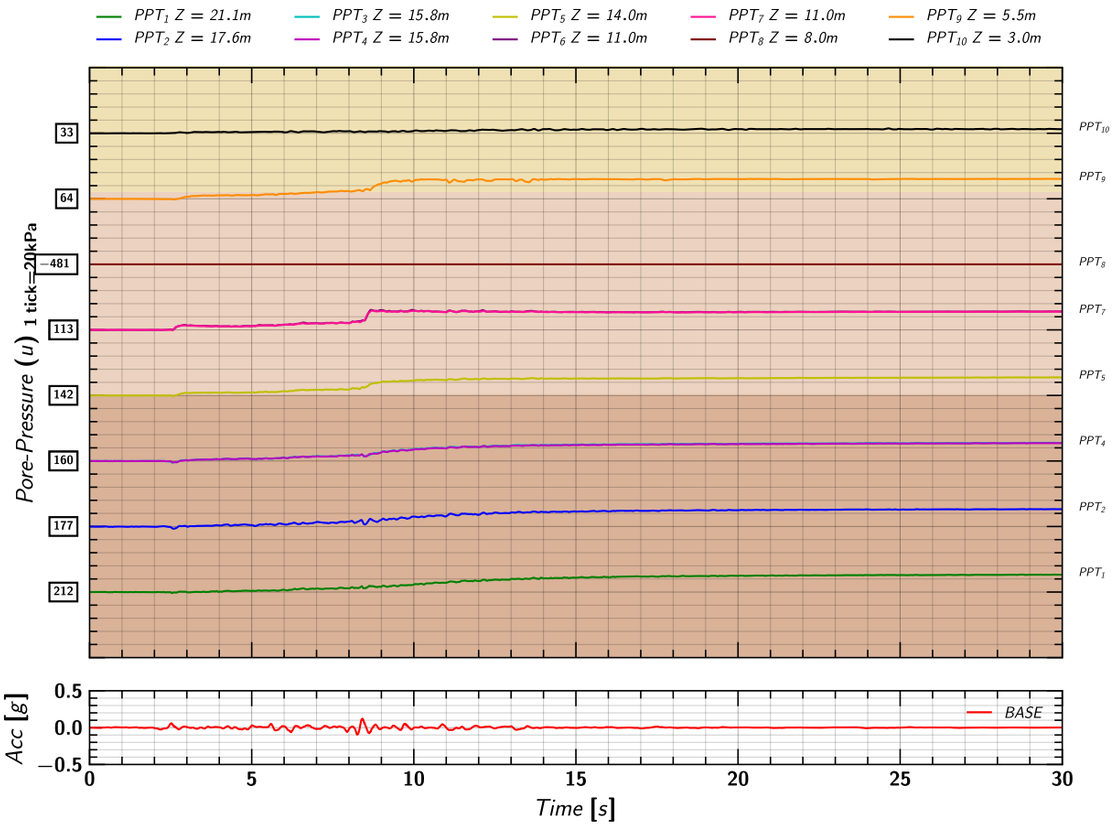

Figure 155. EQM4: Pore pressure measurements in soil from Keller transducers during the applied earthquake motion.

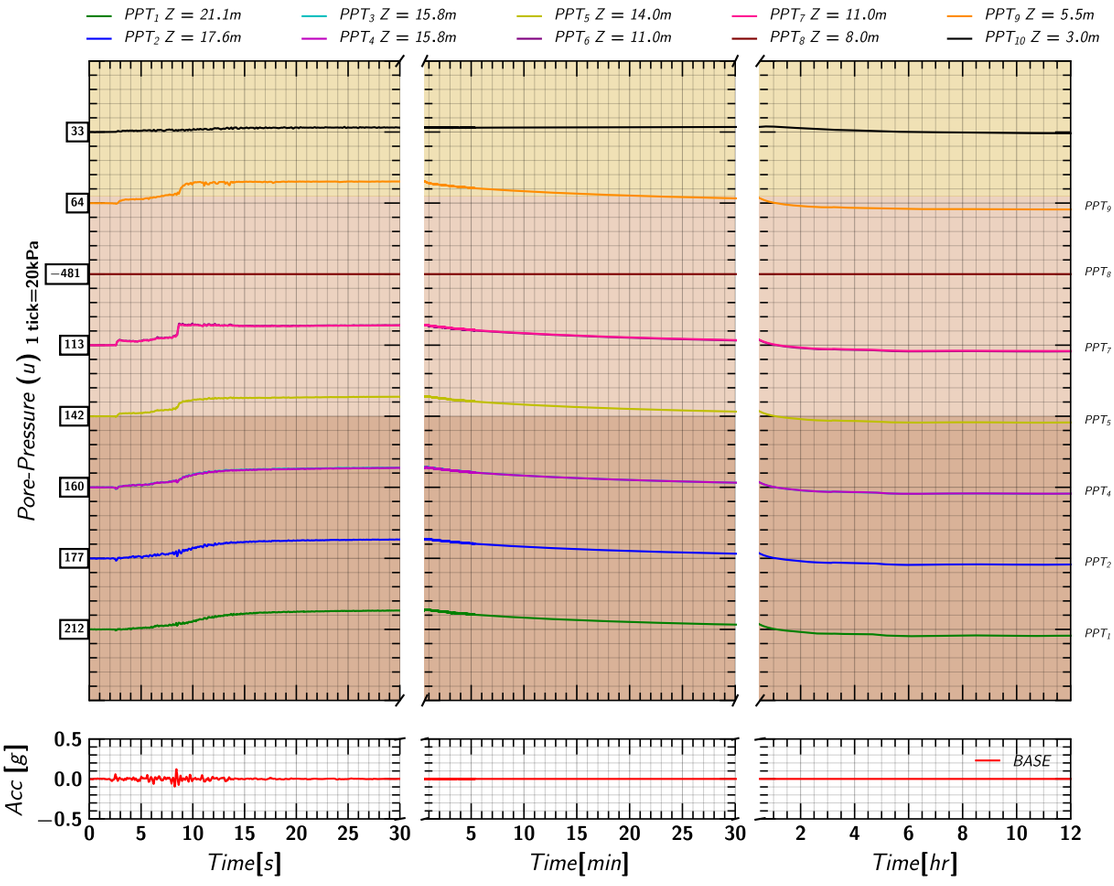

Figure 156. EQM4: Pore pressure measurements in soil from Keller transducers during and post the applied earthquake motion.

H.7 Pore pressure measurements in Soil (MS54XXX Transducers)

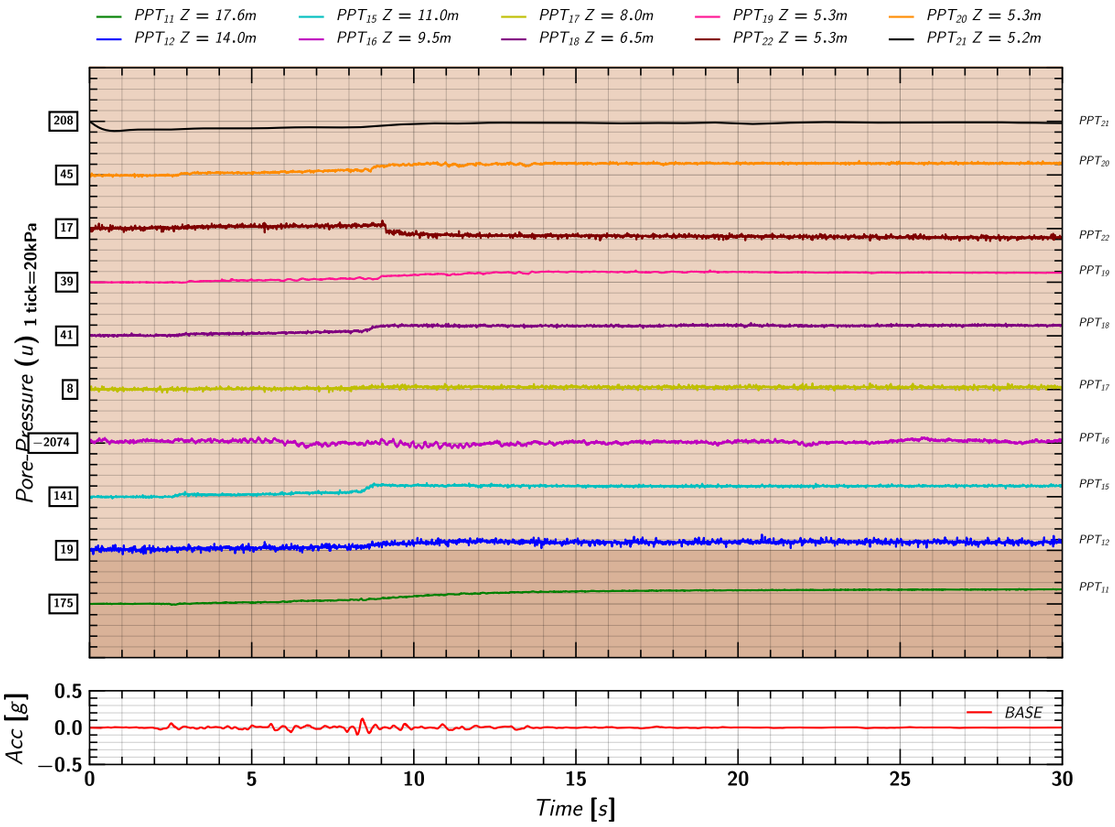

Figure 157. EQM$_4$: Pore pressure measurements in soil from MS54XXX transducers during the applied earthquake motion.

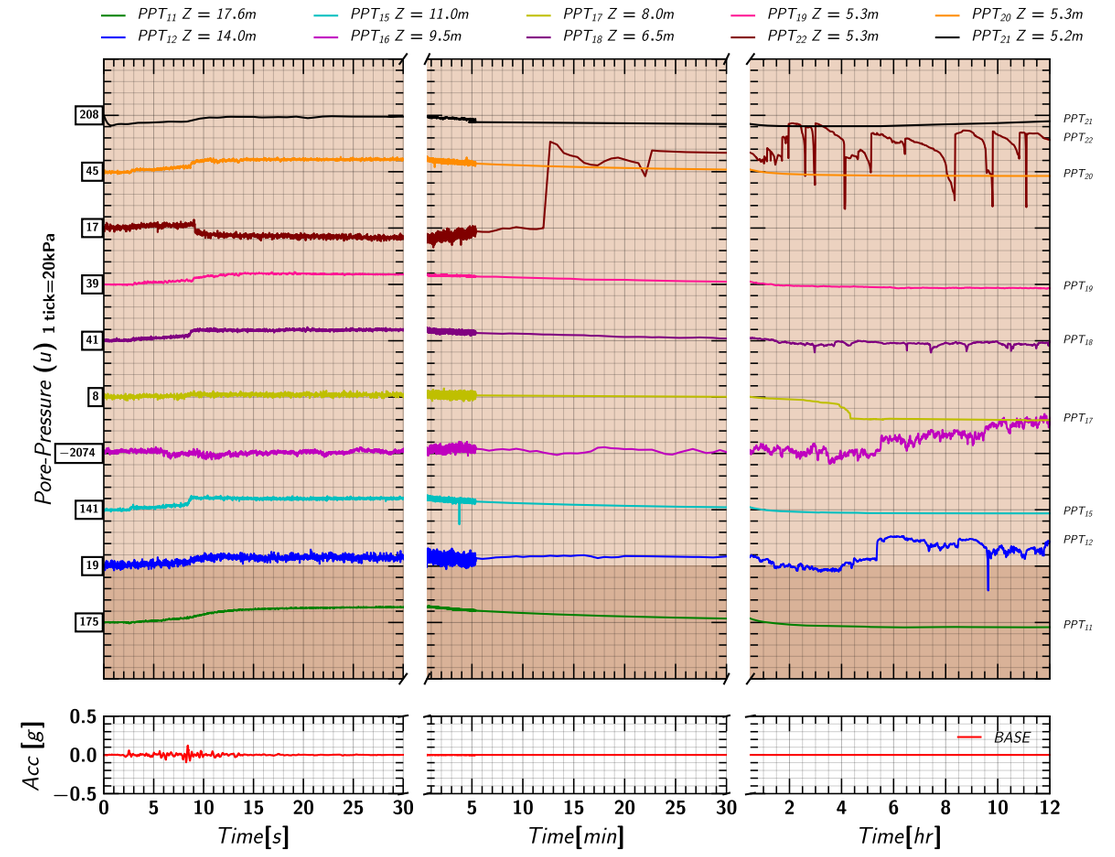

Figure 158. EQM$_4$: Pore pressure measurements in soil from MS54XXX transducers during and post the applied earthquake motion.

H.8 Excess Pore pressures Ratio (r_u) Estimated from Keller Transducers

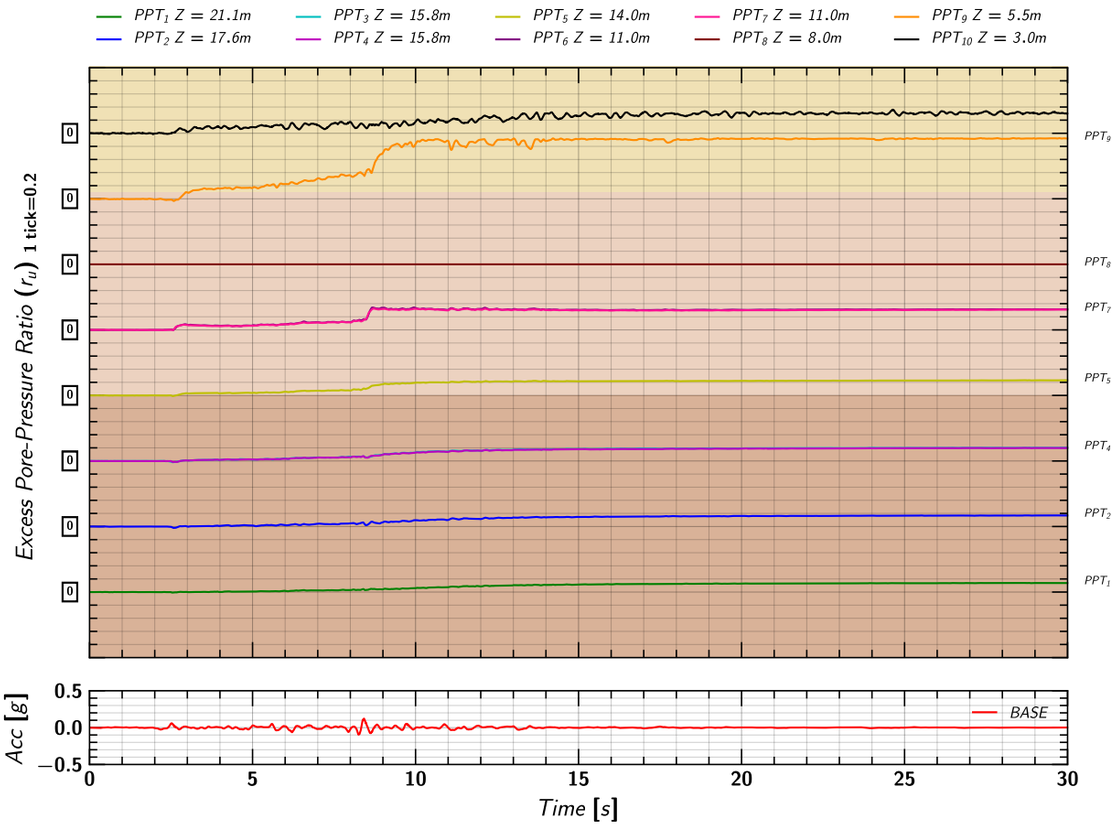

Figure 159. EQM4: Excess pore pressure ratio (r_u) estimated from measurements by Keller transducers during the applied earthquake motion.

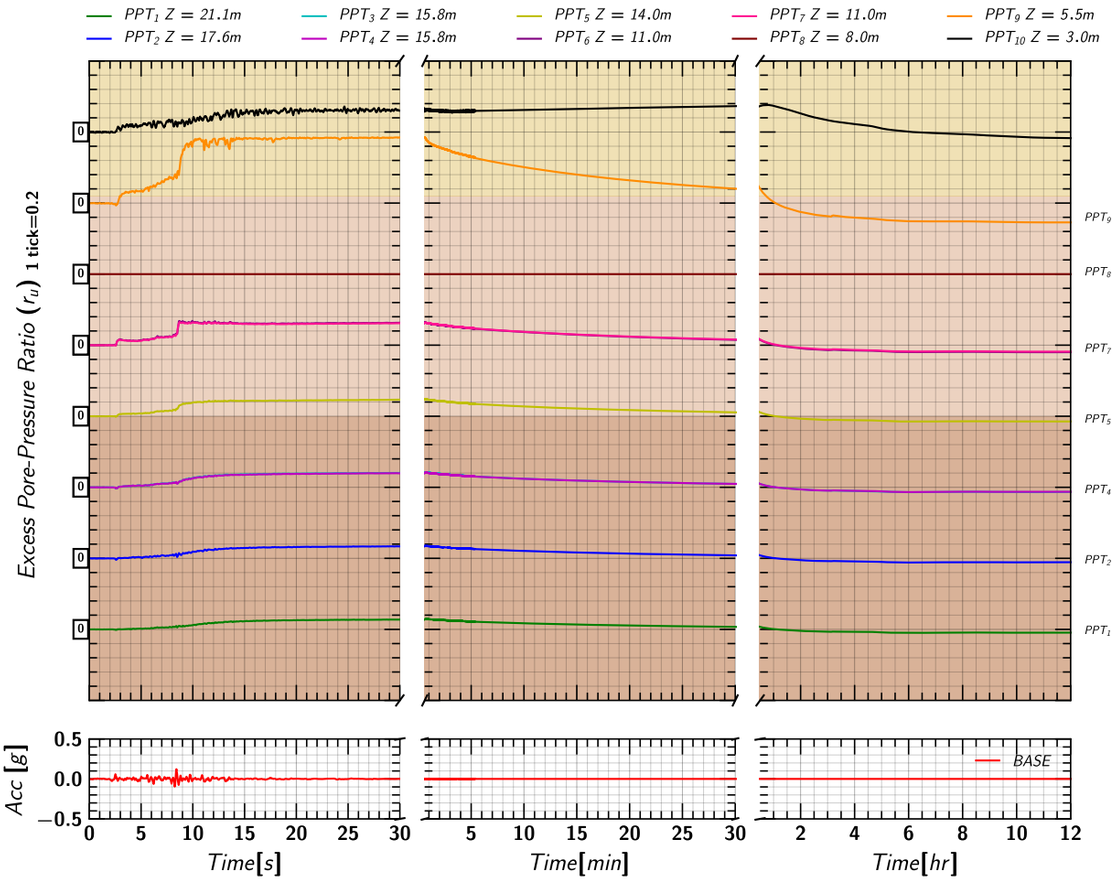

Figure 160. EQM3: Excess pore pressure ratio (r_u) estimated from measurements by Keller transducers during and post the applied earthquake motion.

H.9 Excess Pore pressure Ratio (r_u) Estimated from MS54XXX Transducers

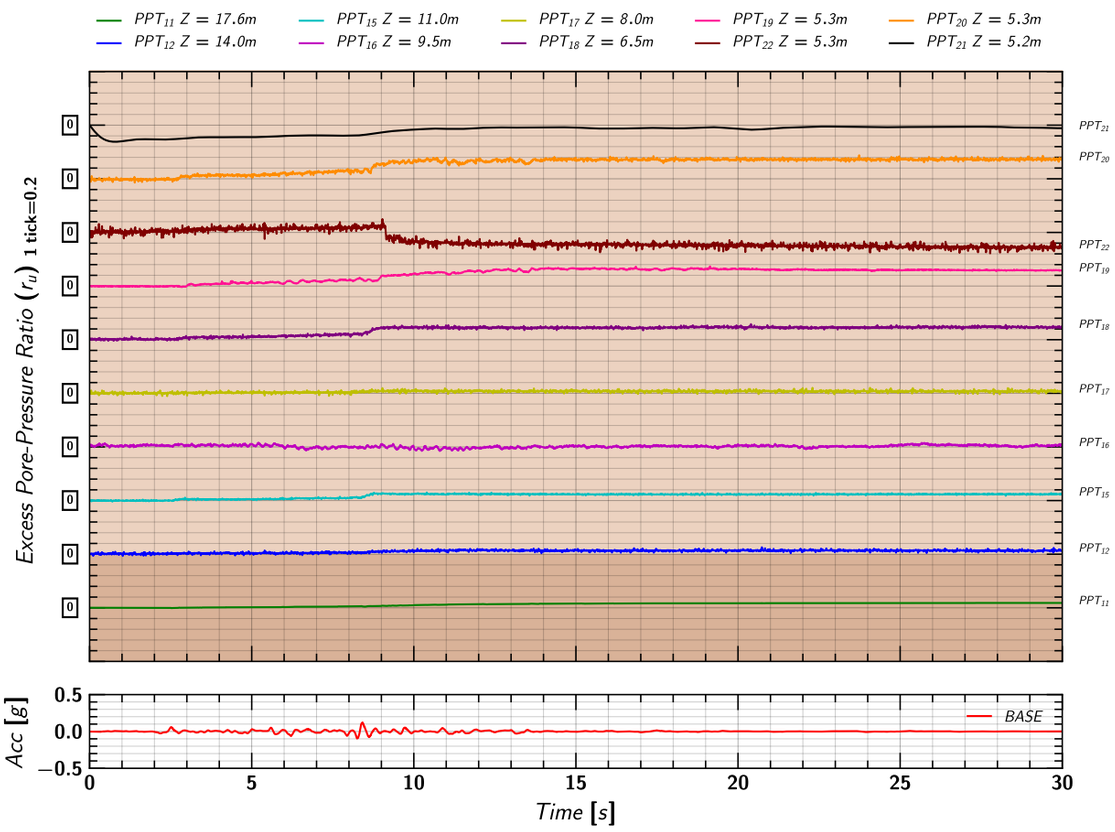

Figure 161. EQM4: Excess pore pressure ratio (r_u) estimated from measurements by MS54XXX transducers during the applied earthquake motion.

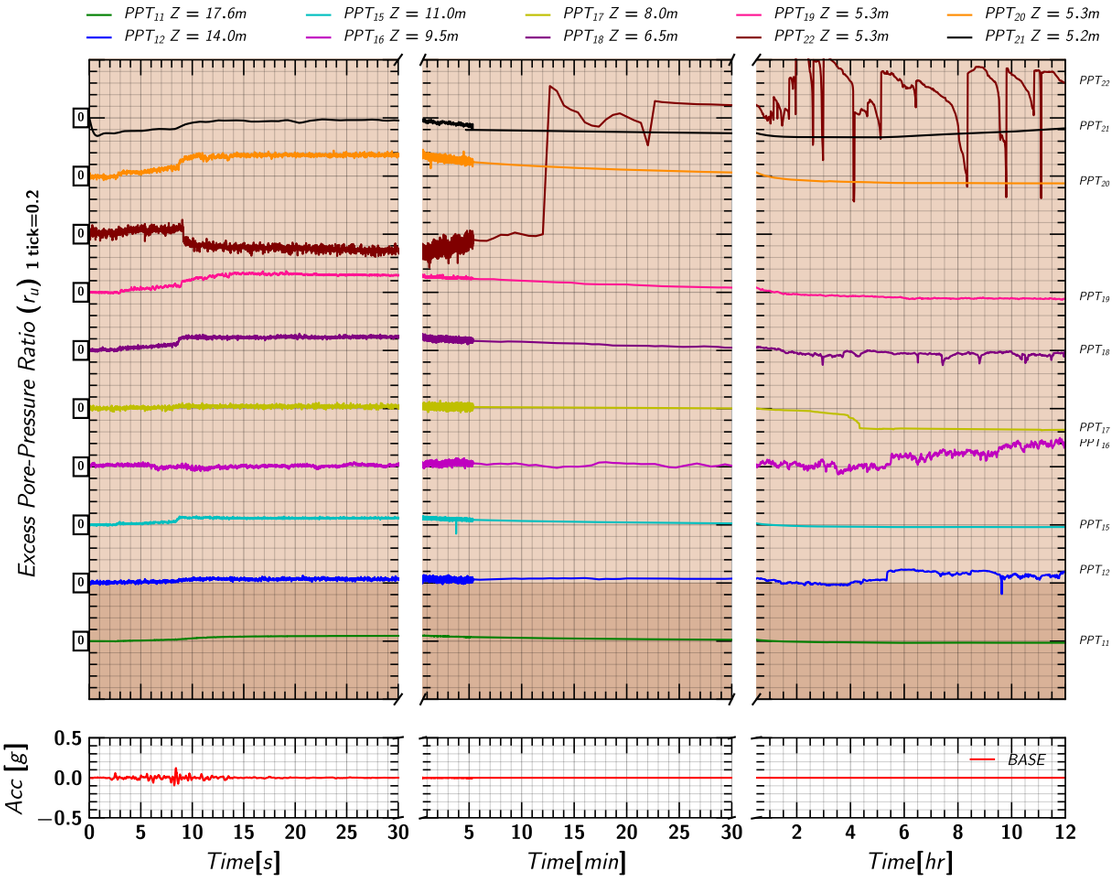

Figure 162. EQM4: Excess pore pressure ratio (r_u) estimated from measurements by MS54XXX transducers during and post the applied earthquake motion.

H.10 Axial Load in Pile 1

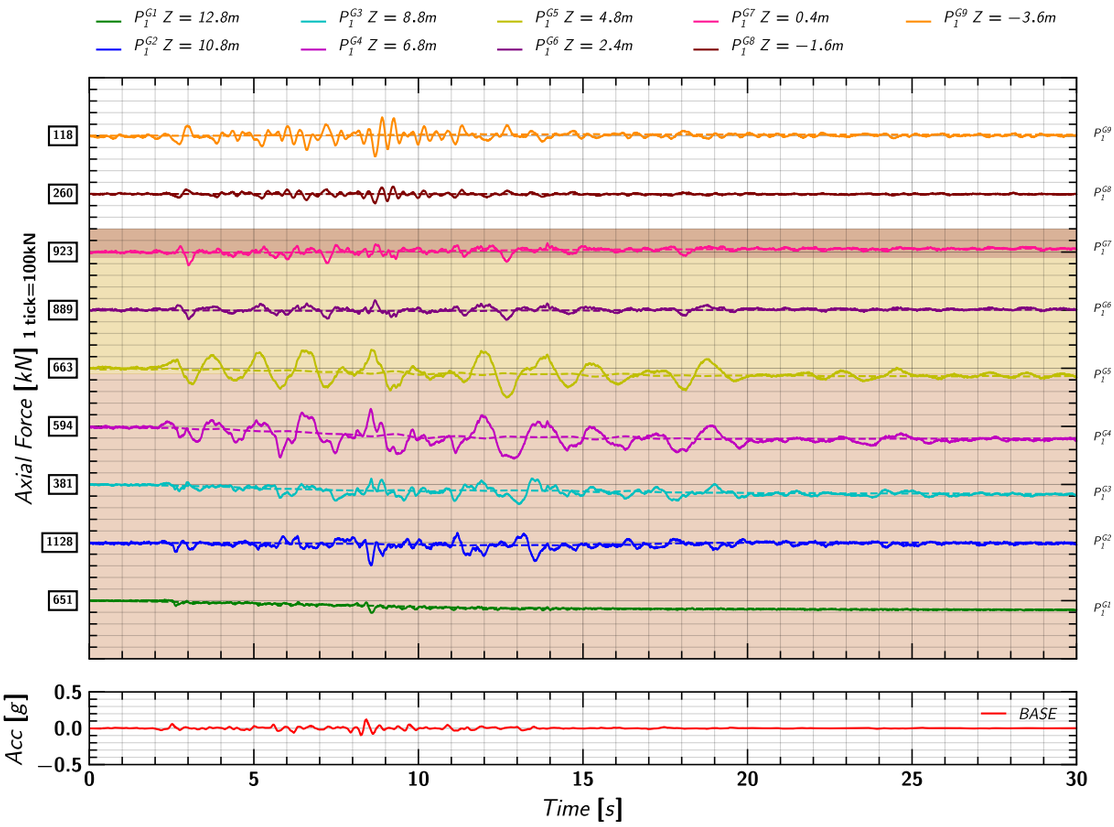

Figure 163. EQM4: Axial load measurements from pile 1 strain gages during the applied earthquake motion.

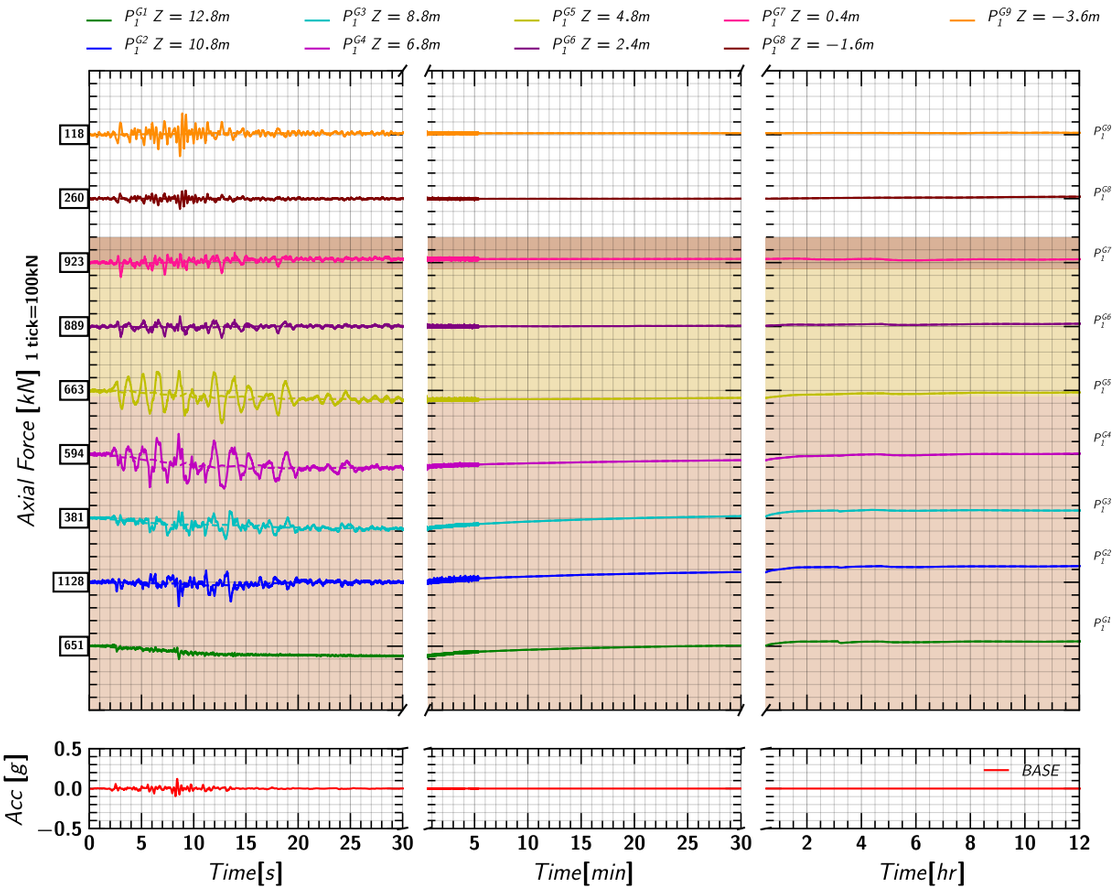

Figure 164. EQM4: Axial load measurements from pile 1 strain gages during and post the applied earthquake motion.

H.11 Axial Load in Pile 2

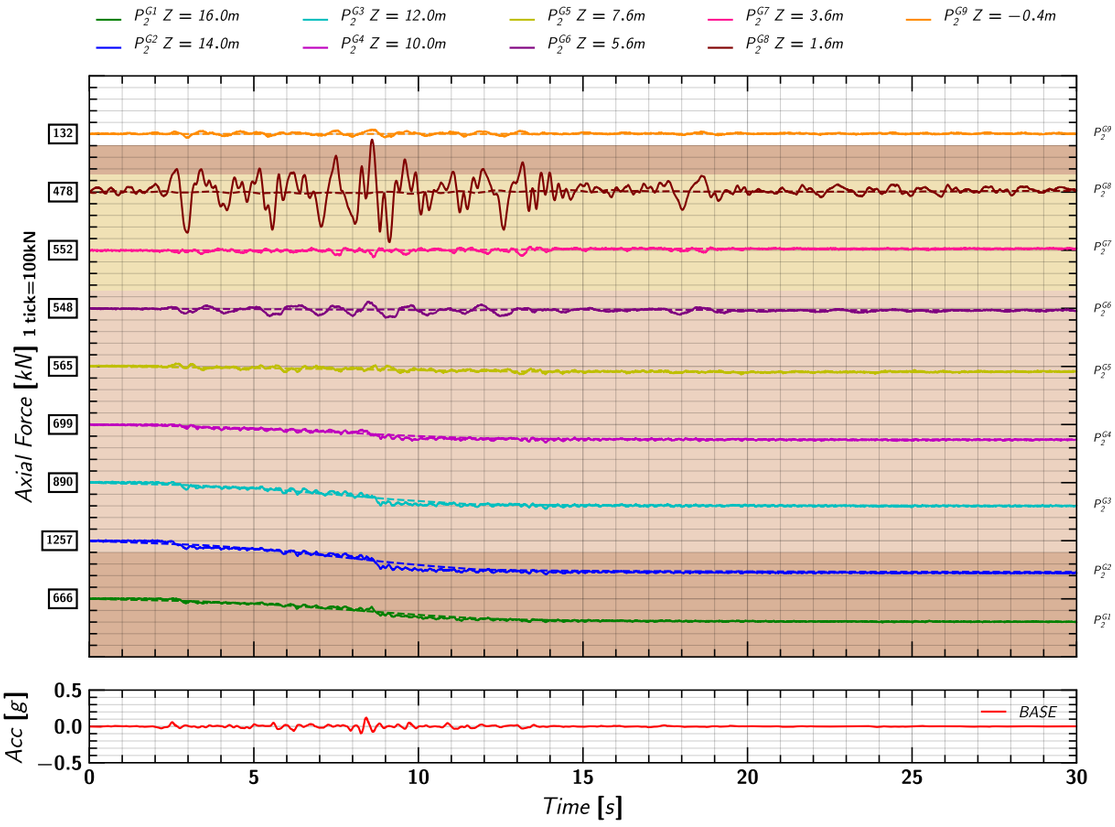

Figure 165. EQM4: Axial load measurements from pile 2 strain gages during the applied earthquake motion.

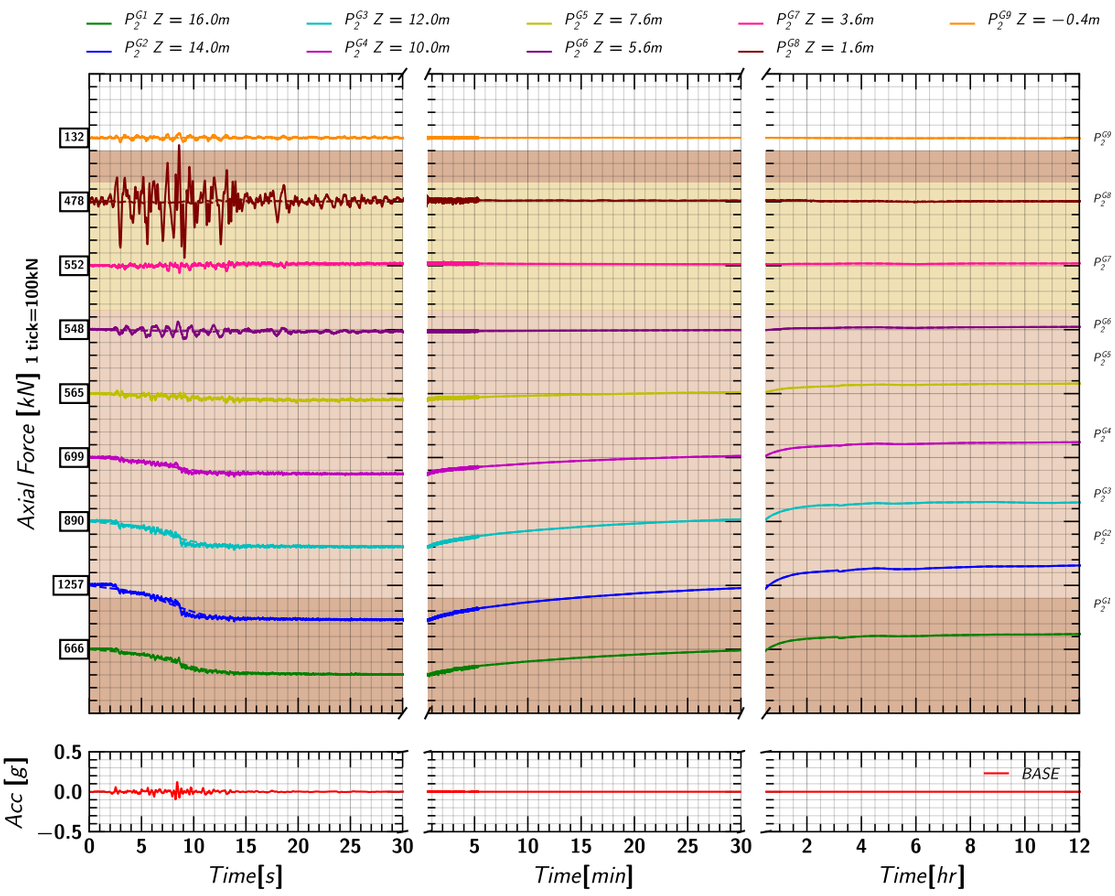

Figure 166. EQM4: Axial load measurements from pile 2 strain gages during and post the applied earthquake motion.

H.12 Pore pressure and Axial Load Profile

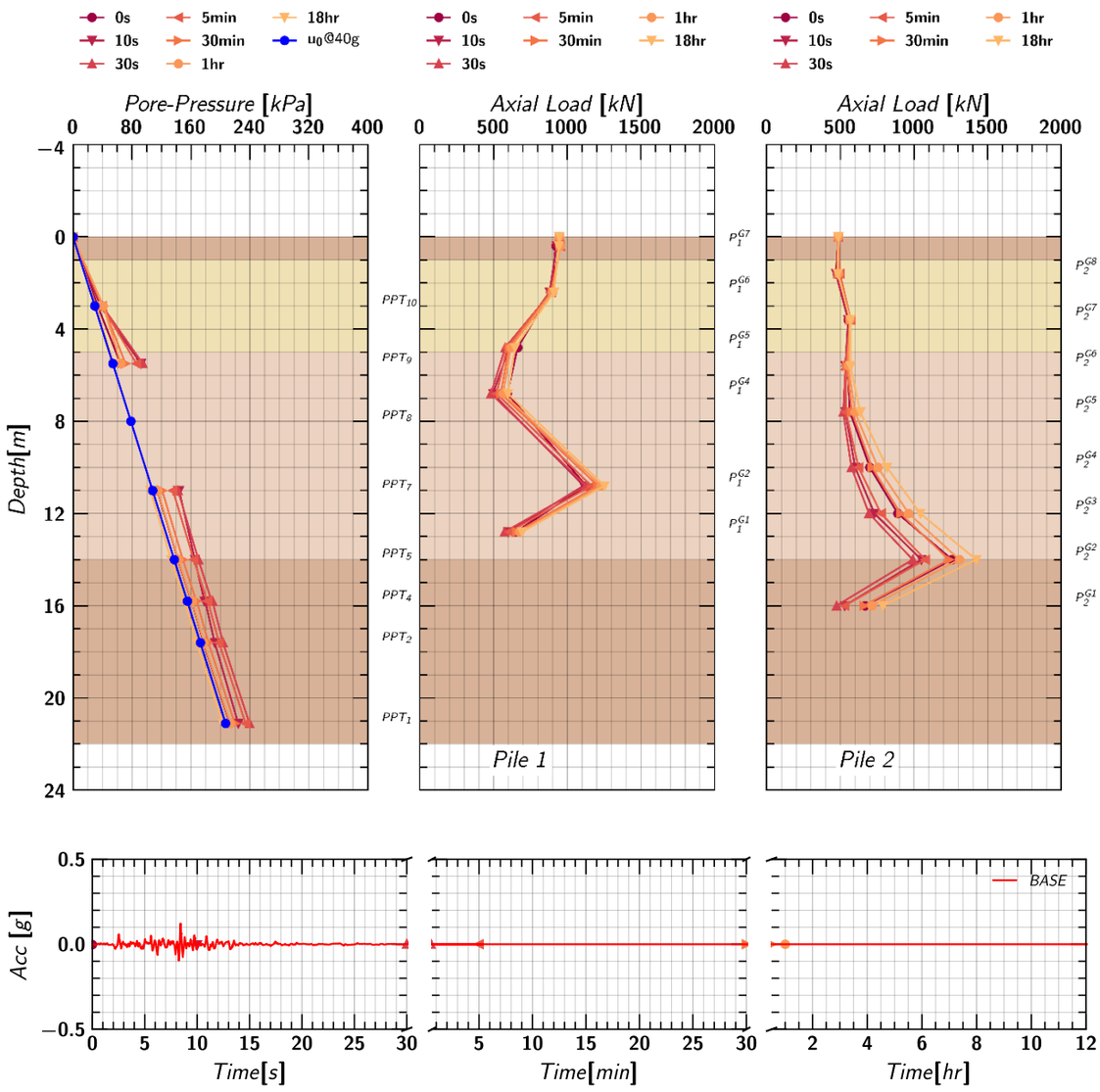

Figure 167. EQM4: Pore pressure and axial load profile in pile 1 and pile 2 at different times during and post the applied earthquake motion.

I. EQM5 - Large Santa Cruz Earthquake Motion (PGA = 0.32g)

I.1 Input Motion

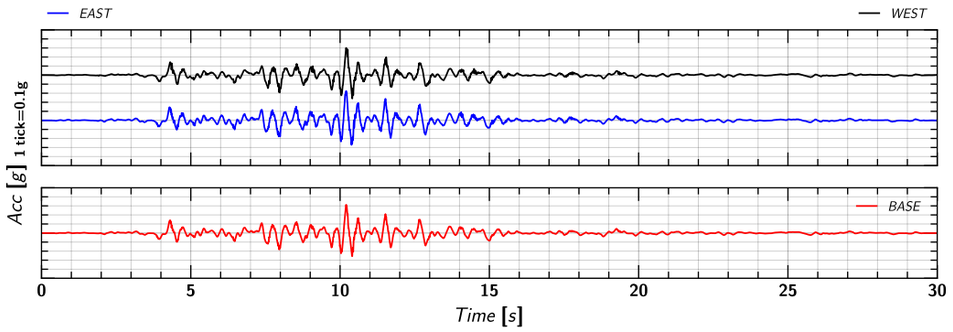

Figure 168. EQM5: Input motion.

I.2 Acceleration in Container

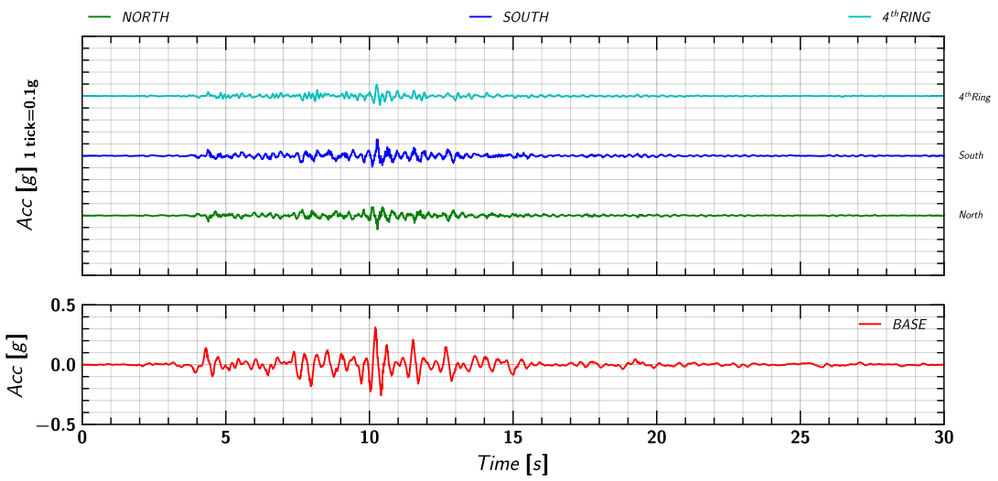

Figure 169. EQM5: Acceleration measurement on container.

I.3 Acceleration in Soil

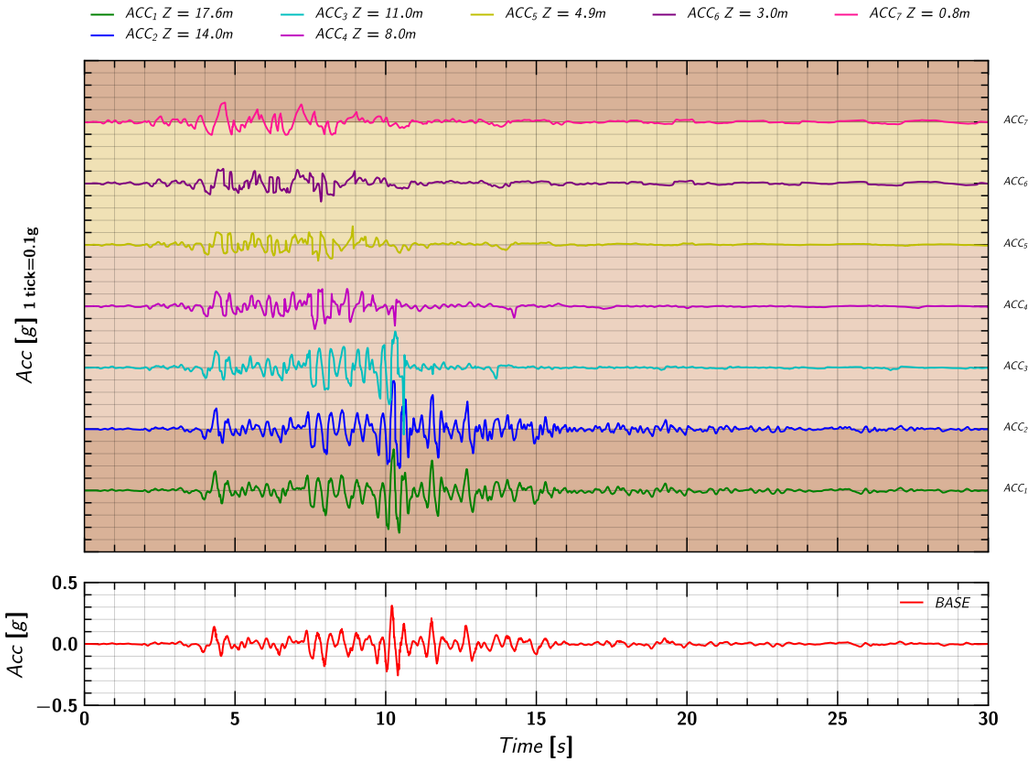

Figure 170. EQM5: Acceleration measurement in soil.

I.4 Acceleration in Pile

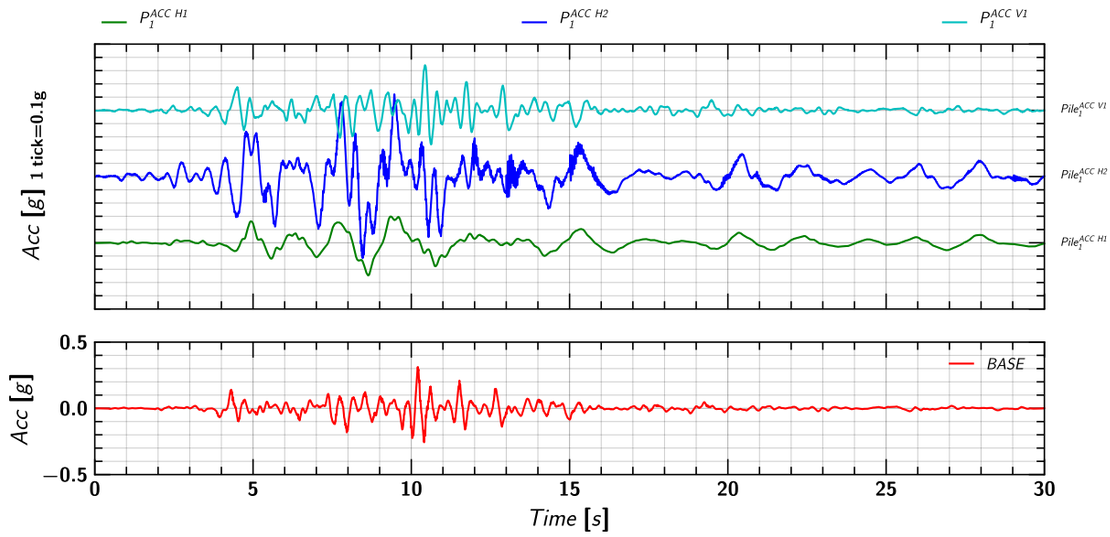

Figure 171. EQM$_5$: Acceleration measurement on pile 1.

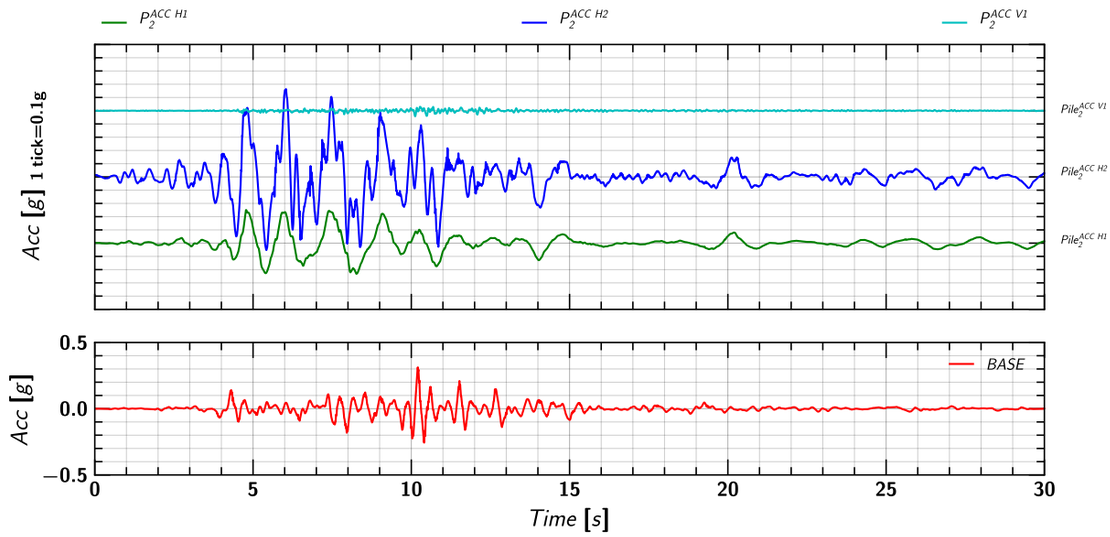

Figure 172. Acceleration measurement on pile 2.

I.5 Soil and Pile Settlement

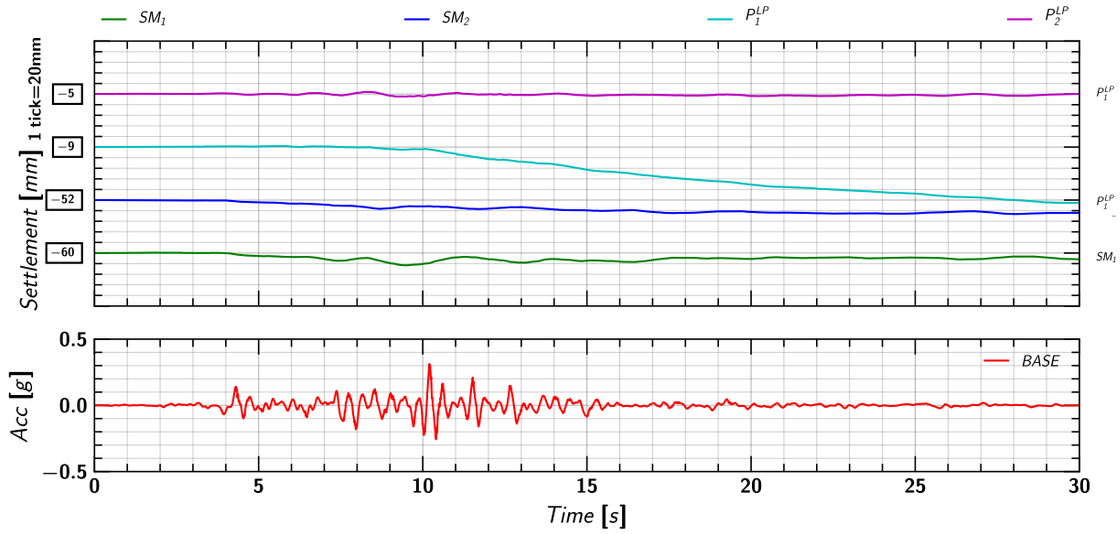

Figure 173. EQM5: Settlement measurement in soil and pile during the applied earthquake motion.

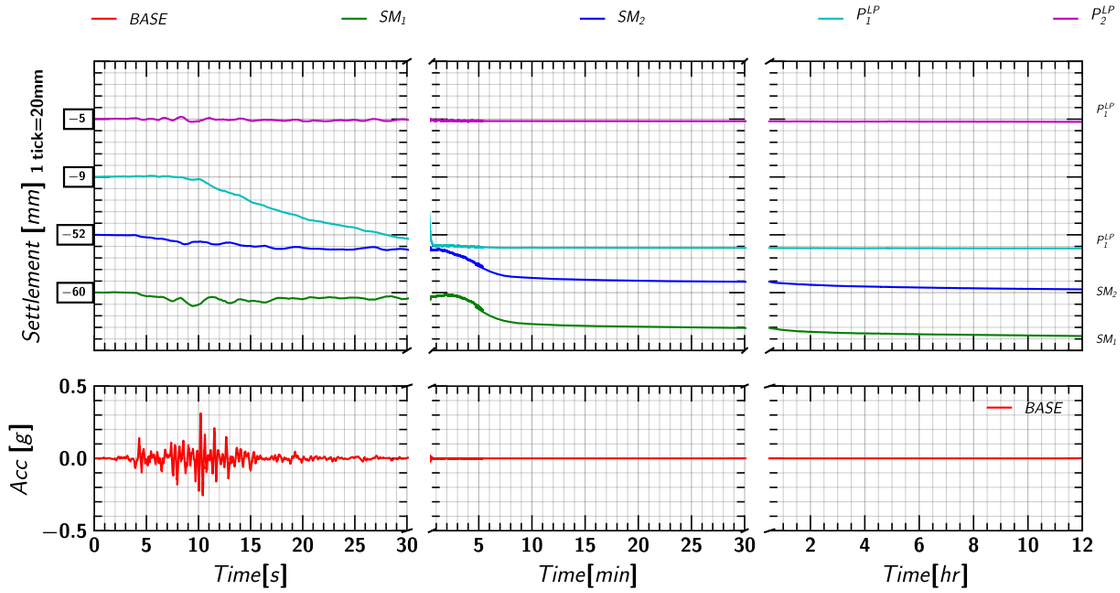

Figure 174. EQM5: Settlement measurement in soil and pile during and post applied earthquake motion.

I.6 Pore pressure measurements in Soil (Keller Transducers)

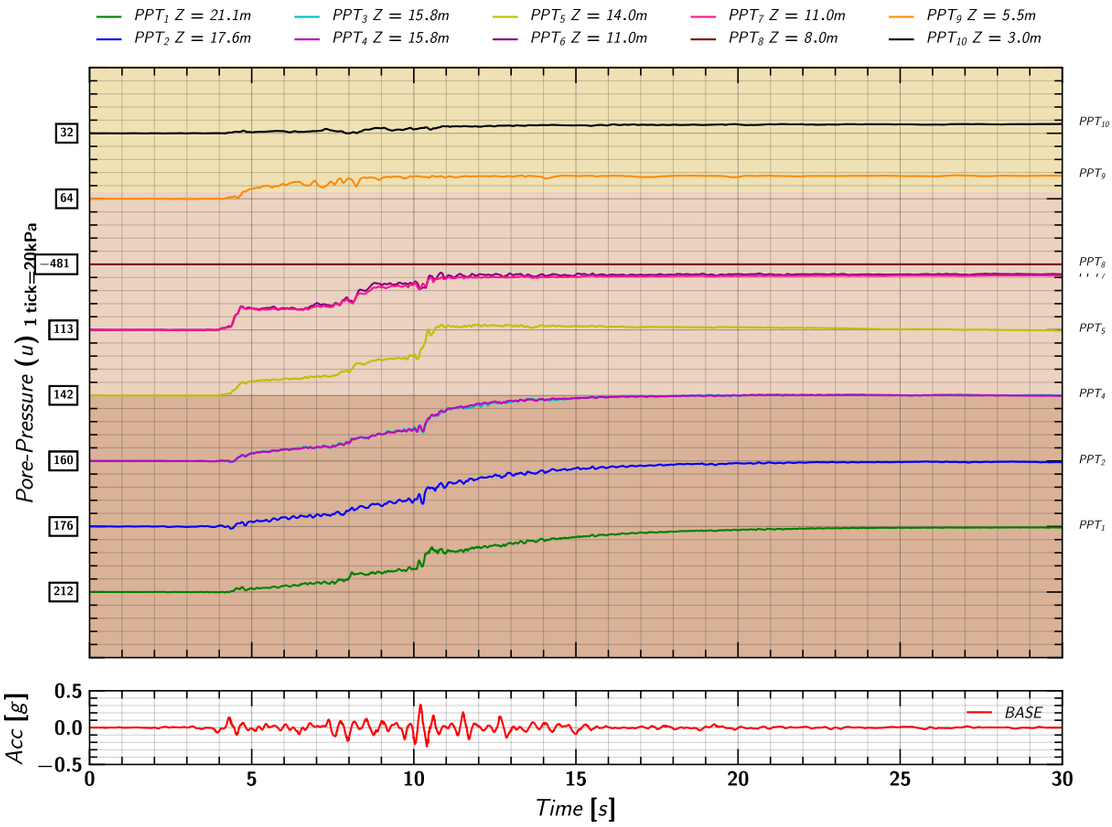

Figure 175. EQM5: Pore pressure measurements in soil from Keller transducers during the applied earthquake motion.

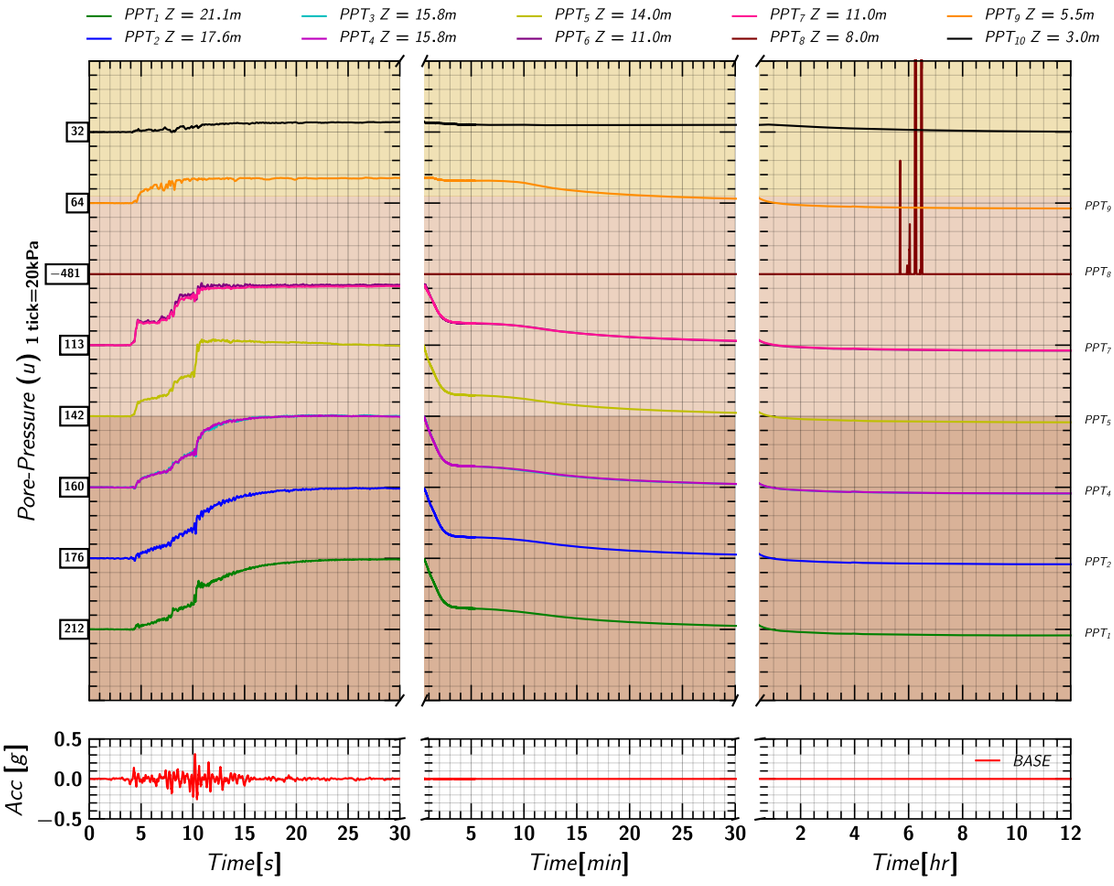

Figure 176. EQM5: Pore pressure measurements in soil from Keller transducers during and post the applied earthquake motion.

I.7 Pore pressure measurements in Soil (MS54XXX Transducers)

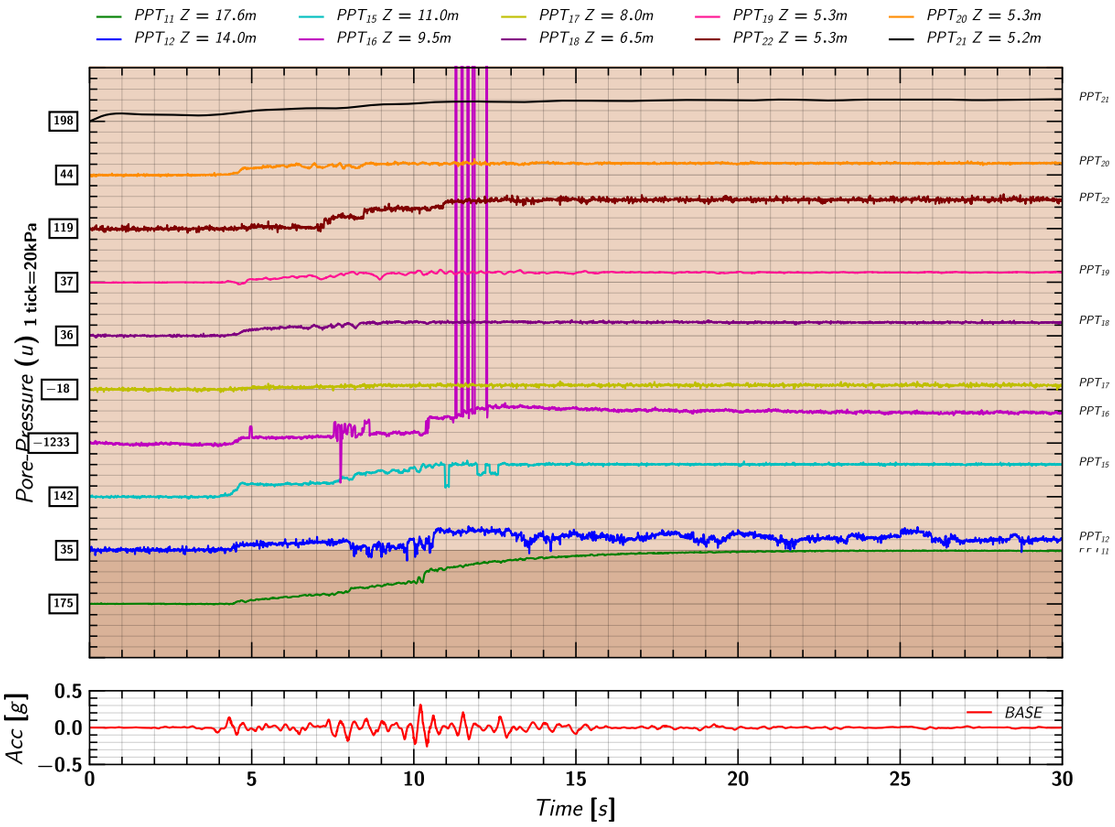

Figure 177. EQM$_5$: Pore pressure measurements in soil from MS54XXX transducers during the applied earthquake motion.

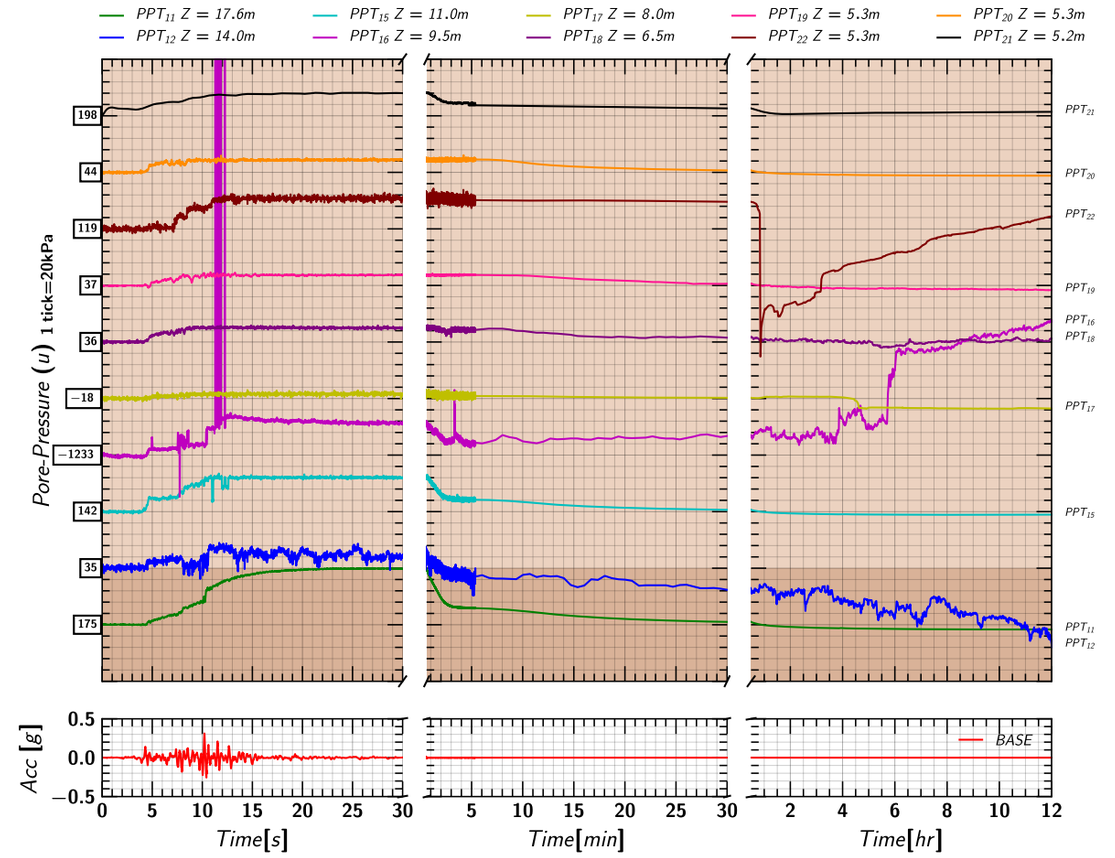

Figure 178. EQM$_5$: Pore pressure measurements in soil from MS54XXX transducers during and post the applied earthquake motion.

I.8 Excess Pore pressures Ratio (r_u) Estimated from Keller Transducers

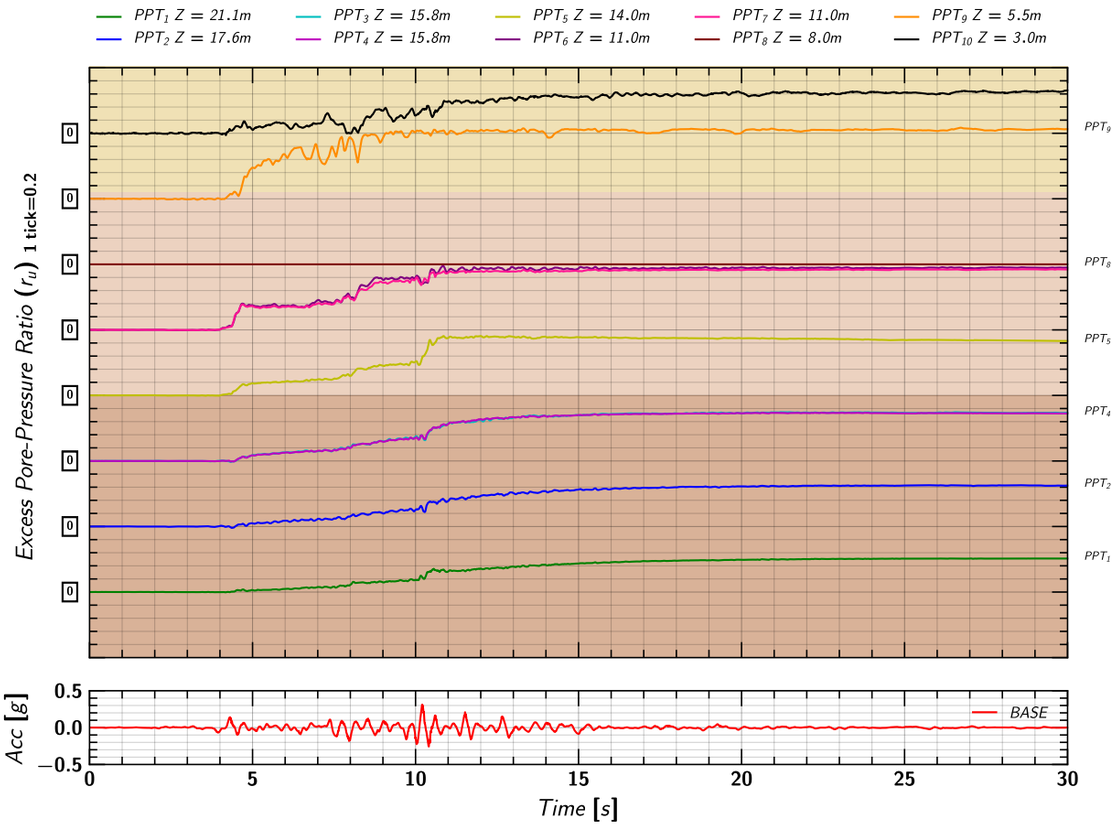

Figure 179. EQM$_5$: Excess pore pressure ratio (r_u) estimated from measurements by Keller transducers during the applied earthquake motion.

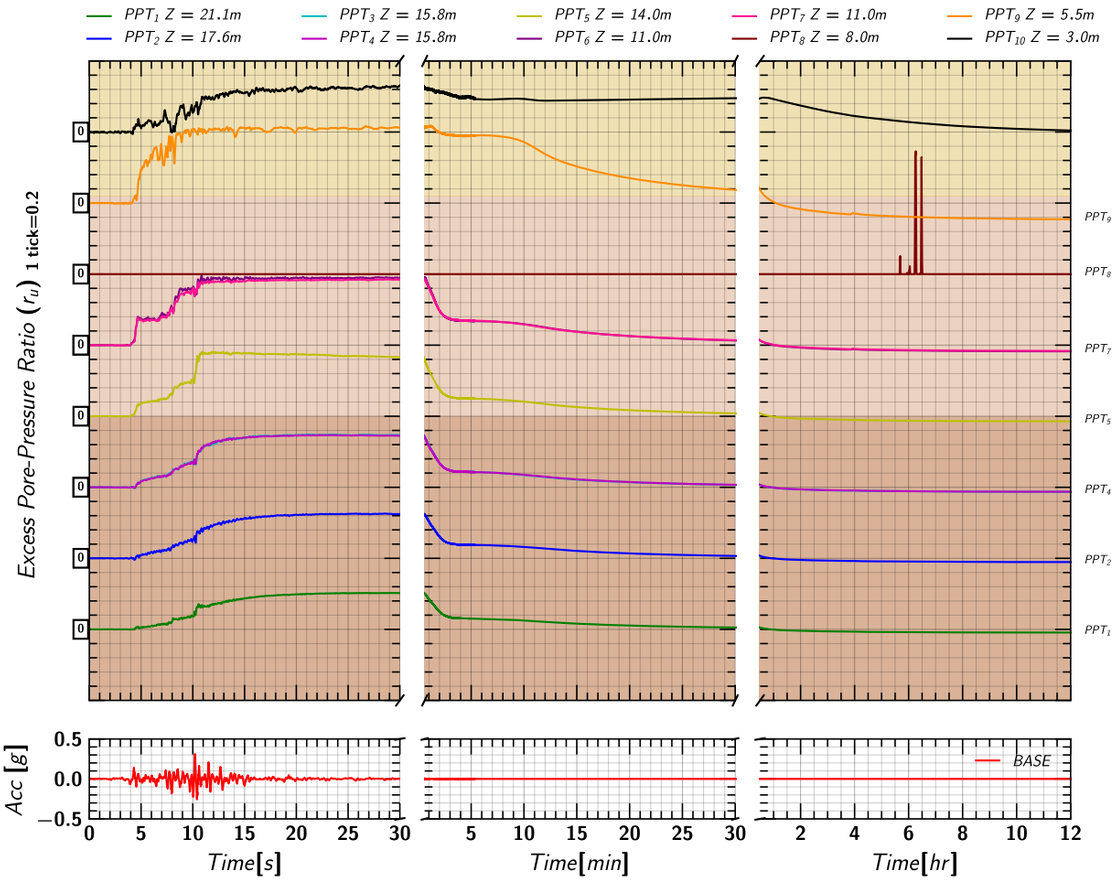

Figure 180. EQM$_5$: Excess pore pressure ratio (r_u) estimated from measurements by Keller transducers during and post the applied earthquake motion.

I.9 Excess Pore pressure Ratio (r_u) Estimated from MS54XXX Transducers

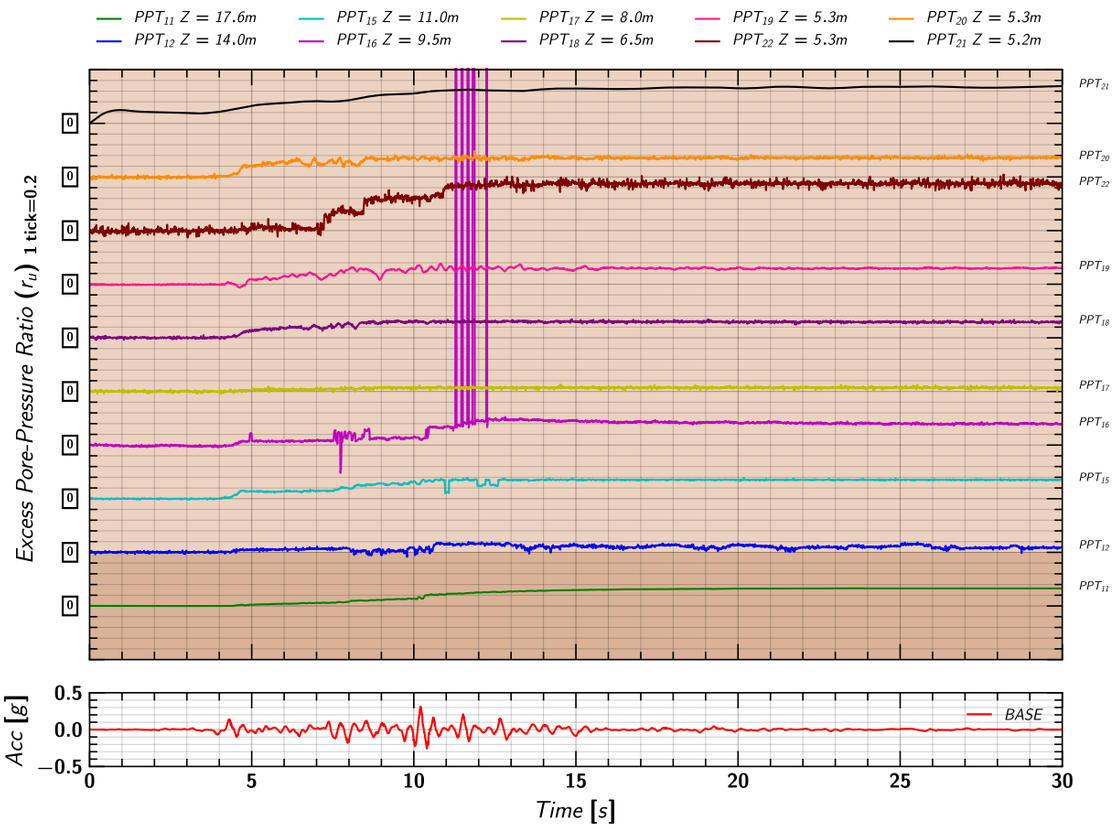

Figure 181. EQM$_5$: Excess pore pressure ratio (r_u) estimated from measurements by MS54XXX transducers during the applied earthquake motion.

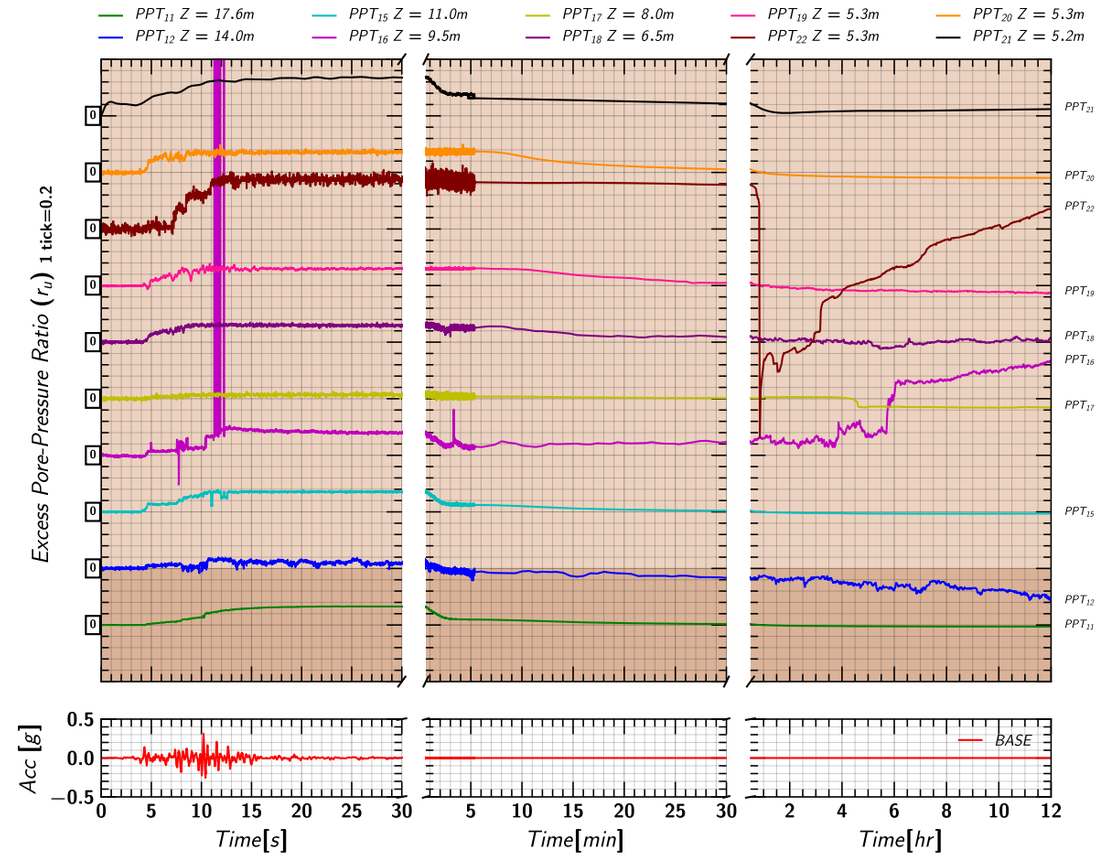

Figure 182. EQM$_5$: Excess pore pressure ratio (r_u) estimated from measurements by MS54XXX transducers during and post the applied earthquake motion.

I.10 Axial Load in Pile 1

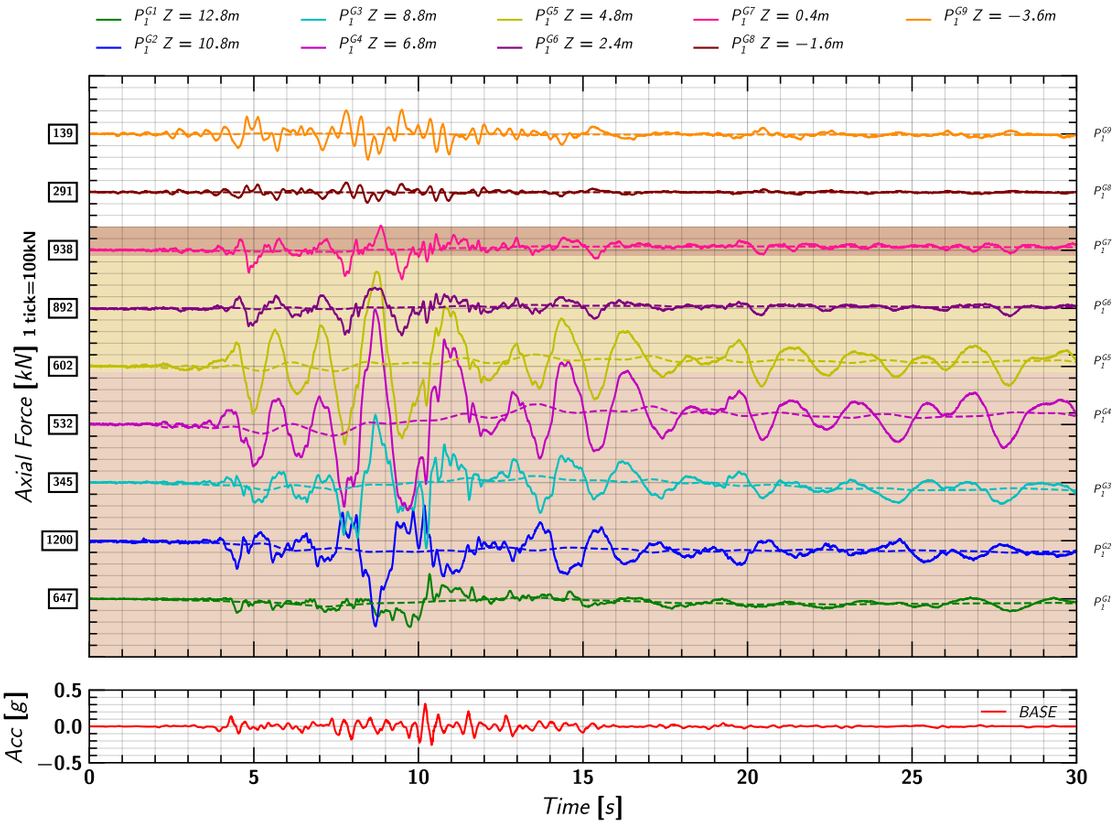

Figure 183. EQM5: Axial load measurements from pile 1 strain gages during the applied earthquake motion.

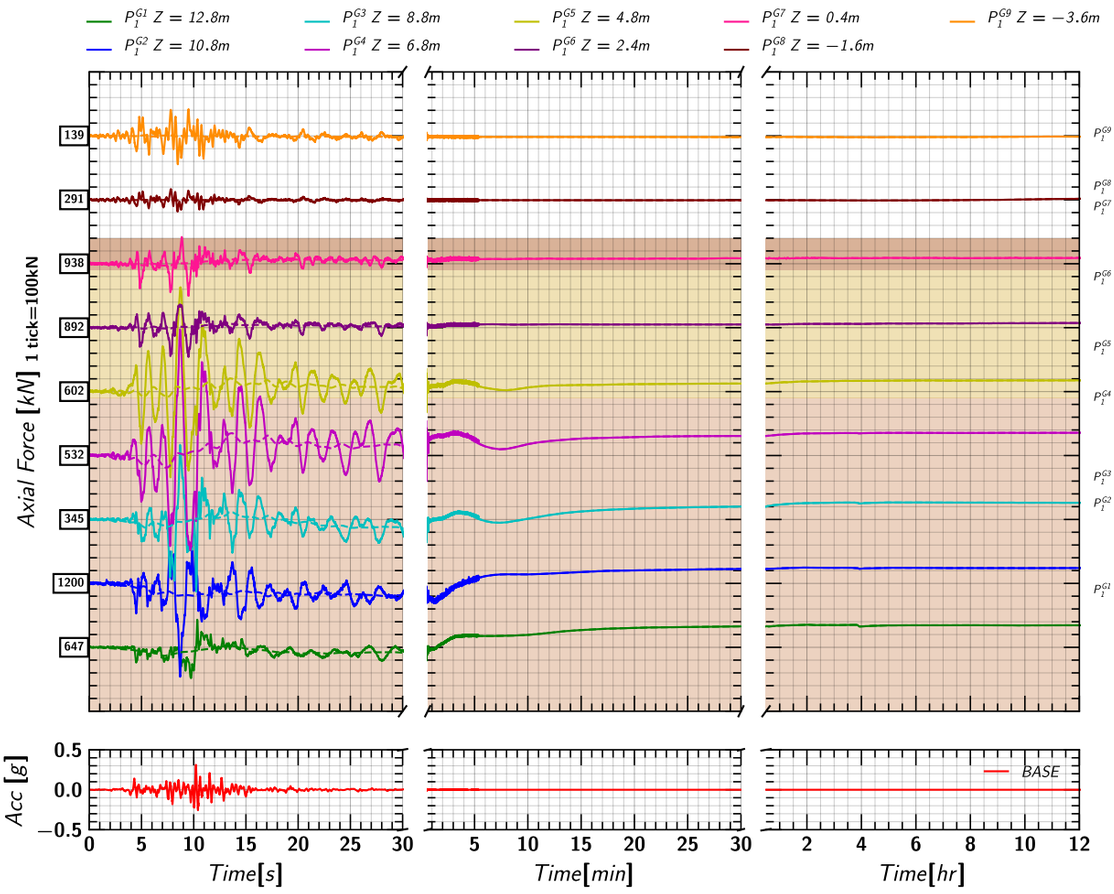

Figure 184. EQM5: Axial load measurements from pile 1 strain gages during and post the applied earthquake motion.

I.11 Axial Load in Pile 2

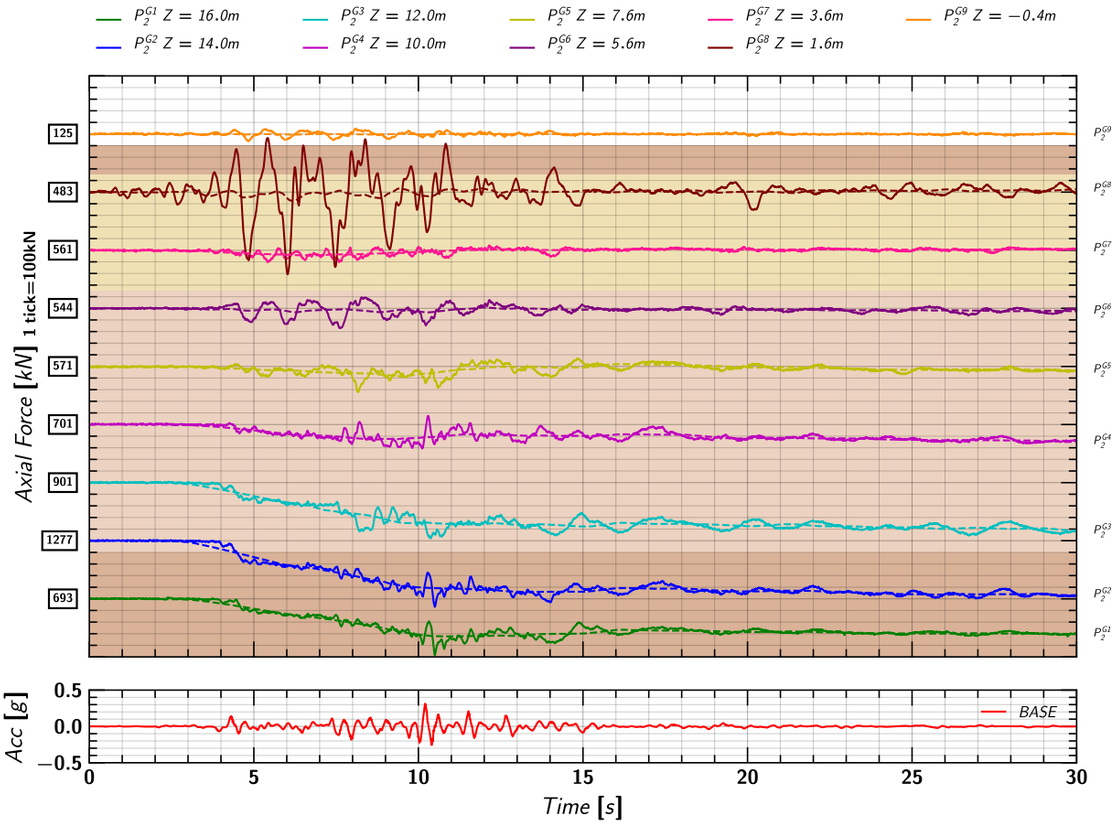

Figure 185. EQM5: Axial load measurements from pile 2 strain gages during the applied earthquake motion.

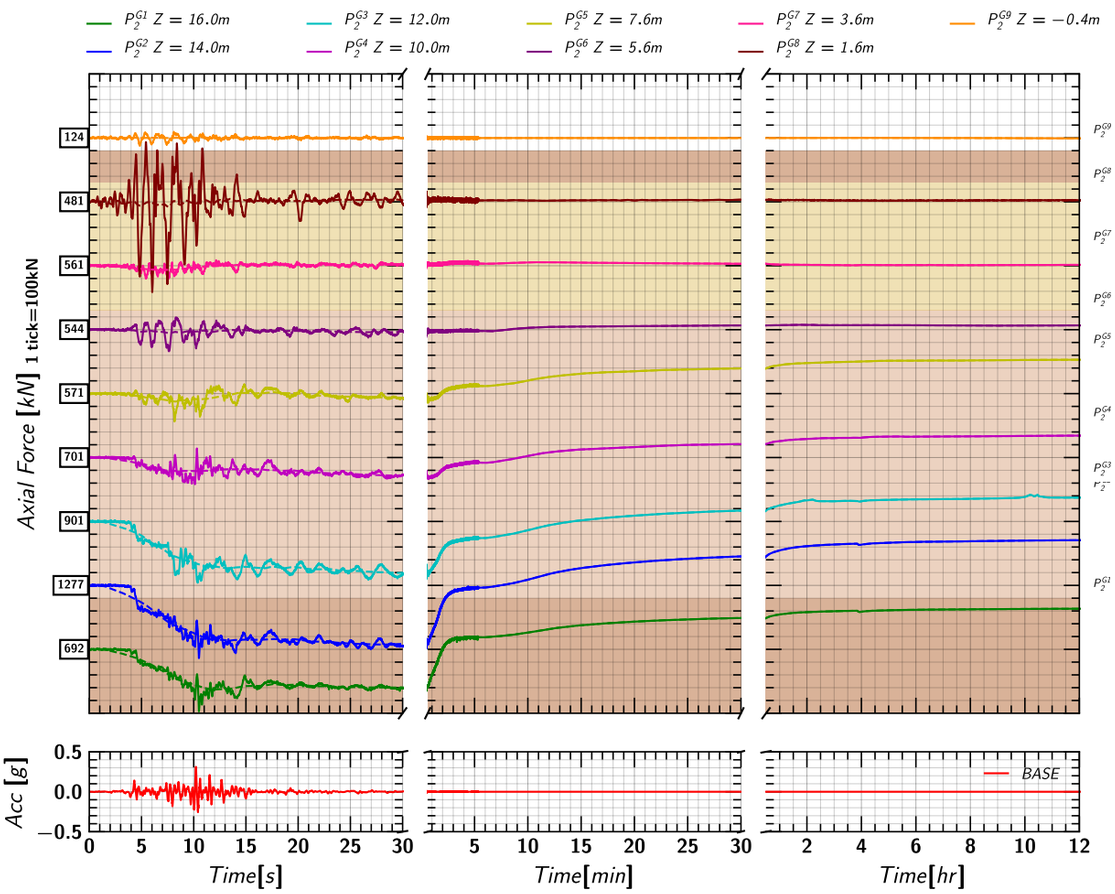

Figure 186. EQM5: Axial load measurements from pile 2 strain gages during and post the applied earthquake motion.

I.12 Pore pressure and Axial Load Profile

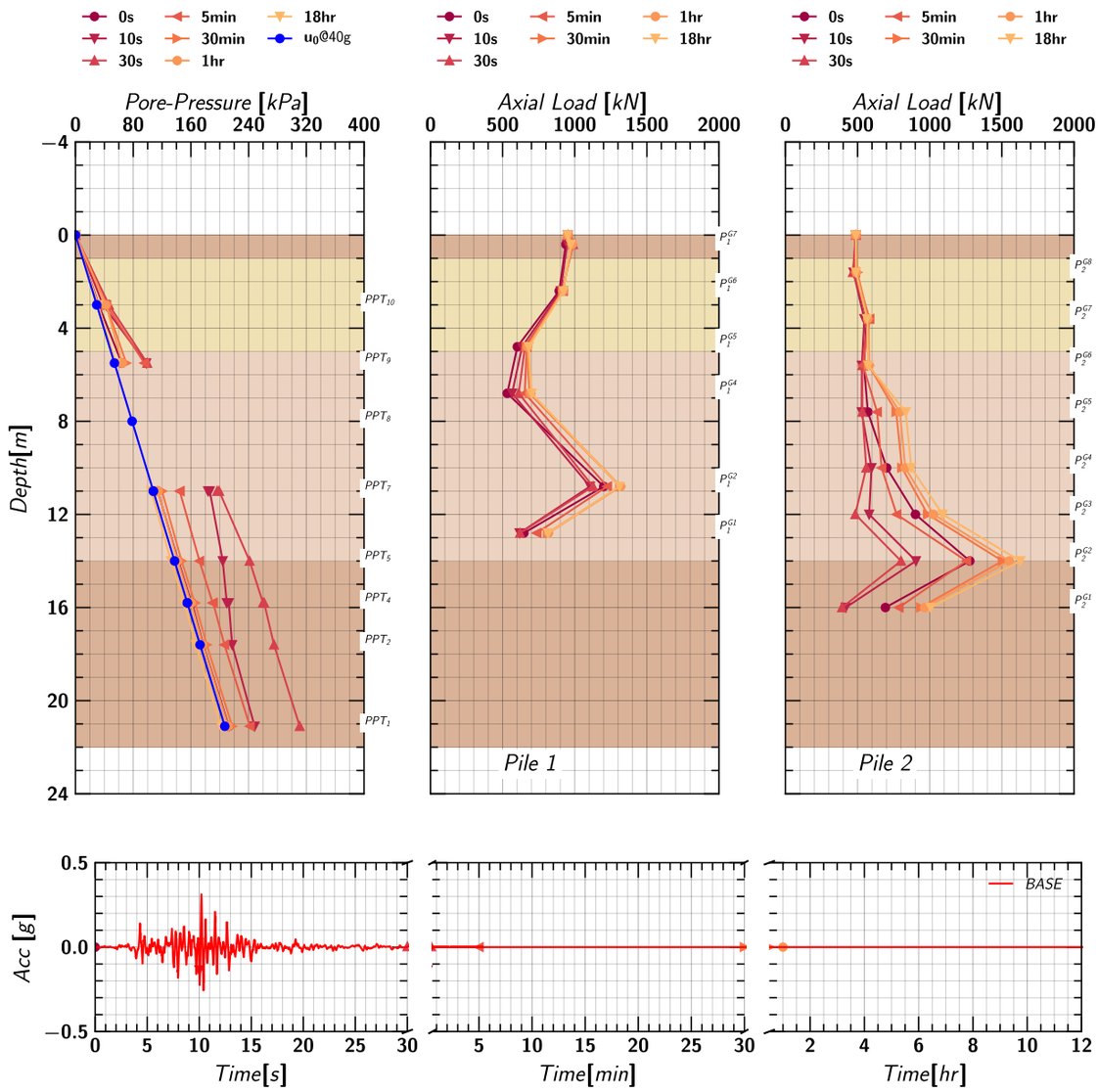

Figure 187. EQM5: Pore pressure and axial load profile in pile 1 and pile 2 at different times during and post the applied earthquake motion.

J. EQM$_6$ - Large EJM01 Earthquake Motion (PGA = 0.40g)

J.1 Input Motion

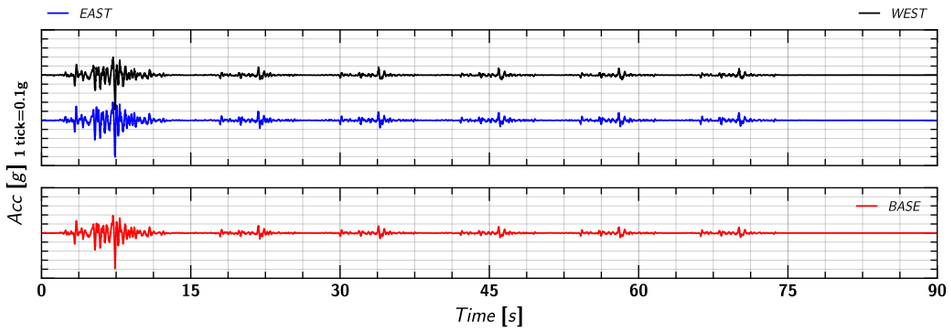

Figure 188. EQM$_6$: Input motion.

J.2 Acceleration in Container

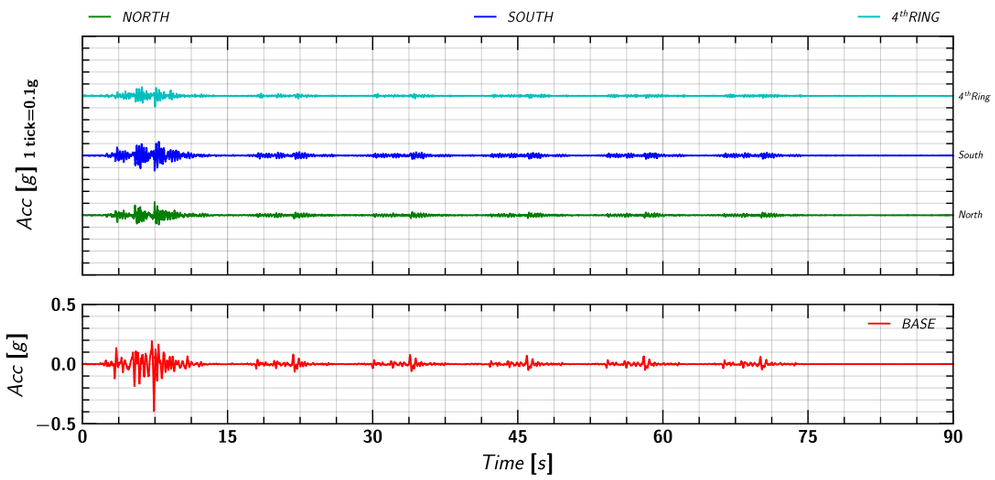

Figure 189. EQM$_6$: Acceleration measurement on container.

J.3 Acceleration in Soil

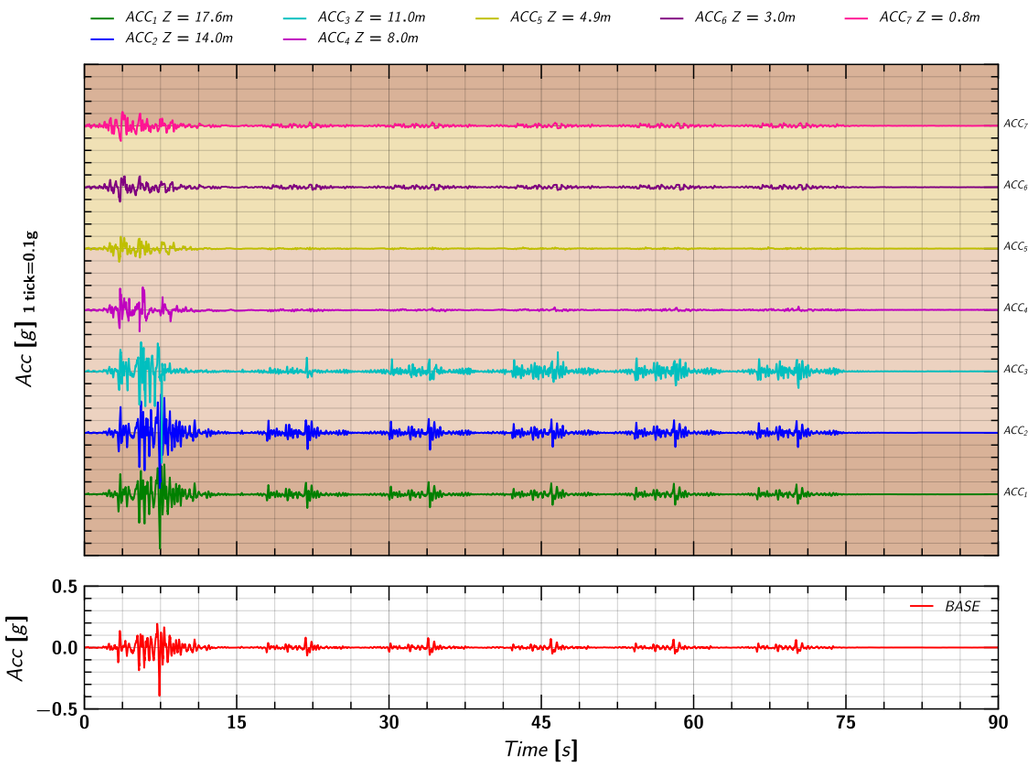

Figure 190. EQM$_6$: Acceleration measurement in soil.

J.4 Acceleration in Pile

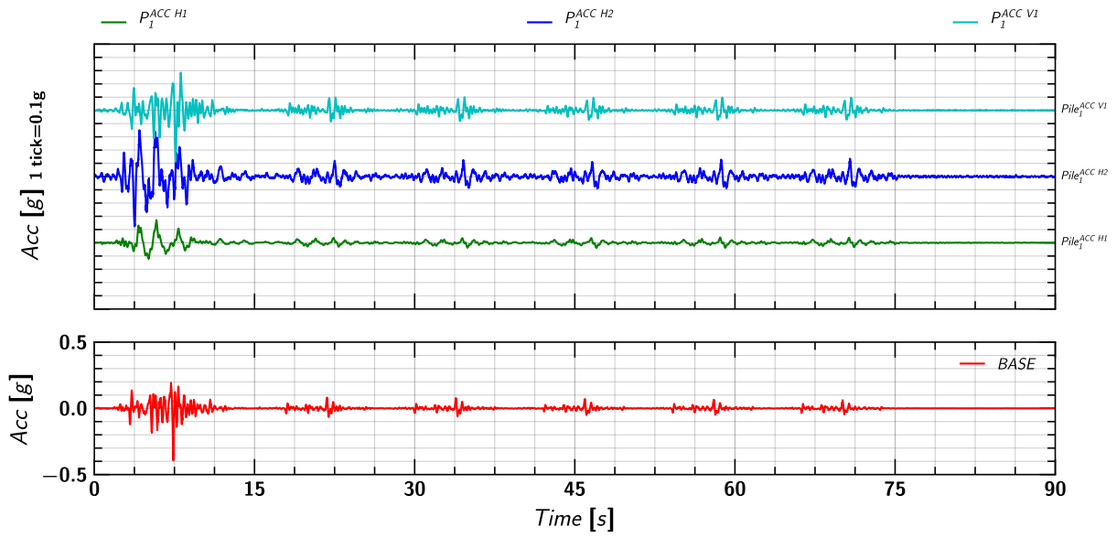

Figure 191. EQM$_6$: Acceleration measurement on pile 1.

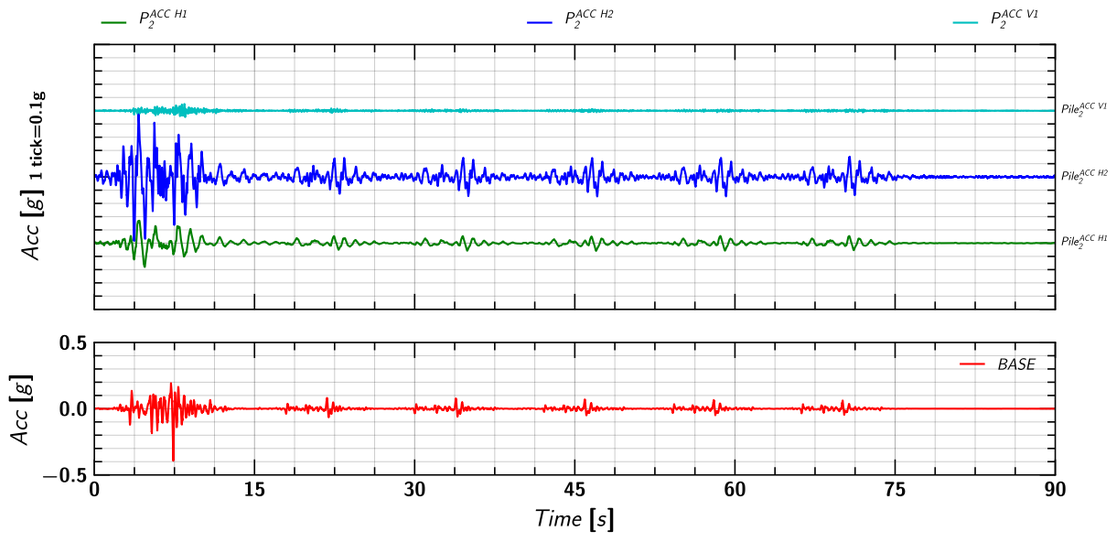

Figure 192. EQM$_6$: Acceleration measurement on pile 1.

J.5 Soil and Pile Settlement

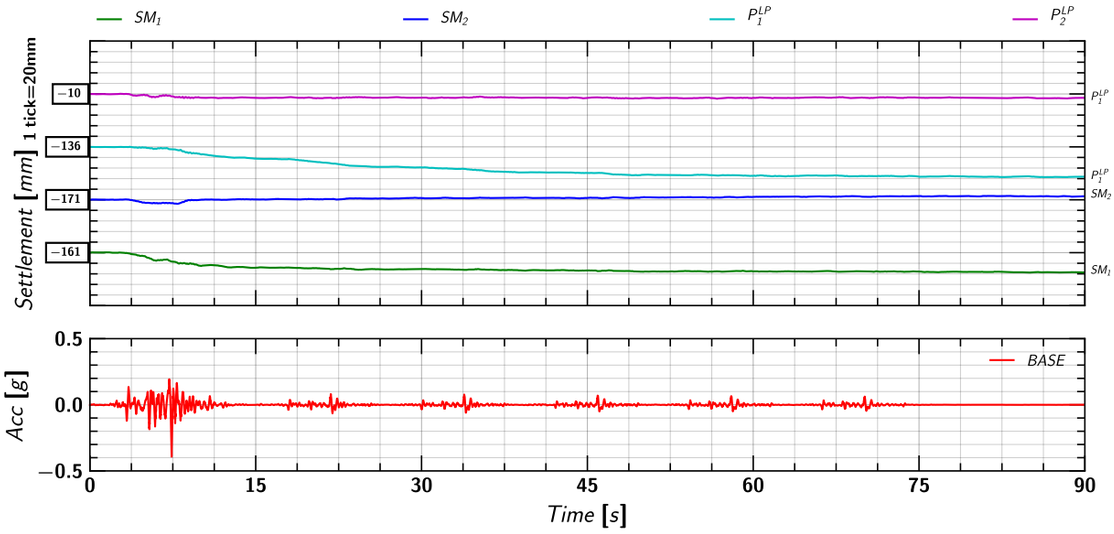

Figure 193. EQM$_6$: Settlement measurement in soil and pile during the applied earthquake motion.

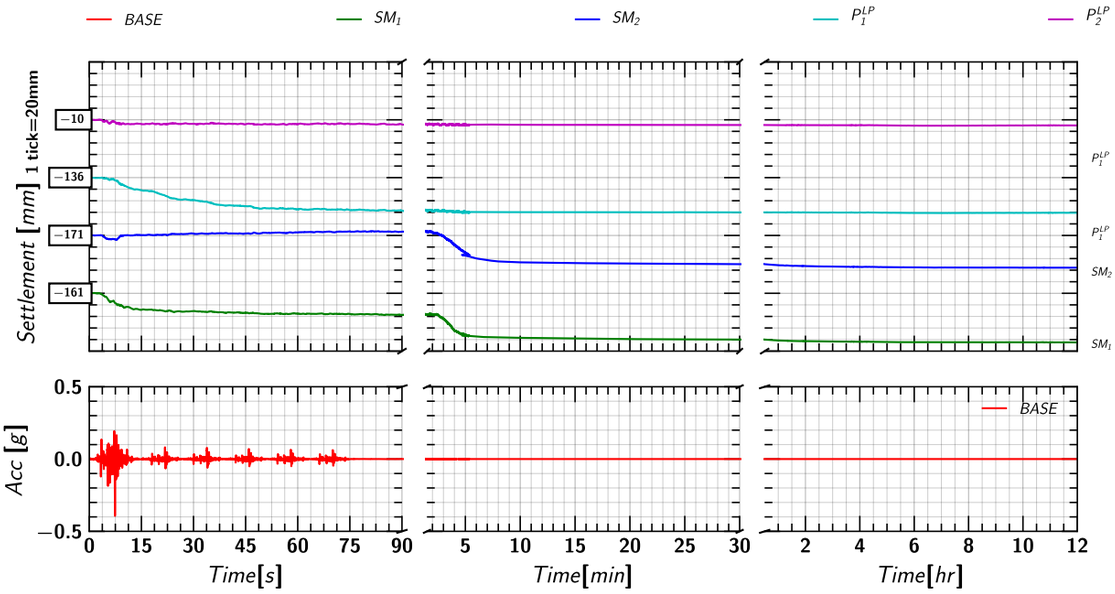

Figure 194. EQM$_6$: Settlement measurement in soil and pile during and post applied earthquake motion.

J.6 Pore pressure measurements in Soil (Keller Transducers)

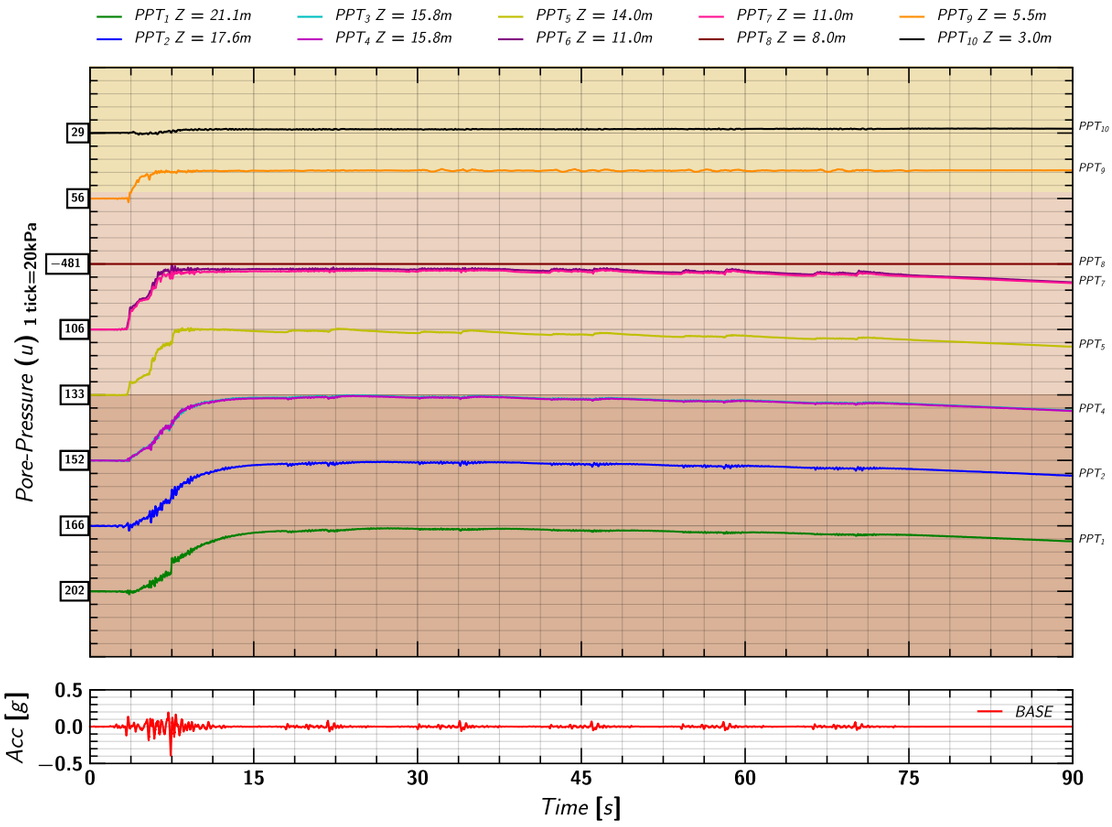

Figure 195. EQM6: Pore pressure measurements in soil from Keller transducers during the applied earthquake motion.

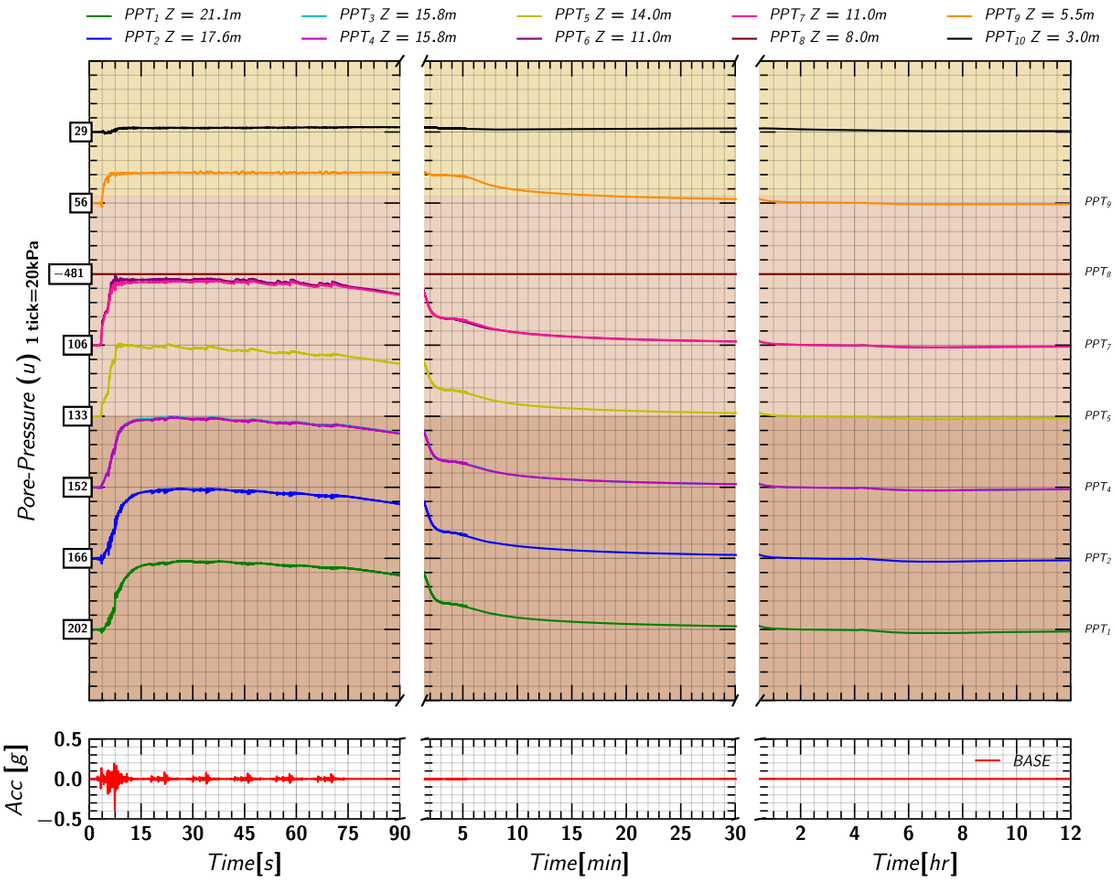

Figure 196. EQM6: Pore pressure measurements in soil from Keller transducers during and post the applied earthquake motion.

J.7 Pore pressure measurements in Soil (MS54XXX Transducers)

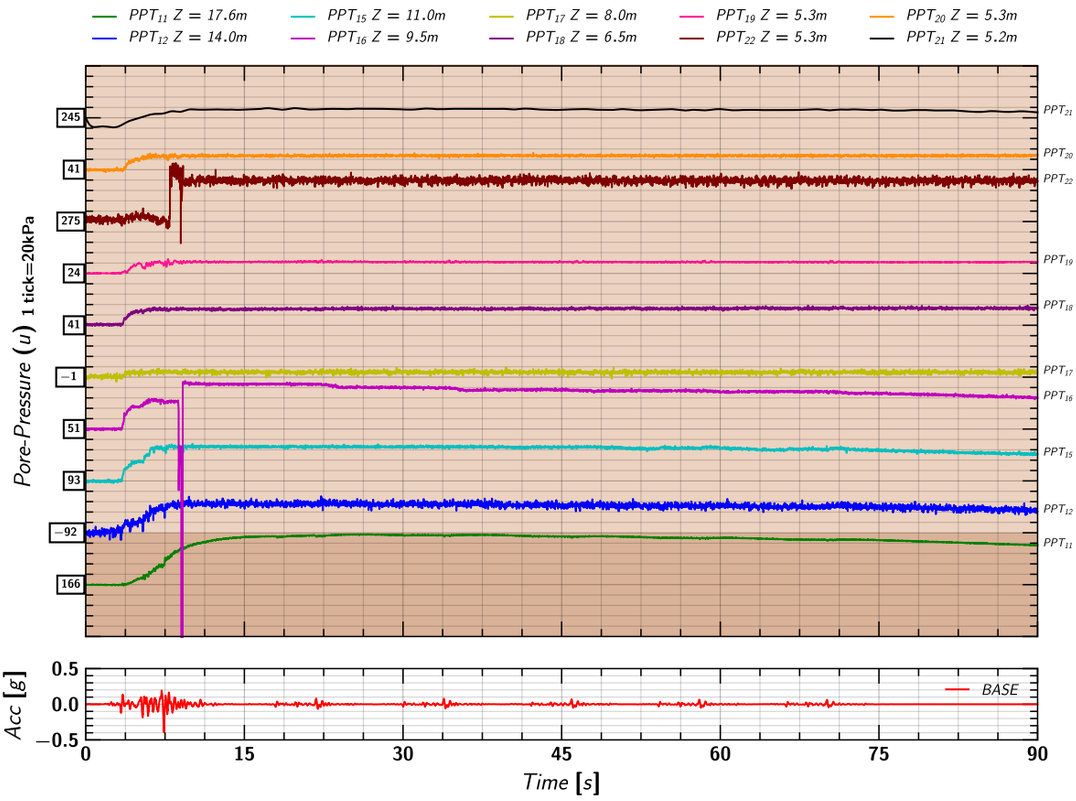

Figure 197. EQM$_6$: Pore pressure measurements in soil from MS54XXX transducers during the applied earthquake motion.

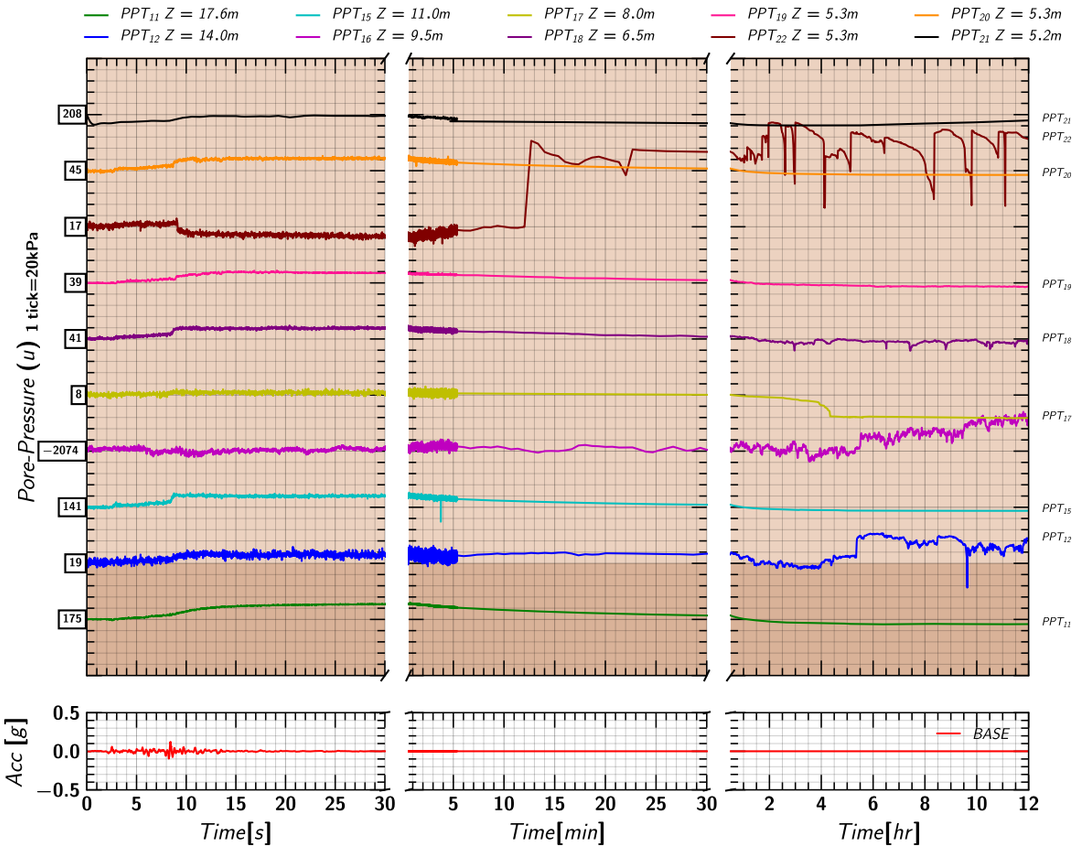

Figure 198. EQM$_6$: Pore pressure measurements in soil from MS54XXX transducers during and post the applied earthquake motion.

J.8 Excess Pore pressures Ratio (r_u) Estimated from Keller Transducers

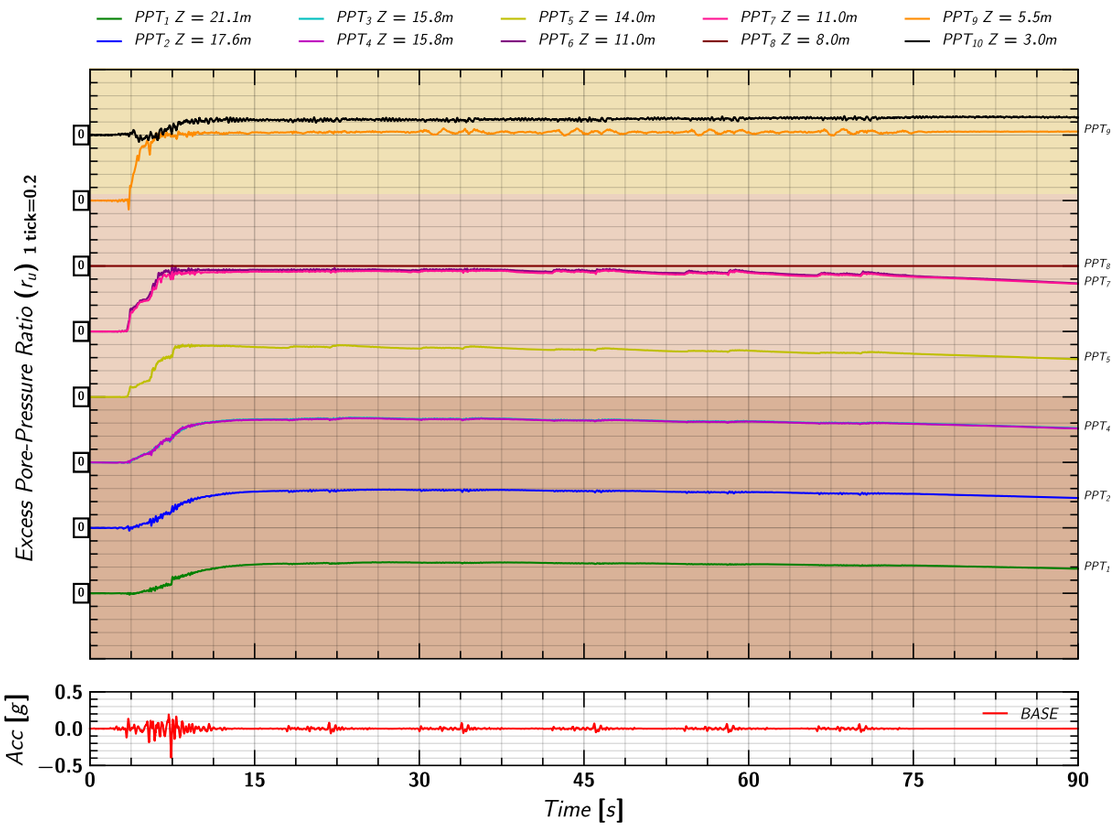

Figure 199. EQM$_6$: Excess pore pressure ratio (r_u) estimated from measurements by Keller transducers during the applied earthquake motion.

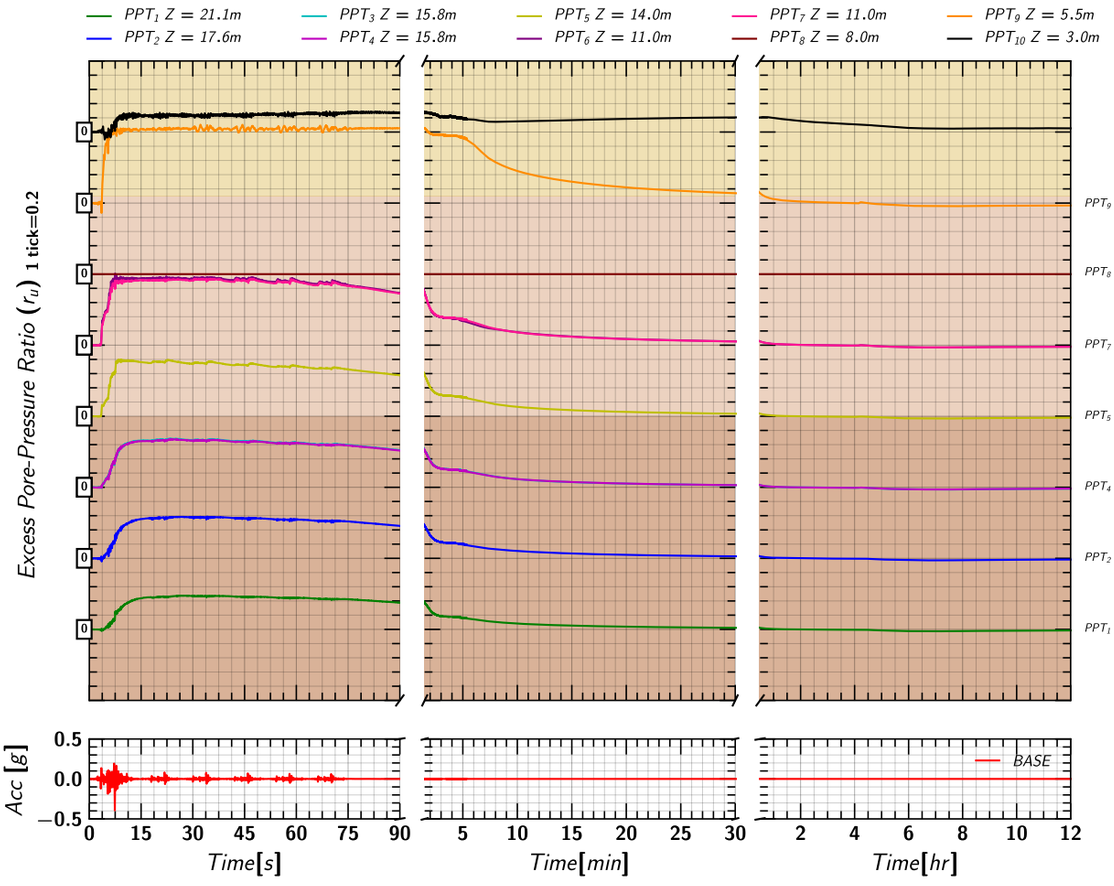

Figure 200. EQM$_6$: Excess pore pressure ratio (r_u) estimated from measurements by Keller transducers during and post the applied earthquake motion.

J.9 Excess Pore pressure Ratio (r_u) Estimated from MS54XXX Transducers

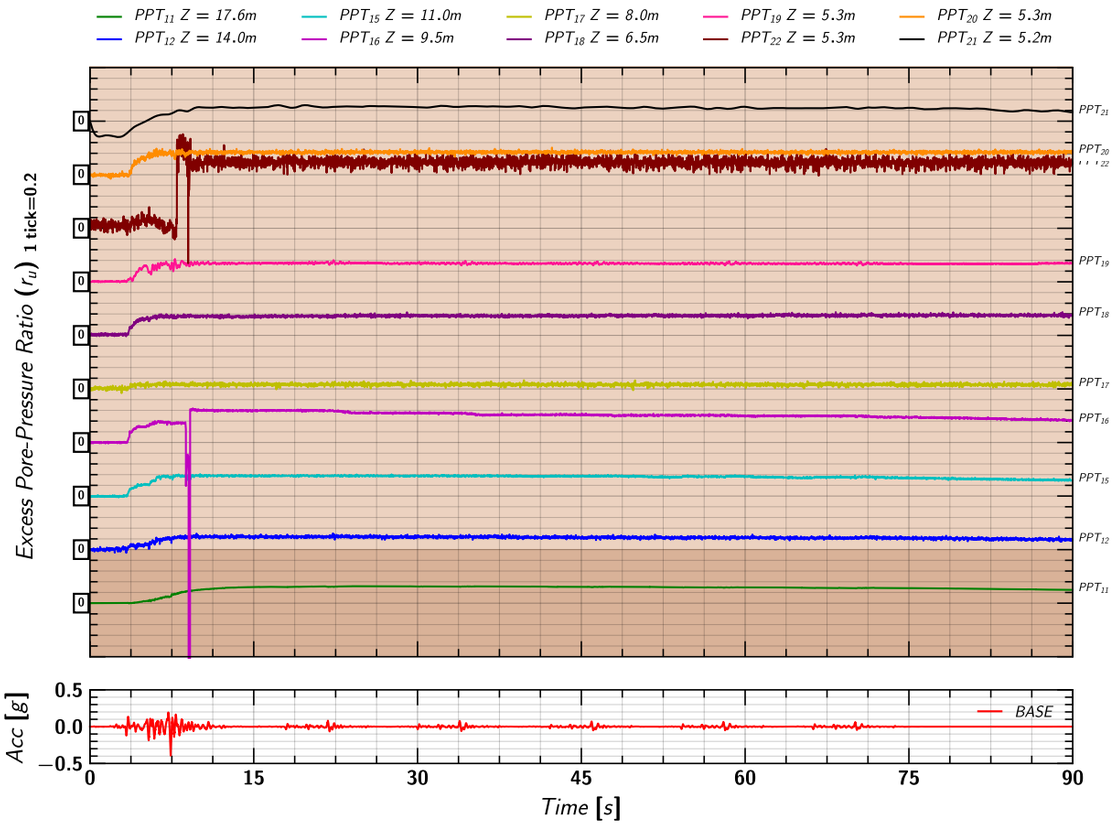

Figure 201. EQM$_6$: Excess pore pressure ratio (r_u) estimated from measurements by MS54XXX transducers during the applied earthquake motion.

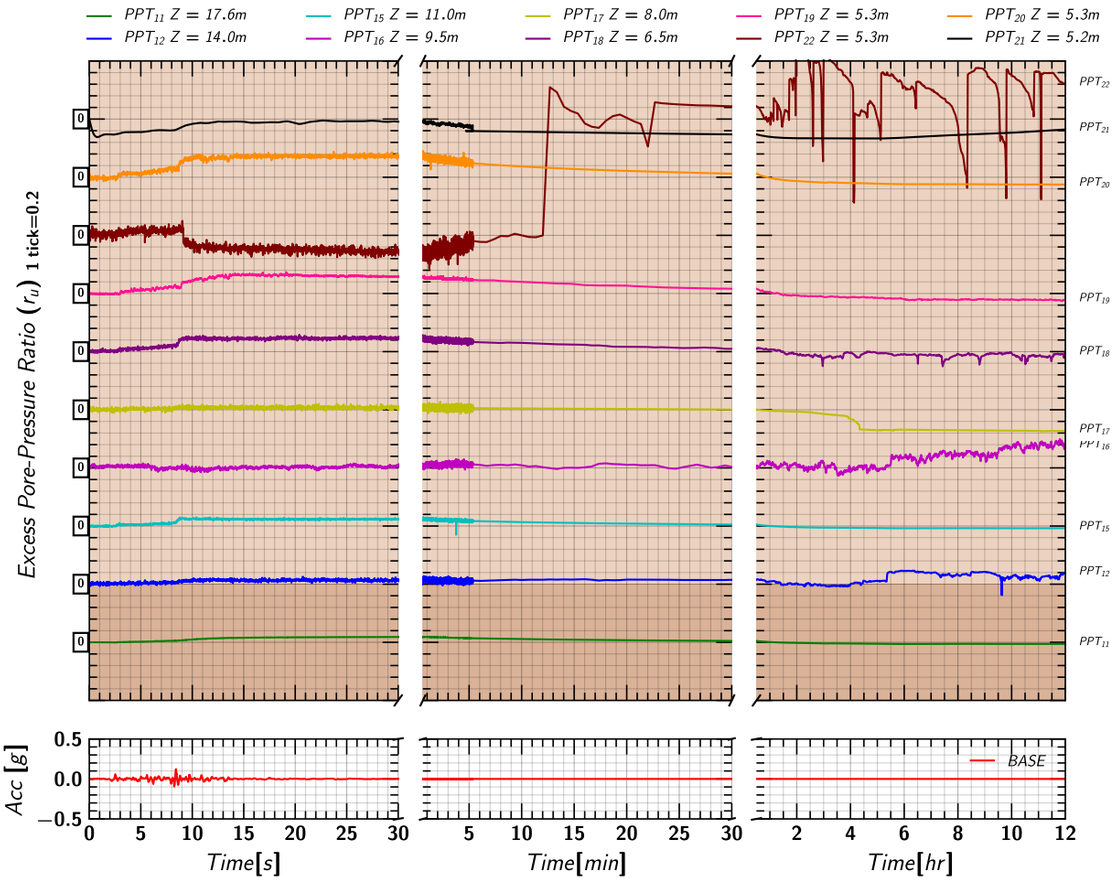

Figure 202. EQM$_6$: Excess pore pressure ratio (r_u) estimated from measurements by MS54XXX transducers during and post the applied earthquake motion.

J.10 Axial Load in Pile 1

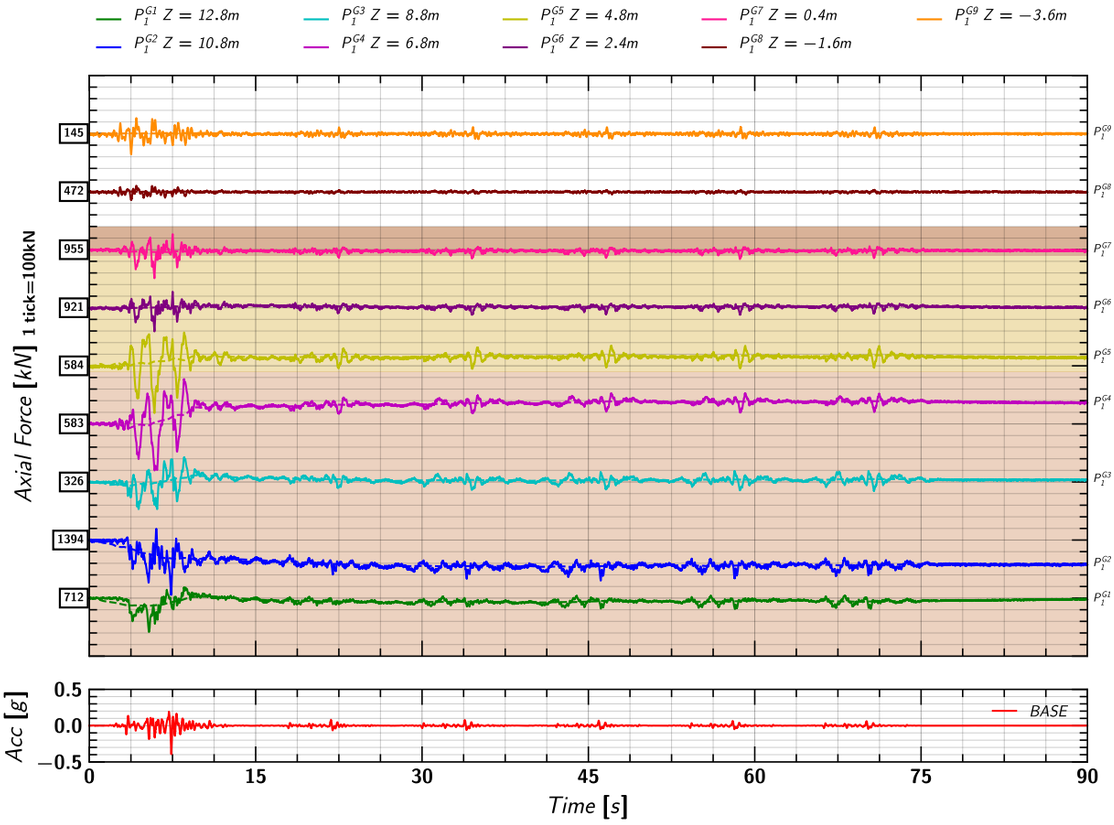

Figure 203. EQM$_6$: Axial load measurements from pile 1 strain gages during the applied earthquake motion.

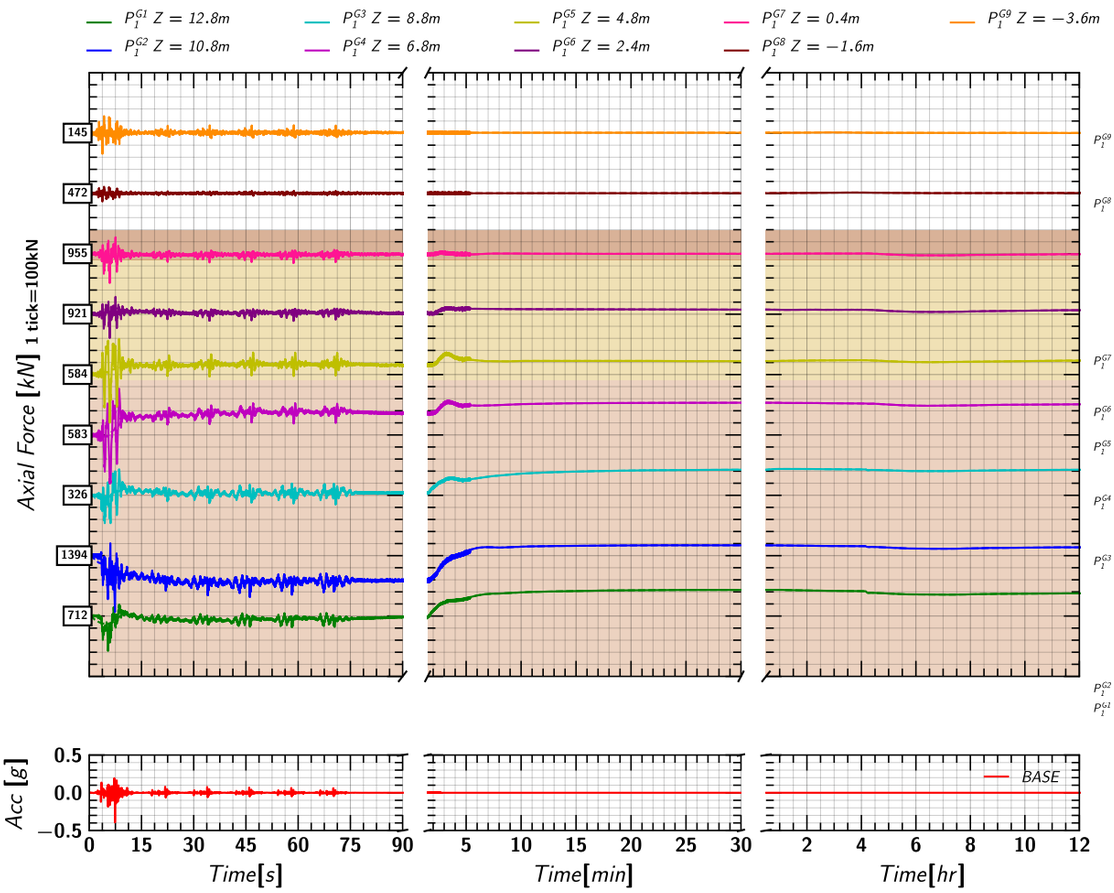

Figure 204. EQM$_6$: Axial load measurements from pile 1 strain gages during and post the applied earthquake motion.

J.11 Axial Load in Pile 2

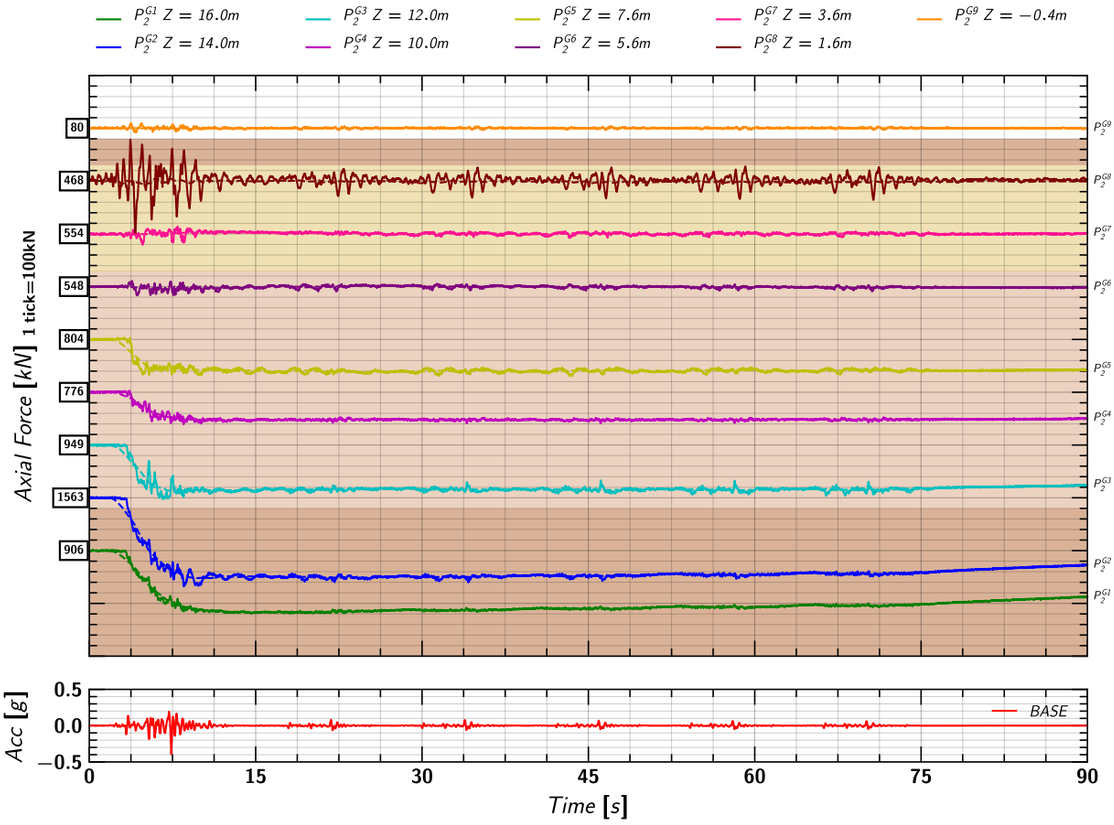

Figure 205. EQM$_6$: Axial load measurements from pile 2 strain gages during the applied earthquake motion.

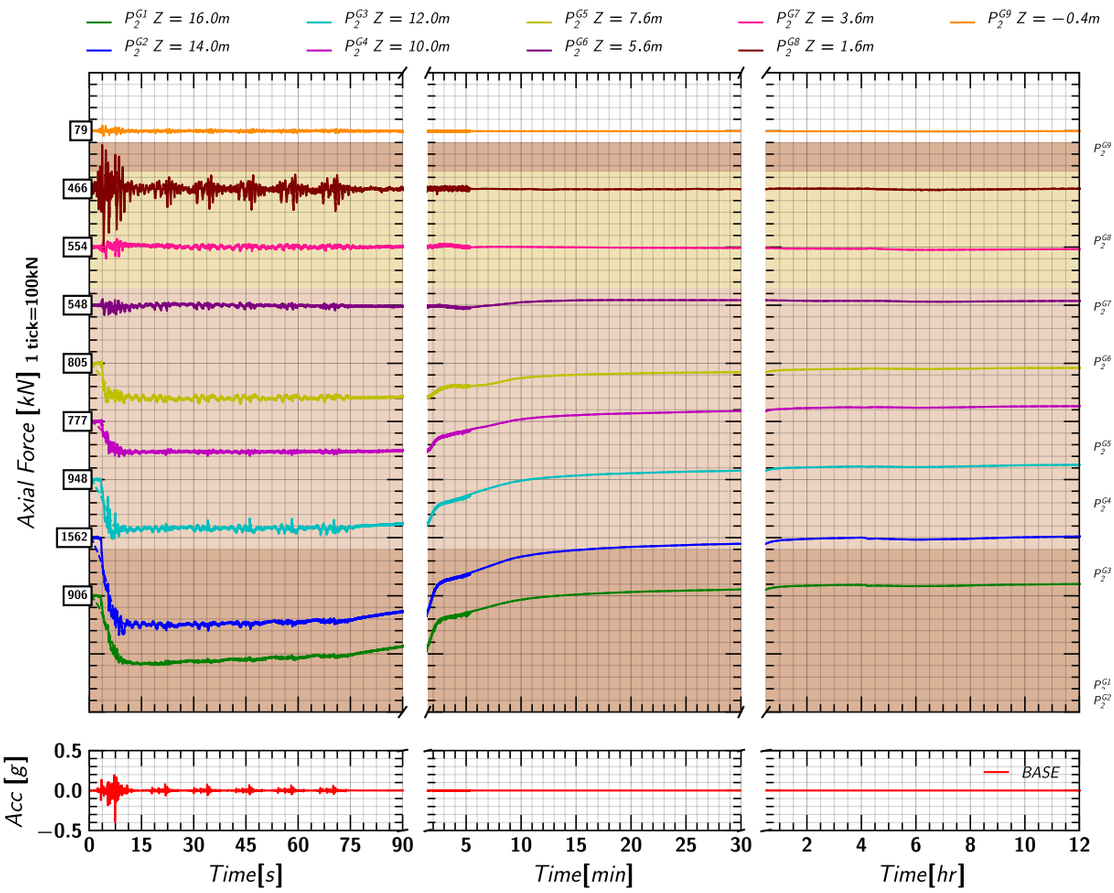

Figure 206. EQM$_6$: Axial load measurements from pile 2 strain gages during and post the applied earthquake motion.

J.12 Pore pressure and Axial Load Profile

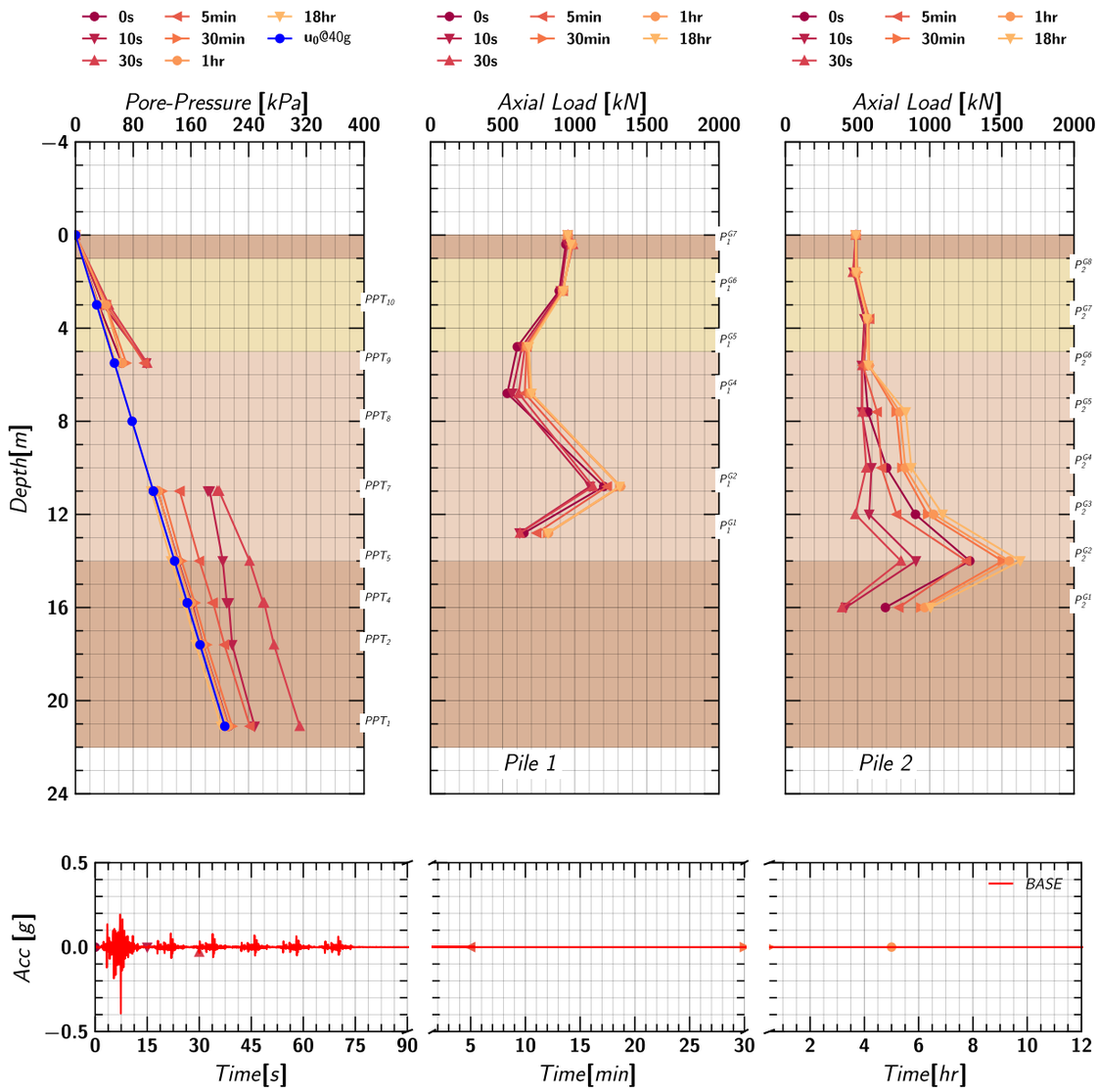

Figure 207. EQM6: Pore pressure and axial load profile in pile 1 and pile 2 at different times during and post the applied earthquake motion.

K. Day 2 Spin 2 Spin Up/Down Cycles

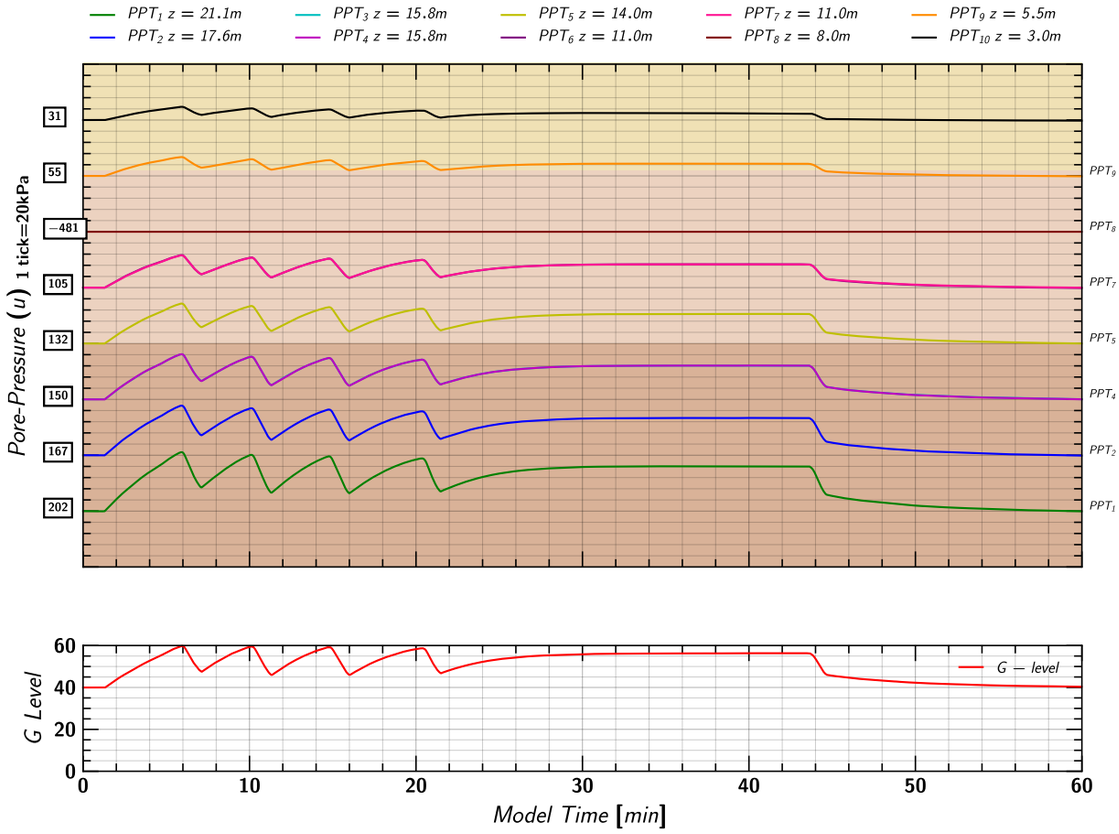

Figure 208. Day 2 Spin 2 Spin Up/Down Cycles: Pore pressures measurements in soil from Keller transducers.

Figure 209. Day 2 Spin 2 Spin Up/Down Cycles: Pore pressures measurements in soil from MS54XXX transducers.

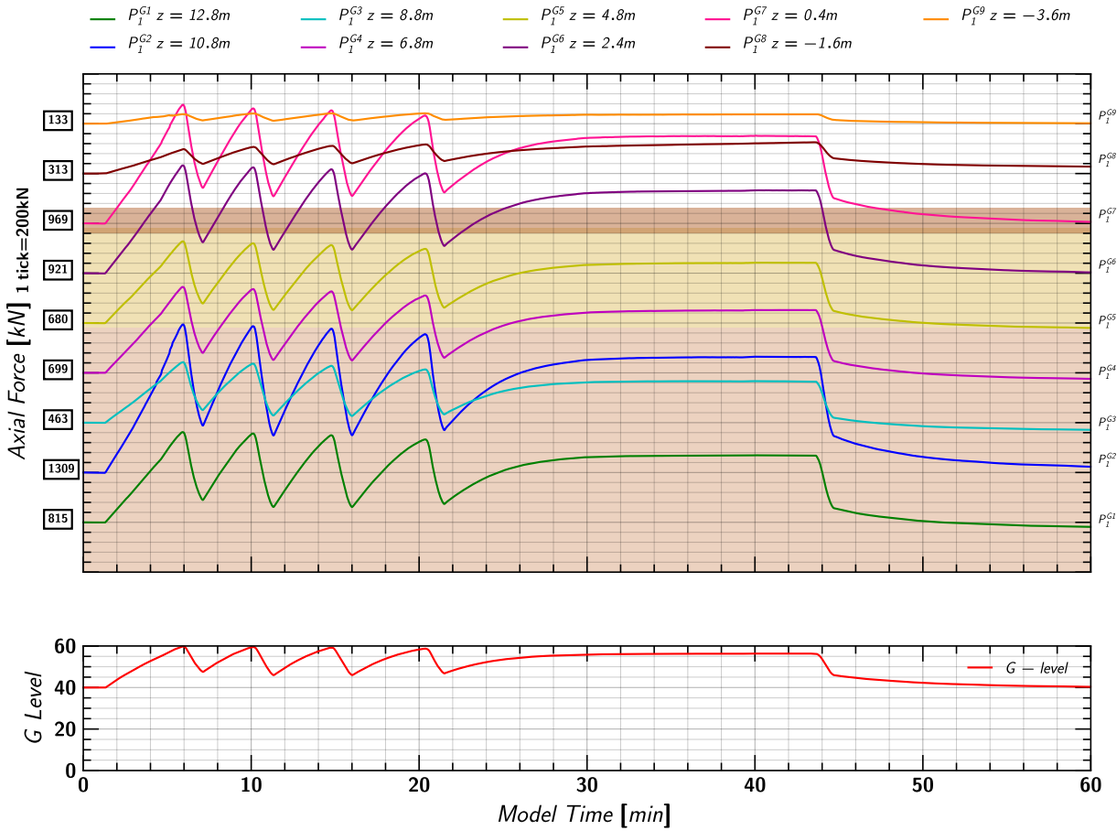

Figure 210. Day 2 Spin 2 Spin Up/Down Cycles: Axial load measurements in Pile 1.

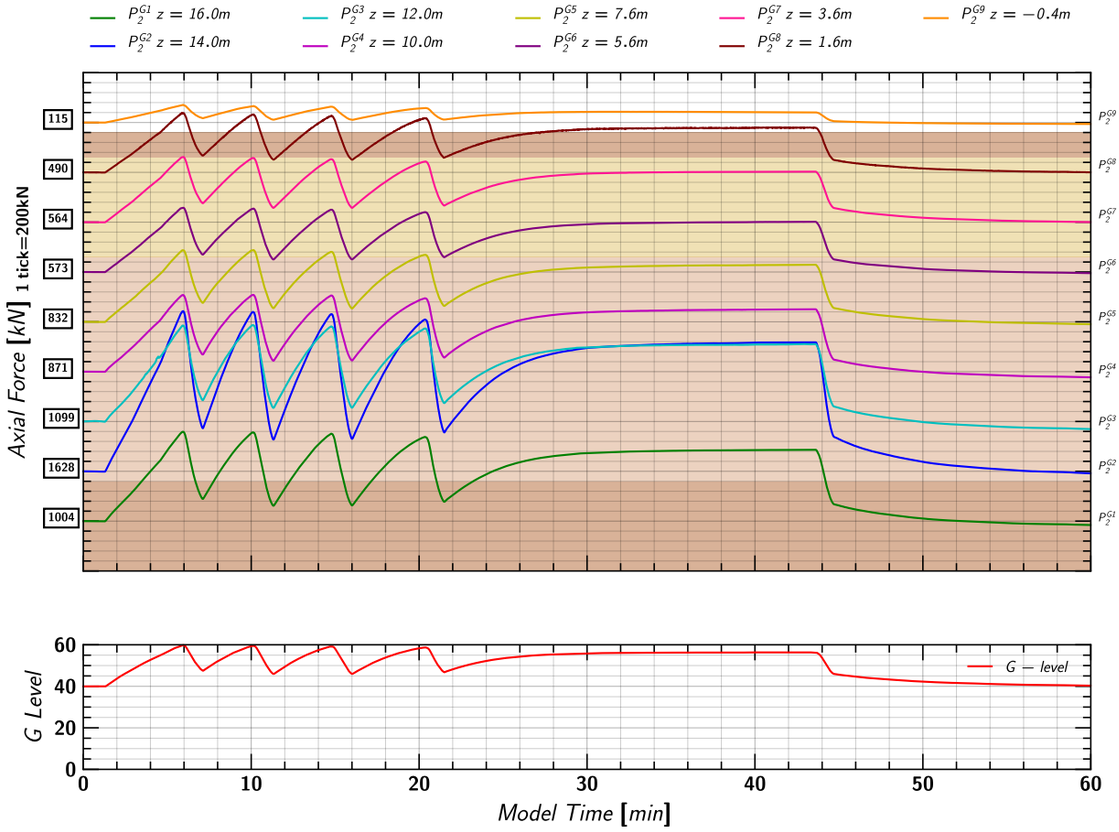

Figure 211. Day 2 Spin 2 Spin Up/Down Cycles: Axial load measurements in Pile 2.

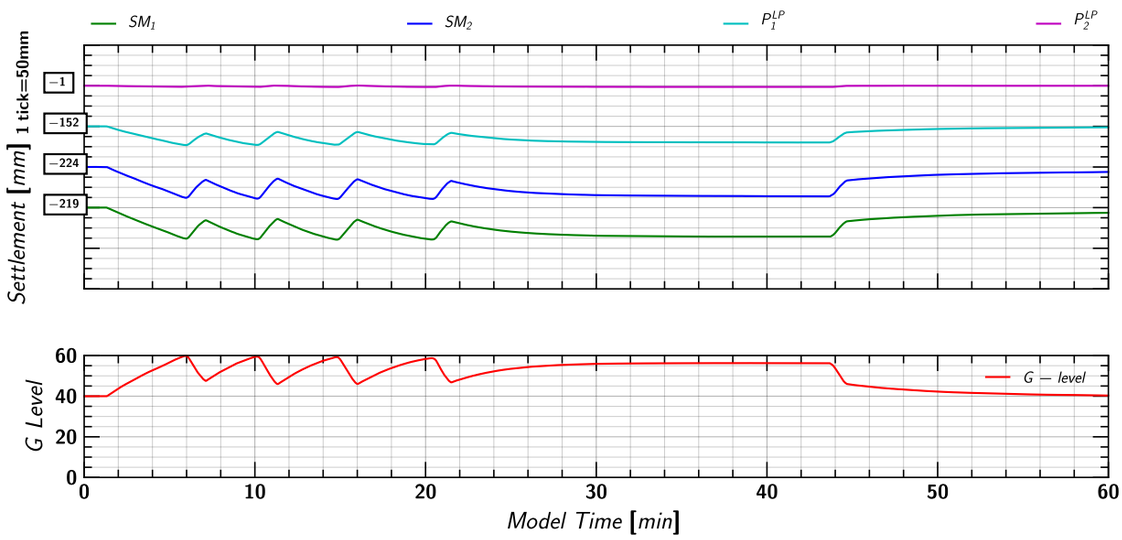

Figure 212. Day 2 Spin 2 Day 2 Spin 2 Spin Up/Down Cycles: Settlement measurements of soil and pile from linear potentiometers.

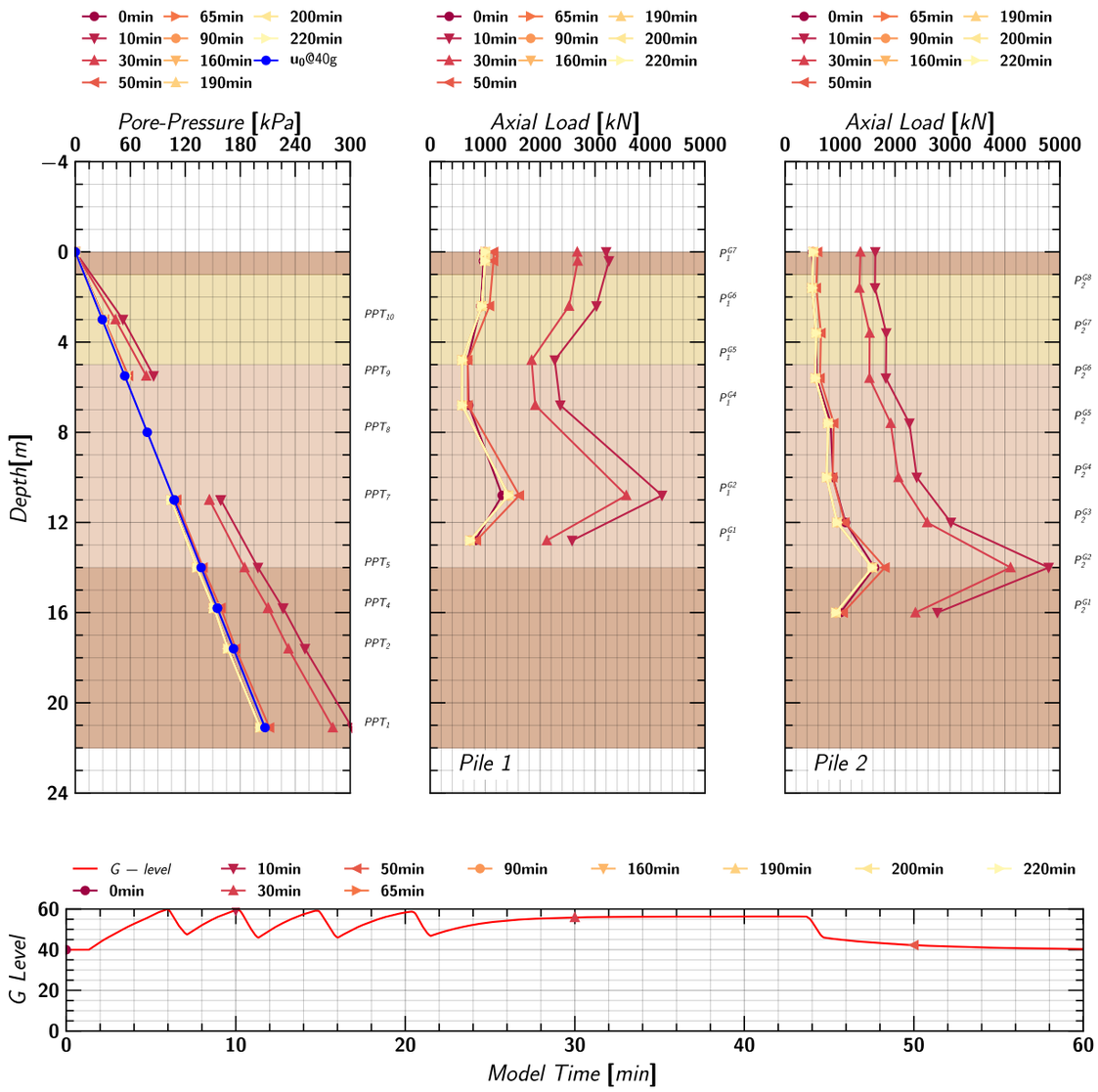

Figure 213. Day 2 Spin 2 Day 2 Spin 2 Spin Up/Down Cycles: Axial load profile of pile 1 and pile 2 at different times during the test.

L. Temperature Corrections on Centrifuge Cone Penetration Tests

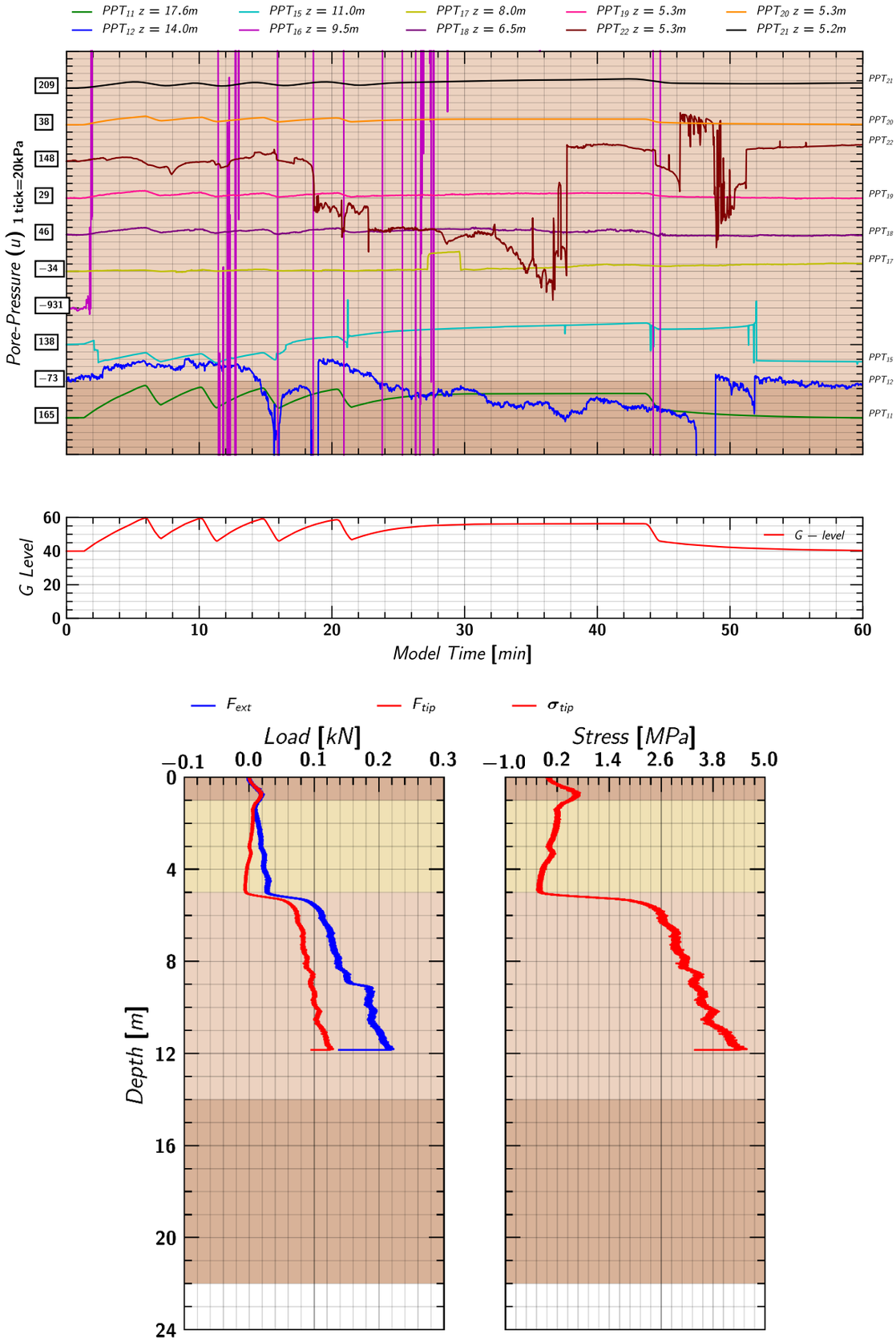

Figure 214. Raw results from centrifuge cone penetration test CPT₃.

Close inspection of CPT_3 results (Figure 214), showed a decreasing tip load in the clay layer. While a smaller tip load is expected to be in the clay layer, a negative value is alarming. Past centrifuge tests performed by Price (2018) on the 6 mm diameter cone (the one used in this test) in Shavitz at CGM, UC Davis also witnessed temperature effects on the CPT probe. Temperature change in the strain gage can result in shift of the zero reading of the load cell. Since the tip load cell gage is installed close to the cone's tip, any temperature change during the insertion can result in error in the recorded tip load (F_{tip}). The

external load cell being outside soil would not have any temperature effects on the load measured during the test.

Changes in temperature can significantly affect the cone-tip load especially if the change in temperature is large or the measured loads are very small. During a centrifuge test, the temperature in the room increases while the model temperature remains almost constant because of water (having high latent heat) evaporation. This leads to rise in the temperature of the CPT probe hanging in the air. During the test, when the probe gets inserted in the model, the temperature of the probe quickly comes down resulting in shift in the zero load and error in the tip load measurement. On the large centrifuge especially during hot days, the temperature difference can become 10-20° Celsius. Price (2018) kept the cone's tip submerged in water just above the model to minimize any temperature change near its tip.

Since this test was done in the month of July, the ambient air temperature was quite high (~30-35° C). Also, during the test the cone tip was hanging in the air which because of the centrifuge spinning further increased its temperature before it was pushed in the soil. This could have resulted in the shifting of the zero reading throughout the test leading to anomality in the tip load data.

To apply temperature corrections to the raw CPT data, experiments were carried to find out the temperature sensitivity of the CPT probe and the rate of cooling constants of the probe in different media (water and air) as described in the sections below.

L.1 Calibration of CPT for Temperature Sensitivity

The temperature sensitivity of the cone tip was measured at 1 g using a calibration water bath maintained in the range of 30°-62° Celsius. The results are shown in Figure 215. The temperature sensitivity of the probe was approximated by a linear fit of 0.65 lbf/°C within the temperature range of 30°-62° C. The sensitivity when projected with the cone tip area would result in 0.12 MPa/°C.

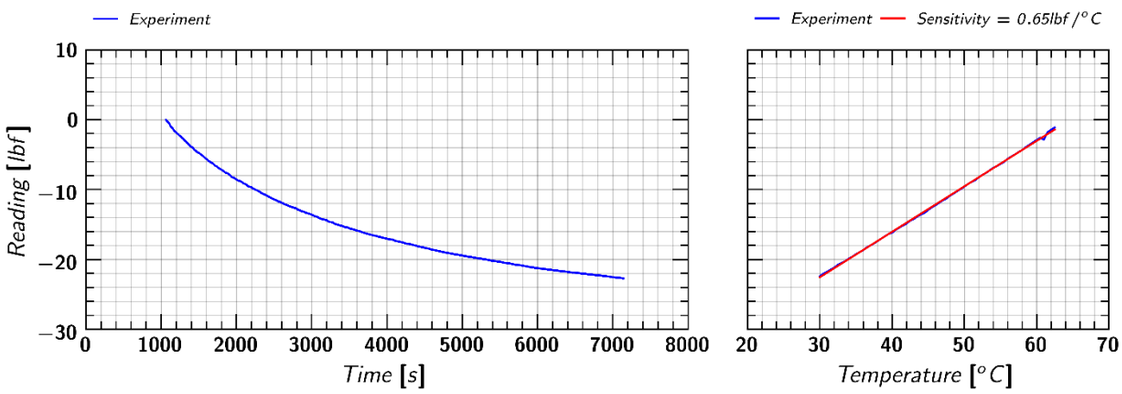

Figure 215 Temperature sensitivity of 6mm CPT#33667-03.

L.2 Rate of Cooling Constants, k

Multiple tests on cone tip temperature changes in air, water and soil were carried out to determine the rate of cooling constant (k) assuming Newton's Law of cooling. Section L.2.1 and Section L.2.2 and Section describes the experiments and their results. Table 30 summarizes the rate of cooling constants in different mediums and the time it took to decrease to 1% of temperature difference (ΔT).

L.2.1 CPT Penetration and Retraction Test

Three sets of experiments were performed in which, the cone tip was pushed in the bucket with saturated soil maintained at 20° Celsius and retracted back to a calibrated water bath maintained at 36° Celsius. The results are shown in Figure 216 and Figure 217 respectively. From these tests, assuming Newton's law of cooling, the average rate of cooling constant in water (k_w) and soil (k_s) was found to be k_w=0.1/s and k_s= 0.12/s respectively.

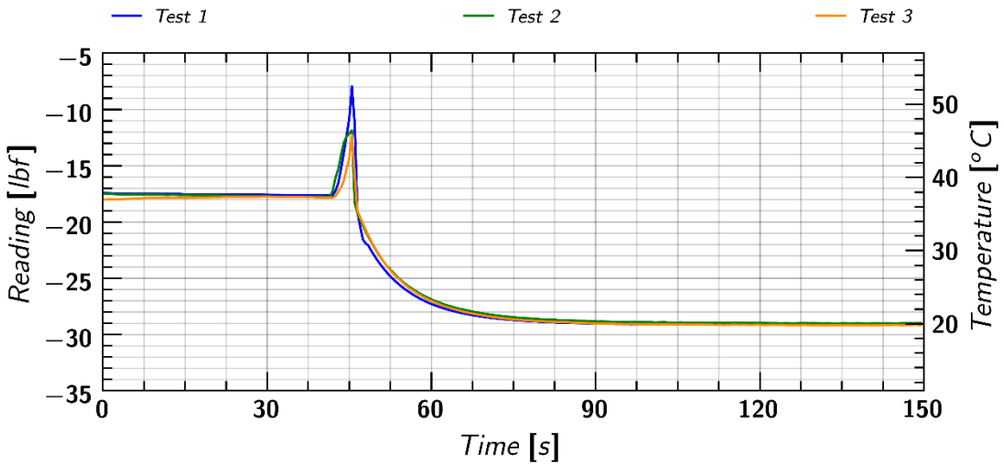

Figure 216. Temperature change of CPT probe while insertion in the bucket of sand maintained at ~ 20º C.

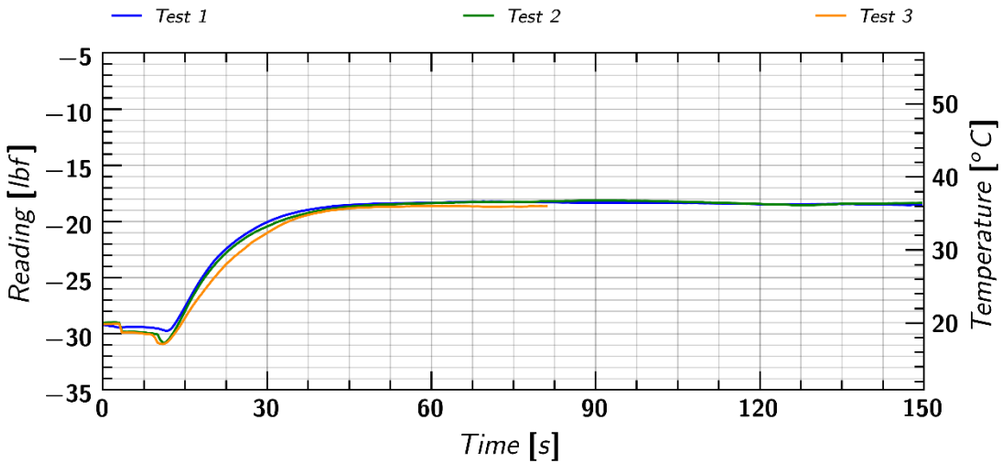

Figure 217. Temperature change of CPT probe in water at maintained at ~36º C after retraction from soil.

L.2.2 Rate of Cooling Constant (k_a) in Air

Multiple experiments were performed in which the temperature of the cone tip was increased in a calibrated hot bath and then allowed to decrease in air. On an average, the rate of cooling constant constant (k_a) was measured to be k_a=0.01/s.

Similarly, the rate of constant ($k_{a,cen}$) during the centrifuge test was determined from the slow data recordings during the test. On an average the rate was measured to be $k_{a,cen}$=0.03/s. The higher rate during the spinning could be attributed to the blowing of the wind during the spinning of centrifuge.

Table 30. Rate of cooling constant of cone tip in different mediums.

Rate of cooling (k) in		***Time for 1% of ΔT (s)***
Water (k_w)	0.10	46
Soil (k_s)	0.12	38
Air (k_a)	0.01	530
Air in centrifuge ($k_{a,cen}$)	0.03	140

L.3 Temperature Corrections

Section L.1 and Section L.2 forms the base of the temperature correction. If the cone sensitivity and the temperature changes of the tip with time (during the push and retraction) is known, temperature corrections on the tip reading can be accordingly applied. With the temperature sensitivity of the cone tip estimated as 0.12 MPa/ºC (Section L.1), the methodology described below was used to determine the temperature of the tip during its penetration and retraction.

L.3.1 Methodology

For estimating the temperature changes in tip during the CPT test, the following assumptions with appropriate justifications were made.

Assumption 1: In ideal conditions, if there is no temperature effect, the reading before the probe insertion and after retraction would be the same. Any change in the reading would attribute to the change in temperature of the tip.

Assumption 2: The undrained shear strength (s_u) of the clay estimated from the hand vane shear tests (see Section 6.2), can be used to estimate the corresponding cone tip resistance. This can give the cone tip temperature change in the clay layer during insertion. From undrained shear strength (s_u), the cone tip resistance (q_t) can be estimated as $q_t=\sigma_{vo} + s_u N_{kt}$, where N_{kt} is the empirical cone factor (Lunne et al. 1997). On an average the N_{kt} factor can be taken as 15.

Assumption 3: Assuming Newton's Law of cooling with rate constant (k_s) in soil, the temperature change with time can be estimated during penetration and until retraction. As shown in Table 25, in soil the cone tip would take 38 seconds to reach the 1% of ΔT (i.e. the temperature difference between the cone tip and the model). The probe insertion in the model took 30 seconds and at least another 10-15 seconds before the retraction started. This gave enough time for the cone tip to come in equilibrium with the model temperature before retraction started.

Assumption 4: The temperature of the cone tip just after retraction is assumed to be equal to the temperature of the model surface. This assumption can be validated from 1 g calibration tests performed on the bucket of sand (see Section L.2.1 above). From Figure 217, the temperature of the tip just after retraction was measured to be 20° Celsius, which would correspond to the temperature of the model surface.

Assumption 5: To further constrain the correction, a linear increase in temperature of 3° C from the penetration depth (300mm) to the model surface was assumed. Since the cone tip temperature is assumed to achieve equilibrium with the model, during retraction it is assumed to follow the temperature of the model.

L.4 Applying Temperature Correction on Raw CPT Recordings

The assumptions described in the above section were used on slow data recordings to estimate the temperature changes in tip during the CPT test. Figure 218 show the estimated temperature change in cone tip during CPT_3 sounding. Once the temperature change in the cone tip was estimated, the tip stress was corrected by multiplying it with temperature sensitivity. Figure 218 shows the raw and corrected CPT_3 tip stress.

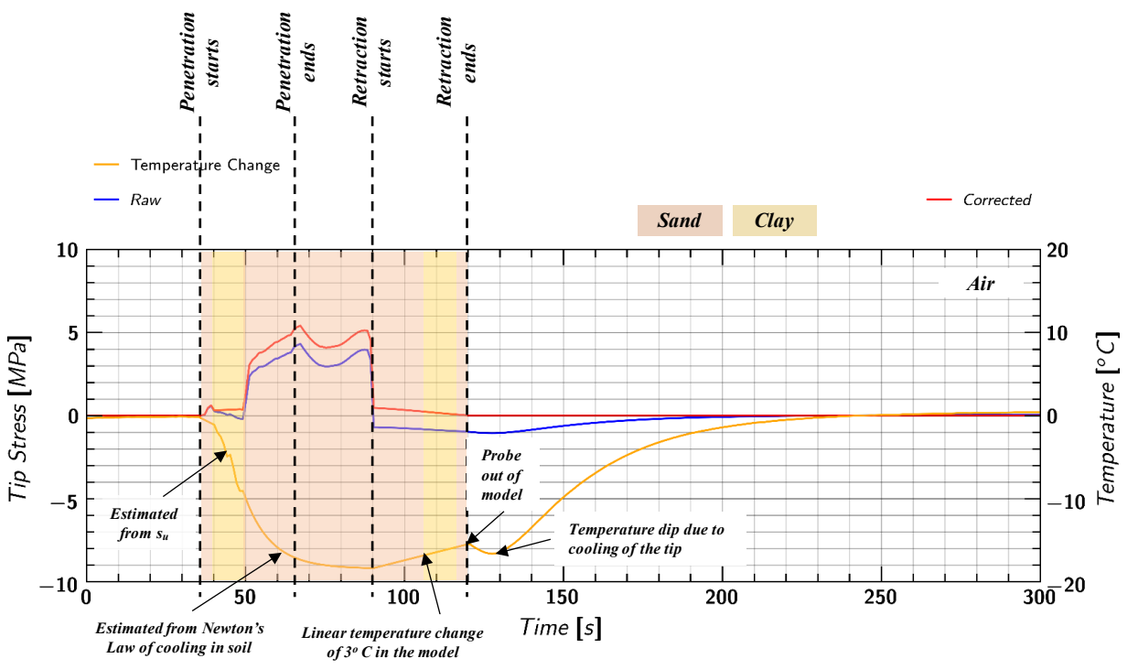

Figure 218. Temperature change in the cone tip and its correction applied on CPT_3 sounding.

It must be noted that while applying the above corrections, the temperature changes from frictional heat generated during cone penetration is not explicitly considered. However, such changes are expected to be very small in submerged soil conditions.

Like Figure 218, temperature corrections were applied to all CPT recordings. The recorded temperature of centrifuge room measured during the day of test matched with the one estimated from the correction method. The model temperature was found to be 20^{o} C on the surface and 17^{o}C at the depth of 30 cm and remained almost constant during the two days of the test.

M. Interpreting Tip Stress from Centrifuge Pile Load Test

Since, the external load cell attached to the pile load test probe measured the total resistance offered on the pile i.e., the sum of the skin friction and the tip resistance, a rational methodology was developed to extract the tip load. Additionally, the effect of pile tip angle on the measured tip load was also considered and quantified. The following section describes the methodology used to extract the tip load from pile load tests.

M.1 Centrifuge Test SKS01: Tip Load as a Factor of External Load (α)

In SKS01, several 10 mm CPTs with cone tip angle of 60 degrees were performed on dense-dense (DD), dense-loose (DL), loose-loose (LL) and loose-dense (LD) dry Ottawa F-65 sand layers. The model consisted of 2 layers of sand at different densities: loose (L) at relative density of D_r=40% and dense (D) at relative density of D_r=85%. The thickness of the layers were 20 cm and 29 cm, respectively. The test was performed on the large centrifuge with a scale factor of 40. Figure 219 plots the cone tip load (α) as a factor of external load with protype depth.

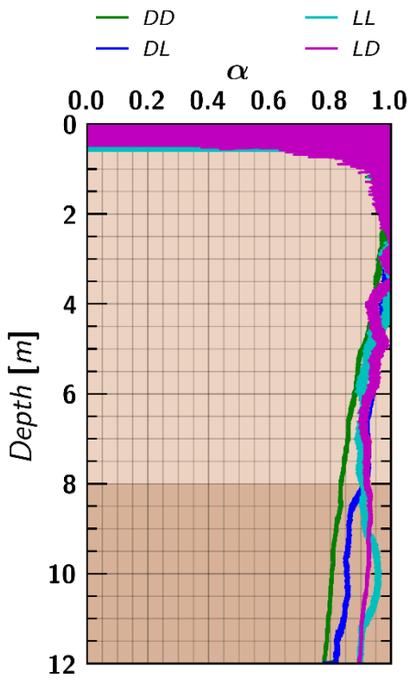

Figure 219. Cone tip load (α) as a factor of external load in different soil profiles (from centrifuge test SKS01).

The following observations can be made from the above plot:

1) The factor α is almost constant with depth for the LD and LL layers to approximately 0.9.
2) The factor α for DL and DD profiles seems to decrease with depth. However, it is in the range of 0.7 to 0.9.

M.1.1 Effect of Pile Tip Angle on Measured Tip Resistance

Experimental results from Nowatzki and Karafiath (1972) and Durgunoglu and Mitchell (1973) shows that the cone tip resistance increases with apex angle for smooth bases. Durgunoglu and Mitchell (1973) found that for rough bases, the tip resistance does not change for apex angles greater than 30 degrees but increase for angle below 30 degrees. This was due to the formation of a soil wedge in front of blunt rough bases (tip) during penetration. For smooth bases, the bearing capacity factors N_c and N_q increased approximately 1.5-2 times for an apex angle of 120 degrees as compared to 60 degrees.

Nowatzki and Karafiath (1972) conducted a series of penetration tests on Jones Beach sand at different relative densities and cone apex angles. For soils with high relative densities, the cone tip resistance increased significantly with apex angle. However, for low relative densities, the effect of tip apex angle was very little. For dense soils, the cone tip resistance increased by a factor of ~1.4 for an apex angle of 120 degree as compared to 60 degrees. Recent works of Johnson (2003), used statistical micromechanics theory to simulate the effect of apex angle on tip resistance.

M.1.2 Methodology to Extract Tip Load from Pile Load Test

The current test SKS02 had similar soil profiles and relative densities as SKS01. The only difference was the submerged soil condition and a 10 cm of clay layer at the surface overlain by 2.5 cm of Monterey sand layer. Assuming similar conditions existed across test SKS01 and SK02, the cone tip load was extracted from the external load with the factor α as found out in the Section M.1. However, it must be noted that in SKS01 although the CPT probe had the same diameter of 10 mm, the apex angle was 60 degrees. Thus, effect of cone apex angle was also be considered in interpreting the tip load.

The following equations can be written for two identical CPT probes with same diameter and under same loading conditions but having different tip apex angles of 60 degrees and 120 degrees, respectively.

$$F_{ext}^{60} = F_{tip}^{60} + F_{shaft}^{60} \quad where \;\; F_{tip}^{60} = \alpha F_{ext}^{60} \tag{1}$$

$$F_{ext}^{120} = F_{tip}^{120} + F_{shaft}^{120} \quad where \;\; F_{shaft}^{120} = F_{shaft}^{60} \tag{2}$$

It must be noted that the second equation above corresponds to the pile load test (apex angle of 120 degrees). Considering the effect of tip apex angle, tip load F_{tip}^{120} can be written as

$$F_{tip}^{120} = \beta F_{tip}^{60} \tag{3}$$

Where, β is the factor to account for increase in tip resistance for larger apex angle of 120 degrees as compared to 60 degree. Equation 1 and 2 can then be solved to get F_{tip}^{120} and equivalent loads $F_{tip}^{60}, F_{ext}^{60}$ for apex angle 60 degrees.

$$F_{tip}^{120} = \frac{\alpha\beta F_{ext}^{120}}{\beta\alpha-\alpha+1}, \qquad F_{ext}^{60} = \frac{F_{ext}^{120}}{\beta\alpha-\alpha+1}, \qquad F_{tip}^{60} = \frac{\alpha F_{ext}^{120}}{\beta\alpha-\alpha+1}, \tag{4}$$

Knowing the factors α and β in the above Equation 4, the cone tip resistance can be estimated for both apex angles of 120 and 60 degrees.

M.1.3 Interpreting the Results of Pile Load Test

Assuming similar soil profiles across SKS01 and SKS02 tests, the cone tip load factor α could be taken in the range of $\alpha \approx$ 0.8-0.9. The experimental results from Durgunoglu and Mitchell (1973) and Nowatzki and Karafiath (1972) on an average suggest increase of cone tip resistance by 40-60% for an apex angle of 120 degrees as compared to 60 degrees. Thus, the value of factor β was taken can be taken in the range of $\beta\approx$1.4-1.6. Figure 40 plots the raw pile load test results and interpreted tip load with the factors; α=0.8 and $\beta\approx$1.4.